A First Measurement of the Charged Current DIS Cross Sections with Longitudinally Polarised Electrons in the H1 Experiment at HERA

Dissertation
an der Fakultät für Physik
der Ludwig-Maximilians-Universität München

vorgelegt von
Biljana Antunović
aus Sarajevo (Bosnien)

München 2007

1. Gutachter:	Prof. Dr. Christian Kiesling
2. Gutachter:	Prof. Dr. Otmar Biebel
Tag der mündlichen Prüfung:	16. März 2007

Abstract

The analysis presented in this thesis is based on data from electron-proton collisions with longitudinally polarised electron beams at a centre-of-mass energy of $\sqrt{s} = 319$ GeV. The data were taken with the H1 detector at the HERA collider in the year 2005 corresponding to two polarisation states: a left-handed electron polarisation of -27% and a right-handed electron polarisation of $+37\%$, corresponding to integrated luminosities of 68.6 pb^{-1} and 29.6 pb^{-1}, respectively. The inclusive total deep inelastic charged current cross section and the differential cross sections are measured for both helicities in the kinematic domain $Q^2 > 400$ GeV^2 and $y < 0.9$. The entire analysis chain necessary for the determination of the cross sections is described with emphasis on the understanding of the performance of the Liquid Argon trigger system. The experimental results obtained are consistent with the predictions of the Standard Model. In particular, the measurement of the total polarised charged current cross section confirms the Standard Model expectation that there are no weak charged current interactions mediated by a hypothetical right-handed W boson. In addition, a measurement of the charged current structure function F_2^{cc} has been performed at the H1 experiment for the first time. The measurements are well described by the theoretical expectations based on parton distributions derived from inclusive neutral current measurements in H1, and are in agreement with published data from the ZEUS ($e^{\pm}p$) and CCFR ($\overset{(-)}{\nu}_{\mu}Fe$) experiments.

Kurzfassung

In dieser Arbeit wird die Analyse von der Streuung von longitudinal polarisierten Elektronen an Protonen bei einer Schwerpunktsenergie von $\sqrt{s} = 319$ GeV präsentiert. Die Daten wurden mit dem H1 Experiment am HERA Beschleuniger im Jahre 2005 aufgenommen. Sie bestehen aus zwei Datensätzen: linkshändig polarisierte Elektronen mit einer Polarisation von -27% und rechtshändig polarisierte Elektronen mit einer Polarisation von 37% mit integrierten Luminositäten von 68.6 pb^{-1} und 29.6 pb^{-1}. Der inklusive totale Wirkungsquerschnitt für die tief-inelastische Streuung mit geladem Strom und die differentiellen Wirkungsquerschnitte werden für beide Helizitäten in der kinematischen Region $Q^2 > 400$ GeV^2 und $y < 0.9$ gemessen. Die gesamte Analysekette, welche für die Bestimmung der Wirkungsquerschnitte notwendig ist, wird beschrieben. Besonderer Wert wird auf das Verständnis des Flüssig-Argon Kalorimetertrigger-Systems gelegt. Die erhaltenen experimentellen Resultate sind mit den Voraussagen des Standardmodells gut verträglich. Insbesondere bestätigt die Messung des totalen polarisierten Wirkungsquerschnitts für den geladenen Strom die Vorhersage des Standardmodells, dass es keine schwachen Wechselwirkungen durch hypothetishe rechtshändige W-Bosonen gibt. Zusätzlich konnte zum ersten Mal die Strukturfunktion F_2^{cc} für geladene Ströme mit dem H1 Experiment gemessen werden. Die Messungen stimmen mit den theoretischen Erwartungen gut überein, die auf den Messungen der Partonenverteilungen mittels der inklusiven Streuung mit neutralem Strom mit dem H1 Detektor gewonnen wurden. Sie stimmen auch mit publizierten Werten von ZEUS ($e^{\pm}p$) und CCFR ($\overset{(-)}{\nu}_{\mu}Fe$) überein.

Contents

Chapter 1

Introduction

Elementary particle physics deals with the understanding of the structure of matter, identification of its building blocks and interactions between them.

In our present knowledge the most fundamental constituents of matter are two types of fermions, the *leptons* and the *quarks*. The leptons exist in three families: the electron (e) and the electron neutrino (ν_e); the muon (μ) and the muon neutrino (ν_μ) and the tau (τ) and the tau neutrino (ν_τ). Similarly the quarks are belonging to three generations: up (u) and down (d), strange (s) and charm (c), bottom (b) and top (t).

The interactions among the particles are mediated by four forces: *gravitational*, *electromagnetic*, *weak* and *strong forces*. However, gravitation is too weak to influence elementary particle interactions. All known interactions are mediated via the exchange of *gauge bosons*. The electromagnetic interaction is mediated by the *photon*. The weak interaction involves the *heavy gauge bosons* Z^0 and $W^\pm$, while the strong interaction is mediated by the *gluons* g. Furthermore, each interaction is associated with a *charge*. Quarks as well as the e, μ and τ leptons are electrically charged. The leptons and quarks both carry in addition a "weak charge". "Colour charge", characteristic for the strong interaction, is carried by the quarks and gluons.

The fundamental nature of forces is summarised in the so-called *Standard Model*, describing the strong interactions of quarks and gluons as well as the unified theory of *electroweak interactions*.

From the experimentalists point of view the examination of the structure of matter is based on a very simple idea: in order to uncover substructure we smash a beam of particles onto a target. The higher the energy we use in these scattering experiments, the better will be the resolution to see what is inside the piece of matter that we are interested in. McAllister and Hofstader [1] managed to measure the size of the proton using a beam of electrons. The experiment showed that the proton has a substructure, unlike the electron which behaves as a point-like particle.

In the late sixties the first experiments on *Deep Inelastic Scattering* (DIS) of electrons on a liquid hydrogen target were carried out at SLAC[1] [2]. DIS means that the energies of the beam particles are sufficiently high to probe the proton substructure

[1]Stanford Linear Accelerator Centre

with a resolution of a fraction of the proton's radius, resulting in a "break up" of the proton where other additional particles are produced. The experiments showed that the proton was not just an extended object with uniform charged density, but an object composed of point like charged constituents. Furthermore, they confirmed *Bjorken's* prediction that at high energies the functions describing the structure of the proton do not depend on the four-momentum transfer squared ("scale invariance"). *Feynman* immediately gave an explanation of the new results with the *Quark Parton Model* (QPM) where the proton is viewed as built up of non-interacting point-like particles, called *partons*. These partons were later identified with the *quarks*, which Gell-Man [3] introduced in order to explain the increasing number of particles observed in the scattering experiments.

However, this simple theoretical model was not able to explain why only about half of the proton momentum is carried by the quarks. In addition, new DIS experiments observed the violation of scale invariance, *scaling violation*. A new theory of the strong interaction, *Quantum-Chromodynamics* (QCD), was able to describe these findings.

The *weak interactions*, first observed in nuclear β-decay were successfully explained by *Fermi's* vector theory as e.g. the transition of a neutron to a proton, an electron and a massless neutral particle called *neutrino* ($n \rightarrow pe^-\bar{\nu}$). But the theory ran into some difficulty because the weak interaction did not conserve parity. It means that a weak interaction, viewed in a mirror, does not occur in a Nature, as *Lee and Yang* [4] proposed in 1956. A number of different experiments have demonstrated that only *left-handed neutrinos* ν_L (and *right-handed anti-neutrinos* $\bar{\nu}_R$) are coupled to charged leptons by weak interactions, giving a clear evidence for *parity violation*. Therefore, a new theory was independently proposed by *Feynman* and *Gell-Mann* (1958) [5] and by *Sudarshan* and *Marshak* (1958) [6]. In order to explain parity violation they suggested a universal charged weak current involving both *vector* and *axial vector currents* (V-A theory). *Glashow* (1961) [7], *Weinberg* (1967) [8] and *Salam* (1968) [9] later proposed a unified *electroweak* theory, in which the weak and electromagnetic interactions are understood as different manifestations of the same (electroweak) force. It took until 1983 that the electroweak unification got its experimental evidence with the discovery of the heavy bosons Z^0 and $W^{\pm}$ by the $p\bar{p}$ collider in CERN.

The worldwide only electron-proton collider, HERA[2], was built with the prime physics goal to study the structure of the proton. After running for almost 10 years, the HERA collider was upgraded during 2000-2001 in order to increase the instantenous luminosity and to provide longitudinally polarised electron beams ("HERA II"). The upgrade made it possible to look into the proton structure with a better precision and, even more, to have improved possibilities to test the electroweak theory of the Standard Model using the DIS interactions. Particularly interesting are *Charged Current* (CC) DIS interactions in which the exchanged particle is a charged boson ($W^{\pm}$), with a neutrino or antineutrino in the final state, i.e. $e^-p \rightarrow \nu X$ or $e^+p \rightarrow \bar{\nu}X$. A characteristic dependence of the CC cross section is predicted within the Standard

[2]Hadron Elektron Ring Anlage

Model framework as being directly proportional to the longitudinal electron polarisation, leading to the absence of right-handed weak charged currents. Additionally, the CC DIS probe specific types of quarks within the proton: With positrons in the initial state the d quark can be studied while with electrons the u quark is probed.

The main aim of this thesis is to measure the polarisation dependence of the total CC DIS cross section in interactions taken with longitudinally polarised electrons at the H1 experiment at the HERA II. A measurement of the total CC DIS cross section is performed in the kinematic range defined by the momentum transfer squared $Q^2 > 400$ GeV^2 and the Bjorken inelasticity $y < 0.9$. The analysis is based on a data set collected in the year 2005 for two polarisation states of the electron beam: a left-handed electron polarisation of $P_e = -27\%$ and a right-handed electron polarisation of $P_e = +37\%$, corresponding to integrated luminosities $L = 68.6$ pb^{-1} and $L = 29.6$ pb^{-1}, respectively. The total, the single differential, and the double differential cross sections are measured. The experimental results are compared to the Standard Model predictions. By merging the left-handed and the right-handed data, an unpolarised CC event sample, with a 6 times larger statistics than the previous H1 measurement, is obtained. Thus, the unpolarised data are used to probe the u quark density within the proton. Furthermore, the first measurement of the charged current structure function F_2^{cc} has been performed with the H1 experiment. The F_2^{cc} results are compared to the Standard Model prediction as well as to the published results from previous experiments.

This thesis is organised in the following way: In chapter 2 a theoretical overview of the CC DIS interactions together with the QCD and the electroweak theory is given. The experimental set up of the HERA accelerator and the H1 detector with emphasis on the components relevant for the present analysis is described in chapter 3. Since the Liquid Argon (LAr) trigger is the most important trigger not only for CC, but for all high Q^2 physics, a detailed description of its principle of operation, readout and simulation is also given in this chapter. The basic principles of the CC cross section measurement are discussed in chapter 4. Chapter 5 deals with the reconstruction of the kinematic variables and the hadronic calibration as important aspects of the CC cross section measurement. It is followed by a discussion of the performance of the LAr trigger at the HERA II, presented in chapter 6. Chapter 7 is concerned with the complete CC analysis. The systematic error discussion is outlined in chapter 8. Finally, the results of the cross section measurement together with the extraction of the structure function F_2^{cc} are given in chapter 10, and the thesis is summarised in chapter 11.

Chapter 2

Theoretical Overview of Charged Current Interactions

Deep Inelastic Scattering (DIS) processes are used to study the proton structure and to test the electroweak part of the *Standard Model*. In this chapter first the DIS process and the kinematic variables needed to describe such processes are introduced. Then the cross section is discussed and its relation to the structure of the proton is explained within the *Quark Parton Model* (QPM) and the theory of *Quantum-Chromodynamics* (QCD). An outline of the *Electroweak Interactions* which form the physical basis of the DIS reactions with polarised leptons is briefly given in the next sections.

2.1 Deep Inelastic Scattering

The scattering of a high energy electron[1] on a nucleon with large momentum transfer (typically a few GeV) leading to a multihadronic final state is called Deep Inelastic Scattering [10,11]. Two types of particle interactions can take place in DIS at HERA: An interaction, in which an electron is scattered on a proton, leading to a scattered electron and a number of hadrons in the final state as the result of the collision, is called a *Neutral Current Interaction* (NC). Since this interaction is mediated by the electrically neutral massless photon and the massive Z^0 boson, electroweak forces are involved. When an electron collides with a proton leaving a neutrino and hadrons in the final state the interaction is referred to as a *Charged Current Interaction* (CC). It is mediated via the charged $W^{\pm}$ boson and therefore subject only to the weak force.

The Feynman diagram of both processes is shown in figure 2.1, using the following notation: k, k' are the four momenta of the incident and outgoing electron and P, P' are the four momenta of the incoming proton and the hadronic final state X, respectively. The exchanged gauge boson carries the four-momentum $q = k - k'$.

In order to describe DIS processes the following kinematic variables are used:

[1] Electron is used for electrons and positrons throughout this thesis, unless specified otherwise.

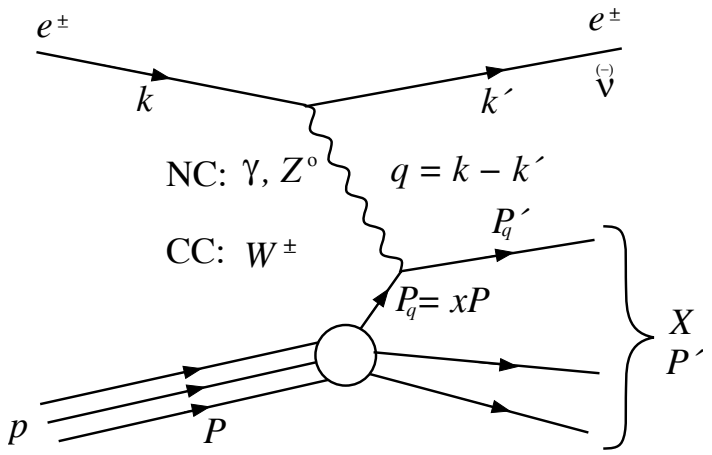

Figure 2.1: Deep inelastic *ep* scattering via virtual boson exchange. The electron interacts with the quark from the proton via the exchange of a γ or Z^0 boson (in NC interactions) and the charged $W^{\pm}$ boson (in CC interactions). The exchanged gauge boson carries the four-momentum $q = k - k'$. Here, k and k' are the four momenta of the incident and outgoing electron (neutrino for CC), whereas P and P' represent four momenta of the incoming proton and the hadronic final state X, respectively. P'_q is the four momentum of the scattered quark.

- The squared four-momentum transfer in the scattering process, representing the virtuality of the exchanged boson:

$$Q^2 = -q^2 = -(k - k')^2. \tag{2.1}$$

- The inelasticity y :

$$y = \frac{P \cdot q}{P \cdot k} \tag{2.2}$$

  which corresponds, in the proton rest frame, to the fraction of the incident electron energy carried by the exchanged boson.

- The Bjorken scaling variable x:

$$x = \frac{Q^2}{2P \cdot q} \tag{2.3}$$

  which is the fraction of the proton momentum carried by the struck quark.

- The centre-of-mass energy squared:

$$s = (k + P)^2 \approx 4E_e E_p \tag{2.4}$$

  where the masses of the electron and proton are neglected,and E_e and E_p are the energies of the electron and proton beam, respectively.

Neglecting all masses the kinematic variables are related by:

$$Q^2 = sxy. \tag{2.5}$$

Since at HERA the centre-of-mass energy is fixed by the energies of electron and proton ($\sqrt{s} \approx 319$ GeV), the scattering process can be described by any two of the variables x, y, and Q^2.

2.2 The Structure of Hadrons

The cross section for deep inelastic electron-proton scattering is described by the tensor product of the leptonic tensor $L_{\mu\nu}$ and the hadronic tensor $W^{\mu\nu}$:

$$d\sigma \propto L_{\mu\nu} W^{\mu\nu}. \tag{2.6}$$

The leptonic tensor $L_{\mu\nu}$ describes the interaction between the lepton and the exchanged boson. The electron is a spin 1/2 particle and obeys the Dirac equation [11], thus the leptonic tensor in Quantum-Electrodynamics (QED) can be written as:

$$L_{\mu\nu} = 2\left[k'_\mu k_\nu + k'_\nu k_\mu + (q^2/2) g_{\mu\nu})\right]. \tag{2.7}$$

In the case of unpolarised particles, $L_{\mu\nu}$ is a function of the four-momenta of the incoming k and the outgoing k' lepton.

Since the real scattering partner of the electron at HERA is the proton, which is not an elementary fermion, it needs a more general description by a hadronic tensor $W^{\mu\nu}$. For electromagnetic interactions its form is given by [11]:

$$W^{\mu\nu} = W_1(-g^{\mu\nu} + \frac{q^\mu q^\nu}{q^2}) + \frac{W_2}{M^2}\left[(p^\mu - \frac{p\cdot q}{q^2} q^\mu) + (p^\nu - \frac{p\cdot q}{q^2} q^\nu)\right]. \tag{2.8}$$

In the case of unpolarised scattering the hadronic tensor $W^{\mu\nu}$ can be represented in terms of the functions $W_{i=1,2}$. The functions W_1 and W_2 are used to describe the structure of the proton and are therefore called *structure functions*. They depend on two Lorentz variables, usually taken as Q^2 and x. It is very common that instead of W_1 and W_2 the following expressions of the structure functions are used:

$$F_1 = M_p W_1 \tag{2.9}$$

$$F_2 = \frac{P\cdot q}{M_p} W_2. \tag{2.10}$$

With the structure functions defined in this way the cross section for the DIS electron-proton interaction [12] can be written as:

$$\frac{d^2\sigma}{dx dQ^2} = \frac{4\pi\alpha^2}{xQ^4}\left(\frac{y^2}{2} 2xF_1 + (1-y)F_2\right) \tag{2.11}$$

where $\alpha = e^2/4\pi$ is the fine structure constant while the helicity dependence of the structure function is given by $(1-y)$ and y^2.

Relations which connect the structure functions and the cross sections for NC and CC interactions will be discussed in sections 2.7 and 2.8.

2.3 Quark Parton Model

In the late sixties, two ideas were put forward motivating experimentalists to have a closer look into the proton structure and its understanding.

Bjorken predicted that at high energies the *structure functions* do not depend on the four-momentum transfer Q^2, but only on the dimensionless variable x. The assumption is known as the *Bjorken scaling hypothesis* [13]. The scale invariance got its physical explanation within the *Quark Parton Model* (QPM) introduced by Feynman [14]. The QPM model describes the proton as a system made of non-interacting point-like constituents (*partons*). These partons are identified as quarks, i.e. particles with spin $\frac{1}{2}$, each carrying a fraction x of the proton momentum. In QPM the electron-proton deep inelastic scattering is interpreted as an *elastic* scattering of the electron on one of the charged partons. As the point-like nature of partons does not introduce any length scale such as $1/Q$ into the description of the proton structure, the scale invariance of the structure functions is explained by the QPM model.

Experimentally Bjorken's hypothesis was confirmed for the first time in the electron-scattering experiments at SLAC in the early seventies [2].

An important prediction of QPM was given by *Callan and Gross* [15] (1968) who suggested that Bjorken's scaling functions F_1 and F_2 are related. For spin $\frac{1}{2}$ partons, the structure functions F_1 and F_2 are related to the distribution functions $q_i(x)$ of the charged partons within the proton as:

$$F_1(x) = \frac{1}{2x} \sum_i e_i^2 x q_i(x) \tag{2.12}$$

$$F_2(x) = \sum_i e_i^2 x q_i(x) \tag{2.13}$$

where $q_i(x)dx$ is the probability to find a parton of electric charge e_i carrying a fraction of the proton momentum in the interval $[x, x + dx]$. These distribution functions are often called the *Parton Distribution Functions* (PDFs) of proton. PDFs can not be calculated within the theory of strong interactions (QCD), but have to be parametrised. As can be seen from equations 2.12 and 2.13 the two structure functions F_1 and F_2 are related by:

$$F_2(x) = 2x \cdot F_1(x) \ . \tag{2.14}$$

This dependence was experimentally confirmed by SLAC for low values of Q^2 indicating spin 1/2 for the partons [2]. The Callan and Gross relation implies that the so-called longitudinal structure function is, in QPM, equal to zero:

$$F_L(x) \equiv F_2 - 2x \cdot F_1(x) = 0 \tag{2.15}$$

meaning that the charged partons only couple to transversely polarised photons. Therefore, with the help of the Callan and Gross relation (equation 2.14) the cross

section for the DIS ep interactions in QPM is simplified to:

$$\frac{d^2\sigma}{dxdQ^2} = \frac{2\pi\alpha^2}{xQ^4}\left((1+(1-y)^2)F_2(x)\right) \tag{2.16}$$

depending only on one structure function, F_2.

Although the Bjorken scaling behaviour and the Callan-Gross relation were experimentally confirmed at SLAC, contradictions soon arose. If the proton is composed of the charged particles (quarks), as it was thought, the integration of the parton densities over all partons inside the proton and over the whole kinematic range has to be equal to unity:

$$\int_0^1 xdx \sum_f q_f(x) = 1\ . \tag{2.17}$$

As the experimental value turned to be ≈ 0.5 [16] it was concluded that half of the proton momentum was carried by neutral particles, later identified as the gluons. Even more, QPM does not predict several other experimental results like quark confinement, logarithmic violation of the scaling behaviour etc.

2.4 Scaling Violations and Quantum Chromodynamics

The fixed target lepton-nucleon scattering experiments have observed deviations of the structure function from perfect scaling behaviour at high Q^2 [17, 18]. The QPM did not give an explanation of the observed phenomenon of *scaling violation* and therefore a phenomenologically richer theory was needed.

Scaling violations are indeed expected in the theory of *Quantum Chromodynamics* (QCD), the theory of strong interactions [10]. It describes the interactions between the constituents of the proton. In QCD the partons are introduced as *quarks* carrying an additional quantum number, the *colour*[2], and interacting by the exchange of *gluons*. The gluons are the *gauge bosons* of QCD binding the quarks inside the proton[3]. In addition, the gluons carring *colour* interact themselves via the strong interaction.

Running Coupling Constant and Asymptotic Freedom

The self-interaction of the gluons leads to a unique variation of the coupling constant α_s with the scale Q^2, which in leading order can be written as [12]:

$$\alpha_s(Q^2) = \frac{12\pi}{(33-2N_f)\cdot\ln(Q^2/\Lambda^2_{QCD})}\ . \tag{2.18}$$

[2]There are 3 different colours: red, green and blue.

[3]In QCD only colour neutral particles can exist as a free particles. Since both quarks and gluons carry colour they do not exist as a free particles, but are bound into hadrons.

Here N_f is the number of quark *flavours* and Λ_{QCD} is the QCD scale parameter characterising the energy scale at which the coupling constant becomes infinite. At low momentum transfer, corresponding to large distances, the coupling strength *increases*, leading to the *confinement* of quarks and gluons. At high momentum transfer, corresponding to short distances, the coupling constant *decreases*, allowing the quarks to behave as almost free particles inside the proton. This phenomenon is known as *asymptotic freedom* [19, 20]. Asymptotic freedom leads naturally to the Quark Parton model.

DGLAP Evolution Equations

The parton density functions, which in QCD are functions of x and Q^2, cannot be calculated from first principles, but their Q^2 dependence can be calculated within perturbative QCD. The scale dependence of PDFs has its origin in the interactions of the quarks and gluons via elementary processes: gluon emission from quarks $q \to qg$, creation of quark-antiquark pairs from gluons $g \to q\bar{q}$ and gluon emission by gluons $g \to g\bar{g}$. The Q^2 variation of the parton distribution functions is described by the DGLAP (Dokshitzer-Gribov-Lipatov-Altarelli-Parisi) evolution equations [21–24]:

$$\frac{\partial q(x,t)}{\partial t} = \frac{\alpha_s(t)}{2\pi} \int_x^1 \frac{dy}{y} \left(q(y,t) P_{qq}\left(\frac{x}{y}\right) + g(y,t) P_{qg}\left(\frac{x}{y}\right) \right) \tag{2.19}$$

$$\frac{\partial g(x,t)}{\partial t} = \frac{\alpha_s(t)}{2\pi} \int_x^1 \frac{dy}{y} \left(q(y,t) P_{gq}\left(\frac{x}{y}\right) + g(y,t) P_{gg}\left(\frac{x}{y}\right) \right) \tag{2.20}$$

where $t = \ln(Q^2/\Lambda_{QCD})$. The *splitting functions* $P_{ij}\left(\frac{x}{y}\right)$ denote the probability that a parton i with momentum fraction x is emitted by a parton j with momentum fraction y. The Feynman diagrams corresponding to the four splitting functions are shown in figure 2.2, where each diagram corresponds to one splitting function P_{ij}. The Standard

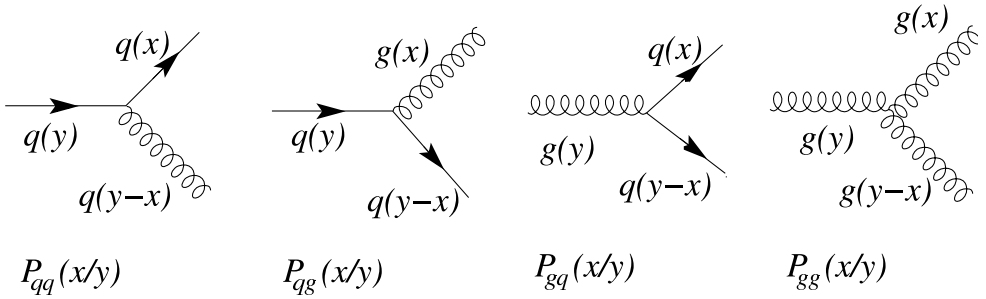

Figure 2.2: Leading order diagrams contributing to the splitting function P_{ij}. The splitting function gives the probability for a parton j with momentum fraction y to split into a parton i with momentum fraction x.

Model predictions in this thesis are calculated using PDFs obtained by the H1 PDF 2000 fit [25] which is a fit to the H1 NC and CC data collected during HERA I.

Experimental Observation of Scaling Violation

The experimentally measured violation of Bjorken scaling from the H1 experiment together with the Standard Model prediction based on the H1 PDF 2000 fit is shown in figure 2.3. It can be seen that the proton structure function F_2 increases with increasing Q^2 at low x and decreases at high x. In the QCD framework this behaviour is explained by *gluon interactions*. The quarks inside the proton emit and absorb gluons. The gluons can split into virtual quark-antiquark pairs which are known as the *sea quarks*. The virtual sea quarks are different from the *valence quarks* which are the constituents of the proton defining the external properties of the proton such as charge and baryon number.

The size of the sea quark contribution to the proton structure function depends on the momentum transfer Q^2 which represents the spatial resolution of the probing current. At small momentum transfer Q^2 only the main constituents of the proton, the individual valence quarks can be seen. However, at high momentum transfer the sea quarks become "visible". If the photon scatters off one of the sea quarks only a small fraction of the proton momentum x is carried by these quarks, giving rise to the structure function at low x. The decrease of the structure function at high x with increasing Q^2 can be understood in the following way: If the photon scatters off one of the valence quarks that has radiated gluons, the struck quark carries less of the proton momentum x than it would if it had not emitted any gluons, decreasing the structure function at high x. In QCD, taking into account interactions of the quarks and gluons, the *scaling property of QPM is broken* and the structure functions depend not only on Bjorken x, but on the momentum transfer Q^2 as well. From figure 2.3 one can see the systematics of this dependence. Around $x = 0.2$ the structure function does scale, corresponding roughly to the value at which the structure function was measured at SLAC when scale invariance was discovered. The HERA measurements show, however, that for $x \leq 0.15$ the structure function increases and for $x \geq 0.25$ decreases with increasing Q^2.

In QCD, due to the observed scaling violation, the Callan and Gross relation is no longer true i.e. $2xF_1 \neq F_2$. Therefore, the longitudinal structure function F_L no longer vanishes (see equation 2.15).

2.5 Electromagnetic Interactions of Charged Spin 1/2 Fermions

The interaction of the charged particles via the electromagnetic force is described by *electrodynamics*. A classical formulation was given by Maxwell about hundred-fifty years ago. However, using quantum theory the electromagnetic interaction mediated by the *photon* was described in full detail by *Tomonaga*, *Feynman* and *Schwinger* in the 1940s. The new theory was consequently called *Quantum Electrodynamics* (QED) [10].

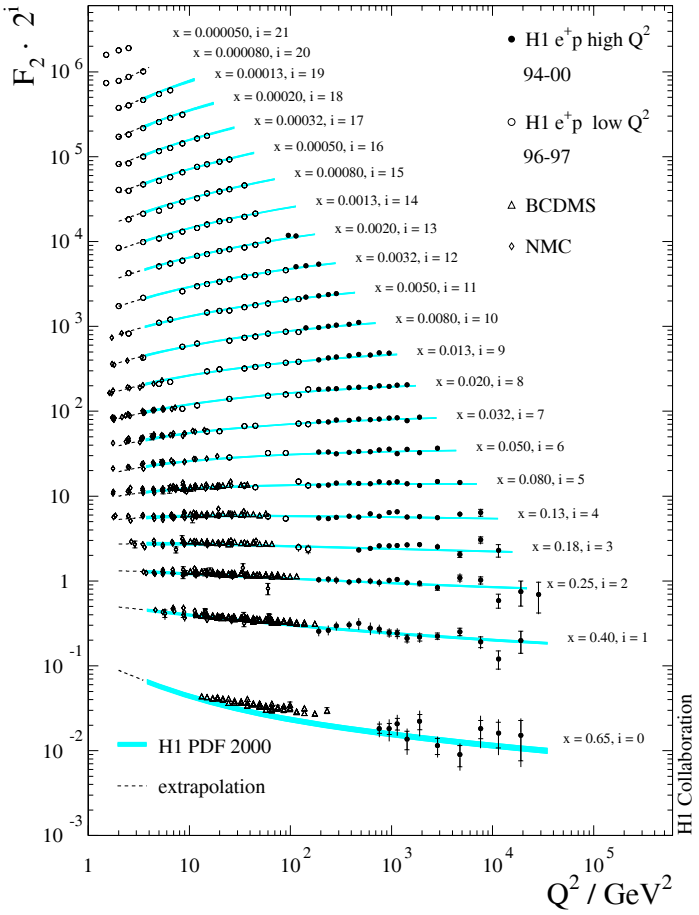

Figure 2.3: The proton structure function $F_2(x, Q^2)$ as a function of Q^2 for different values of x. The presented H1 data (solid points) is compared to the corresponding Standard Model expectation determined from the H1 PDF 2000 fit (error bands) [25]. At low Q^2, the H1 data are complemented by the data from the fixed-target experiments BCDMS [26] and NMC [27].

The typical electromagnetic interaction measured at HERA is that of the electron scattered on a proton (quark), exchanging a massless photon. The invariant amplitude of the underlying process $e^{\pm}q \rightarrow e^{\pm}q$ (shown in figure 2.1) can be written as:

$$M \propto \bar{\psi}_q \gamma^\mu \psi_q (-\frac{g_{\mu\nu}}{q^2})(\bar{\psi}_e \gamma^\nu \psi_e) \tag{2.21}$$

where the terms $\bar{\psi}_q \gamma^\mu \psi_q$ and $\bar{\psi}_e \gamma_\mu \psi_e$ represent the *quark* and the *electron currents*, respectively, while the *photon propagator* is given by $\frac{1}{q^2}$. The four-momentum squared q^2 (the mass squared of the virtual photon) is determined by four-momentum conservation at the vertices.

Following the well known properties of *Dirac particles* the wave function $\psi_q(\psi_e)$, from the equation 2.21, can be decomposed into left-handed and right-handed parts,

introducing a new quantity called *helicity*. Helicity is the projection of spin along the direction of motion $\vec{s}\cdot\vec{p}/|\vec{s}|\cdot|\vec{p}|$. Spin 1/2 particles can occur with helicity $\lambda = \pm 1$ as illustrated in figure 2.4, corresponding to the spin projection parallel (see figure 2.4 (a)) and antiparallel (see figure 2.4 (b)) to the direction of motion. The particle of spin $s = 1/2$ having helicity -1 ($m_s = -1/2$) or $+1$ ($m_s = 1/2$), are called *left-handed* and *right-handed* particles, respectively.

Figure 2.4: Helicity is the projection of spin along the direction of motion $\vec{s}\cdot\vec{p}/|\vec{s}|\cdot|\vec{p}|$. A particle with spin parallel (helicity $+1$) and antiparallel (helicity -1) to the direction of motion is called *right-handed* (a) and *left-handed* (b), respectively.

In terms of helicity the electromagnetic current J^μ in the high energy limit can be written as [10]:

$$J^\mu \equiv \bar{\psi}\gamma^\mu\psi = (\bar{\psi}_L + \bar{\psi}_R)\gamma^\mu(\psi_L + \psi_R) \quad (2.22)$$

$$= \bar{\psi}_L\gamma^\mu\psi_L + \bar{\psi}_R\gamma^\mu\psi_R \quad (2.23)$$

where for a fermion of energy $E >> m$ one defines[4]:

$$\psi_L = \frac{1}{2}(1-\gamma^5)\psi \quad (2.24)$$

$$\psi_R = \frac{1}{2}(1+\gamma^5)\psi \quad (2.25)$$

where $\frac{1}{2}(1-\gamma^5)$ represents the *spin projection operator*, i.e. it projects out the helicity $\lambda = \pm 1$ components of the spinor. This leads to the conclusion that *the helicity of a scattered fermion obeying the Dirac equation is conserved at high energies.*

2.6 Weak Interactions

The first *weak interactions* were observed in nuclear β decay:

$$n \rightarrow p + e^- + \bar{\nu}_e \quad (2.26)$$

where the neutron has become a proton, and an electron and an antineutrino are emitted. This is the so-called β^- decay which got the first phenomenological explanation

[4]The equation 2.23 follows from equation 2.22 because $P_L^2 = P_L$, $P_R^2 = P_R$ and $P_L P_R = 0$ using notation $P_L = \frac{1}{2}(1-\gamma^5)$ and $P_R = \frac{1}{2}(1+\gamma^5)$.

by *Fermi* in 1934 who formulated the first theory of weak interactions. In order to explain β-decay Fermi made an analogy between the electromagnetic and the weak force. By this analogy the invariant amplitude for the β-decay can be expressed via a current-current $(J^\mu - J_\mu)$ coupling:

$$M = \frac{G_F}{\sqrt{2}} J^\mu J_\mu \tag{2.27}$$

$$M = G_F(\bar{\psi}_p \gamma^\mu \psi_n)(\bar{\psi}_e \gamma_\mu \psi_\nu) \tag{2.28}$$

where G_F is the weak coupling constant also called the *Fermi constant* which has to be determined from experiment ($G_F = 1.16$ x 10^{-5} GeV^{-2} [28]).

Obviously, the current $\bar{\psi}\gamma^\mu\psi$ transforms like a vector. The differences between the electromagnetic and weak interactions are: the weak currents are assumed interacting at a point ("4-fermion coupling"), have the weak constant G_F instead of e^2, and the electric charge of baryons and leptons involved in the weak interactions is changed by one unit. Due to the charge change in the Dirac current the β interactions are called *charged current weak interactions*.

Discovery of Parity Violation

Until 1956 the assumption was made that in the weak interactions parity is conserved like in the electromagnetic interactions. To explain peculiarities in the weak decays of strange mesons, known as the $\theta^+ - \tau^+$ *puzzle*, this assumption was dropped[5]. In 1956 *Lee and Yang* [4] came to the conclusion that parity is not conserved in weak interactions.

In order to test parity violation a famous experiment by *Wu* and collaborators [29] was performed in 1957. A sample of radioactive *cobalt* nuclei was polarised in an external magnetic field and the direction of emission of the decay electrons was measured. It was found that most of the electrons were emitted in the direction opposite to that of the nuclear spin.

The explanation came from the correlation between the electron momentum and nuclear spin: the observed state J_Z is formed by a *left-handed electron* and a *right-handed antineutrino*.

Soon a number of different experiments had demonstrated that only left-handed neutrinos ν_L (and right-handed anti-neutrinos $\bar{\nu}_R$) are coupled to charged leptons by weak interactions. *The absence of a left-handed anti-neutrinos and a right-handed neutrinos is a clear evidence of (maximal) parity violation.*

[5]The puzzle was the fact that the so-called τ meson and θ meson had the same mass and spin zero, but had apparently different parity.

$$K^+(=\theta^+) \rightarrow \pi^+\pi^0(J^P = 0^+) \tag{2.29}$$
$$K^-(=\tau^+) \rightarrow \pi^+\pi^+\pi^-(J^P = 0^-). \tag{2.30}$$

2.6.1 The $V - A$ Nature of the Weak Currents

Based on the observation of parity violation a generalisation of Fermi's vector theory was independently proposed by *Feynman* and *Gell-Mann* (1958) [5] and by *Sudarshan* and *Marshak* (1958) [6]. The new scheme proposed a universal charged weak current J^μ involving both *vector* and *axial vector currents* $(V - A)$.

The total weak charged current J^μ is defined as the sum of *leptonic*(l) and *hadronic*(h) currents [30]:

$$J^\mu = J^\mu(l) + J^\mu(h). \tag{2.31}$$

The leptonic part is a combination of the different leptons involved in the interaction:

$$J^\mu(l) = \bar{e}\gamma^\mu \frac{1-\gamma^5}{2}\nu_e + \bar{\mu}\gamma^\mu \frac{1-\gamma^5}{2}\nu_\mu + \bar{\tau}\gamma^\mu \frac{1-\gamma^5}{2}\nu_\tau. \tag{2.32}$$

The hadronic charged weak current is expressed in terms of the quark fields:

$$J^\mu(h) = \bar{u}\gamma^\mu \frac{1-\gamma^5}{2} d_c + ... \tag{2.33}$$

where $\bar{u}$ represents the Dirac spinor of the quark u, γ^μ describes the vector coupling and $\gamma^\mu\gamma^5$ accounts for the axial coupling, which was missing in Fermi's proposal from 1934. The theory which involves both the vector and the axial vector couplings is bound to violate parity as will be discussed below.
The charged weak interactions of quarks are described by *Cabibbo theory* (1963) [31]. In this theory, the Cabibbo-rotated quark field d_c is defined as:

$$d_c = d\cos\theta_c + s\sin\theta_c \tag{2.34}$$

where the d and s quarks participating in the weak interactions are *rotated* by a *mixing angle* called the *Cabibbo angle* θ_c, and experimentally determined to be $\theta_c \approx 13^\circ$ [10]. By the analogy with the lepton doublets (ν_e, e), (ν_μ, μ) and (ν_τ, τ) involved in the charge changing, the u, d and s quark (see equation 2.34) can be introduced in terms of *left-handed* (q_L) doublets:

$$q_L = \begin{pmatrix} u \\ d_c \end{pmatrix}_L. \tag{2.35}$$

In these notations, *weak isospin* is introduced via the $SU(2)$ group. In order to distinguish between strong and weak isospin, the symbols t and t_3 are assigned to the weak isospin and its third component. All left-handed fermions can be assigned to isodublets with respect to the weak interaction in the following way:

$$t = \frac{1}{2} \quad t_3 = \begin{matrix} -\frac{1}{2} \\ +\frac{1}{2} \end{matrix} \quad \begin{pmatrix} e \\ \nu_e \end{pmatrix}_L, \begin{pmatrix} \mu \\ \nu_\mu \end{pmatrix}_L, \begin{pmatrix} \tau \\ \nu_\tau \end{pmatrix}_L. \tag{2.36}$$

Similarly, for quarks

$$t = \frac{1}{2} \quad t_3 = \begin{array}{c} +\frac{1}{2} \\ -\frac{1}{2} \end{array} \quad \begin{pmatrix} u \\ d_c \end{pmatrix}_L, \begin{pmatrix} c \\ s_c \end{pmatrix}_L, \begin{pmatrix} t \\ b' \end{pmatrix}_L . \tag{2.37}$$

Note that the b quark is not Cabibbo rotated as a member of the third quark generation[6]. The subscript L means that only the left-handed parts of the wave function are involved in the weak transitions. To emphasise this fact the weak isospin group is called the $SU(2)_L$.

2.6.2 The Weak Coupling Constant

At the first-order of perturbation theory the Feynman and Gell-Mann scheme together with the Cabibbo hypothesis provided a very good description of the weak charged current interactions. The cross sections are proportional to the centre of mass energy s in the $V-A$ theory. However, at the high energies ($s \geq 1/\sqrt{G_F}$) the conservation of probability ("unitarity") is violated. Unitarity can be saved by introducing a massive charged boson as a mediator of the weak force, the $W^{\pm}$. From the Yukawa-Wick [32] argument that the range of force is inversally proportional to the mass of the mediated boson follows another difference between the electromagnetic and the weak force. The massive boson propagator is given by:

$$\frac{-g^{\mu\nu}}{q^2 - M_W^2} \tag{2.38}$$

where in the denominator the mass of W appears. For nuclear β decay, $q^2 \ll M_W^2$. Following the analogy between the two forces, the strength of the weak interaction expressed in terms of the *Fermi coupling constant* G_F is proportional to a new quantity, the weak charge g, squared divided by the mass of the weak boson squared:

$$\frac{G_F}{\sqrt{2}} = \frac{g^2}{8M_W^2}. \tag{2.39}$$

As can be seen from the equation 2.39 the weak interaction is weak at low energies due to a large boson mass M_W. However, introducing the $W^{\pm}$ as a massive mediator was not satisfactory for processes involving the production of $W^{\pm}$ pairs, for example in hypotethical e^+e^- collisions because the cross section led to infinity and energies ≥ 1 TeV.

Yang and Mills(1954) used $SU(2)_L$ gauge transformations to introduce three gauge fields, transforming as a $t = 1$ multiplet under the group. By analogy to the ordinary $SU(2)$ strong isospin, the members of the weak isodublet will differ by one unit of charge (see equation 2.36). The two gauge bosons responsible for the transitions

[6]With six quark flavours the weak current can be described by unitary transformations among three quark doublets using the *Cabibbo-Kobayashi-Masakawa* (CKM) 3x3 *matrix* as an extension of the original Cabibbo 2x2 matrix [12].

between doublet members will have the charge ±1. These bosons are identified with $W^{\pm}$ mediating the charged current interactions. The third member of the gauge isotriplet will be electrically neutral. In 1957 *Schwinger* tried to identify the neutral boson with the photon.

However, in the Schwinger model the W boson somehow must acquire mass, while the photon remains massless. This problem was solved by introducing appropriate couplings of the vector bosons to the scalar and pseudo-scalar fields. But these couplings were arbitrary and no constraint on the W mass could be made. In addition, the Schwinger model did not account for the existence of *neutral weak currents*. A year later *Bludman* (1958) [33] proposed a scheme in which the weak neutral currents are purely left-handed as the charged currents. As was experimentally found later, this was not the case. In addition, there was no link with the electromagnetic interactions.

2.6.3 Electroweak Unification

An important contribution to the development of the Standard Model was made by *Glashow* (1961), *Salam* and *Ward* (1964) who suggested enlarging the Schwinger-Bludman scheme $SU(2)_L$ by an additional $U(1)$ gauge group, resulting in a $SU(2)_L$ x $U(1)$ gauge group structure. The new Abelian U(1) group is associated with the *weak hypercharge*, as $SU(2)_L$ was associated with the *weak isospin*. In addition, Glashow proposed that the *Gell-Mann-Nishijima* relation known from the strong interactions, also holds for the weak interaction, defining the weak hypercharge y:

$$Q = (t_3 + y/2). \tag{2.40}$$

Here Q (in units of e) is the electric charge of a member of a weak isomultiplet with the third weak isospin component t_3. From this relation one deduces that the lepton doublets, (ν_e, e^-) etc. have $y = -1$, whereas the quark doublets, (u, d_c) have $y = +1/3$.

Glashow (1961), Salam (1968) and Weinberg (1967) independently proposed the existence of weak neutral current interactions, making a major step forward in the unification of the electromagnetic and weak interactions into the so-called *electroweak interactions* (GSW model). In the electroweak theory the electric charge (e) and the weak charge (g) are related by the *weak mixing angle* (θ_W) often referred to as the *Weinberg angle*. The electroweak relationship is given by:

$$e = g \sin\theta_W. \tag{2.41}$$

In the GSW model the fundamental vector bosons are represented as a vector isotriplet $W_\mu = W_\mu^{(1)} W_\mu^{(2)} W_\mu^{(3)}$ [for $SU(2)_L$] and an isosinglet B_μ [for U(1)]. The physical states of a heavy neutral boson (Z_μ) and a massless photon (A_μ) are obtained by mixing of the W_μ^3 and B_μ fields:

$$A_\mu = \cos\theta_W B_\mu + \sin\theta_W W_\mu^3 \tag{2.42}$$

$$Z_\mu = -\sin\theta_W B_\mu + \cos\theta_W W_\mu^3. \tag{2.43}$$

2.6.4 The Higgs Mechanism

In order to enable the gauge bosons to have a mass without spoiling the renormalisability of the theory[7] *Weinberg* and *Salam*, invoked *spontaneous symmetry breaking*. This is the so-called *Higgs mechanism* [34,35] based on the idea of introducing a new scalar Higgs field ϕ, which couples to the gauge fields. Weinberg and Salam proposed to use the $SU(2)_L$ x $U(1)$ gauge model with the mixing relations (2.42) and (2.43). They defined a (complex) scalar doublet transforming as a $t = 1/2$ multiplet under $SU(2)_L$. Thus, the Higgs field may be written in form:

$$t = \frac{1}{2} \quad t_3 = \begin{array}{c} +\frac{1}{2} \\ -\frac{1}{2} \end{array} \quad \phi = \begin{pmatrix} \phi_1 + i\phi_2 \\ \phi_3 + i\phi_4 \end{pmatrix} \quad = \begin{pmatrix} \phi^+ \\ \phi^0 \end{pmatrix}$$

in which four real scalar fields appear. Choosing a specific representation for the Higgs doublet

$$\phi = \begin{pmatrix} 0 \\ v/\sqrt{2} \end{pmatrix}$$

the basic mechanism is a non-vanishing vacuum expectation value (v) of the Higgs field ϕ which gives mass to three of the (originally massless) gauge bosons $W^{\pm}$, Z^0, while the photon remains massless.

Masses of the Gauge Bosons Z^0 and $W^{\pm}$

The Higgs doublet is used to generate the gauge boson masses and the fermion masses as well. The masses of the weak bosons may be expressed in the terms of the vacuum expectation v, and the gauge couplings, g and $g^{'}$:

$$M_W = \frac{1}{2} g v \tag{2.44}$$

$$M_Z = \frac{1}{2} v \sqrt{g^2 + g'^2} \tag{2.45}$$

with the mixing angle θ_W defined as [36]:

$$\tan \theta_W = \frac{g}{g'}. \tag{2.46}$$

The Weinberg angle is not predicted by the theory, but from its relation to the boson masses it can be determined experimentally:

$$\cos \theta_W = \frac{M_W}{M_Z}. \tag{2.47}$$

The mass eigenstates are a massless photon field A_μ (see equation 2.42) and a massive boson field Z_μ (see equation 2.43) with $M_Z \geq M_W$. Experimentally the masses of

[7] Mass terms in the Lagrangian spoil gauge invariance.

the bosons were determined for the first time when, in 1983, the Z^0 and W where discovered at the CERN $p\bar{p}$ collider via the processes [37, 38]:

$$p\bar{p} \rightarrow W^{\pm}X \rightarrow (e^{\pm}\nu)X \quad (2.48)$$
$$p\bar{p} \rightarrow Z^0X \rightarrow (e^{+}e^{-})X \quad (2.49)$$

with X representing all other particles produced in the high energy collision. The masses of the gauge bosons were determined by studying the momentum distribution of the emitted decays of electrons and positrons. All experiments so far confirmed agreement between the standard electroweak model predictions and the experimental results. The latest values for the gauge boson masses are [28]:

$$M_W = 80.425 \pm 0.038 \text{ GeV} \quad (2.50)$$
$$M_Z = 91.188 \pm 0.002 \text{ GeV}. \quad (2.51)$$

2.6.5 Parity Violation in the Electroweak Model

The coupling constants $C(t_3, Q)$ of the fermions to the Z^0 field can be expressed in terms of the Weinberg angle θ_W (see equation 2.41) and the fermion's weak isospin and electric charge:

$$C(t_3, Q) = \frac{ie}{\sin\theta_w \cos\theta_W} c(t_3, Q) \quad (2.52)$$
$$c(t_3, Q) = t_3 - 2Q\sin^2\theta_W. \quad (2.53)$$

If parity violation exists in the weak neutral currents, the constants $c(t_3, Q)$ will be different for the right-handed and the left-handed states. For example, right-handed neutrinos cannot couple to the Z^0 by construction, as their charge is zero and all right-handed fermions are weak singlets ($t_3 = 0$). Therefore, the neutrino-induced neutral weak interactions are induced only by left-handed neutrinos and therefore violate parity maximally like all charged weak currents. For the charged fermions on the other hand, the degree of parity violation depends on their quantum numbers (see equation 2.52).

The Z^0 vertex factor, characteristic for the neutral current interactions, can be written as [39]:

$$\frac{-ie}{2\sin\theta_W cos\theta_W}\gamma^{\mu}\left(c_V^f - c_A^f\gamma^5\right) \quad (Z^0 \text{ vertex factor}) \quad (2.54)$$

The coefficients c_V^f and c_A^f depend on the particlar quark or lepton (f) involved and are determined by the single parameter θ_W (see table 2.1).

In contrast to the neutral currents, charged current transitions proceed only within the weak isospin doublets and are limited to the left-handed particles. As has been

f	c_V	c_A
ν_e, ν_μ, ν_τ	$\frac{1}{2}$	$\frac{1}{2}$
e^-, μ^-, τ^-	$-\frac{1}{2} + 2\sin^2\theta_W$	$-\frac{1}{2}$
u, c, t	$+\frac{1}{2} - \frac{4}{3}\sin^2\theta_W$	$\frac{1}{2}$
d, s, b	$-\frac{1}{2} + \frac{2}{3}\sin^2\theta_W$	$-\frac{1}{2}$

Table 2.1: Neutral vector and axial vector couplings in the GSW model.

fermion	t	t_3	y	e
e_L, μ_L,τ_L	1/2	-1/2	-1	-1
ν_e, ν_μ, ν_τ	1/2	1/2	-1	0
e_R, μ_R,τ_R	0	0	-2	-1
$u_L^{'}$, $c_L^{'}$, $t_L^{'}$	1/2	1/2	1/3	2/3
$d_L^{'}$, $s_L^{'}$, $b_L^{'}$	1/2	-1/2	1/3	-1/3
u_R, c_R, $t_R^{'}$	0	0	4/3	2/3
$d_R^{'}$, $s_R^{'}$, $b_R^{'}$	0	0	-2/3	-1/3

Table 2.2: Weak isospin and hypercharge assignments for the fermions.

discussed in section 2.6.1, the coupling of quarks and leptons to $W^\pm$ has a pure $V-A$ form leading to the characteristic charged current vertex factor, given as:

$$\frac{-ie}{2\sqrt{2}\sin\theta_W}\gamma^\mu(1-\gamma^5) \quad (W^\pm \text{ vertex factor}) \tag{2.55}$$

In charged current interactions the *left-handed lepton doublets* can couple to each other via W exchange: Although the neutrinos exist only in one helicity state, the electrons, muons and taus have both (see equation 2.36). But there are no weak transitions that couple their right-handed components

$$\psi_R(l) = \frac{1+\gamma^5}{2}\psi(l)$$

to other states i.e. the right-handed leptons being *singlets* ($t = 0; t_3 = 0$) do not couple as can be seen from table 2.2. Similarly, the quarks are grouped in the weak isospin doublets and can couple to each other or to a lepton doublet via W exchange (see equation 2.37). Since the hadronic charged current transitions proceed only via the *left-handed quarks*, the left-handed members of the each generation form weak isospin doublet $(u, d^{'})$, $(c, s^{'})$ and $(t, b^{'})$ (see table 2.2)[8].

[8]Here $'$ for d and s quark is very close to the Cabibbo rotation and for b it corresponds to transformation accounted for in the CKM matrix. The b mixes very little with the lighter quark flavours.

2.7 Neutral Current Cross Section and Structure Functions

In *electroweak* NC DIS an additional exchange of a Z^0 is possible, correspondingly the cross section can be expressed as [40]:

$$\frac{\mathrm{d}^2\sigma^{e^\pm p}_{\mathrm{NC}}}{\mathrm{d}x\,\mathrm{d}Q^2} = \frac{2\pi\alpha^2}{xQ^4}\,\phi^\pm_{\mathrm{NC}}(x,Q^2) \tag{2.56}$$

$$\phi^\pm_{NC} = Y_+\tilde{F}_2^\pm \mp Y_- x\tilde{F}_3^\pm - y^2\tilde{F}_L^\pm. \tag{2.57}$$

The structure function term $\phi^\pm_{NC}$ is expressed as a linear combination of the NC structure functions $\tilde{F}_2$, $x\tilde{F}_3$ and $\tilde{F}_L$. The helicity dependences of the electroweak interaction is given by $Y_\pm = 1 \pm (1-y)^2$.

The contribution from the structure function F_L is only important at large y and is expected to be negligible at large x and Q^2. The generalised proton structure functions $\tilde{F}_2$ ($x\tilde{F}_3$) can be written as linear combinations of the hadronic structure functions F_2, $F^{\gamma Z}_{2,3}$ and $F^Z_{2,3}$ associated to pure photon exchange, to γZ^0 interference and to pure Z^0 exchange, respectively:

$$\tilde{F}_2^\pm = F_2 - (c_V^e \pm P_e c_A^e)\eta_Z F_2^{\gamma Z} + ({c_V^e}^2 + {c_A^e}^2 \pm 2P_e c_V^e c_A^e)\eta_Z^2 F_2^Z \tag{2.58}$$

$$\tilde{x}F_3^\pm = -(c_A^e \pm P_e c_V^e)\eta_Z x F_3^{\gamma Z} + (2c_V^e c_A^e \pm P_e({c_V^e}^2 + {c_A^e}^2))\eta_Z^2 x F_3^Z \tag{2.59}$$

with $\eta_Z = \frac{kQ^2}{Q^2+M_Z^2}$, $k^{-1} = 4\frac{M_W^2}{M_Z^2}(1-\frac{M_W^2}{M_Z^2})$, where M_W and M_Z are the masses of Z^0 and $W^\pm$. Here c_V^e and c_A^e are the vector and axial-vector couplings of the electron to the Z^0 [41]. The longitudinal lepton polarisation P_e is defined as:

$$P_e = \frac{N_+ - N_-}{N_+ + N_-} \tag{2.60}$$

where N_+ and N_- are the numbers of right-handed and left-handed electrons ($e^\pm$) in the beam, respectively.

In QPM the structure functions F_2, $F_2^{\gamma Z}$ and F_2^Z are related to the sum of the quark and anti-quark densities:

$$[F_2, F_2^{\gamma Z}, F_2^Z] = x\sum_q [e_q^2, 2e_q c_V^q, {c_V^q}^2 + {c_A^q}^2]\{q+\bar{q}\} \tag{2.61}$$

and the structure functions $xF_3^{\gamma Z}$ and xF_3^Z are related to the difference of the quark and anti-quark densities:

$$[xF_3^{\gamma Z}, xF_3^Z] = 2x\sum_q [e_q c_A^q, c_V^q c_A^q]\{q-\bar{q}\}. \tag{2.62}$$

The summation goes over active quark flavours, e_q is the charge of quarks in units of the electron charge and c_V and c_A vector and axial-vector couplings of the quarks.

2.8 Charged Current Cross Section and Structure Functions

In order to study electroweak interactions and possible physics beyond the standard model, a longitudinal polarisation of the electron beam has been provided at HERA II. This is an important tool for the charged current interactions which are sensitive to the longitudinal polarisation of the lepton beam. Thus, they can be used to test the weak part of the SM (only left-handed currents) and to search for right-handed CC interactions which would be mediated via a right-handed W. The *weak polarised charged current cross section* at the lowest order is given by [42]:

$$\frac{d^2\sigma_{cc}^{e^\pm p}}{dxdQ^2} = (1 \pm P_e)\,\frac{G_F^2}{2\pi x}\left[\frac{M_W^2}{Q^2+M_W^2}\right]^2 \phi_{cc}^{\pm}(x,Q^2) \tag{2.63}$$

$$\phi_{cc}^{\pm} = \frac{1}{2}(Y_+\tilde{F}_2^{cc\pm} \mp Y_- x\tilde{F}_3^{cc\pm} - y^2\tilde{F}_L^{cc\pm}). \tag{2.64}$$

Here the Fermi constant G_F is given by:

$$G_F = \frac{\pi\alpha}{\sqrt{2}\sin^2\theta_W M_W^2} \tag{2.65}$$

M_W is the mass of the W boson, P_e is the polarisation of the electron beam (see equation 2.60) and $\phi_{cc}^{\pm}$ is the structure function term. The generalised proton structure functions $\tilde{F}_2^{cc\pm}$, $x\tilde{F}_3^{cc\pm}$ and $\tilde{F}_L^{cc\pm}$ are defined in a similar manner to the NC structure functions. However, since CC are purely weak interactions the structure functions do not contain the electromagnetic and the interference terms. The contribution from $\tilde{F}_L^{cc\pm}$ is important only at large y and thus negligible at large x and large Q^2. The generalised proton structure functions $\tilde{F}_2^{cc\pm}$, $x\tilde{F}_3^{cc\pm}$ are related to the probability densities of the quarks within the proton as:

$$\tilde{F}_2^{cc+} = 2x(d(x,Q^2)+s(x,Q^2)+\bar{u}(x,Q^2)+\bar{c}(x,Q^2)) \tag{2.66}$$

$$x\tilde{F}_3^{cc+} = 2x(d(x,Q^2)+s(x,Q^2)-\bar{u}(x,Q^2)-\bar{c}(x,Q^2)) \tag{2.67}$$

$$\tilde{F}_2^{cc-} = 2x(u(x,Q^2)+c(x,Q^2)+\bar{d}(x,Q^2)+\bar{s}(x,Q^2)) \tag{2.68}$$

$$\tilde{x}F_3^{cc-} = 2x(u(x,Q^2)+c(x,Q^2)-\bar{d}(x,Q^2)-\bar{s}(x,Q^2)). \tag{2.69}$$

It follows that the structure function term $\phi_{cc}^{\pm}$ is expressed in terms of the quark densities as:

$$\phi_{cc}^{+} = x[\bar{u}+\bar{c}] + (1-y)^2 x[d+s] \tag{2.70}$$

$$\phi_{cc}^{-} = x[u+c] + (1-y)^2 x[\bar{d}+\bar{s}]. \tag{2.71}$$

2.8.1 Comparison of the e^-p and e^+p CC Cross Sections

While the NC cross section is mainly sensitive to the u quark density in e^+p as well as in e^-p collisions, the CC cross section depends strongly on the beam lepton charge. This can be seen from equations 2.70 and 2.71. In e^+p collisions the CC cross section is sensitive to the *down* quark density in the proton, however, in e^-p collisions the CC cross section is mainly sensitive to the density of *up* quarks within the proton. Since the proton consists of two u and one d quark it also explains why the e^-p is larger than e^+p CC cross section (see figure 2.6). But this is only one part of the answer. Another reason lies in the fact that total angular momentum conservation gives rise to the factor $(1-y^2)$ in equations 2.70 and 2.71. In e^+p CC interactions back-scattering of the antineutrino is forbidden since for the initial state, made of a right-handed *positron* and a left-handed *down quark* $J_z = 1$. Due to this the amplitude is a function of the scattering angle θ as illustrated in figure 2.5. On the other hand in e^-p CC interaction, since $J_Z = 0$ in the initial state, composed of a left-handed *electron* and a left-handed *up quark*, the neutrino can be scattered in any direction (isotropically). This leads to an amplitude being independent on the scattering angle θ as shown in figure 2.5. Angular momentum conservation thus brings an additional factor of 3 to the difference between two cross sections (see figure 2.6).

Electroweak Unification at HERA

Figure 2.6 shows the Q^2 dependence of the CC and NC cross sections for e^-p and e^+p scattering measured at HERA I [40]. As can be seen, at low Q^2 the NC cross section is about three orders of magnitude larger than the CC cross section. The main contribution to the NC cross section at low Q^2 comes from the dominant photon exchange cross section $\propto 1/Q^4$. In contrast, the CC cross section $\sim [M_W^2/Q^2 + M_W^2]^2$ approaches a constant at low Q^2. With increasing Q^2 they become more similar, and at high $Q^2 \sim 10^4$ GeV^2 the photon and Z^0 exchange contributions to the NC cross section are also of similar size to those of the $W^\pm$ to the CC contribution. These measurements demonstrate clear evidence of "electroweak unification".

The Total Charged Current Cross Section

The total CC cross section measured in a given phase space as a function of the polarisation P_e can be written in the following way:

$$\sigma_{cc}^{e^\pm p} = \frac{1}{2}(1 \pm P_e)\sigma_{cc,L}^{e^\pm p} \tag{2.72}$$

where $\pm$ denote the initial lepton charge. More generally, for electrons the CC cross section can be written as:

$$\sigma_{cc}(e^-p \to \nu X) = \frac{1}{2}(1-P_e)\sigma_{cc}^L(e^-p \to \nu X) + \frac{1}{2}(1+P_e)\sigma_{cc}^R(e^-p \to \nu X) \tag{2.73}$$

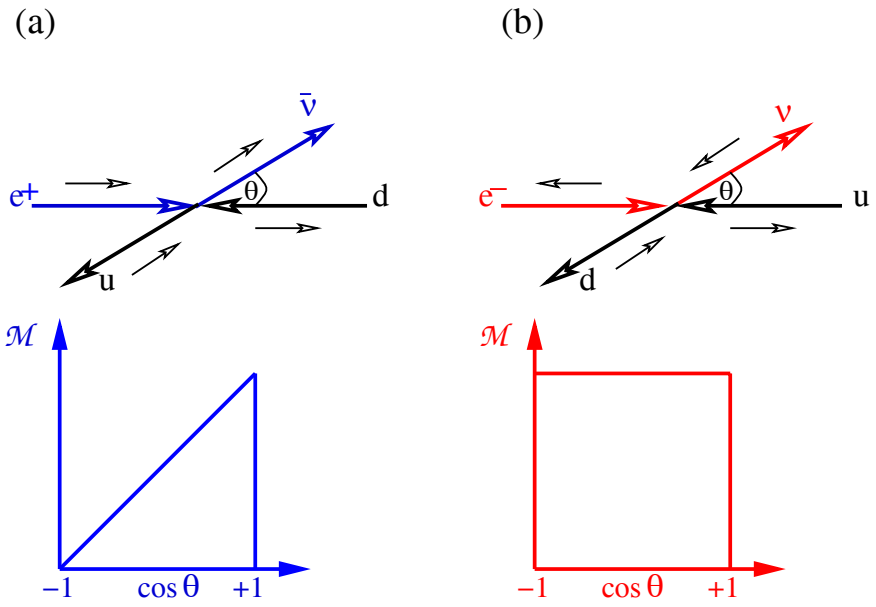

Figure 2.5: Two interactions allowed by the SM are shown. The positron can couple only to the right-handed antineutrino (a) and electron only to the left-handed neutrino (b). The two lower pictures show why the e^- CC cross section is larger by roughly a factor of 6 compared to the e^+ CC cross section. The angular momentum conservation of ($J_z = 1$ for the e^+d system) does not allow the antineutrino $\bar{\nu}$ to be back-scattered. Therefore the amplitude as a function of the scattering angle θ is 0 at $\theta = 180°$ and maximal at the $\theta = 0°$. Angular momentum conservation allows the neutrino to be scattered isotropically ($J_z = 0$ for the e^-u system) leading to an amplitude $\mathcal{M}$ being independent on the scattering angle θ.

and for positrons as:

$$\sigma_{cc}(e^+p \to \bar{\nu}X) = \frac{1}{2}(1 + P_e)\sigma^L_{cc}(e^+p \to \bar{\nu}X) + \frac{1}{2}(1 - P_e)\sigma^R_{cc}(e^+p \to \bar{\nu}X) \qquad (2.74)$$

where σ^L_{cc} is the purely left-handed SM cross section and σ^R_{cc} comes from a hypothetical right-handed weak interaction. The equation 2.72 shows the SM prediction where only left-handed CC reactions ($\sigma^R_{cc} = 0$) exist. The SM expectations for CC e^-p reactions is that $\sigma_{cc} \to 0$ for $P_e = +1$ (see equation 2.73) giving sensitivity to the right-handed boson W_R.

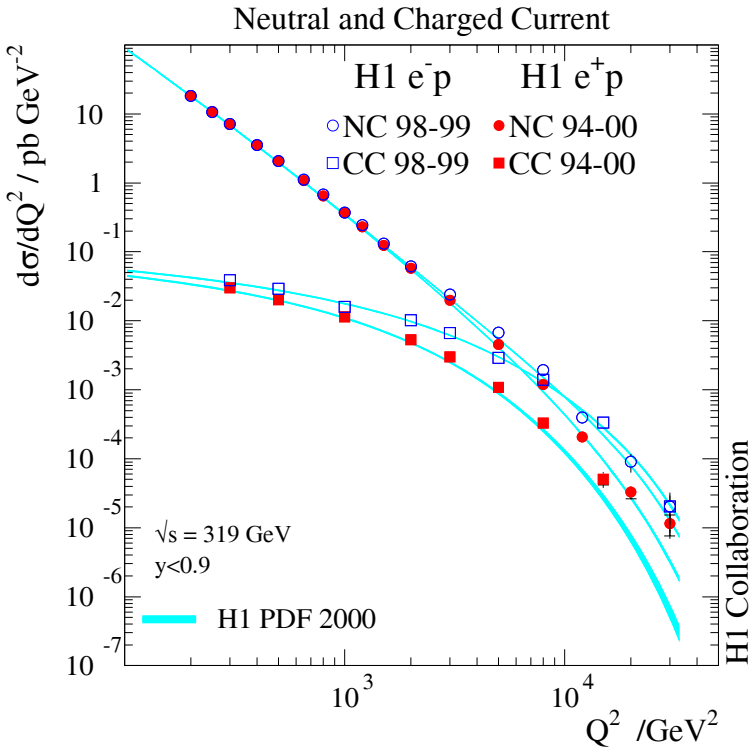

Figure 2.6: The Q^2 dependence of the NC and CC cross sections measured at HERA I in e^+p and e^-p collisions. The experimental results are compared to the Standard Model prediction using H1 PDF 2000 fit [25].

Chapter 3

The HERA collider and the H1 Detector

In this chapter the electron-proton collider HERA (Hadron-Elektron Ring Anlage) and the H1 detector are introduced. A brief description of the HERA collider is given first. Then the measurement of the electron beam polarisation at HERA which is essential for the measurements presented in this thesis is discussed. The next section gives an overview of the H1 detector with emphasis on the components which are important for the analysis presented. Finally, within the H1 trigger system a detailed description of the Liquid Argon trigger, most important for the present analysis, is given.

3.1 The HERA collider

The HERA collider (see figure 3.1) is the only electron-proton collider in the world, with the prime physics goal to study the structure of the proton. It is situated at the research centre DESY[1] in Hamburg. The collider [43] consists of two separate accelerator rings in a common ring tunnel of 6.3 km circumference. The electrons are accelerated to an energy $E_e = 27.6$ GeV and the protons to an energy $E_p = 920$ GeV. The electron and proton beams are brought into collision at two interaction points, the North and South Halls where the experiments H1 [44] and ZEUS [45] are located, respectively. The resulting centre-of-mass energy is $\sqrt{s} \approx 319$ GeV. The fixed-target experiment HERMES [46], located in the West Hall, uses the polarised electron beam in collision with a polarised gas target for studying the spin structure of the proton. In order to prepare well-collimated, intense beams and to bring the energy of electrons and protons up to the necessary injection energy (12 GeV and 40 GeV, respectively) a system of pre-accelerators (LINAC, DESY, PETRA) is used (see figure 3.1).

Electrons and protons are stored in HERA in groups of particles called *bunches*. The circulating bunches, containing up to 10^{11} particles each, collide every 96 ns,

[1] Deutsches Elektronen-Synchrotron

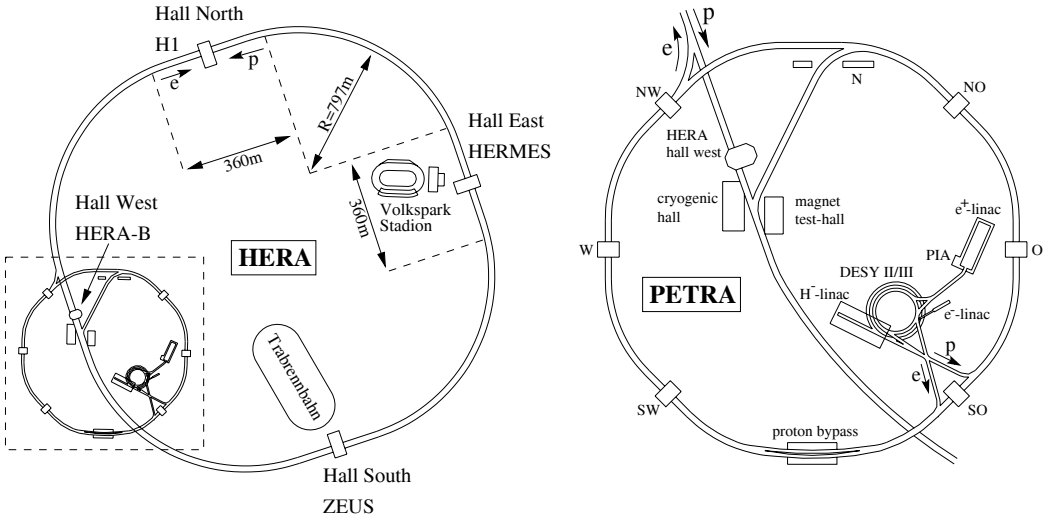

Figure 3.1: The electron-proton collider HERA with two colliding beam experiments, H1 [44] and ZEUS [45], and the fixed-target experiment HERMES [46] is shown on the left side. The pre-accelerator chain to HERA is shown on the right side.

corresponding to a *bunch-crossing frequency* of 10.4 MHz. About 180 bunches of electrons and protons circulate in the machine and are brought to collision. They are so-called *main bunches*. In addition, there are bunches known as *pilot-bunches* which are not colliding with any bunch from the other beam, but are used for studying background from beam-gas and beam-wall reactions. Due to complicated longitudinal structure of the proton beam there are also several *satellite bunches* near to the main bunch.

At HERA, data are delivered in periods corresponding to one filling of electron and proton bunches into the HERA ring, called *luminosity fills (runs)* (see figure 3.2). Depending on the running conditions one luminosity fill may last up to ≈ 12 hours.

3.2 Luminosity

The luminosity is one of the most important parameters of the HERA collider and represents a measure of its performance. It determines the number of events of a certain reaction occurring per second.
The luminosity $\mathcal{L}$ is proportional to the number of electrons N_e and the number of protons N_p in the beam and to the colliding frequency f. It is inversely proportional to the transverse bunch sizes σ_x and σ_y at the interaction point:

$$\mathcal{L} = f\frac{N_p N_e}{4\pi\sigma_x\sigma_y} \quad [\frac{1}{\mathrm{cm}^2\mathrm{s}}]. \tag{3.1}$$

$\mathcal{L}$ is also called the *instantenous luminosity*. In order to collect a certain number N of events of a specific physics reaction (e.g. CC events) the *integrated luminosity*

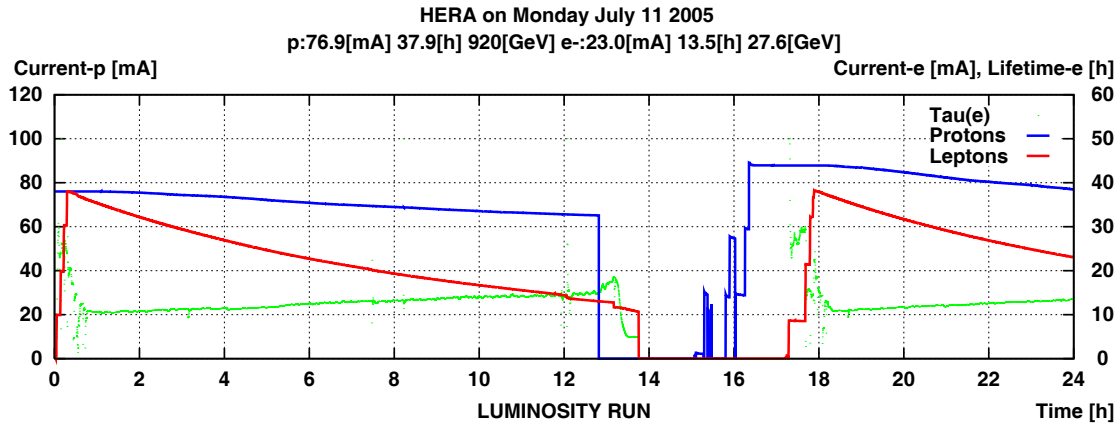

Figure 3.2: The beam currents (electron right scale, proton left scale) as a function of time during a typical luminosity operation day. The decrease of the electron current is mainly caused by particle losses due to synchrotron radiation.

$L = \int \mathcal{L}\, dt$ enters:

$$N = \sigma L. \tag{3.2}$$

This basic formula connects the cross section σ for a reaction to the number N of observed events. The integrated luminosity is usually measured in units of *events per picobarn*: $L[\mathrm{pb}^{-1}]$ where is $1\mathrm{pb} = 10^{-36}\mathrm{cm}^2$.
As one can see from the formula 3.2 the larger the accelerator's luminosity the more interactions can be observed. Since the cross sections of the measured ep processes are extremely low, the luminosity must be high in order to get a sufficiently high number of events while keeping the measurements within reasonable time constraints.
The HERA accelerator has been upgraded during the 2001 shutdown to reach two goals: First, to increase the instantaneous luminosity [47] by a factor of 3 and, secondly, to provide longitudinal electron beam polarisation to the HERA colliding experiments. Since the electron current is limited by the electron RF power and the proton current is limited due to the pre-accelerator chain and the background, the luminosity upgrade was achieved by reducing the transverse beam size (σ_x,σ_y) at the interaction point (IP). This is realized by installing superconducting focusing magnets inside the collider detector, close to IP.

After the upgrade ("HERA II"), the HERA experiments have been running with polarised electron beams and the total integrated luminosity collected by H1 at HERA II in different years is shown in figure 3.3. For the present analysis only the electron-proton data from 2005 with a corresponding luminosity of 98.2 pb^{-1} are used.

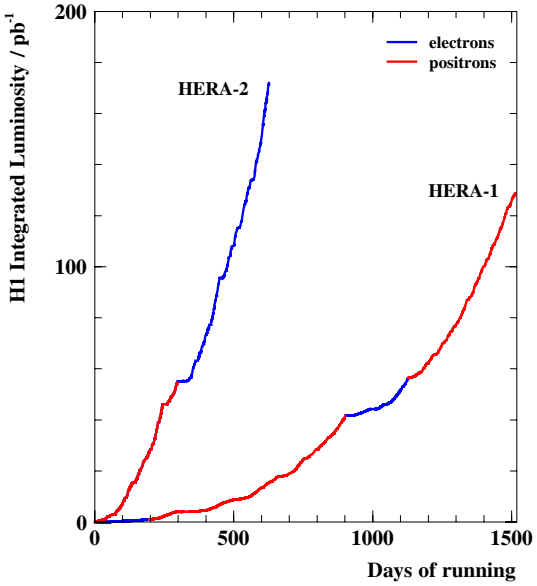

Figure 3.3: Luminosity collected by H1 experiments in HERA I and HERA II.

3.3 Lepton Polarisation at HERA

During long shutdown in 2001, terminating the first running phase of HERA ("HERA I"), spin rotators (see figure 3.4) have been installed around the interaction regions of the H1 and ZEUS experiments in order to enable these experiments to run with longitudinally polarised electrons. Before year 2000 only the HERMES experiment had this possibility.

In a storage ring, the electrons become naturally polarised in the transverse direction (normal to the plane of the storage ring) through emission of synchrotron radiation. The effect is known as the *Sokolov-Ternov effect* [48]. The longitudinal polarisation is achieved by spin rotators as will be discussed in the subsection 3.3.2. The electron transverse polarisation is measured by the transverse polarimeter (TPOL [49]) close to the HERA-B experiment, and the longitudinal polarimeter (LPOL [50]), located behind the HERMES interaction point, is used to measure the longitudinal polarisation of the beam. Two independent measurements are important to explore systematic effects and provide system reducancy. Figure 3.5 shows the transverse and longitudinal polarisation as functions of time for one luminosity fill, corresponding to one day of HERA operation.

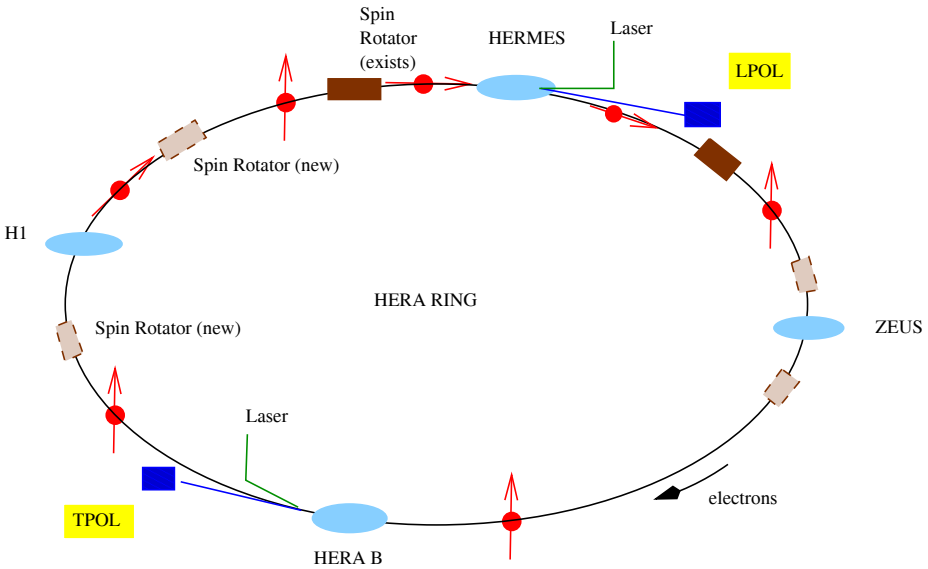

Figure 3.4: The HERA with the polarimeters LPOL and TPOL and spin rotators placed around each of HERA running experiments HERMES, ZEUS and H1.

3.3.1 Tranverse Electron Beam Polarisation

The electron beam, deflected by the magnetic guide field, radiates photons which may cause the electron to flip its spin. Only a very small fraction (10^{-11} of the emitted power) of the total synchrotron radiation is *spin-flip synchrotron radiation*. Due to the difference in energy of the two spin states of the electron with respect to magnetic guide field, the spin-flip probabilities per unit of time $w_{\uparrow\downarrow}$ (spin up $\rightarrow$ spin down) and $w_{\downarrow\uparrow}$ (spin down $\rightarrow$ spin up) differ and therefore build up a tranverse electron beam polarisation. The spin-flip probabilities per unit of time are:

$$w_{\uparrow\downarrow} = \frac{5\sqrt{3}}{16}(1 + \frac{8}{5\sqrt{3}})c\lambda_c r_0 \frac{\gamma^5}{\rho^3} \; ; \quad w_{\downarrow\uparrow} = \frac{5\sqrt{3}}{16}(1 - \frac{8}{5\sqrt{3}})c\lambda_c r_0 \frac{\gamma^5}{\rho^3}; \tag{3.3}$$

where γ is the electron Lorentz factor and the ρ is the bending radius of the magnetic field,

$$\lambda_c = \frac{h}{2\pi m_e c} = 3.8616 \times 10^{-13} m \tag{3.4}$$

is the reduced electron Compton wavelength and:

$$r_0 = \frac{e^2}{4\pi_0 m_e c^2} = 2.8179 \times 10^{-15} m \tag{3.5}$$

is the classical electron radius. The difference between the two transition rates $w_{\uparrow\downarrow}$ and $w_{\downarrow\uparrow}$ gives the polarisation of the electron beam:

$$P_{ST} = \frac{w_{\uparrow\downarrow} - w_{\downarrow\uparrow}}{w_{\uparrow\downarrow} + w_{\downarrow\uparrow}} = \frac{8}{5\sqrt{3}} = 92.4\% \tag{3.6}$$

This is the maximal value for the transverse polarisation in a storage ring under the assumption that there are no depolarising effects. The polarisation is built up as a function of time according to:

$$P(t) = P_{ST}(1 - \exp(\frac{-t}{\tau_{ST}})) \tag{3.7}$$

where the time constant τ_{ST} is given by:

$$\tau_{ST} = \frac{1}{w_{\uparrow\downarrow} + w_{\downarrow\uparrow}} = \frac{8\rho^3}{5\sqrt{3}\lambda_c r_0 \gamma^5}. \tag{3.8}$$

The characteristic polarisation time τ_{ST} depends on the beam energy (γ) and the curvature radius in the bending magnets (ρ). For HERA, the time constant τ_{ST} is about 40 min.

In reality, the build up of the maximal polarisation is limited by depolarisation effects. Furthermore, betatron oscillations around the ideal orbit lead the electrons into regions where non vertical magnetic field components exist, thus decreasing the polarisation perpendicular to the accelerator plane. Additional depolarising effects occur due to Columb interactions with the proton beam during collisions. All the depolarising effects reduce the characteristic time and maximum polarisation. The maximum polarisation achieved at HERA is about 60%, with a characteristic time constant τ_{pol} of about $20 - 24$ min.

The Transverse Polarimeter

The transverse polarimeter (TPOL) [49] measures the up-down asymmetry relative to the accelerator plane in the polarised Compton scattering in order to determine the beam polarisation. Circularly polarised laser light is back-scattered on the electron beam and registered in a sensitive calorimeter. TPOL works in a *single-photon mode*, meaning that the energy and the position of each single photon is measured in the calorimeter. The helicity of the laser light is flipped at a rate of 90 Hz. The observed up-down asymmetry produced due to the helicity of the laser light is proportional to the electron beam polarisation.

The total systematic uncertainty of the TPOL measurement of 3.5% comes from the calibration procedure and corrections to the raw polarisation measurement [51,52].

3.3.2 Longitudinal Electron Beam Polarisation

In the previous section it was described that electrons are transversally polarised at HERA. In order to convert the transverse into longitudinal polarisation [50] *spin rotators* are employed. Their principle is very simple: A transverse magnetic field is used to force the spins to precess around the field lines. Spin rotators are installed

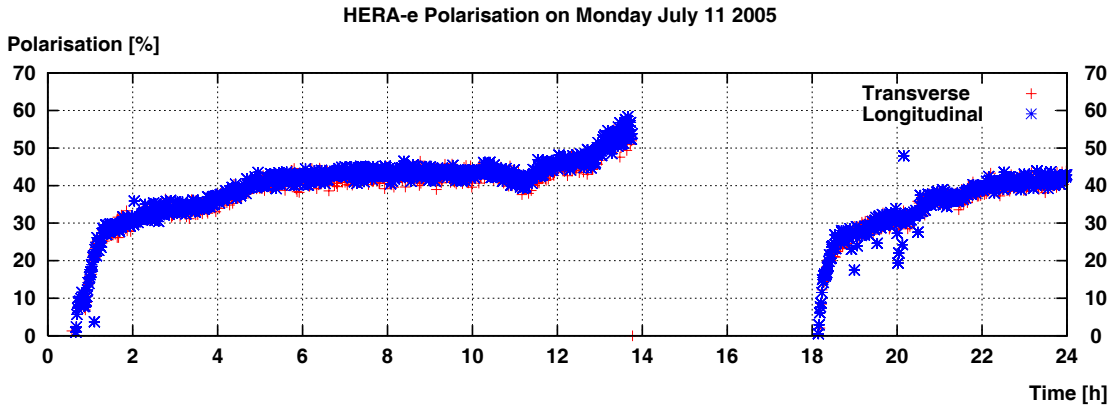

Figure 3.5: The longitudinal and transverse electron beam polarisation for the luminosity fill shown in figure 3.2.

in pairs around each experiment, before and after the interaction point in order to restore the beam's transverse polarisation after passing through the IR.

The longitudinal polarisation of the electron beam is measured using again Compton backscattering, with circularly polarised laser light [51]. The cross section of this process can be written as [50]:

$$\frac{d\sigma}{dE_\gamma} = \frac{d\sigma_0}{dE_\gamma}[1 + P_\lambda P_e A_Z(E_\gamma)] \tag{3.9}$$

where $d\sigma_0/dE_\gamma$ represents the unpolarised cross section, E_γ is the energy of the backscattered photon, P_λ is degree of circular polarisation of the incident photons for two helicity states $\lambda = \pm 1$, P_e is the longitudinal polarisation of the electron beam, and $A_Z(E_\gamma)$ is the longitudinal asymmetry function.

When an intense laser pulse interacts with an electron bunch a large number of Compton photons is produced. These photons are detected by a calorimeter, which measures their energy sums. Depending on the helicity of the electron, two scattering amplitudes contribute, one for a total spin projection 1/2 leading to an intensity $I_{1/2}$ and another for a total spin projection 3/2 leading to an intensity $I_{3/2}$ (see figure 3.6). Therefore, an energy asymmetry is measured:

$$A_{meas} = \frac{I_{3/2} - I_{1/2}}{I_{3/2} + I_{1/2}} = P_c P_e A_p(E_\gamma) \tag{3.10}$$

where $A_p(E_\gamma)$ is the analysing power of the process.

Longitudinal Polarimeter

The longitudinal polarimeter (LPOL) [50] used by HERMES was commissioned in the fall of 1996. It provides an independent measurement of polarisation of the electron

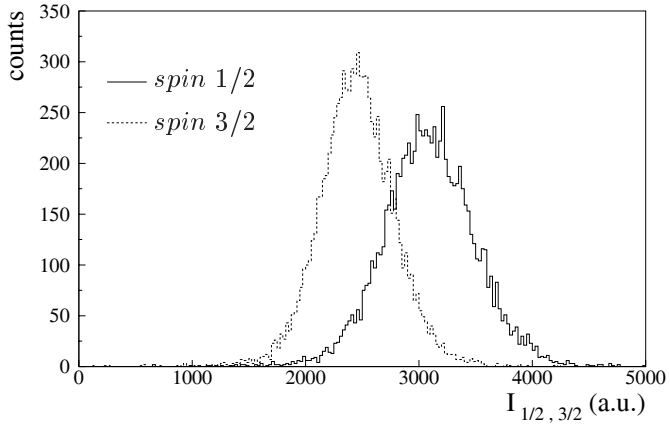

Figure 3.6: Spectra of experimental photon energy distributions taken in the multi-photon mode for $S_3 = +1$ (spin 3/2 in the plot shown as dashed line) and $S_3 = -1$ (spin 1/2 in the plot shown as dashed line) for a specific electron bunch with polarisation 0.59.

beam based on the energy asymmetry of the Compton back-scattering cross section of circularly polarised laser light off the longitudinally polarised electron beam (see figure 3.7). The high background of bremsstrahlung from the HERMES target and

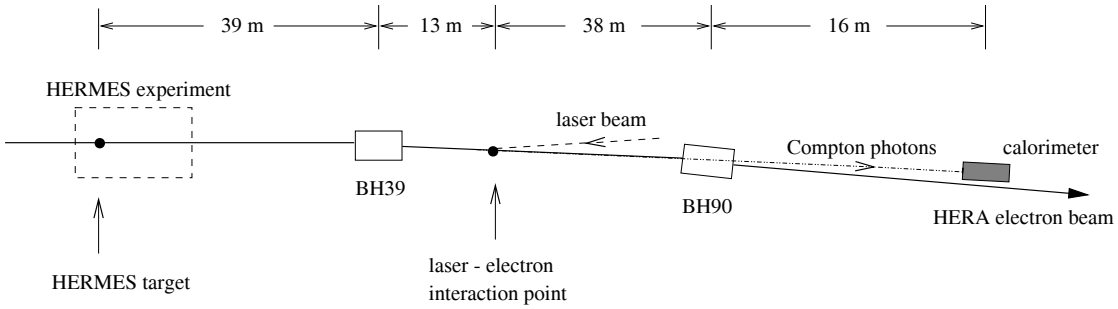

Figure 3.7: Schematic view of the Longitudinal Polarimeter at HERA.

of synchrotron radiation from the bending magnet do not allow LPOL to operate in a single-photon mode. Instead, the LPOL works in the *multi-photon mode*. That means that during electron-laser light interaction due to intense laser source many photons are Compton scattered and their total deposited energy is measured by the calorimeter (photon detector). The polarisation of each single bunch is measured every minute as the time average of the observed asymmetry.

Compton Photon Detector

The Compton photon detector is positioned close to the electron beam pipe (figure 3.7). It consist of 4 optically isolated $NaBi(WO_4)_2$ crystals. The crystals are read out individually by a 4 photo-multipliers to allow measuring the centre of the electromagnetic shower induced by the Compton photons. In front of the crystals two tick lead plates are mounted which serve as pre-shower and shielding against the synchrotron radiation. When the Compton photon enters the detector it generates an electromagnetic shower in the lead and the crystals. The charged particles of the electromagnetic shower produce *Cherenkov light* which is detected in one of the multiplier tubes.

The LPOL provides a polarisation measurement with an uncertainty of 1.6% dominated by the energy calibration of the calorimeter [50].

3.4 The H1 Detector

The H1 detector [53, 54] is located at the northern interaction point of HERA. It is designed as a multipurpose detector in order to measure all aspects of high-energy electron-proton interactions.

The H1 detector is cylindrically symmetric around the beam line having almost hermetic coverage around the beam axis. Since the incoming proton has a significantly higher momentum than the electron, most of the particles produced in an ep collision are Lorentz-boosted in the proton direction. This is the reason for the asymmetric design of the H1 detector, with more instrumentation in the outgoing proton direction which is also called the *forward* direction. Similarly, the electron beam direction is referred to as the *backward* direction. The origin of the H1 coordinate system is the nominal interaction point with coordinates chosen so that x points to the centre of the HERA ring, y in the upward direction and z in the proton beam direction. A general view of the H1 detector with all its components is shown in figure 3.8.

The region around the interaction point is surrounded by tracking detectors. They are used to detect tracks left behind the charged particles as well as the interaction point. A magnetic field deflects the course of the charged particles and allows their momentum to be determined. The tracking system is enclosed by the Liquid Argon Calorimeter (LAr) used to measure the energy and direction of particles. The inner electromagnetic part measures the particle showers created by electrons and photons, the outer layer measures the hadrons. A large superconducting solenoid surrounds the LAr calorimeter and inner tracking system. The solenoid provides an almost uniform magnetic field of 1.15 T parallel to the beam line. This allows the measurement of particle momenta from their curvature radius and of their charge from the direction of curvature. The outermost part of the H1 detector is equipped with a drift tube detector in order to detect muons which can penetrate the layers of dense calorimeter material without being absorbed.

In order to prepare HERA for the luminosity upgrade the interaction regions,

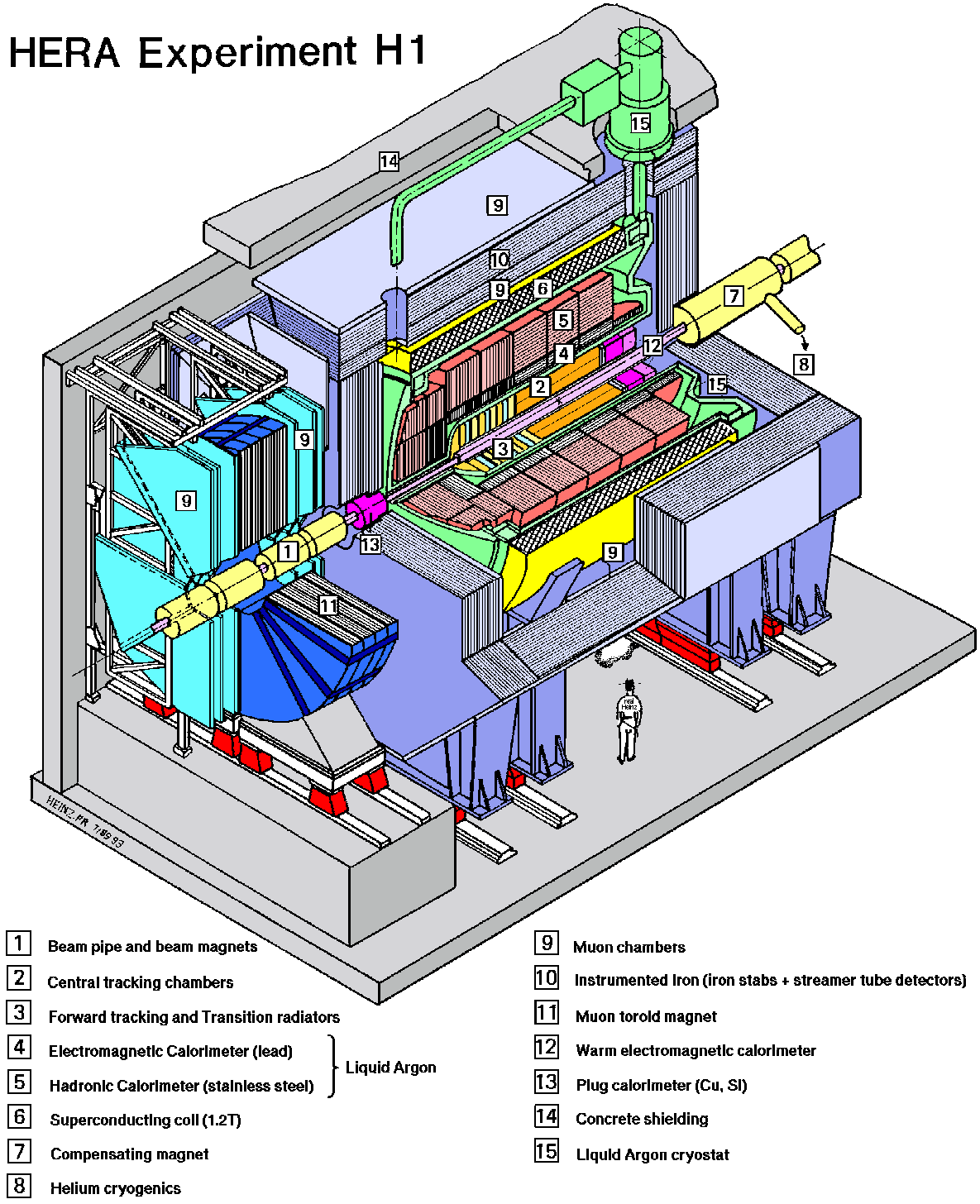

Figure 3.8: View of the H1 detector with all detector components.

H1 and ZEUS have been equipped with two superconducting magnets each, one in the forward and one in the backward direction. Furthermore, the H1 detector has been upgraded (for details see [55–57]) and only upgrade of the detector components important for this analysis will be further discussed.

3.4.1 Tracking System

The H1 tracking system is used for track reconstruction, momentum measurement and accurate determination of the interaction point. It is located in the innermost part of the H1 detector (see figure 3.9). The main components of the tracking system are: the *Central Jet Chambers* (CJC1, CJC2) [58], *Central Outer Tracker Z-Chamber* (COZ), *Central Proportional Inner and Outer Chambers* (CIP, COP) [59,60], *Forward Tracking Detector* (FTD) [61,62], *Backward Proportional Chamber* (BPC). The *Forward Silicon Tracker* [63] (FST) has been added during the upgrade. The other silicon devices are *Central Silicon Trackers* (CST) and *Backward Silicon Tracker* (BST) [64]. Only components relevant for the present analysis will be described further.

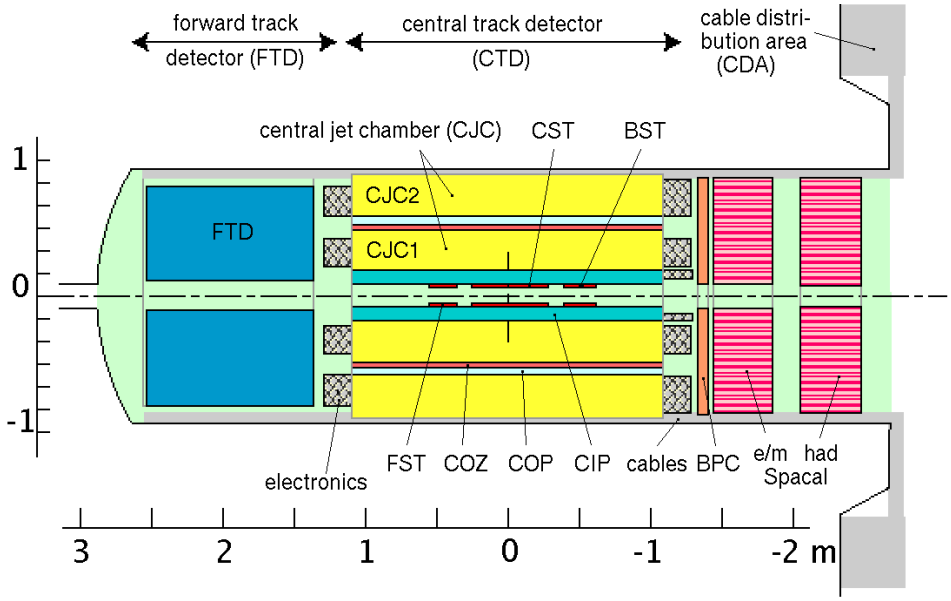

Figure 3.9: The side view of the H1 tracking system.

Central Tracking Detector

The central tracking detector provides the track reconstruction and triggering in the central part of the H1 detector. It consists of 5 cylindrical tracking subdetectors arranged concentrically around the beam-axis, as shown in figure 3.10. The inner (CJC1) and outer (CJC2) central jet chambers [58] are used for an accurate reconstruction of the transverse momentum and azimuthal angle of the charged particles.

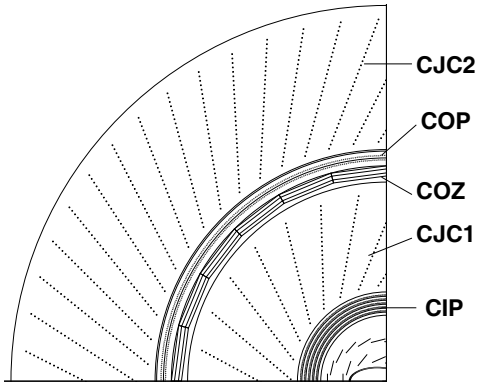

Figure 3.10: Cross-sectional view of the central tracking system.

The CJC1 consists of 30 cells with 24 sense wires in each cell covering a polar angular range of $22.5° < \theta < 157.5°$. The CJC2 consists of 60 cells with 32 sense wires each and has an angular acceptance of $39° < \theta < 141°$. From the measured drift time single hits are reconstructed with a spatial resolution of $\sigma = 170$ μm in the $r - \phi$ plane and 22 mm in z. In addition, the event timing can be determined with the precision of about 1 ns, allowing the determination of the interaction time which is very powerful for rejection of non-ep background. The CJCs provide a measurement of the transverse momentum, p_T, with a resolution:

$$\frac{\Delta p_T}{p_T} = 0.01 \mathrm{p_T GeV^{-1}}. \tag{3.11}$$

During H1 upgrade CIZ and two planes of CIP [65] have been replaced with five planes of cylindrical proportional chambers CIP2k [66]. Additional planar chambers improve the track determination in the forward region: The MWPCs and transition radiators were replaced by three planar drift chambers.

The Central Outer Z-chamber (COZ) is a drift chamber with sense wires perpendicular to the beam axis, complementing the accurate $r - \phi$ measurement provided by CJC chambers with an accurate z-position of the particle tracks. It is placed in between CJC1 and CJC2. Its spatial resolution in the z-direction depends on the polar angle of the traversing charged particle within the range $\sigma = 200 - 500$ μm.

The central proportional chambers CIP and COP are Multi-Wire Proportional Chambers which provide fast timing signals with a resolution of 21 ns which is sufficient to determine the bunch crossing time. Since for trigger purposes the estimated position of the vertex along the beam pipe is most important, the segmentation is finer in the z-direction than in the ϕ-direction.

3.4.2 Calorimeters

Calorimeters are used to measure the energy and position of particles and serves for the identification of different types of particles. Calorimeters are sensitive not

only to charged, but also to neutral particles by detecting their charged secondaries. Calorimeters play a very important role at high energies since the relative energy resolution improves as $\Delta(E)/E \sim E^{-1/2}$ at large E, and in addition, they can provide reasonably fast signal, important for making the trigger decisions.

The H1 calorimeter system contains four separate detectors: The *Liquid Argon calorimeter* (LAr) covers the central and forward region of the H1 detector. In the very forward part it is complemented by the PLUG calorimeter and in the backward region by the *Spaghetti Calorimeter* (SpaCal). Finally, the hadronic *Tail Catcher* measures the energy leaking out of the LAr calorimeter.

3.4.2.1 The Liquid Argon Calorimeter

The Liquid Argon calorimeter [67] is the most important detector for measurements of energies and emission angles of particles produced in the *ep* collisions.

In order to detect electromagnetic as well as hadronic final state particles the LAr calorimeter is designed as a sampling calorimeter composed of two sections: an inner electromagnetic (EM) region and an outer hadronic (HAD) region, as shown in figure 3.11. The LAr calorimeter has an acceptance in polar angular range $4^\circ \leq \theta \leq 154^\circ$. It has a high granularity of ≈ 45000 cells to ensure good spatial resolution of the deposited energies. As a sampling calorimeter it has cells constructed from absorber material plates separated by gaps filled with Liquid Argon as active medium. The absorber material is lead in the EM section and stainless steel in the HAD section.

When an incident particle interacts with the absorbing material it produces secondary particles which will generate further particles. A particle shower, or cascade, will develop in this way while the energy of the initial particle is shared among the cascade particles. This process will continue until the shower particles lose their energy in the calorimeter via interactions with the atoms of the detector material. The energy lost in the active layers is measured. Electrons and photons lose their energy in the absorbing material via bremsstrahlung and pair production, respectively. The electromagnetic secondaries interact themselves electromagnetically at the characteristic scale of the *radiation length*. Hadronic particles scatter inelastically and elastically on the absorber nuclei. A hadronic shower develops through the secondary particles interaction, at the scale determined by the *nuclear apsorbtion length*. Since this length is larger than the corresponding radiation length, hadronic calorimeters are larger than electromagnetic shower detectors. The depth of the EM section is $\approx 20 - 30$ radiation lengths. The HAD section depth is $\approx 5 - 8$ interaction lengths. In the longitudinal direction the calorimeter is split into 8 different "wheels" as can be seen from the schematic view presented in figure 3.11 (a):

- Inner and Outer Forward calorimeters (IF, OF);
- Forward Barrel calorimeter modules (FB1, FB2);
- Central Barrel calorimeter modules (CB1, CB2, CB3);

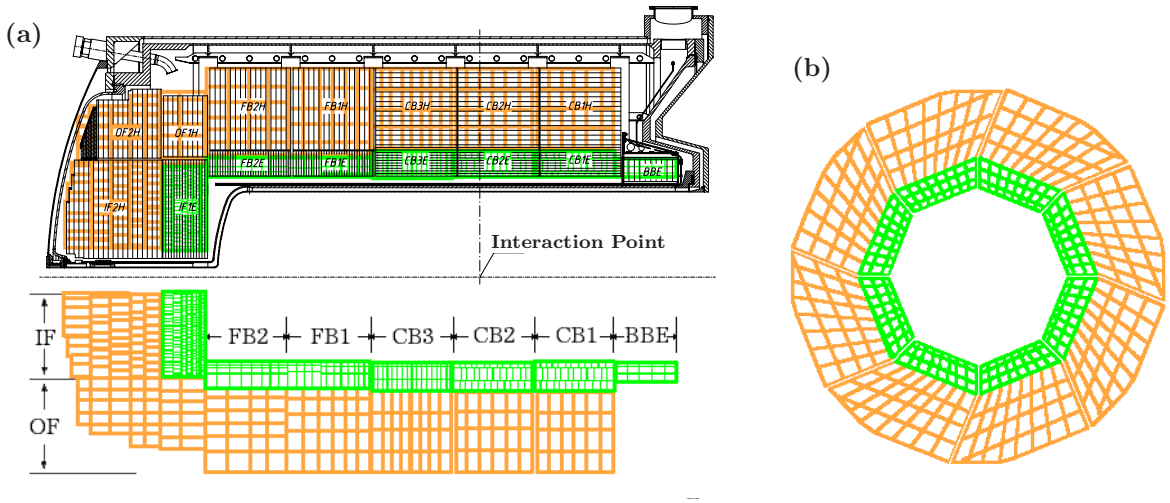

Figure 3.11: The Liquid Argon calorimeter. (a) Side view ($r-z$ plane), showing the orientation of the absorber layers in the upper and the segmentation into read-out channels ($\approx$ 45000) in the lower half. As can be seen, the calorimeter is composed of an inner electromagnetic and the outer hadronic section. In addition, the segmentation into wheels is shown: inner forward (IF), outer forward (OF), forward (FB), central (CB) and backward barrel (BBE). (b) The radial view, showing the segmentation into read-out cells in the $r-\phi$ plane.

- Backward Barrel Electromagnetic calorimeter (BBE).

In the azimuthal direction, each wheel is divided into the 8 octants (figure 3.11 (b)). Due to mechanical tolerances there are narrow regions between the wheels (z-cracks) and between the phi octants (ϕ-cracks) without active medium.

It is a typical non-compensating calorimeter. Non-compensating means that the response for hadrons of a given energy is not equal to that of electrons or photons. For the same energy hadrons deposit $\sim 20-30\%$ less energy than electromagnetic particles of the same original energy due to losses in nuclear excitations and break-up of nuclei, as well as production of neutrinos and muons (mostly from π decay). The hadronic energy response is corrected in software through the weighting techniques [68].

The advantages of LAr calorimeters are: good stability, homogeneity of the response [69], ease of calibration and high granularity which opens up the possibility to measure precisely the angles of scattered photons. Furthermore, the LAr calorimeter is used to identify the local electromagnetic energy depositions. The disadvantage of this calorimeter is electronic noise pickup because the un-amplified signal from the ionisation needs to be transported over many meters to the amplifier electronics located outside of the detector.

The energy resolution is determined from test beam measurements [67,70,71] to be $\sigma(E)/E = 11\%/\sqrt{E/\mathrm{GeV}} \oplus 1\%$ for electromagnetically interacting particles (electrons and photons), and $\sigma(E)/E = 50\%/\sqrt{E/\mathrm{GeV}} \oplus 2\%$ for hadrons.

The Spaghetti Calorimeter

The Spaghetti calorimeter [72,73] (SpaCal) consists of lead sheets in which scintillating fibres ("spaghetti") are embedded. Particle showers in the lead cause the fibres to scintillate and the light is transported to photo-multipliers where it is converted into an electric pulse. It has an electromagnetic and a hadronic component and provides information in the backward region of the detector ($153^\circ < \theta < 178^\circ$). In SpaCal the scattered electrons from NC reactions with low Q^2 (< 100 GeV^2) are measured. The SpaCal signals have a time resolution of about 1 ns which is useful in the first trigger level to reject background events coming from upstream together with the protons. In the analysis presented here the SpaCal is used only to reject background (beam-wall, beam-gas) and to veto non-CC ep interactions.

3.4.3 The Muon System

The main purpose of the muon detector [54] is to identify muons with momenta $\geq$ 2 GeV. The muon system is composed of the forward muon detector and the instrumented iron surrounding the calorimeter and the magnet cryostat.

The Forward Muon Detector

The Forward Muon Detector consists of 6 double layers of drift chambers and a toroidal magnet with angular acceptance $3^\circ < \theta < 17^\circ$. The toroidal field allows to measure the momentum of muons in the range 5 GeV$< p <$ 200 GeV. The lower limit is determinated by the energy loss in the forward part of the LAr calorimeter and the iron yoke (the muons will not reach the drift chamber after the toroid) and the upper one is determinated by the maximum bending field of the toroid and the spatial resolution of the drift chambers.

Instrumented Iron

An iron yoke surrounds the LAr calorimeter and returns the magnetic flux of the solenoid magnet. The yoke is made of 10 layers of iron plates which are separated by slits filled with drift chambers. The angular acceptance of the instrumented iron is $4^\circ < \theta < 172^\circ$. The instrumented iron serves a dual purpose: First, it acts as a detector for penetrating muon tracks. Second, it is used as a tail catcher calorimeter to detect and measure the hadronic energy leaking out from the LAr and the backward calorimeters.

3.4.4 The Time-of-Flight System

The Time-of-Flight (ToF) system is used to reject beam gas background arriving out of time in the H1 detector. The ToF consists of three scintillation detectors positioned along the beam pipe: the backward ToF (BToF) at $z = -275$ cm, the forward ToF

(FToF) at $z = 790$ cm and the Plug ToF (PToF) at $z = 540$cm. In addition there are two scintillator walls (Veto Wall) installed at $z = -810$ cm and $z = -650$ cm. A side view of the ToF system is shown in figure 3.12. The ToF system discriminates between particles arising from beam-induced background and those from ep interactions on the basis of the excellent scintillator time resolution ≈ 1 ns. Particles originating from non-ep background will be tagged by an arrival time in the scintillator earlier than the bunch-crossing time.

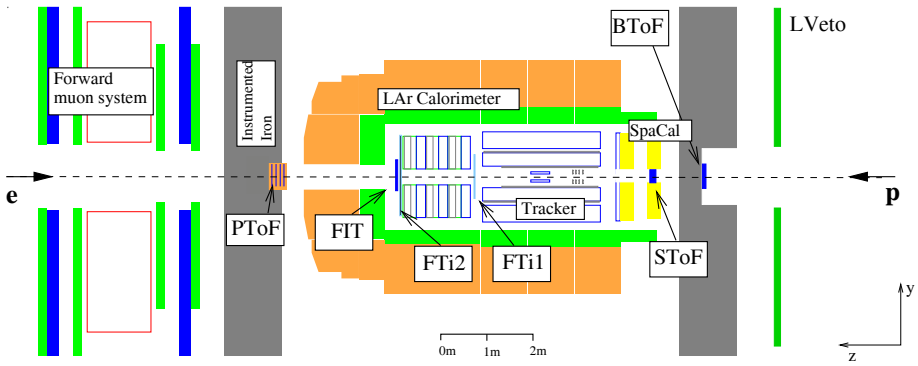

Figure 3.12: The Time of Flight system at HERA II.

3.4.5 The Luminosity System

The luminosity L is measured using the bremsstrahlung (Bethe-Heitler) [74] process $ep \rightarrow ep\gamma$: Since the cross section σ_{BH} of this process is large and theoretically well known, the luminosity can be determined from an accurate measurement of the event rate taking into account the detector acceptance. The luminosity is measured by counting the rate N_{BH} coincidence between a photon and an electron in two calorimeters positioned far away from the interaction region, the photon detector at $z = -102.9$ m (PD) and the electron tagger at $z = -33.4$ m (ET) as:

$$L = \frac{N_{BH}}{\sigma_{BH}}. \tag{3.12}$$

An offline correction of the luminosity is made taking into account the luminosity coming from so-called satellite bunches [75] i.e. parasitic proton bunches which follow the main bunch by some 10 ns. A layout of the luminosity system is shown in figure 3.13.

3.5 Trigger System

The purpose of the H1 trigger system is to separate interesting physics events from the background and to initiate the complete readout of the selected events [76].

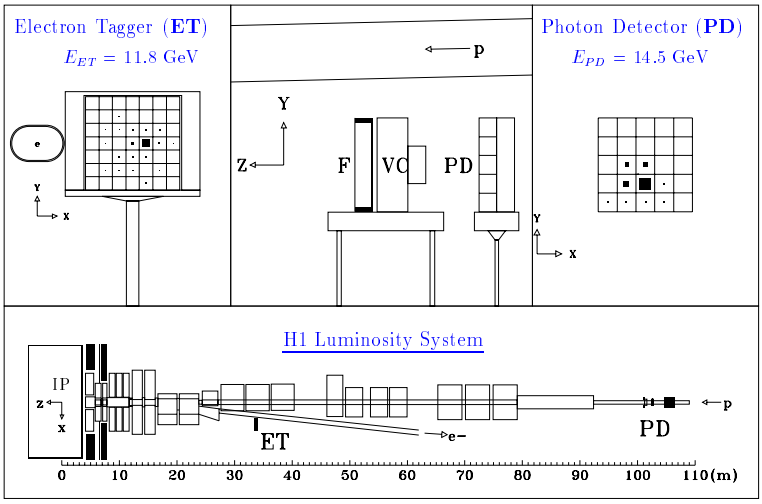

Figure 3.13: Schematic view of the luminosity system. The position of the electron tagger (ET) and photon tagger (PD) with respect to the nominal interaction point (IP) is shown at the bottom. At the top an *xy* view of the ET and the electron beam pipe (left) as well as the PD (right) is shown. The PD is protected from high synchrotron radiation flux by a water Cherenkov veto counter (VC) and a lead filter ("F").

However, the rate of background events is up to the factor of 1000 higher than the rate of interesting *ep* events and the time between the bunch-crossings containing potential events (96 ns) is much shorter than the time needed to fully readout and permanently store an event. In order to cope with these problems the H1 trigger system, as illustrated in figure 3.14, is composed of four levels, designed to reduce the trigger rate from the bunch-crossing input frequency of 10.4 MHz to the output rate of writing events to tape of about 10 Hz.

3.5.1 The First Trigger Level

The first trigger level selects the candidates from interesting *ep* interactions within 2.3 μs. The selection is based on information derived from the different subdetectors in form of 256 conditions, called *trigger elements*. Since the decision is longer than bunch crossing time, the trigger information is stored for each bunch cross in so-called *pipelines*. The circular pipelines have a depth of 30 bunch crosses, corresponding roughly to the memory time of the individual subdetectors. The trigger elements coming from the various subdetectors are synchronised and combined by logical operations in the *Central Trigger Logic* (CTL) into 128 *raw subtriggers*. From the raw sub-triggers actual subtriggers are formed by taking into account *prescale factors*. Prescaling means that not all events fulfilling the raw subtrigger condition are kept, but only a fraction of them [77]. This is done in order to reduce the trigger rate of some high rate subtriggers.

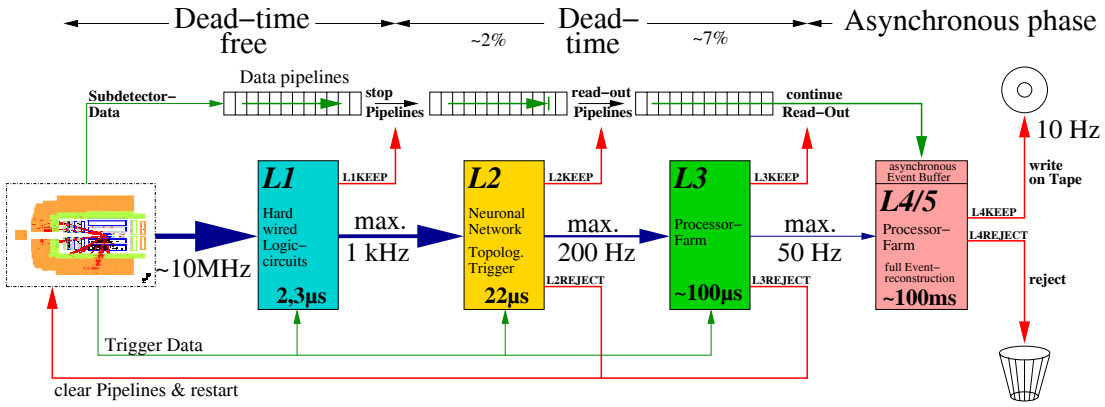

Figure 3.14: A schematic view of the four level H1 trigger system. The input and output rates of each trigger level as well as the decision time is shown. The rate is reduced from the input value of 10.4 MHz to an output rate of about 10 Hz.

The L1 trigger decision is determined by the actual subtriggers. If at least one of the 128 actual subtriggers is set, the event is kept. After a positive trigger decision the pipelines are stopped and the trigger data are sent to the second trigger level. During this time the H1 detector is insensitive to further *ep* interactions, generating *dead time*. In the case that none of actual subtriggers is set for a given bunch cross, the event information is pushed forward in the pipelines by the succeeding bunch cross.

All trigger elements relevant for this analysis are discussed below with the special emphasis on the LAr trigger and its trigger elements as the main trigger for high Q^2 physics.

3.6 The Liquid Argon Trigger

This section contains a description of the LAr trigger. First the hardware components of the LAr trigger are described, following the trigger signal from the LAr calorimeter cells until the trigger elements are formed and supplied to the central trigger logics. In addition, the main trigger quantities are described such as the timing signals ("t0"), the energy signals ("FADC"), the quantities derived from the energy signals (energy sums), and the LAr trigger elements constructed from the energy sums.

The LAr calorimeter trigger is used to identify events with large momentum transfer. It has to satisfy two requirements: First to derive energy signals, second to determine a timing signal ($t0$) [78]. A schematic view of the LAr trigger is shown in figure 3.15. The trigger is divided into an analog and a digital part.

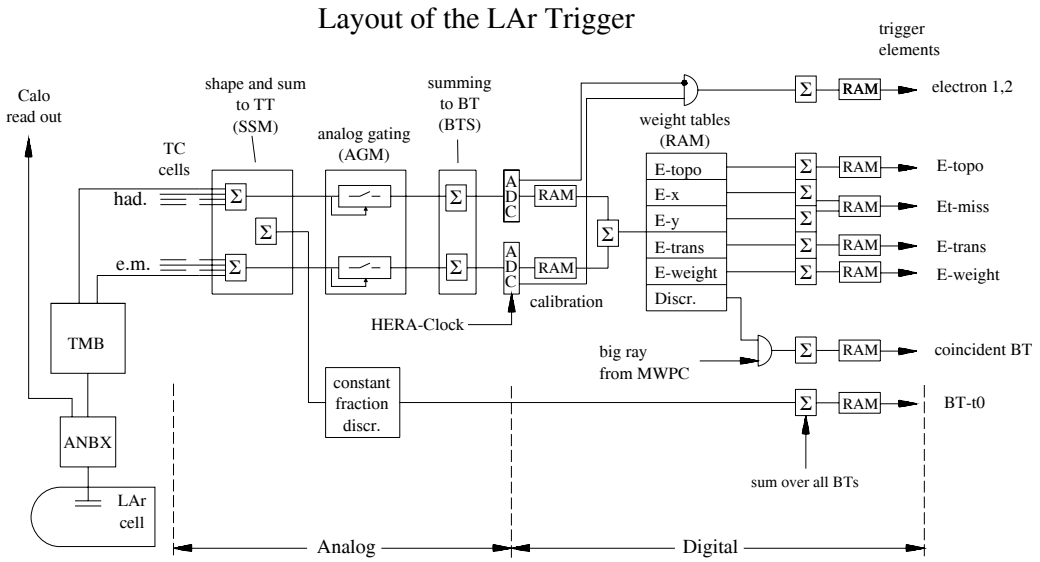

Figure 3.15: Schematic view of the Liquid Argon Trigger (LAr) electronic. The LAr trigger is divided into an analog and a digital part.

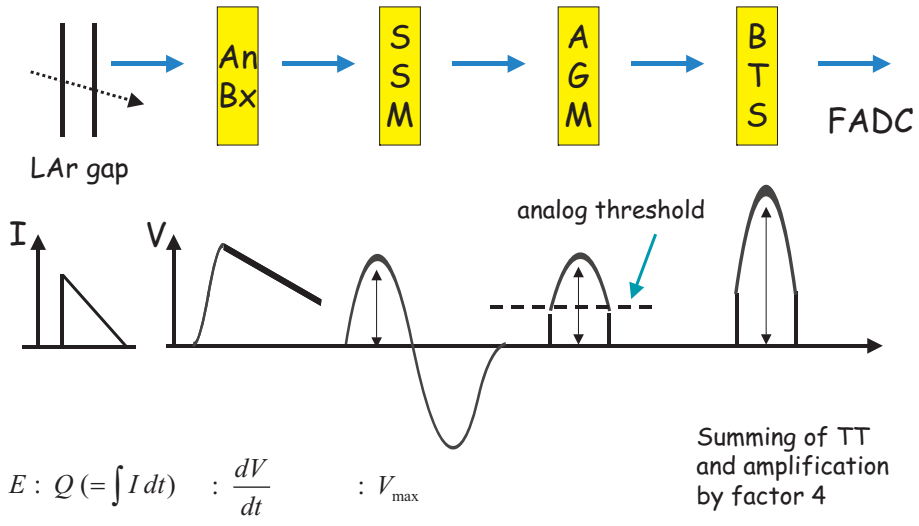

Figure 3.16: The various stages of the analog chain.

3.6.1 Analog Part of the Liquid Argon Trigger

The analog signal has its origin in the ionisation produced by the particles in an electromagnetic (EM) or hadronic (HAD) shower. The ionisation charges are generated mainly by the charged shower particles traversing the LAr gaps between the absorber material. These charges are collected on 45000 geometric pads (GP) and the resulting signals are fed into analog cards located in the analog boxes (ANBX) outside of the LAr cryostat. In the following only the electronic signals relevant to the LAr trigger are discussed leaving out details of the 45000 calorimeter cells.

On the analog cards the charge collected on the GPs is amplified and the signals of the GPs are summed up into 4845 trigger cells (TC) so that one EM TC contains 16 neighbouring GP and one HAD TC contains 4 GPs. The signals are then transferred to the trigger merging board (TMB) where the trigger cells are arranged to projective trigger towers (TT) pointing to the interaction region. The actual summing of the TCs to a TT is done in the summing and shaping modules (SSM) where the TC signals are adjusted individually in amplitude and timing. In the SSM the signals are transformed to a bipolar (sinus-like) shape with an amplitude proportional to the deposited energy. The width of the shaped signal is about 1 μs. Up to 4 EM cells give one EM tower, up to 6 HAD cells give one HAD tower. In order to suppress large unphysical signals (e.g. from HV problems in the LAr gap) the signal from each individual trigger cell can be excluded from the summation. After the SSM, the trigger tower signals are discriminated in the analog gating modules (AGM) to suppress remaining electronic noise: both EM and HAD parts of the TT signal are compared to adjustable thresholds, for each TT independently. The signals which are lower than the requested thresholds are suppressed.

As the last step in the analog chain, the TTs (a total of about 1200) are summed up to big towers (BT,total of 512) in the big tower summing units (BTS). The EM and HAD signals from up to 4 TT are summed separately to give the EM and HAD big tower energies which are digitised later. In parallel to the BTS unit, the sums of the EM and HAD parts are used to derive the bunch crossing time when the *ep* interaction happened ("event $t0$").

3.6.1.1 The $t0$ Signal

A very important aspect of the LAr trigger is its capability to determine the *time of interaction (bunch crossing time or event $t0$)* of an interesting event. In order to derive a timing signal for each TT, the pulse is delayed by 500 ns and compared to the original, undelayed pulse. The crossing point of both signals is independent of the amplitude. To avoid distortions of the signal by noise, a high threshold (typically 5 GeV) is applied in order to generate a $t0$ signal. This signal is synchronised with the HERA clock. A logical 'OR' of all $t0$s belonging to a given BT is used to define the $t0$ for this BT [79]. The corresponding "$t0$ bits" are transmitted individually to the digital adder tree where they are summed logically to the event $t0$ (see below).

In order to become insensitive to noise and to guarantee stability in tagging the

correct bunch crossing, the analog $t0$ is formed only for those TT which exceeds a sufficiently high energy threshold. The calorimeter is divided into 14 polar angle bins (θ) and up to 32 azimuthal angle bins (ϕ), depending on the theta position. The $t0$ threshold is θ-dependent and it is higher in the forward region since there are large energy depositions and narrow jets are expected. In addition, a high background rate of $t0$-signals is expected in the very forward region due to beam-gas interactions and remnants of the target jets. The innermost 3θ rings are therfore excluded (masked) and cannot contribute to the event $t0$. The masking is done in the digital part of the LAr trigger.

After masking the BTs, all remaining $t0$s are summed and discriminated against a threshold number (usually 1) and then sent to the CTL. This signal is called the *digital* $t0$. At the same time the so-called *analog* $t0$ is formed by summing all $t0$s without masking. Again the sum is discriminated against a threshold number (usually the same as for the digital $t0$) and the resulting signal is sent to the CTL.

3.6.2 Digital Part of the Liquid Argon Trigger

The digital part of the LAr trigger receives the analog signals of the 512 BTs and the logical information (bits) from the timing signals. The digital part processes all these informations to provide trigger elements (TE) to the CTL. The pulses from the EM and HAD parts of the BT's are digitised in Fast Analog to Digital Converters (FADC's; in figure 3.15 they are labelled as "ADC") with a precision of 8 bits, clocked at a frequency of 10 MHz, corresponding to the bunch crossing frequency. The EM and HAD sections are added to total BT energy sums after weighting by look-up tables (LUT). The weighting takes care of the proper energy calibration of each BT, the effects from the different energy depositions in the EM and HAD parts of the calorimeter, and a possible threshold applied to suppress noise. The BT sums are used to calculate global quantities in the Adder tree:

- topological energies Etopo which consist of energies from the different topological regions in detector (IF, CB, FB, see figure 3.11);
- transverse energy LAr_Etrans;
- missing transverse energy LAr_Etmiss, calculated as separate sums of the two transverse components E_x and E_y (see subsection 3.6.2.1);
- weighted energy LAr_Eweight.

All four energy sums are derived by summing the individual BT sums after suitable transformation via look-up tables ("RAM" in figure 3.15). They can thus be regarded as *global sums*.

The $t0$ bits are counted in the digital part for each BC. The total number is compared to a threshold (again usually 0) and the $t0$ TE is generated if the threshold is exceeded. Finally, the LAr trigger provides a trigger for electrons, based on the energy

depositions in the EM and HAD parts. For each BT a minimal energy is required in the EM part and a maximal energy in the HAD part. If both conditions are met, an "electron bit" is set for the BT. Again the electron bits are summed and compared to a threshold. As can be seen from figure 3.15, two sets of energy and number thresholds are realized in the hardware, so that an "electron 1" and an "electron 2" trigger can be provided. Two different trigger elements LAr_electron1 and LAr_electron2 are set for two different thresholds and are sent to the CTL. LAr_electron1 is used for triggering of the CC and NC events as will be discussed in chapter 6.

3.6.2.1 Adder tree

The most complex part of the LAr trigger is in the so-called adder tree electronics, where the global energy sums are calculated. The process of summing in the adder tree has three steps: the first is done on the adder boards, located in the FADC crate, summing up the calibrated EM and HAD parts. There are 8 such crates one for each of the different topological regions of the calorimeter. The second step is adding the weighted BT sums in the topological boards, where the partial sums in the various topological areas are built. Finally, the summing board calculates the global quantities over the entire calorimeter. In addition to the BT bits discussed above the following quantities are calculated:

The *topological sums* are formed from the FADC energies deposited in the various calorimeter regions (IF, FB, CB): The FADCs from the EM and HAD parts are weighted by look up tables and then added to form the energy sums quadrant by quadrant for each of the topological regions. Before summing the weighted BTs are discriminated against the individual thresholds. The sums are finally compared to thresholds, building up trigger elements. These bit quantities are sent to the CTL and to the trigger systems at the second trigger level (see subsection 3.7.2).
The *transverse energy sum* LAr_Etrans is the scalar sum of all transverse energies:

$$\text{LAr\_Etrans} \equiv \sum_{BT_i} E_i \sin(\theta_i) \tag{3.13}$$

where θ_i is the polar angle of the big tower BT_i.
The *missing transverse energy sum* LAr_Etmiss trigger element is the transverse vector sum:

$$\text{LAr\_Etmiss} \equiv \sqrt{E_x^2 + E_y^2} \tag{3.14}$$

where:

$$E_x = \sum_{BT_i} E_{x_i} = \sum_{BT_i} E_i \sin(\theta_i)\cos(\phi_i) \tag{3.15}$$

$$E_y = \sum_{BT_i} E_{y_i} = \sum_{BT_i} E_i \sin(\theta_i)\sin(\phi_i). \tag{3.16}$$

Here, ϕ_i is the azimuthal angle of the big tower BT_i. The functions $\sin(\phi_i)$ and $\cos(\phi_i)$ give rise to signed values for the BT energies for each component x or y. If all

particles in the final state would deposit their total energy in the calorimeter, E_x and E_y would be zero because of momentum conservation. Therefore, NC events should lead, in the ideal case, to LAr_Etmiss ≈ 0, while CC events will have LAr_Etmiss $\gg 0$ (the neutrino cannot be detected). All BTs in the first two θ bins of the IF are excluded from the *LAr_Etrans* and LAr_Etmiss sums because in this region large energy deposition from beam-gas background is expected leading to unacceptably high trigger rates.
There is one freely programmable sum:

$$\text{LAr\_Eweight} \equiv \sum_{BT_i} f(\theta_i, \phi_i, E_i) \tag{3.17}$$

where the arbitrary weighting function $f(\theta_i, \phi_i, E_i)$ can be realized, like $\sin(\theta_i)$ and $\cos(\phi_i)$ above, via look-up tables. Each of the adder tree sums are compared to three different thresholds (see table 3.1) and stored as discriminator outputs in the hardware according to the patterns in table 3.1.

The resulting quantities from the adder tree are used to derive the TEs which are fed into the CTL.

Threshold	Condition	Discriminator output
low	$E - SUM(1) > 0$	01
medium	$E - SUM(2) > 1$	10
high	$E - SUM(3) > 2$	11

Table 3.1: Encoding of 3 trigger thresholds in a 2 bit discriminator output.

3.7 The Track Trigger Elements

The CIP2k z vertex trigger [66] is used to do a fast reconstruction of tracks from the hits in the $r - z$ plane and to determine the z vertex of each track at the first trigger level. The trigger elements used in this analysis are described below.

- CIP_T0 defines a timing signal "T0" of an event. It is set if at least one track is seen in the central region for a given bunch cross. In addition, CIP_T0_nextbc is fired if an event occurs in the previous bunch cross. This is an important tool to reject events which are coming out of time as well as to prevent detectors with relatively poor time resolution, such as the LAr trigger, to fire too early.

- CIP_sig is the so-called significance of the tracks from the central region, defined by the ratio between the number of central to the number of background tracks (backward+forward):

$$N_{ctr} > S(N_{bcw} + N_{fwd}). \tag{3.18}$$

S	0	1	2	4
CIP_sig	0	1	2	3

Table 3.2: The trigger element CIP_sig is set to the given value depending on S.

The value of S is sent to the CTL. $S = 0$ means that the number of central tracks is the same or smaller as the number of background tracks. $S > 0$ means that there are more central than background tracks. According to the track significance 4 corresponding CIP_sig trigger elements are defined as given in table 3.2.

- CIP_mul gives the track multiplicity information of an event. The number of tracks within the CIP acceptance is counted and sent to the CTL. If the number of tracks is above a preset threshold, the trigger element CIP_mul is fired. The number of tracks ranges from 0 to 100 corresponding to $0 \leq \text{CIP\_mul} \leq 7$.

3.7.1 The Veto Conditions

Veto conditions are applied to all subtriggers used in this analysis. They are used to reject non-physics background. Veto conditions can be divided into three groups with respect to the subdetectors which send them:

Veto-Wall Forward-ToF

Due to the good time resolution of the ToF system (see subsection 3.4.4) these trigger elements are able to place an event in an interaction point (IP) or background (BG) timing window. The veto conditions used in the present analysis are the following:

- BToF_BG: Backward TOF background window, characteristic to an signal coming in time with the proton bunch;
- VETO_BG: Veto Wall background window giving an early signal;
- FIT_IA: Forward Interacting Timing hit in proton time window which tags the correct time;
- FIT_BG: Forward Interacting Timing hit in background time window fires an early signal in time with the electron bunch.

SpaCal Vetos

- SToF_BG: SpaCal ToF background window, characteristic to an signal coming in time with the proton bunch;
- SPCLh_ToF_E_1: Energy deposition in the hadronic part of the SpaCal in time with the upstream proton bunch.

CIP Vetos

- CIP_sig, CIP_mul. These signals are used to veto background coming from the collimators close to the H1 interaction region, i.e. either having more background tracks than central tracks (CIP_sig == 0), or having too many tracks where majority are background tracks (CIP_mul == 7).

3.7.2 The Second Trigger Level

The second trigger level has 20 μs to make more sophisticated decisions on an event. It validates the *L1keep* decision using information from two independent systems, *The Topological Trigger* (L2TT) [80] and *The Neural Networks Trigger* (L2NN) [81].

The L2TT uses a 2D projection of the trigger information for an event in θ and ϕ and defines 16 event topologies.

The L2NN exploits multidimensional correlations between input quantities from the L1 trigger systems and performs a pattern recognition in a high dimensional "trigger" space. It is composed of 13 different neural networks which are individually trained to identify specific *ep* interactions. The input to the networks are the level 1 trigger quantities provided by the different subdetectors. The outputs of the networks are compared to suitably chosen thresholds to suppress the background rate to an acceptable level. The outputs of the 13 neural networks and the L2TT provide the L2 trigger elements. If at least one L1 actual subtrigger passes an L2 subtrigger validation the event is accepted and the data readout starts, collecting the information from all subdetectors to be used at the fourth and final trigger level. An L2 reject signal restarts the L1 pipelines.

Only high rate L1 triggers are filtered by L2.

3.8 The Third Trigger Level

The third trigger level has been installed at HERA II as a part of the Fast Track Trigger (FTT) [82] in order to cope with high trigger rates from the track triggers. It is implemented as a software level running on a multi-processor system. The third trigger level can reduce the trigger rate by rejecting events within 100 μs. A *L3Reject* signal interrupts the detector read out.

3.9 The Fourth Trigger Level and Event Reconstruction

The fourth trigger level does a complete reconstruction and classification of an event. This is realised by software algorithms running on a processor farm. The processing of the event information of the level 4 starts once the central event builder of the data-acquisition system has received the raw event data from all subdetectors. The

pipe-lines are started again, terminating the dead-time of the detector. At this moment the H1 reconstruction software [83] is employed in order to reconstruct clusters and tracks for the event which are then used to reconstruct the full kinematics of an event. The accepted events are classified into *event classes* according to their physics properties (high Q^2, high p_T etc.). If an event cannot be assigned to any physics class it is rejected. The accepted events are written to two different data streams, the Production Output Tapes (POTs) and the Data-Summary-Tape (DST) which are basis for the physics analysis. On the POTs, the complete event information, composed of raw and reconstructed quantities, is stored. A subset of (mainly reconstructed quantities) event information is written to DSTs awaiting further analysis.

Chapter 4

Principles of the CC Cross Section Measurement

In the previous chapters the theory of the DIS CC interactions has been explained and the H1 detector was introduced with which CC reactions are observed. The aim of this chapter is to describe the principles of the CC cross section measurement. The importance of selection criteria is discussed first, followed by a description of the background sources and the data modelling ("Monte Carlo " simulations) including the radiative corrections. Finally, the "pseudo charged current" method used to derive important corrections to the Monte Carlo is explained.

4.1 The Total CC Cross Section Measurement

The total cross section σ^{meas} of the CC process measured in counting experiments such as H1 is defined by the following formula (see equation 3.2):

$$\sigma^{meas} = \frac{N^{data}}{L} \tag{4.1}$$

where N^{data} is the number of observed events and L is the collected luminosity which is a function of the beam currents and the beam size as has been discussed already (see sections 3.2 and 3.4.5). However, equation 4.1 would be correct only for a perfect detector. In reality, counting the number N^{data} of events belonging to the CC process is not trivial, since the CC events need to be selected using an optimised set of selection criteria ("cuts") in order to exclude events not generated by the CC process. These cuts inevitably introduce losses, so the efficiency of the cuts is an important issue. In addition, detector effects and contaminating background events need to be taken into account as well as electroweak radiative effects, when the cross section should be compared to theoretical expectations.

Selection of the CC Events and Data Modelling

The CC events are characterised by the neutrino which leaves the H1 detector unobserved, usually leading to a large unbalanced transverse momentum seen in the detector, belonging to the hadronic final state. This momentum is called $p_{T,miss}$, since it corresponds to the *missing transverse momentum taken by the neutrino*. A typical CC event is shown in figure 4.1 where the transverse energy imbalance can be nicely seen. In addition, any *ep* interaction has to come from the interaction region which means to have a well defined "vertex". However, many events are collected by the H1 detector containing mainly backgrounds which do not originate from *ep* interactions, called *non-ep background* such as cosmic rays and halo muons. Furthermore, the CC interactions have a relatively small cross section with respect to the other physics processes taken by the H1 detector and therefore constitute only a minority of the collected events.

In order to extract the CC events from the collected sample of all events we have to

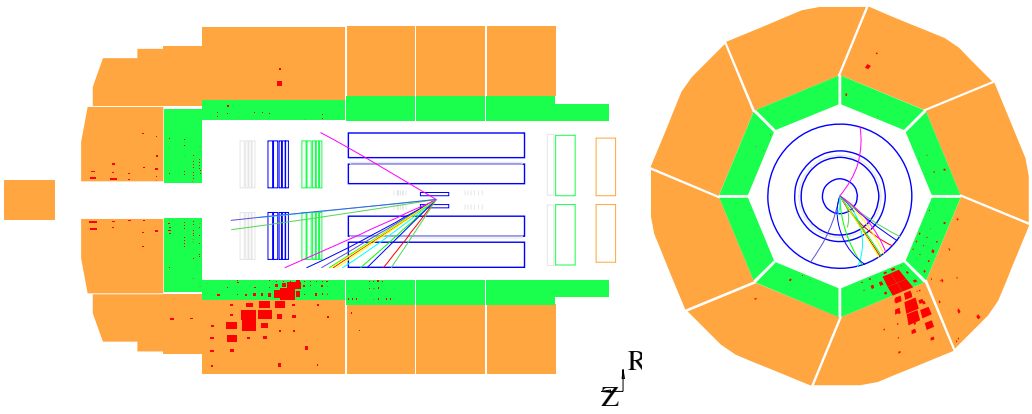

Figure 4.1: The CC event event in the H1 detector shows large deposition of energy in the LAr calorimeter characteristic to CC events. Since the neutrino escapes undetected this energy is unbalanced.

apply a set of *selection criteria* ("cuts") as will be discussed in detail in chapter 7. The typical selection cuts used in the CC analysis are to require high missing transverse momentum $p_{T,miss}$ and a well defined vertex (see subsection 7.2.4). The selection criteria are used to reject the contaminating background, but do also reject some real signal CC events and thus introduce *inefficiencies* which must be properly estimated and taken into account. Due to the selection criteria applied the observed number of data events N^{data} in equation 4.1, is reduced to a number of selected events N^{data}_{sel}. To correct for the losses in the selection one introduces a *selection efficiency* $\mathcal{E}$ which leads to the following expression for the cross section:

$$\sigma^{meas} = \frac{N^{data}_{sel}}{\mathcal{E} L}. \tag{4.2}$$

The selection cuts are optimised to remove the background contamination, but still some fraction of background may remain in the data sample and therefore has to be removed:

$$\sigma^{meas} = \frac{N_{sel}^{data} - N^{bg}}{\mathcal{E}L}. \tag{4.3}$$

All of the above mentioned effects and the contamination by background must be modelled somehow in order to determine $\mathcal{E}$ and N^{bg}. Due to the complexity of the selection cuts, analytical expressions of $\mathcal{E}$ and N^{bg} are usually impossible to formulate. Thus, the MC simulations have been used for this purpose. Furthermore, MC programs are used for theoretical predictions of particle interactions. In addition, a major part of the background events N^{bg} in the final selected sample is estimated with the help of MC. Any discrepancy between data and simulation must be taken into account as a correction to the MC in order to model the selection procedure as good as possible. Therefore, some efficiencies, such as the trigger efficiencies, were determined from the data themselves and MC has been adjusted properly (see section 7.5).

Finally, the MC corrected for all effects observed in the data represents the real theoretical expectation of the cross section and can be compared to the experimental results. The theoretically predicted number of events is determined from the MC using the same basic cross section formula 4.1 which was used for the data:

$$N_{sel}^{MC} = \mathcal{E}L\sigma^{MC}. \tag{4.4}$$

Having verified that the MC describes the data, taking into account inefficiencies, detector effects and assuming the same luminosity in data and MC one obtains an expression for $\mathcal{E}L$ in equation 4.3:

$$\mathcal{E}L = \frac{N_{sel}^{MC}}{\sigma^{MC}}. \tag{4.5}$$

Since we do not want to limit the precision of the measurement by the statistical error of the MC events we generate many MC events corresponding to a much larger luminosity than that collected in data. This means that equation 4.5 will be changed accordingly to:

$$\mathcal{E}L = \frac{N_{sel}^{MC}}{\sigma^{MC}} \rightarrow \frac{N_{sel}^{MC}}{\sigma^{MC}} \cdot \frac{L^{data}}{L^{MC}} \tag{4.6}$$

taking care about the proper weighting of the MC via the factor $\frac{L^{data}}{L^{MC}}$ to correct for the difference in the luminosity with respect to the data. In the end, implementing the last expression in the cross section formula 4.3 we obtain the measured cross section:

$$\sigma^{meas} = \frac{N_{sel}^{data} - N_{bg}}{N_{sel}^{MC}} \cdot \frac{L^{MC}}{L^{data}} \cdot \sigma^{MC}. \tag{4.7}$$

Electroweak Radiative Corrections

One should note that the experimentally measured cross section σ^{meas} in equation 4.7 contains also *radiative* CC events. These are for example events with additional photons radiated from the electron before the interaction. Such events cannot easily be distinguished experimentally from those without radiation. Therefore, the MC used to model the CC events in equation 4.6 must include the radiative corrections as well. That means that the MC cross section σ^{MC} is also "radiative". More generally, the radiative processes arise from the exchange or emission of additional bosons $(\gamma, Z^0, W^{\pm})$ and from diagrams containing additional loops (quantum corrections) as will be discussed in section 4.3.

However, the theory prediction of a cross section is usually given at the *Born approximation*, which means including only the first order processes. Thus, in order to compare the measurement to the theory we must correct the experimental cross section to the Born level [84], taking into account the radiative effects via a correction factor δ^{rad}. Then the measured σ^{meas} and the simulated σ^{MC} radiative cross section can be expressed as a function of the Born cross section and the radiative corrections:

$$\sigma^{meas} = \sigma^{meas}_{Born}(1+\delta^{rad}) \quad \text{and} \quad \sigma^{MC} = \sigma^{MC}_{Born}(1+\delta^{rad}). \tag{4.8}$$

Using the measured Born cross section σ^{meas}_{Born} from equation 4.8:

$$\sigma^{meas}_{Born} = \sigma^{meas}\frac{1}{1+\delta^{rad}} \tag{4.9}$$

and implementing it in equation 4.7 one gets the "measured" Born cross section:

$$\sigma^{meas}_{Born} = \frac{N^{data}_{sel} - N_{bg}}{N^{MC}_{sel}} \cdot \frac{L^{MC}}{L^{data}} \cdot \sigma^{MC} \cdot \frac{1}{1+\delta^{rad}}. \tag{4.10}$$

If the data are described by MC in every respect then the Born cross section can be obtained from the measured number of events by replacing the σ^{MC}_{Born} defined in the right equation 4.8 into the measured cross section given in equation 4.10:

$$\sigma^{meas}_{Born} = \frac{N^{data}_{sel} - N_{bg}}{N^{MC}_{sel}} \cdot \frac{L^{MC}}{L^{data}} \cdot \sigma^{MC}_{Born} \tag{4.11}$$

where N^{MC}_{sel} is derived from the radiative MC after the selection criteria and other experimental inefficiencies.

Corrections to MC: Efficiencies

In contrast to the MC simulation where many effects are only approximately described, for instance the noise in the LAr trigger, in data all detector effects are there by definition. As an example for the inedaquacy of the MC simulation, the trigger response of certain subdetectors, as for example the LAr timing information "T0", is

not completely and properly simulated. Thus, *MC cannot be used to determine the trigger and the timing efficiencies*. Due to the limited statistics of the CC events, the data itself should not be used for this purpose either. Therefore, a new model which describes the CC events in every respect with a sufficiently high statistics is needed. For this purpose the *Pseudo Charged Current Method* based on the NC events has been developed [85], as will be described in section 4.4.

After introducing the main principles of the cross section measurement a more detailed discussion of some steps in the cross section measurement will be given in the rest of this chapter.

4.2 Sources of Background

The background sources contributing to the CC event sample with respect to their origin can be classified in two major groups:

- *ep* **background** originating from other *ep* interactions than CC;
- **non-***ep* **background** which does not originate from *ep* interactions.

Both sources together with the explanations why do they fake the CC events will be now desribed.

4.2.1 Sources of *ep* Background

The main contamination of physics background in sample of CC events originates from *photoproduction* and, to a lesser extent, from *NC events*. These backgrounds can fake CC event sample due to mismeasurement of energies or limited geometrical acceptance of the detector.

Photoproduction events

The process where an almost real photon ($Q^2 \approx 0$), radiated by the incoming electron, interacts with the proton is called photoproduction (γp). In general, the photoproduction events have balanced $p_{T,miss}$, so the $p_{T,miss}$ cut already removes a lot of these events. However, the hadronic final state in photoproduction may contain muons or neutrinos (from weak decays of the hadrons) leading to imbalanced transverse energy in the LAr calorimeter and may therefore fake a CC event. Also it may happen that the jet produced in the final state goes into a crack region of the calorimeter (see section 3.4.2) and thus its corresponding energy is not well measured by the LAr calorimeter leading to an apparent $p_{T,miss}$.

Neutral current events

The NC events usually do not pass the $p_{T,miss}$ cut, since the electron in the final state balances $p_{T,miss}$. However, due to energy loss in the final state caused by the electron scattered into a crack region, for example, NC events can be misidentified as the CC events.

4.2.2 Sources of non-*ep* Background

The sources of the non-*ep* background are *cosmic rays*, *beam halo* and *beam-gas events*. Non-*ep* background events occur at a rate about 10^4 times higher than interesting *ep* interactions in the H1 detector and have to be rejected therefore with high efficiency.

Cosmic rays

Cosmic rays hit the surface of the earth at a rate of roughly 200 Hz per square meter. Since the H1 detector is 15 m under ground, the rate is strongly reduced by absorption and only the high energy component of the cosmic ray spectrum (mostly muons) survives. The rate of cosmic muons which hit the H1 detector with an energy deposit sufficient to pass the LAr energy threshold is about 1 Hz. The experimental signature of cosmic rays is two isolated tracks "back-to-back" and the energy deposits in the instrumented iron and the LAr calorimeter. The energy is usually deposited along a straight line, penetrating the detector. The high energy muons which arrive at the detector can radiate photons and therefore leave large energy depositions in the calorimeter.

A typical cosmic ray event is shown in 4.2. The cosmic rays may fulfil the $p_{T,miss}$ condition if the muon interacts in the detector such that enough energy is deposited in the calorimeter, and the primary muon or secondary particles fulfil the vertex requirement by accident.

Beam halo

Beam halo events occur when off-momentum protons leave the beam-pipe and collide with elements of the magnetic guide field system. The pions produced in such interactions will decay into muons and follow the beam trajectory in time with the proton bunch, as displayed in figure 4.3. The high energy muons may radiate and deposit large "transverse energy" and thus pass the CC selection criteria. The experimental signature of the beam halo is a muon track, parallel to the beam axis, seen in the backward iron end cap, the LAr calorimeter and the forward iron end cap.

Beam gas background

Beam gas events originate from collisions of beam protons with the residual gas nuclei within the beam pipe. In beam gas events the hadronic final state energy can escape

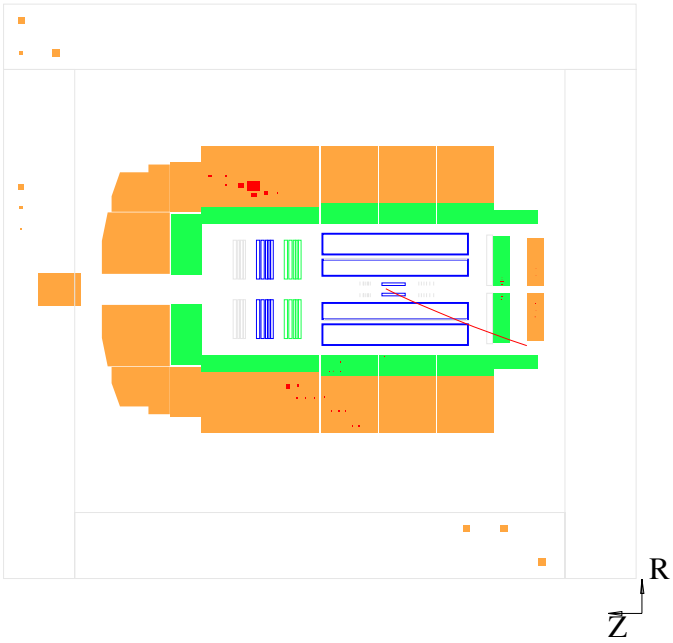

Figure 4.2: The cosmic ray event in the H1 detector.

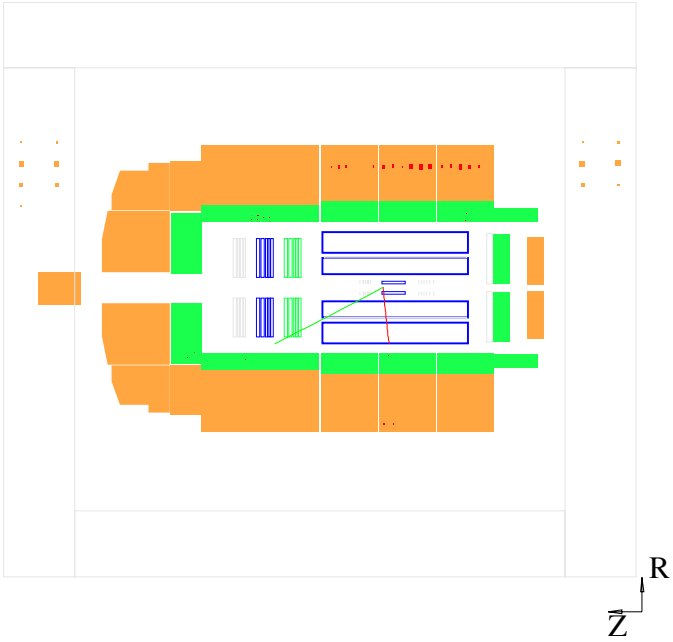

Figure 4.3: The beam halo event in the H1 detector.

through the beam pipe resulting in missing transverse energy and thus may fake a CC event. Due to the high proton momentum the particles produced in these interactions are boosted in the forward region of the H1 detector. The beam gas events are recognised by the energy deposits mostly in the forward direction and high multiplicity of low p_T tracks isotropically distributed in azimuth. Only a small fraction of these events originate by chance from the region of the primary interaction vertex. An event display of the beam gas background is illustrated in figure 4.4.

These three different types of background may *overlap* with underlying physics event such as for example γp, where the muon from the cosmic ray is superimposed over a γp event which by definition satisfies the vertex requirement.

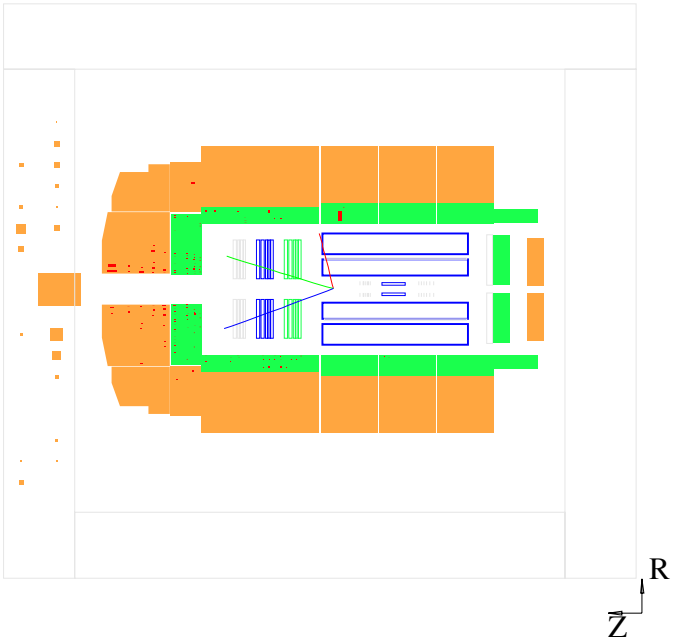

Figure 4.4: The beam-gas event in the H1 detector.

4.2.3 Monte Carlo Simulation

MC programs are used to simulate the signal DIS CC and NC events as well as the contaminating *ep* background reactions. In this section first the different phases of the MC programs are introduced. Then, processes contributing to the CC background and the event generators used to model these backgrounds are described.

There are three phases which the MC has to model in order to simulate *ep* interactions in a real detector.

- **Generation**
  First, the elementary electron-quark scattering process is generated using

Standard Model electron-parton cross sections and empirically determined parametrisations for the parton density functions (PDFs) as obtained e.g. by the MRSH [86, 87]. In the second step higher order QED and QCD radiation effects are taken into account. Finally, phenomenological models take care of the hadronisation [88] of the generated partons and provide the 4 vectors of all final state particles.

- **Simulation**
  For each generated event the H1 detector response to the particles is simulated in detail using the simulation package H1SIM [89] which makes use of the GEANT [90] program. The parameters used in the simulation were determined in beam test measurements and optimised during the *ep* data taking. The energy response in the calorimeters is simulated using a fast parametrisation of the electromagnetic and hadronic showers, as implemented in H1FAST [91, 92].

- **Reconstruction**
  The simulated events are then passed through the same reconstruction program H1REC [83] as the real data (see chapter 5). That means that tracks, momenta and energies of all particles are reconstructed from the detector signals (simulated or real).

The Monte Carlo events not only are the basis to estimate the cut efficiencies (see equation 4.7) but are also a very useful tool for tuning the selection cuts for discrimination between data and background.

The generation step is now described in more detail.

4.2.4 Generation of DIS Events

The Deep Inelastic Scattering processes are generated at the parton level using the DJANGO [93, 94] program package (version Djangoh 1.2). In order to give a complete description of the parton final states in *eq* interactions, DJANGO consists of the programs HERACLES [95] and LEPTO [88] or ARIADNE [96]. The purpose of the HERACLES part of the program is to describe NC and CC *eq* interactions using parameterisations of the parton densities with radiative corrections (single photon emission from the lepton line, self energy corrections and the complete set of one-loop weak corrections (see section 4.3)). LEPTO describes the QCD dynamics using ARIADNE in order to simulate QCD cascades implementing the colour dipole model. The hard subprocess is generated according to the cross section obtained from parametrisations for PDFs e.g. MRSH [86, 87]. The simulated cross section is then reweighted using the H1 PDF 2000 fit for parametrisation of parton distribution functions [40]. In the last step the fragmentation of partons into hadrons is done using the JETSET [97, 98] program.

4.2.5 Generation of Background Events

Photoproduction

Photoproduction events constitute the main background source in the CC interactions as explained in section 4.2.1. There are two different photoproduction processes, *direct* and *resolved*. Both will be shortly characterised now.

In direct photoproduction as shown in figure 4.5 (a) and (b) the photon interacts directly with a quark from the proton or a quark generated by dissociation of gluon, emmited from the proton. Hadrons which are produced in such processes are characterised by high transverse momentum.

In resolved processes (see figure 4.5(c)) the proton dissociates into a quark-antiquark pair and one of the quarks produced by the photon interacts with one of the quarks in the proton. Therefore, in addition to the proton remnant, the hadronic remnant from the photon is created as well. The photoproduction process is modeled by the PYTHIA [99] event generator using the parton density function GRV LO [100, 101] for the proton and the photon.

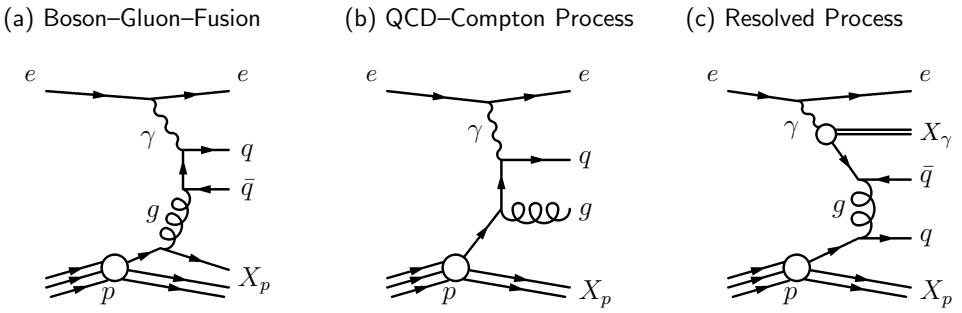

Figure 4.5: The Feynman diagrams of the direct (a) and (b) and resolved (c) photoproduction in leading order.

Real $W^{\pm}$ Production

Real $W^{\pm}$ bosons can be produced at HERA via CC and NC interactions. If the boson decays leptonically and the charged lepton escapes through the beam-pipe the event may be misidentified as a real CC event. Although these events have a very small cross section at HERA $\sigma \approx 0.1$ pb they have to be properly taken into account as a background source (since the CC cross section is only 30-60 times higher). Production of real W's is modelled using the EPVEC [102] generator.

Lepton-Pair Production

Lepton-pair production is also contributing to the CC background through the process $ep \rightarrow eXl^+l^-$ $(l = e, \mu, \tau)$ when the outgoing electron escapes undetected through

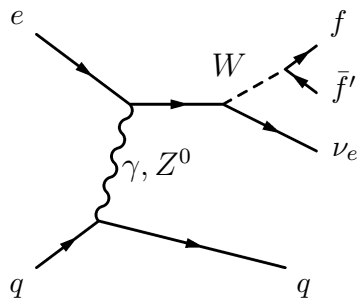

Figure 4.6: Leading order W production diagram leading to a neutrino in the final state .

the beam pipe. Multi-lepton processes are the most likely to occur at HERA via $\gamma\gamma$ collisions. If the produced lepton pair consists of μ or τ leptons the event may be misidentified as a real CC event since their energy deposition is not measured completely in the calorimeter. In such cases a momentum imbalance is introduced into the event which therefore may be misidentified as a CC event.

Lepton-pair events are generated by GRAPE [103], the corresponding lowest order Feynman diagram is shown in figure 4.7.

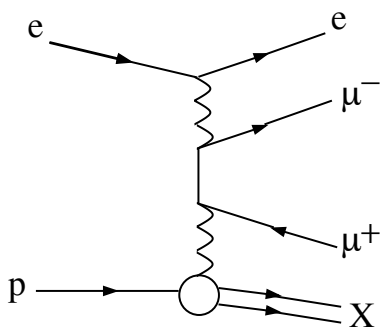

Figure 4.7: Leading order Feynman diagram for lepton-pair production.

4.3 Electroweak Radiative Corrections

The main radiative corrections come from the emission of "soft" additional photons which cannot be resolved in the detector. Soft γ's can be radiated from the incoming quark or lepton or from the outgoing lepton or quark, called *initial state* (ISR) and *final state* (FSR) radiation, respectively. In the case of ISR radiation the energy of the incoming lepton will be reduced and therefore will affect the kinematics with respect to the Born-level calculation.

The radiative correction (see equation 4.9) can be separated in two parts: the electromagnetic QED effects and those involving weak ones,

$$1 + \delta^{rad} = (1 + \delta^{QED})(1 + \delta^{weak}) \; . \tag{4.12}$$

The radiative corrections [104] for the CC interactions have to take into account *real* and *virtual* corrections.
The real radiative corrections include contribution of radiation from the incoming lepton, the incoming and the outgoing quark and the exchanged boson as shown in figure 4.8.
The virtual radiative effects include corrections to the $e\nu W$ and $q_f q_{f'} W$ vertices, self energy corrections to the external lines and graphs for the W self energy as well as box diagrams, as illustrated in figure 4.9. Both together, the real and the virtual corrections, can be separated into three contributions from the *lepton line*, the *quark line* and the *interference terms*. However, it was shown [104, 105] that the quarkonic and interference terms can be neglected, so the only contribution included in the CC simulation is the photon emission from the incoming lepton line (see diagram (a) in figure 4.8).

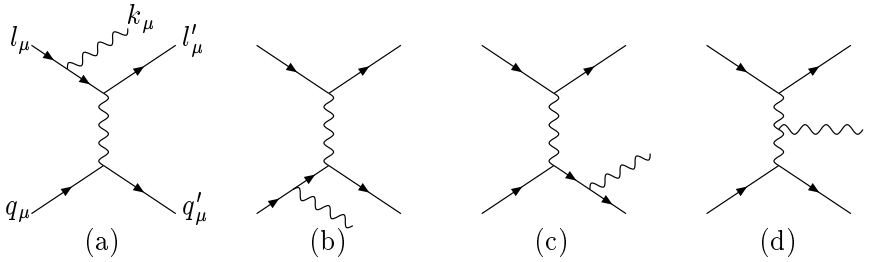

Figure 4.8: Feynman diagrams for $eq \to \nu q'\gamma$ via the W boson exchange.

4.4 The Pseudo Charged Current Method

In order to derive a realistic simulation of the measured cross sections, the MC must be corrected for the effects that are not taken into account in the detector simulation. Some corrections cannot be determined from MC, as for example, the trigger efficiencies (see section 4.1). These efficiencies are obtained from the NC data making use of the fact that the NC and CC events leave very similar signatures in the detector, with the exception of the scattered electron in an NC event. In an NC event (see figure 4.10), the scattered electron balances the transverse momentum of the hadronic final state. Without the scattered electron in the final state, an NC event would look exactly like a CC event (see figure 4.11).

The *Pseudo Charged Current* (PsCC) technique [106] was developed on the basis of this idea. PsCC events are constructed from NC events by removing all information related to the scattered electron in the following way:

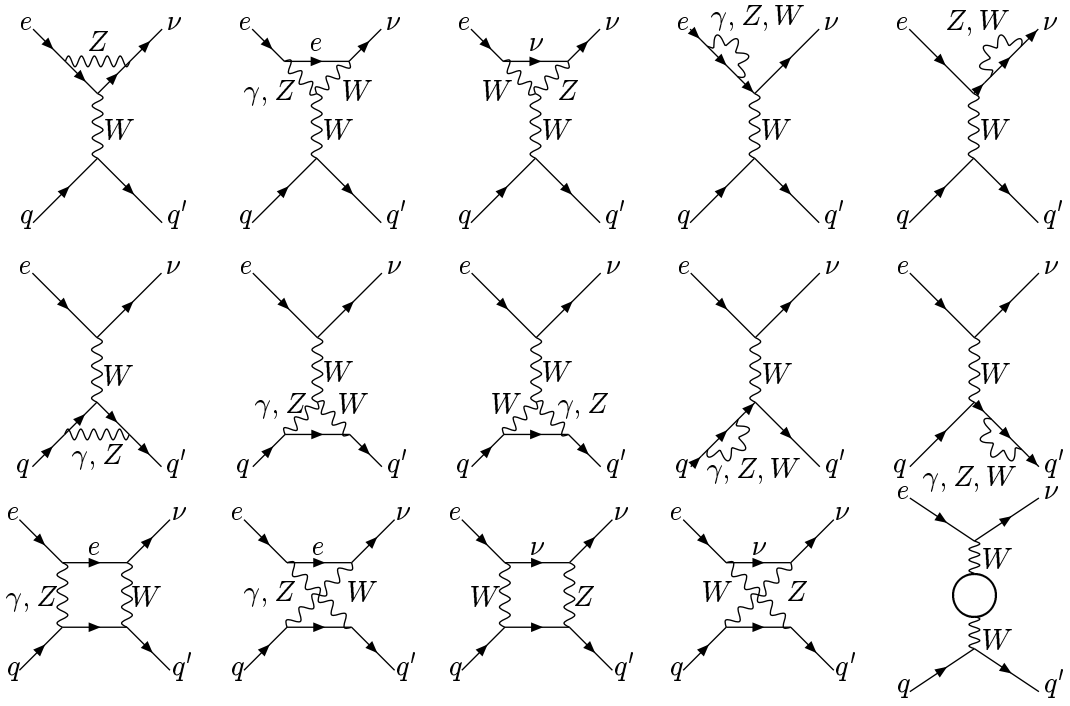

Figure 4.9: One loop Feynman diagrams for $eq \to \nu q'$.

- The electron is identified using a special algorithm designed for that purpose [106].

- A cone with opening angle of 29° is defined with origin at the vertex position of the NC event and its axis going through the centre of the energy deposition in the LAr calorimeter, left by the scattered electron.

- All signals of the scattered electron inside the cone are removed in the following subdetectors:
  (a) the hits in the Central Inner Proportional Chamber CIP;
  (b) the signals from the Central Jet Chambers CJC;
  (c) the information related to the scattered electron from the Fast Track Trigger FTT;
  (d) the FADCs belonging to the LAr calorimeter which are in the geometrical area of the cells inside the cone.

- The trigger elements from the LAr calorimeter, CIP and FTT as well as the corresponding subtriggers are removed. After the electron removal new trigger decisions are calculated based on the hadronic final state alone.

- The events are then fully reconstructed from the remaining hadrons.

With all detector and all trigger information from the electron discarded NC events are the same as CC events (see figure 4.11). This method, of course, is based on the assumption that the hadronic final state in NC and CC interactions is very similar, as was verified in [107]. Since the NC cross section is significantly higher than the CC cross section, the statistics of the PsCC events is much more suitable for an accurate efficiency determination.

In order to correctly reproduce the kinematic variables, the PsCC events are reweighted with respect to the CC cross section. The weight as function of x and Q^2 is given as:

$$w(x, Q^2) = \frac{d^2\sigma_{CC}/dxdQ^2}{d^2\sigma_{NC}/dxdQ^2} \tag{4.13}$$

where the NC and CC cross sections $d^2\sigma_{NC}/dxdQ^2$ and $d^2\sigma_{CC}/dxdQ^2$ are calculated using the H1 PDF 2000 parton density functions [40][1].

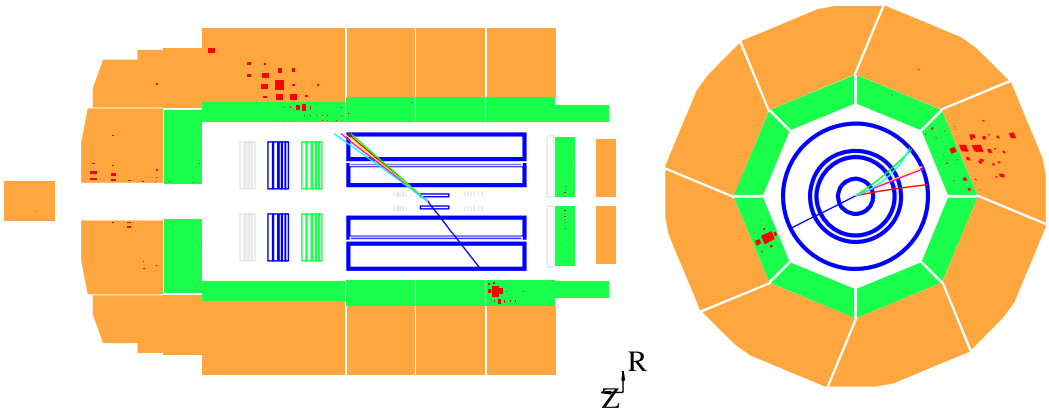

Figure 4.10: A typical NC event in the side (left) and the radial (right) views. The deposited energy from the hadronic final state (mainly in the outer part of the LAr calorimeter) is balanced by the compact energy deposition in the electromagnetic part of the LAr calorimeter (the inner region) assigned to the scattered electron.

[1]The kinematic variables x and Q^2 are measured as in NC event.

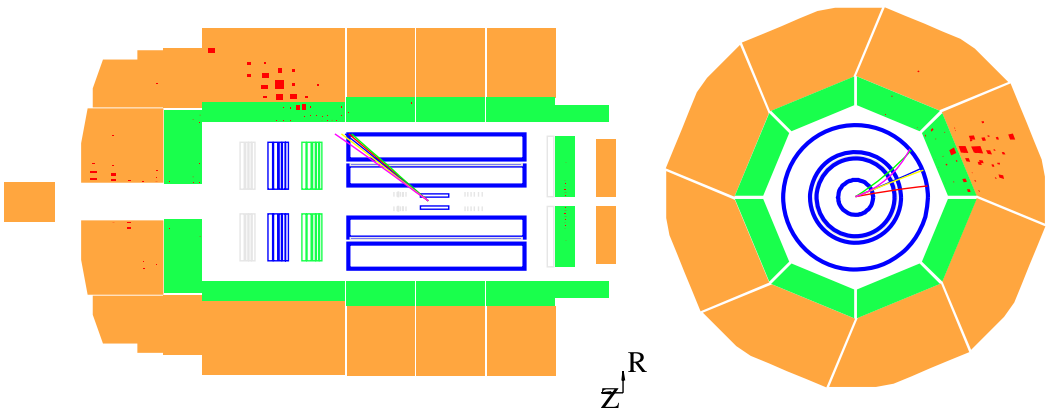

Figure 4.11: The PsCC event reconstructed from the NC event shown in figure 4.10 after the electron removal in the side (left) and the radial (right) views. The event has an imbalanced transverse energy of the hadronic final state, characteristic for the CC events.

Chapter 5

Reconstruction of Kinematic Variables in Charged Currents

The accurate reconstruction of kinematic variables is essential for the cross section determination in bins of the two independent variables x and Q^2. The CC events can be reconstructed only from the *hadronic final state* since the neutrino escapes the interaction region undetected. On the other hand, in the NC interactions information is available from both the scattered electron and the hadronic final state. Thus, an NC event can be reconstructed using different methods which rely on information only from hadronic final state, only the scattered electron, or both. Therefore, these events are used for energy calibration, the trigger efficiency determination and the systematic checks.

In this chapter first the vertex reweighting is described. It is followed by a discussion of the reconstruction methods for both CC and NC interactions, the hadronic energy measurement, and the hadronic final state calibration using the DIS NC events.

5.1 Neutral Current Events for Charged Current Data Analysis

The NC events are a very important ingredient for the CC analysis. There are few reasons for that.

First of all high Q^2 NC events cover the same kinematic domain as the CC events. Furthermore, the NC events have a much larger cross section (due to the additional photon exchange) and therefore are essential from the statistical point of view for many purposes such as the estimation of the systematic uncertainties or cross checks of the data stability. The electron in the final state of the NC events gives the possibility to reconstruct the kinematic variables with different methods and to calibrate the hadronic energy. It is also very important tool for the reconstruction of the interaction vertex as well as determination of the proper description of the interaction vertex in MC. Finally, the NC events are used to calculate the CC trigger efficiency, background

finding efficiency, timing efficiency and vertex reconstruction efficiency, as will be discussed in chapter 7.

5.2 Vertex Reweighting in the MC

Accurate determination of the *primary interaction vertex* is crucial for the correct determination of the kinematic quantitates x and Q^2 and thus for the cross section measurement. Therefore, it has to be properly reconstructed in the data and described in the MC. In addition, the vertex reconstruction efficiency which is determined from the data is cross-checked by the MC.

During a luminosity fill (see section 3.1) the interaction points are distributed around the nominal interaction point ($z_{vtx} = 0$) due to the spatial extension of the electron and proton bunches (see section 3.1). In the beam direction and near the nominal interaction point this distribution is approximately Gaussian with a spread of $\sigma = 10$ cm which corresponds to the distribution of the particle density in the proton bunches. Besides the nominal interaction point, in the range +70 cm, in addition, smaller peaks originating from collisions of so-called satellite bunches are present. Since the detector acceptance and resolution are optimised for the *ep* collisions at the nominal interaction point, only events with vertex reconstructed near the interaction point are accepted.

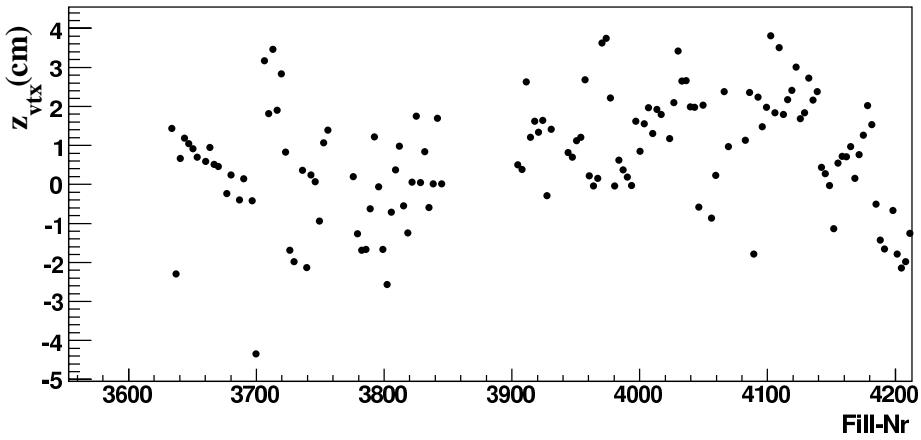

Figure 5.1: The average vertex position as a function of time i.e. fill number (see section 3.1).

As the Gaussian peak may vary from run to run (see figure 5.1) the nominal vertex position is determined as the run-period averaged value. This variation of the actual Gaussian peak position (not more than a few cm) is caused by the variations in the HERA beam optics.

The MC events are simulated with a z-vertex spread corresponding to a Gaussian distribution with mean $z_{vtx} = 0$ and width $\sigma_{MC} = 13$ cm. Figure 5.2 (a) demonstrates

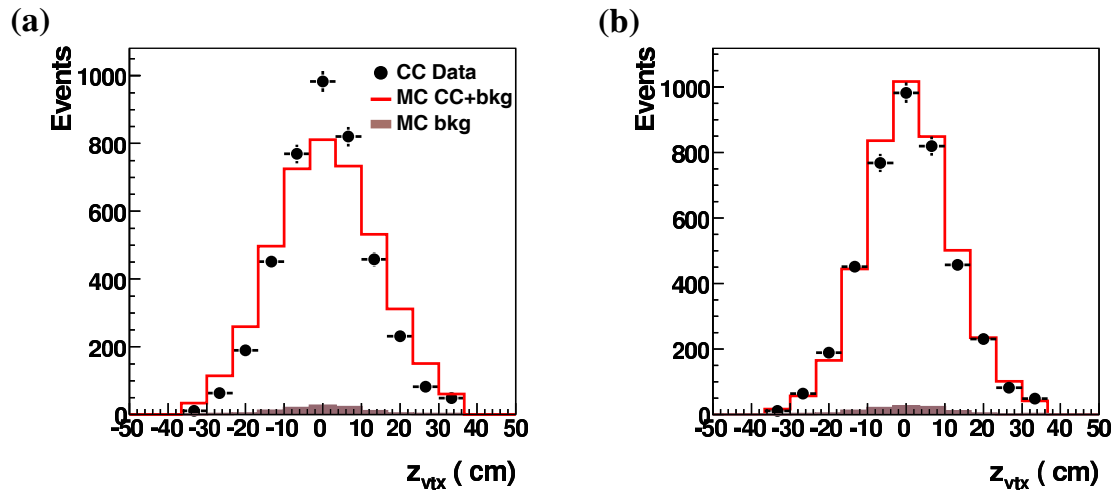

Figure 5.2: The vertex distribution for data and MC before (a) and after reweighting of MC (b). The reweighting factors applied to the MC have been done for the four different data periods.

that the MC needs an adjustment in order to describe the data. Therefore, the MC events are reweighted according to the z_{vtx} distribution obtained from data.

In order to take into account the time dependent variations of the z-vertex position observed in data, the CC MC is weighted accordingly to these values which have been determined for 4 different data periods in year 2005 using the NC events. The effect of the z-vertex reweighting can be seen from the z_{vtx} distribution before and after reweighting of the MC as shown in figures 5.2 (a) and (b), respectively.

5.3 Kinematic Reconstruction Methods

The kinematic reconstruction methods used for the CC and NC events are described below. Firstly the hadron method as the only method to reconstruct kinematic variables for the CC events is introduced. Then other reconstruction methods available and used in different aspects of the NC analysis are discussed.

5.3.1 Kinematic Reconstruction Method for Charged Current Events

The *hadron method* (also called the *Jacquet-Blondel method* [108]) is used to reconstruct the kinematic variables from the hadronic final state particles only. The kinematic variables are determined (neglecting the particle masses) using four-momentum conservation. The hadronic final state is measured using the energy deposits in the calorimeters together with low momentum tracks. Summing over all particles in the hadronic final state the inelasticity y and the squared four-momentum transfer Q^2 are

given by:

$$Q_h^2 = \frac{P_{T,h}^2}{1-y_h} \ , \quad y_h = \frac{\sum_i (E_i - p_{z,i})}{2E_e}. \tag{5.1}$$

The variables E_i and $p_{z,i}$ are the energy and longitudinal momentum components of particle i in the hadronic final state, where the z-direction is defined by the incident proton; $p_{x,i}$ and $p_{y,i}$ are the momentum components of the particle i in the x and y direction. The variable $P_{T,h} = \sqrt{\sum p_{x,i}^2 + p_{y,i}^2}$ is the total transverse momentum of the hadronic final state. Then using these two variables and the centre of mass-energy, Bjorken-x can be derived from equation 2.5:

$$x_h = \frac{Q_h^2}{y_h s}. \tag{5.2}$$

Due to dependence $\frac{1}{1-y_h}$ in equation 5.1, the resolution at large values of Q^2 is decreasing, limiting the hadronic method to low values of y. Therefore, this method is not used in the reconstruction of the NC events.

5.3.2 Kinematic Reconstruction Methods for Neutral Current Events

The Electron Method

The electron method [109] uses information available from the energy $E_e^{'}$ and scattering angle θ_e of the final state electron. In practice, Q^2 and y are experimentally determined and x is calculated using equation 2.5:

$$Q_e^2 = 4E_e E_e^{'} \cos^2 \frac{\theta_e}{2} \ , \quad y_e = 1 - \frac{E_e^{'}}{2E_e}(1 - \cos\frac{\theta_e}{2}) \ , \quad x_e = \frac{Q^2}{y_e s} \ . \tag{5.3}$$

The electron method is accurate at large y corresponding to low electron energy $E_e^{'}$, but at small y the resolution $\frac{\delta y}{y}$ rapidly degrades with $\frac{1}{y}$ as $E_e^{'}$ approaches the electron beam energy E_e.

The Σ Method

The Σ method [110] is constructed to make use of both the electron and the hadronic final state variables, and to be independent of the initial state electron beam energy:

$$Q_\Sigma^2 = \frac{(E_e^{'} \sin\theta^e)^2}{1-y_\Sigma} \ , \quad y_\Sigma = \frac{\Sigma}{E - p_z} \ , \quad x_\Sigma = \frac{Q_\Sigma^2}{s y_\Sigma} \ . \tag{5.4}$$

Here $E - p_z = \Sigma + E_e^{'}(1 - \cos\theta_e)$ is the energy balance, which would be equal to twice the energy of the incoming electron in a fully hermetic, perfect detector. This

method is very important to determine the kinematic quantities because of its low sensitivity to the radiative effects. That means in case a photon is emitted from the incident electron, the effective centre of mass energy of the *ep* system is reduced. Such a radiative photon is usually co-linear with the incident electron beam and escapes in the beam pipe. Radiation reduces the energy of the incoming electron spoiling the measurement of y (see equation 5.4).

The y resolution of the Σ method approaches the y resolution of the hadron method at low y and that of the electron method a high y and is therefore good in the whole kinematic range.

The Electron-Σ Method

The electron-Σ method [111] is designed to combine the best features of the electron and the Σ method. Therefore, it combines the Q^2 reconstruction from the electron method with the x reconstruction from the Σ method:

$$Q^2_{e\Sigma} = Q^2_e \ , \quad x_{e\Sigma} = x_\Sigma \ , \quad y_{e\Sigma} = \frac{Q^2_e}{x_\Sigma s} \ . \tag{5.5}$$

Since the electron-Σ method gives the best resolution in Q^2 and x across the whole kinematic range at HERA, and is relatively insensitive to radiative corrections it is used for NC event reconstruction.

The Double-Angle Method

The kinematic variables in NC events can be reconstructed also with the double-angle method [109] which uses the electron polar angle θ_e, and the inclusive hadronic polar angle γ_h:

$$Q^2_{DA} = \frac{4 \cdot E^2_e \cdot \sin\gamma_h(1 + cos\theta_e)}{\sin\gamma_h + \sin\theta_e - \sin(\theta_e + \gamma_h)} \ , \quad y_{DA} = \frac{\sin\theta_e \cdot (1 - \cos\gamma_h)}{\sin\gamma_h + \sin\theta_e - \sin(\theta_e + \gamma_h)} \tag{5.6}$$

and $x_{DA} = Q^2_{DA}/s \cdot y_{DA}$. The energy of the scattered electron is given by:

$$E_{DA} = \frac{2E_e \sin\gamma_h}{\sin\gamma_h + \sin\theta_e - \sin(\theta_e + \gamma_h)} \ . \tag{5.7}$$

The resolution is worse at small and large angles of both the electron and the hadronic final state corresponding to low and high y. Nevertheless, it is good at medium y where all particles are contained in the central part of the H1 detector.

The double-angle method is not used for the reconstruction of the kinematic variables, but it is important for the calibration of the calorimeter since it is independent on the calorimeter energies.

5.4 Hadronic Energy Measurement

The accurate reconstruction of the Hadronic Final State (HFS) is essential for the CC analysis which is based on the hadronic energy measurement only.

The reconstruction of the HFS as well as the hadronic energy calibration is done using the HADROO II algorithm [112]. This algorithm has to perform two tasks: associating *tracks* with *clusters* and determinating the best estimate of the particles four-vector for the associated tracks and clusters. Since the resolution of the tracking detectors decreases with the increase of the track momentum, while the relative energy resolution of the calorimeter improves, an optimal reconstruction based on the combined information from the track and cluster as input objects is used.

The tracks used in the reconstruction of the HFS are required to be of the "good quality" [113]. Only the vertex-fitted tracks measured in the central part of the H1 detector are considered, since the forward detectors are not well understood so far at HERA II.

A cluster is composed of neighbouring LAr calorimeter cells containing energy. For the HFS energy reconstruction only the calorimetric clusters in the LAr and SpaCal are used. In order to get the appropriate reconstruction of the HFS two important effects have to be taken into account: A correction of the measured energy due to fluctuations of the electromagnetic component within a hadronic shower in the LAr calorimeter called *weighting* and a proper treatment of the *calorimeter noise*.

- **Weighting:** The LAr calorimeter is characterised by a higher response to the electrons than that to the hadrons for the same incident energy. In order to correct for this effect a weighting technique is applied at the reconstruction level within H1REC [83]. This receives a further correction in the HADROO II algorithm. All clusters with at least 95 % of their energy in the EM part and 50% of that energy in the first two layers of the EM part are classified as EM clusters. All other clusters are considered as hadronic and reweighted using H1REC.

- **Noise:** The energy measured in the LAr is affected by the noise contribution which can be up to few GeV per event[1]. The effect of the noise is not negligible and it may bias the reconstruction of the kinematic variables. For example, at low y_h most of the hadronic final state goes in the forward direction and any noisy cluster in the central region of the LAr calorimeter may be misidentified as part of HFS, thus strongly increasing the measured value of y_h. The electronic part of the noise is suppressed by excluding all low energy clusters ($E_{LAr} <$ 0.2 GeV and $E_{SpaCal} <$ 0.1 GeV). The remaining noise is reduced by a set of requirements based on so-called noise finders [114]. Of course, the noise suppression is performed for both the real data and the MC which agree well as illustrated in figure 5.3.

[1]The noise in the LAr calorimeter originates from the electronics noise as well as from pile-up energy deposits from the non-*ep* events such as halo-muons or cosmic rays.

The HFS particles are formed using the HADRO II algorithm in the following way: First, the tracks are associated with a cluster by extrapolating the track up to the surface of the LAr calorimeter as a helix, and inside the LAr calorimeter as a straight line. The calorimetric energy $E_{cylinder}$ is computed as the sum of all clusters in the overlapping volume of a 67.5° cone and two cylinders of radius 25 cm in the electromagnetic and 50 cm in the hadronic section. Furthermore, the track energy E_{track} is compared to the calorimeter energy $E_{cylinder}$ measured inside the cylinder. The estimated uncertainty of the track momentum and the expected resolution of the calorimeter are compared. If the track resolution is better, the particle four-vector is set to E_{track}. However, if the calorimetric energy resolution is better than the track resolution the calorimeter energy is used and the energy is set to $E_{cylinder}$. The track together with its associated cluster is removed from the input list and the algorithm continues with the next track. After all tracks have been treated, particle candidates are made out of the remaining clusters using the calorimetric energies. These particles are considered as originating from neutral particles, or charged particles with a badly measured track. Once all tracks have been associated to the clusters and the particle four-vector has been determined, the HFS reconstruction is completed.

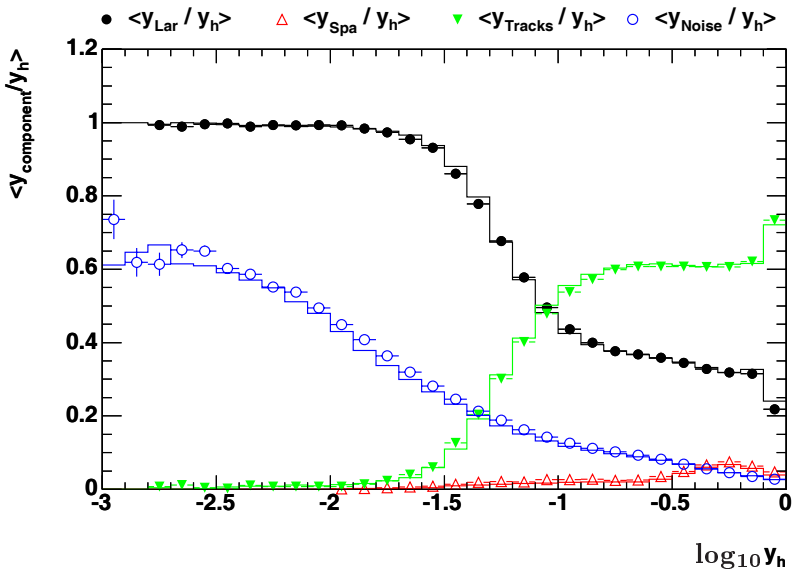

Figure 5.3: Fractional contributions to y_h by tracks (y_{Tracks}/y_h), the LAr (y_{LAr}/y_h) and the SpaCal (y_{SpaCal}/y_h) calorimeters and the fractional contribution from the subtracted noise (y_{Noise}/y_h) measured in the calorimeter are shown for data (points) and for MC (histograms).

The y_h fraction contributed by each of subdetector systems is shown in figure 5.3. As can be seen the hadronic final state energy is distributed between the LAr and SpaCal calorimeter and the tracks by the algorithm described above. The fraction attributed to noise and removed is also shown. All fractional contributions to the

HFS energy as well as the fractional energy of subtracted noise are well described by the simulation.

5.4.1 Hadronic Energy Calibration

The charged and neutral hadrons reconstructed by the HADROO II algorithm are assigned to jets (collimated bunch of HFS particles). Since the selected tracks are already calibrated the jet calibration procedure must not change their energy and is therefore applied only to the calorimeter clusters. The energy of the reconstructed jets is calibrated using the double angle method to reconstruct the reference kinematic quantities[2]. The jet calibration is done using the sample of a DIS NC (for selection criteria see [112]) which select only one jet events. Such events have the hadronic final state entirely contained in a single material region of the LAr calorimeter and an approximation of the difference between the true P_T of the jet (approximated as P_T^{DA}) and the response (or lack of response) of the detector is known. In addition, there is no requirement (cut) on the hadronic energy, because such a cut would bias the kinematic distributions used in the calibration.

In order to determine the calibration constants $F^{\theta}_{P_{T,Bal}}(P_T^{DA})$, the evolution of the mean values of the momentum balance, $P^{DA}_{T,Bal} = P_T^h/P_T^{DA}$ distribution as a function of P_T^{DA} is fitted separately in several θ regions. The obtained calibration factors are applied jet by jet taking care that only cluster jets are calibrated and not jets reconstructed from tracks. As these coefficients are determined using an high P_T selection (> 10 GeV) the extrapolation of $F^{\theta}_{P_{T,Bal}}(P_T^{DA})$ cannot be trusted and only jets with $P_T^{jet} > 4$ GeV are used in the calibration procedure[3].

Figure 5.4 illustrates calibrated and uncalibrated P_T^h/P_T^{da} distribution. The mean values of the P_T^h/P_T^{da} distribution as a function of θ_h^e and P_T^{da} are presented in figure 5.5. The data are described well by the MC simulation within $\pm 2\%$ which is taken to be the systematic uncertainty on the hadronic energy measurement.

The one jet calibration was checked by the two and three jet samples and has confirmed good agreement between the data and the MC, again within the systematic uncertainty of 2%.

As a result, the hadronic final state is reconstructed from the calibrated jets and individual hadrons which are not assigned to jets.

[2]The hadronic transverse momentum determined with this method is independent of the LAr energy calibration to a good approximation and it does not rely on MC which is independently calibrated.

[3]In the very forward region $\theta < 7^\circ$ no reasonable calibration can be applied (due to losses in the beam pipe) as well as for jets reconstructed in SpaCal $\theta > 155^\circ$. These jets and the remaining hadrons which are not part of a jet are calibrated separately (see [115]).

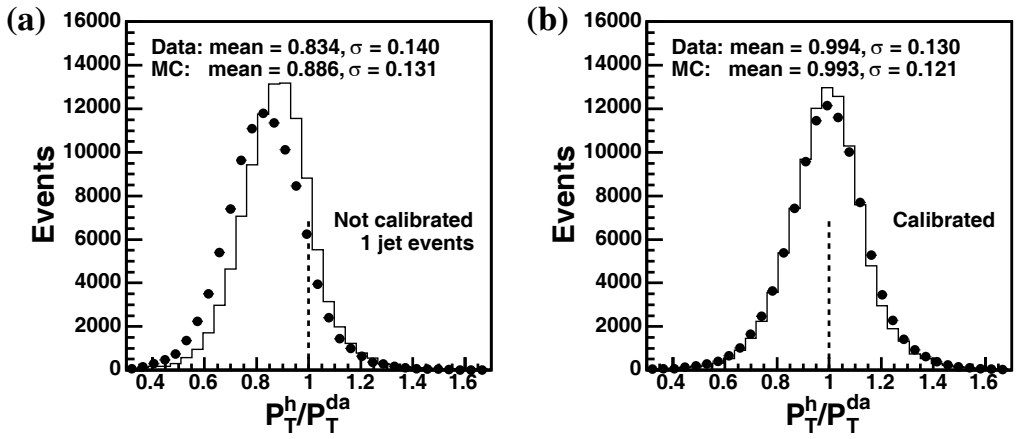

Figure 5.4: Distribution of P_T^h/P_T^{da} for one jet events before (a) and after (b) applying the jet calibration. The mean and σ values are obtained using a Gaussian fit to the central part of the distributions.

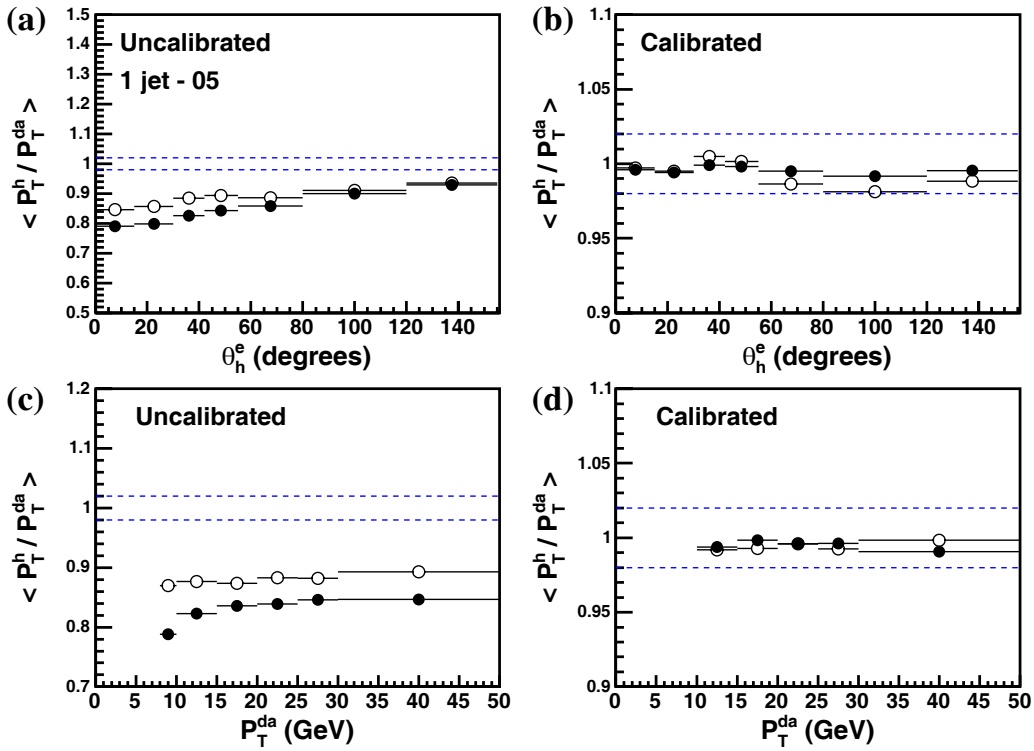

Figure 5.5: Mean of the P_T^h/P_T^{da} distribution for data and MC as a function of the θ_e before (a) and after calibration (b) and as a function of P_T^{da} for one jet events before (c) and after calibration (d). The dashed lines represents the uncertainty on the hadronic energy calibration of $\pm 2\%$.

Chapter 6

LAr Triggers for Charged Current Events and their Performance

In this section the performance of the LAr trigger system during HERA II phase, its internal consistency and comparison to the CTL and the L2 trigger system are discussed.

The LAr calorimeter and its trigger play a dominant role for the high Q^2 physics for CC and NC interactions as well as events with isolated leptons. Therefore, a permanent monitoring of the LAr trigger performance became a natural task at HERA II [116].

In general the LAr trigger operation is monitored *online* during data taking, as for example via the trigger rates or consistency checks of the trigger elements. Serious problems should be realized already during data taking from the data quality histograms. However, there are cases where problems are observed online, but diagnosis of this origin needs more involved studies which can be done *offline* only. The data used in the analysis of the LAr trigger have been taken with the H1 detector in the period from year 2002 until year 2005 and are selected imposing the following conditions:

- Data selected satisfying only the quality criteria:
  (a) luminosity phase 2, i.e. all tracking detectors have been switched on;
  (b) run quality is labelled as *good*, i.e. the high voltage for the main detector components (trackers, LAr etc.) was on.
  This sample of events has been used for the monitoring of the internal performance and consistency of the LAr trigger with CTL and the L2 trigger systems. The reason is that without physics selection all details of the LAr trigger performance can be checked. The data format chosen is *raw data* which means that all information readout from the detector is available. Such format opens up the possibility of the detailed studies of the LAr trigger.

- Pseudo charged current data used to determine the efficiencies of the CC trigger elements.

6.1 Physics Motivation: CC Subtriggers

The triggering of CC events (see figure 6.1) is based on the large energy deposition in the LAr calorimeter being imbalanced due to the undetected neutrino which is complemented by the timing information either from the LAr calorimeter (see subsection 3.6.2.1) or from the CIP (see subsection 3.5.1). In addition, vetoing of the beam induced background by the ToF (see subsection 3.5.1) and the CIP systems is applied. These conditions, called trigger elements, are combined into the physics subtriggers ST66, ST67 and ST77 as given in table 6.1 and described below.

- **Subtrigger 66 (ST66)** is the LAr subtrigger designed for triggering of CC events. It is based on requirement that the large imbalanced energy (LAr_Etmiss > 2) is deposited in the LAr calorimeter where a part of the energy deposition is required to be in the inner forward region of the LAr calorimeter (LAr_IF > 1).

- **Subtrigger 67 (ST67)** is designed for triggering of high Q^2 physics, especially NC events. It is sensitive to the compact energy depositions in the electromagnetic section of the LAr calorimeter (LAr_electron1), as expected for the electromagnetic showers induced by the scattered electron. However, ST67 is very useful as an indication of the energy cluster in the LAr, regardless of its origin.

- **Subtrigger 77 (ST77)** triggers the low imbalanced energy deposits in the LAr calorimeter (LAr_Etmiss > 1). It is used for triggering both CC and NC events. An additional requirement on the track significance in the CIP, which is indeed minimal (CIP_sig > 0), ensures that noisy events are not triggered, significantly reducing the ST77 trigger rate.

The timing information plays an important role in reducing the chance of triggering on electronic noise in the calorimeter and non-*ep* background. The timing information combined with the veto requirements results in the CC trigger rate of a few Hz. Thus, the CC subtriggers are usually not prescaled (for definition see subsection 3.5.1). The prescaling of the CC triggers is very rare and happens only if serious problems during data taking occur resulting in a rate of few tens of Hz as will be discussed in section 6.3.

An example of the CC event triggered by ST67 and ST77 is given in table A.1.

6.2 Efficiencies of the LAr Trigger Elements

The CC trigger efficiencies of the LAr trigger elements based on the missing transverse energy for two different thresholds (LAr_Etmiss > 2 and LAr_Etmiss > 1) as a function of missing transverse momentum $p_{T,miss}$ are shown in figure 6.2. These efficiencies are derived from the PsCC events obtained by removing the electron information from the NC events (detailed description can be found in section 4.4). As can be seen the

subtrigger	definition
ST66	(LAr_IF > 1 && LAr_Etmiss > 2) && (CIP_T0 || (LAr_T0 && !CIP_T0_next_BC)) && (FIT_IA || !FIT_BG) && (!SPCLh_AToF_E_1 && !VETO_BG && !BToF_BG && !SToF_BG) && (!(CIP_MUL > 7 && CIP_sig == 0))
ST67	(LAr_electron_1 && (CIP_T0 || (LAr_T0 && !CIP_T0_next_BC)) && (FIT_IA || !FIT_BG) && !VETO_BG && !BToF_BG && !SToF_BG) (!(CIP_MUL > 7 && CIP_sig == 0))
ST77	(LAr_Etmiss > 1 && CIP_sig > 0) && (CIP_T0 || && (FIT_IA || !FIT_BG) && (!BToF_BG && !SToF_BG) && (!(CIP_MUL > 7 && CIP_sig == 0))

Table 6.1: Definitions of the subtriggers used in the CC analysis. While ST66 represents the typical CC subtrigger, ST67 and ST77 are used for both NC and CC.

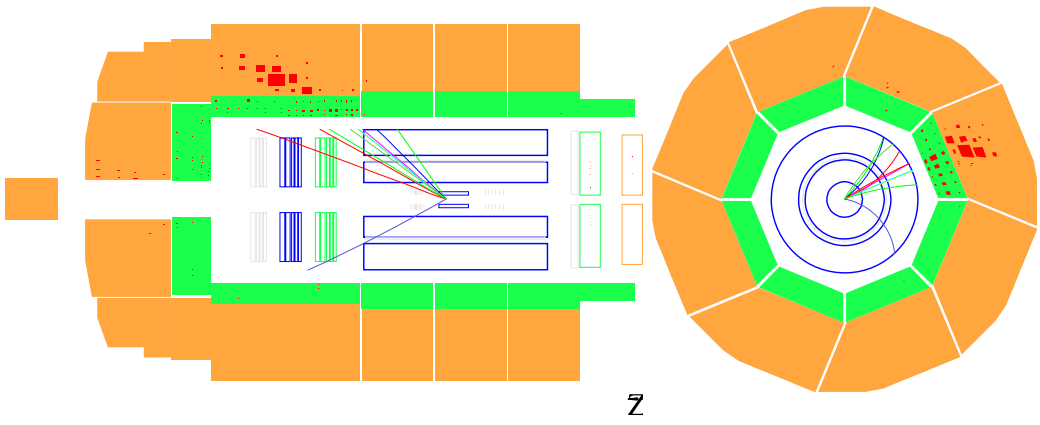

Figure 6.1: The side view (left) and the radial view (right) of CC event taken in $e^- p$ collision by the H1 detector in year 2005 with the large transverse missing energy in the LAr calorimeter caused by hadronic jets as characteristic of real CC events. Since the neutrino escapes undetected this energy is unbalanced

trigger efficiencies at low $p_{T,miss}$ are $> 20\%$ and in region where $p_{T,miss} > 30$ GeV increase to almost 100%. However, at low $p_{T,miss} < 30$ GeV efficiency is limited by the LAr trigger acceptance in the forward detector region as well as the high trigger thresholds in the central region in order to avoid triggering on the noisy energy depositions.

The improvement in the trigger efficiency can be achieved by making use of a Fast Track Trigger (FTT), triggering on multiplicity of tracks with low $p_{T,miss}$. The study

threshold in FADC counts		trigger element
48	low	LAr_Electron_1
42	low	LAr_Etrans
64	medium	LAr_Etrans
72	high	LAr_Etrans
38	low	LAr_Etmiss
44	medium	LAr_Etmiss
52	high	LAr_Etmiss

Table 6.2: Overview of LAr thresholds (in FADC counts) for the main trigger elements used in this analysis.

has been performed and has shown that at efficiency can improve more than 20% in this region.

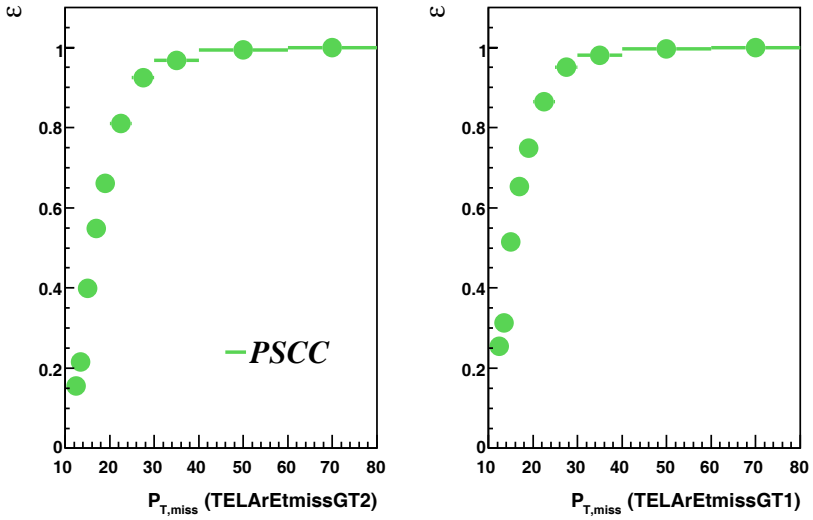

Figure 6.2: Trigger efficiencies of the LAr trigger elements LAr_Etmiss > 2 and LAr_Etmiss > 1 vs $p_{T,miss}$ used in the CC analysis as derived from the Pseudo Charged Current Data.

6.3 Optimising the LAr Trigger Rates

A large total interaction rate which exceeds the readout and the data storage capabilites is characteristic of each collider experiment. In order to keep interesting physics processes with a maximum possible efficiency a multi-level trigger system is used (see section 3.5). There are high rate interactions for which the trigger elements are downscaled using prescaling factors [117]. This is not the case with the LAr trigger which rates are most of the time at the acceptable level which is set by suitable

thresholds, i.e. within expected limits. Furthermore, one should keep in mind that the high Q^2 events do not occur with a high rate, as for instance the photoproduction, and therefore we would like to keep all of them. In oder words, we want to trigger event candidates without prescales. The typical trigger rates of the subtriggers requiring the LAr trigger elements are shown in figure 6.3. The pure LAr triggers as

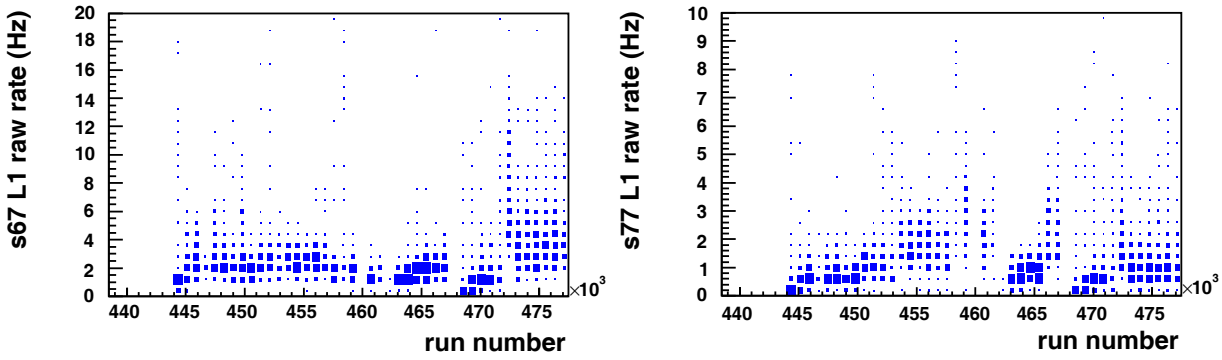

Figure 6.3: Typical trigger rates of ST67 and ST77 at L1 as a function of the run number.

the subtrigger 67 (ST77) and the subtrigger 77 (ST77) based on the requirement of the lower thresholds in the LAr trigger are sensitive to noise.

$$ST67: \quad \text{LAr\_Electron\_1 \&\& (LAr\_T0||CIP\_T0)} \tag{6.1}$$

$$ST77: \quad \text{LAr\_Etmiss} > 1 \text{ \&\& CIP\_T0.} \tag{6.2}$$

Due to noise occurring in the LAr calorimeter usually caused by pick up from certain components of the H1 detector these triggers can occasionally result in excessive trigger rates. Therefore, there was a need to improve the trigger strategy for the future running of H1 in 2006 and 2007 [118].

The main aim of an new trigger strategy is to improve the stability of the $ST67$ and $ST77$ while keeping the high trigger efficiency for the CC, NC and exotic events. For this purpose different trigger strategies were proposed and studied as described below. The trigger rates are checked using so-called L2 and L4 *transparent runs* which are taken without any requirement on the second and the fourth trigger level. A prediction of the trigger rates can be made from the relative number of events fired by a specific trigger condition in the transparent run as given in table 6.3. The trigger efficiencies are checked using Pseudo Charged Current events (see section 4.4 for detailed explanation).

If running conditions are stable subtriggers are planned to run as usual.

6.3.1 Proposal for the Optimising Trigger Rates at L1

A first strategy in controlling trigger rates was supposed to be applied at the first trigger level. The idea is to modify trigger logic only during periods of high LAr

noise, when trigger rate goes up to 30 Hz and to split ST67 into two subtriggers:

$$ST68 : \text{LAr\_Electron1 \&\& CIP\_sig} > 0 \tag{6.3}$$
$$ST65 : \text{LAr\_Electron1 \&\& LAr\_Etrans} > 1\ . \tag{6.4}$$

In addition a tighter condition on the present ST77 was proposed in order to reduce the trigger rate:

$$ST77 : \text{LAr\_Etmiss} > 1 \text{ \&\& CIP\_sig} > 1\ . \tag{6.5}$$

The efficiency of ST68 and ST65 for the CC analysis is still high since the new subtriggers complement each other in phase space. Unfortunately, the NC events at high Q^2 are lost using the new requirements. However, ST77 is the main ST for triggering low energy depositions in the LAr trigger, and 99.9% of the all CC events are triggered by this trigger. On the other hand, only a small fraction ($\approx 7\%$) of them are triggered exclusively by this subtrigger, as illustrated in figure 6.4. Therefore, such CC events would be lost by new requirement while the gain in the trigger rate reduction turned out to be moderate (25%). Thus, the tightening of the ST77 was given up.

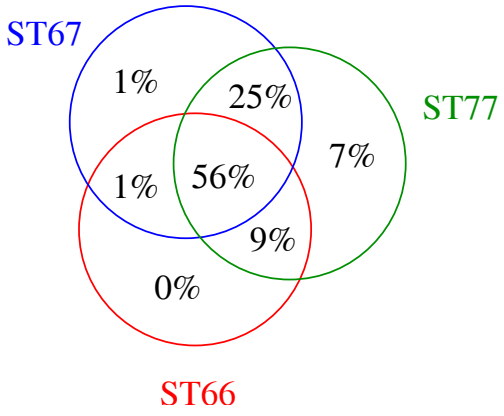

Figure 6.4: The fractions of CC events triggered by subtriggers ST66, ST67 and ST77.

The efficiency and the rate reduction have been studied for each particular subtrigger as well as for their combinations. The actual rate reduction has been studied for different runs taken for the *optimal data taking conditions* and *during noise in the LAr calorimeter and the H1 detector* and is shown in table 6.3. During normal running conditions the rate reduction due to the tightened conditions (see equations 6.4) is significant resulting in $\approx 50\%$ for $ST65$ and $\approx 80\%$ for $ST68$. However, the rate reduction of ST65 is small during high noise level (see table 6.3). This is a consequence of LAr_Etrans trigger element which is sensitive to noise.

Due to all reasons listed above it was decided that this is not satisfying solution for the future trigger running in H1.

Run	ST68	ST65	ST77	ST65 ‖ ST68 ‖ ST77
411871	90%	42%	21%	32%
421381	81%	51%	23%	30%
406125	77%	49%	23%	31%
433754	87%	8%	23%	6%

Table 6.3: Individual and combined rate reduction of ST65 and ST68 and redefined ST77 in 4 runs. During run 433754 the LAr noise was high. Other runs correspond to optimal running conditions.

6.3.2 Optimising Trigger Rates at L2

The better option for the high Q^2 subtriggers was to use the L2NN trigger system for the trigger rate reduction. For this purpose two L2NN networks are trained to reject background (for details see [119]), one for each of the subtriggers ST67 and ST77, to keep both physics channels (NC and CC interactions) using the following definitions:

L2NN-net1= NC and CC events triggered by ST67,
L2NN-net2= NC and CC events triggered by ST77.

The networks use the following L1 informations from the LAr, CIP and FTT:

- **LAr:**
  Energy (electromagnetic+hadronic) in each quadrant of the IF region
  Energy (electromagnetic+hadronic) in each quadrant of the FB region
  Energy (electromagnetic+hadronic) in each quadrant of the CB region
  Energy (electromagnetic+hadronic) total
  Etrans
  Ex and Ey vector components of Etmiss

- **FTT:**
  Total number of tracks
  Number of tracks in p_T bins 1-100 MeV...1800 MeV

- **CIP2K:**
  Number of tracks in the central region
  Number of tracks in the backward region

The efficiency of the combined networks is 99.4% for the CC events. The rate reduction of the new L2NN subtriggers has been determined and is given in table 6.4. The rate reduction is better than factor of two. Especially in the periods of high noise the performance of L2NN improves in contrast to tightening of ST67 at L1. Thus, this was preferred solution for the future trigger strategy in 2006-07.

Run	ST67	ST77	ST67 ‖ ST77
good runs	61%	61%	63%
433754	83%	60%	80%

Table 6.4: Rate reduction of modified ST67 and ST77 with L2NN conditions in 4 run periods. During run 433754 the LAr noise was high. Other runs correspond to normal running conditions.

6.4 Data Quality Checks

The main task of this section is to introduce all different kinds of so-called "errors" or discrepancies between hardware and simulation of the LAr trigger. In order to make clear diagnosis of the problems observed the LAr information has been compared to the information delivered at the second trigger level L2 and to CTL. These informations from different sources make it possible to verify performance of the LAr trigger, its readout and its simulation (see figure A.1) using:

- Comparison of the Adder tree with recalculation (simulation) of the LAr trigger using the FADC values of the BTs. This is the *internal LAr consistency*.
- Comparison between trigger elements from the LAr readout and the CTL readout. For the *final trigger decision* this consistency is very important.
- Comparison between trigger elements from the LAr readout (topological and global energy sums) and information arrived at L2 (important for the *general data quality checks*).

Details of the LAr trigger readout and simulation as well as the data quality checks are given in appendix A.

6.4.1 Internal Consistency

Internal consistency between the actual and the expected (simulated) behaviour of the LAr trigger has been monitored in order to ensure good quality of the data triggered by the LAr trigger. Basic trigger quantities used for this purpose are discussed in the following subsections.

FADC Hit Map

The FADC hit map is shown in figure 6.5. On the x axis the FADC numbers are shown which are in total 512 FADCs. On y axis the rate of firing corresponding FADC is shown. The dead zones correspond to the *switched off* FADCs as few dips belonging to the Plug and SpaCal calorimeters. In addition, there is at 218 one *not operational FADC*. The huge unexpected spikes might occur due to FADCs which contain the noisy trigger cells, but such situation has not been observed except when running conditions at H1 were not stable.

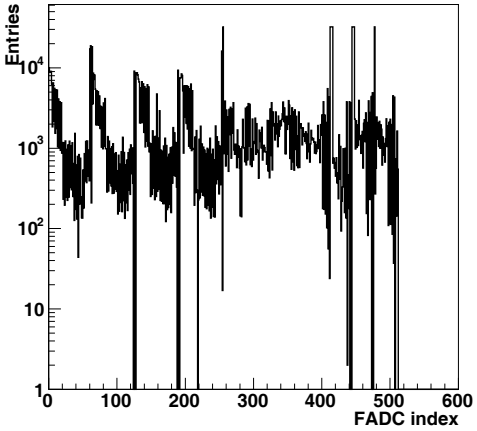

Figure 6.5: FADC hit map illustrates the rate of fired FADCs versus the FADC number for raw data sample. The dip seen at FADC=218 was broken FADC in 2004 data. Other dips seen in the plot present the SpaCal and Plug FADCs.

Adder Tree Consistency

The internal consistency of the LAr trigger can be checked via comparison of the LAr TEs which are generated by the trigger hardware and those which are recalculated using the FADCs (see event in table A.1).

Figure 6.6 shows the LAr trigger readout of the adder tree trigger elements while shadowed area shows disagreement between the LAr trigger readout and its simulation. In the ideal case 100% agreement is expected. However, as can be seen from figure 6.6 there are some discrepancies of 0.02%, mostly related to the central bunch cross readout which is explained is subsection A.3. One should realise that the *wrong readout of the central BC does not affect the final trigger decision given by the CTL* as nicely demonstrated in event A.2 given in appendix.

6.4.2 Comparison of LAr Trigger to the Central Trigger Logic Readout

The big tower trigger elements, the topological and the global energy sums are discriminated against the threshold and sent to the CTL. Since the TEs are read out twice, once by the source (LAr trigger) and once by the receiver (the CTL) this gives the possibility to cross check two readout streams. The data set considered in this analysis has shown disagreement only in the events for which the LAr TEs are not readout properly, but information is correctly delivered to the CTL as it has been discussed already.

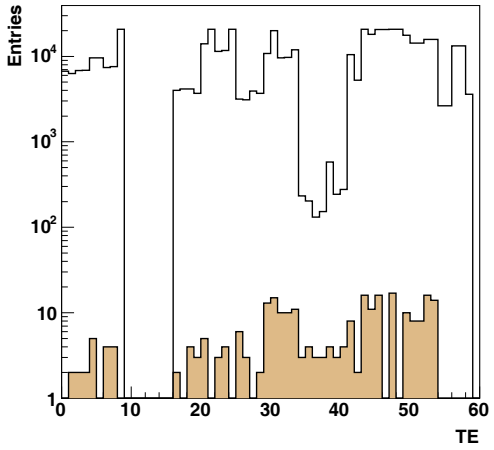

Figure 6.6: LAr trigger elements (TE) from the readout (line) and discrepancy between the readout and simulation (shadowed area). The whole in the range from TE 9 to TE 16 corresponds to the TEs build from the FADCs belonging to the PLUG calorimeter.

6.4.3 Comparison of LAr Trigger to the Second Trigger Level Readout

The LAr trigger elements encoded in bits are sent to the L2 trigger systems as well. Therefore, there is an additional possibility to check the consistency between information readout by the LAr trigger and information readout by the second trigger level (L2NN or L2TT). Such a check was a very useful tool to clarify if problems observed originate from L1 or L2, for example by comparing three different readouts, LAr, CTL and L2. By this method, rare transmission errors between source and receiver could be identified.

During HERA II phase 2002-05 studies of the LAr trigger data quality have shown a very good trigger performance. In general, discrepancies which have occurred are only at the per mil level and the sources were identified. Observed errors are originating from the readout problems and no hardware problems were observed except the one dead FADC.

Chapter 7

Analysis of Charged Current Events

This analysis is based on data taken by the H1 detector, recording collisions from a longitudinally polarised electron beam with an unpolarised proton beam. The data are collected during the year 2005 with positive and negative helicity for the electron, referred to as the *right-handed* (RH) and the *left-handed* (LH) data, respectively. The integrated luminosities and corresponding polarisation values for each data taking period are summarised in table 7.1 resulting in a total integrated luminosity of 98.2 pb^{-1}. This is about a factor of 6 more than the $e^- p$ luminosity collected previously by H1 during the HERA I phase [40].

In this chapter the criteria for the selection of Charged Current (CC) events are described. First, the run selection requirements are introduced to ensure that the data sample is well defined and the luminosity is determined correctly. Then the polarisation requirement, essential for the analyses presented, is described. Furthermore, the trigger requirements as well as the selection criteria of the kinematic phase space used for the CC measurements are introduced. Finally, the criteria used to reject different background sources, and the efficiencies needed for the MC corrections, are discussed.

data sample	$P_e[\%]$	$L[\text{pb}^{-1}]$	**runs**	**dates**
$e^- p$ RH	$+37.0 \pm 1.8$	29.6 ± 0.6	418000-427474	13.06-06.09.2005
$e^- p$ LH	-27.0 ± 1.3	68.6 ± 1.4	402992-414712	03.02-18.05.2005
			427813-436893	09.09-11.11.2005

Table 7.1: Data samples used in the analysis.

7.1 CC Selection Criteria

As has been discussed already in section 4.1, the events passing through the H1 detector are dominated by non-ep interactions (see section 4.2). A good fraction of these events are rejected already during data taking with a help of the H1 trigger system (see section 3.5), but still the collected sample of events contains more than 10% of non-ep background. In addition, the CC events are relatively rare interactions with respect to the other physics processes such as γp and the DIS NC events (see section 4.2). To illustrate this, the output rate of writing events to the tape is about 10 Hz, while a CC event occurs once within 1-2 hours i.e. 10^{-4} Hz. In order to reduce, as much as possible, any background contribution while keeping high selection efficiency of the CC events a set of carefully chosen selection criteria has to be applied to the collected sample of events. Since the removal of the background is an important issue in the CC selection procedure the next sections are devoted to the basic preselection as well as the specific CC selection criteria which led to the final event sample used in the cross section measurement.

7.1.1 Basic Preselection

For the analysis presented in this thesis a common preselection of the high Q^2 NC and CC events has been used. This is done making use of the object-oriented data base [120]. Namely, for each event a number of variables are stored as a tag with the aim to provide a fast and flexible way of selecting events. This helps to reduce considerably the number of events which enter the analysis and by that the computing time as well.

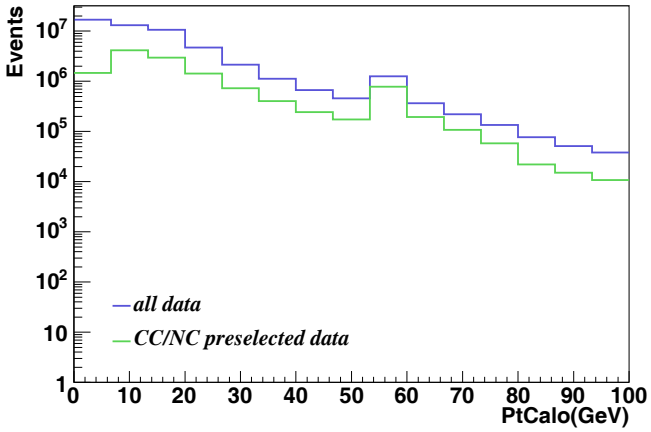

Figure 7.1: The $p_{T,calo}$ distribution for the collected 2005 e^-p data (blue line) and the CC and NC sample after the preselection (green line).

In order to keep all CC events a very loose preselection with the following require-

ments was applied to the collected data:

- the events must have the reconstructed vertex;
- the $p_{T,calo} > 8$ GeV (i.e. a minimum transverse momentum from the clusters measured by the calorimeters).

One should note that by the requirement $p_{T,calo} > 8$ GeV not really all CC events are kept. But this cut is made due to the LAr trigger limitation at low energy and of course due to background contamination at low $p_{T,calo}$. In order to reduce fake NC candidates additional requirements on the existence of a track based electron are made.

Figure 7.1 shows the distribution of the $p_{T,calo}$ for the 2005 data events, before and after applying the common NC and CC preselection criteria. As it can be seen the number of events is significantly reduced, from the starting ≈ 180 million to the preselected ≈ 13 million events.

7.2 Final CC Selection Criteria

The criteria used for the final selection of CC events are briefly summarised and will be discussed in detail subsequently:

- **run quality and polarisation requirement**
- **trigger selection** (see chapter 6.1)
  subtrigger $ST66 \| ST67 \| ST77$
- **vertex requirement**
  reconstructed vertex within -35 cm $< z_{vtx} < 35$ cm
- **kinematic phase space**
  $p_{T,miss} > 12$ GeV
  $0.03 < y_h < 0.85$
  $Q^2_h > 223$ GeV^2
- *ep* **background rejection**
  (a) cuts against γp events
  $V_{ap}/V_p \leq 0.25$
  parabola cut in the $V_{ap}/V_p - p_{T,miss}$ plane
  (b) cuts against NC events
- **non-*ep* background rejection**
  CJC and LAr timing
  topological background finders
- **visual scanning**

7.2.1 Run Selection

The periods of data taking under stable experimental conditions are called *runs*. A run may last from a few minutes up to 2 hours depending on the overall detector performance. For each new run the set of active triggers may be reoptimized (e.g. prescale factors) since the collision rate due to the decrease of the electron beam currents will decrease as well.

7.2.1.1 Run Quality

The status of both the HERA accelerator and the H1 detector are very important for the quality of the analysed data and they are directly defining the run quality.

Depending on the detector performance, background situation or problems with the data acquision system, runs are classified as *Good*, *Medium* or *Poor*.

- **Good:** All major detector systems such as CJC1, CJC2, LAr, Lumi and Central Muons are fully operational.
- **Medium:** One major detector system or several detector subsystems are out of operation.
- **Poor:** Serious hardware or software problems occur during data taking.

In this analysis only *good* and *medium* runs have been used. Additionally, very short runs with an integrated luminosity $L_{run} < 0.2\ nb^{-1}$ are also rejected in order to exclude data taking periods with potentially unstable experimental conditions.

High Voltage

To ensure a well understood detector response, all subdetectors which are essential for the CC analysis are required to be operational and included in the readout. These are the LAr calorimeter, the Central Jet Chambers (CJC1 and CJC2), the Central Inner Proportional Chamber (CIP), the Time of Flight and the Luminosity systems. During data taking each 10 s the information about the high voltage status of each hardware component is stored in a data base. The run is rejected if any of these components was not operational for a large fraction of time. If triggers are disabled during data taking (for example due to excessive rates caused for example by beam instabilities) the run is rejected.

High trigger rates may also be caused by *coherent noise* in the LAr calorimeter during data taking. Such runs are also excluded from the analysis since noise can distort the kinematics of the reconstructed events.

The luminosity is calculated only for runs which satisfy the above mentioned quality criteria.

NC Event Yield

The data quality is defined by the stability of the experimental conditions which is verified by an offline analysis of the *event yield*. The event yield represents the number of selected events per unit of integrated luminosity. Due to much higher statistics, the NC event yield [121] is usually used as cross-check of the stability of the detector and the data taking. The event yield for the 2005 $e^- p$ NC events shown in figure 7.2 is for the full data sample (the LH and the RH data). A few problematic run ranges, given in table 7.2, were observed by studying the NC event yield and were removed so they do not contribute to the final NC sample which is illustrated in figure 7.2. As can be seen the yield after removal of the problematic run ranges is constant during the whole data taking period, confirming stable experimental conditions.

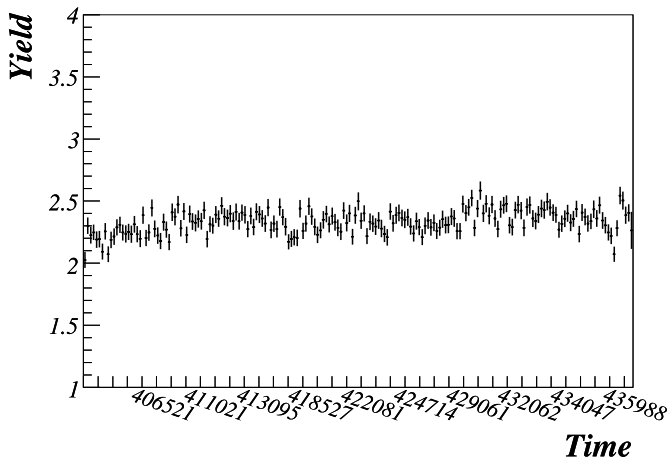

Figure 7.2: The luminosity yield corresponding to the selected 2005 $e^- p$ NC events. The constant yield indicates stable running conditions for the whole year 2005.

run number	problems
404826-404848	test version of the CTL code
408903-408927, 409350-409371	malfunction of the CIP trigger
409345-410185	LAr hot cells
414908-418000	LAr Calibration
424009-424015	LAr noise
423993,423994,432105,436178,436179	LAr HV problems

Table 7.2: List of runs excluded from the analysis due to different hardware problems.

7.2.2 Polarisation Requirement

In addition to the previously mentioned criteria for the run quality a very important quantity for the CC events at HERA II is the *longitudinal electron polarisation*.

The polarisation is measured by the TPOL and LPOL polarimeters (see section 3.3). The LPOL measurements are used when available, otherwise the TPOL measurements are taken. The main reason for this is the smaller systematic uncertainty of the LPOL measurement. If none of the two polarimeters is operational at the time of data taking i.e. the beam polarisation is not measured, the run is rejected. In the present analysis only runs with measured polarisation are considered.

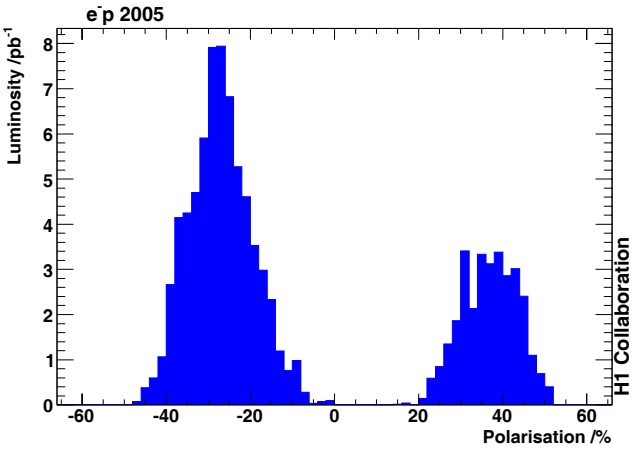

Figure 7.3: The polarisation profile weighted by the luminosity values for the 2005 e^-p CC data. The negative (left distribution) and positive polarisation (right distribution) values correspond to the LH and RH data, respectively.

Accordingly, the luminosity is adjusted for the periods where the polarisation measurement is available. Additionally, at the analysis level any run having a polarisation $0 < \mathrm{P_e} < 20\%$ has been excluded (418029-424474) in order to have the higher average polarisation for the cross section measurement[1] (see figure 7.3).

The luminosity weighted polarisation profile of the data used in the present analysis for both helicity periods is shown in figure 7.3. The mean values of two large distributions correspond to the average polarisations for the LH and the RH periods given in table 7.1.

The run quality and polarisation requirement reduce the number of data events from $\approx$ 13 million events to 7 million events.

[1]Note that the removed sample of events due to low polarisation corresponds to the integrated luminosity of 4.4 pb^{-1}

7.2.3 Trigger Requirement

The triggering of CC events relies on the large imbalanced (missing transverse) energy deposits in the LAr calorimeter together with the timing information from the CIP and the LAr trigger (see section 6.1). In order to trigger CC events efficiently the trigger conditions are combined into three physics subtriggers $ST66$, $ST67$ and $ST77$. In the CC selection procedure anyone of these three subtriggers must be fired, leading to the following requirement:

$$ST66 \| ST67 \| ST77 \tag{7.1}$$

where $\|$ is the logical OR operator. In total 2% of events which are not rejected by any other of the final selection criteria is suppressed by the trigger requirement.

7.2.4 Vertex Requirement

An event vertex determined only by the tracks in the central detector is used. In principle, a vertex could be also reconstructed from the forward detectors, but this is not used at HERA II. A primary interaction vertex is required to be reconstructed within the region of possible ep reaction close to the nominal interaction point ($z_{vtx} = 0$ cm):

$$-35 \text{ cm} < \mathrm{z_{vtx}} < 35 \text{ cm} \tag{7.2}$$

for the full running period. The vertex requirement is chosen on the basis of the longitudinal extension of the proton beam ($\sigma_z = 15$ cm) which helps to significantly reduce the non-ep collision background.

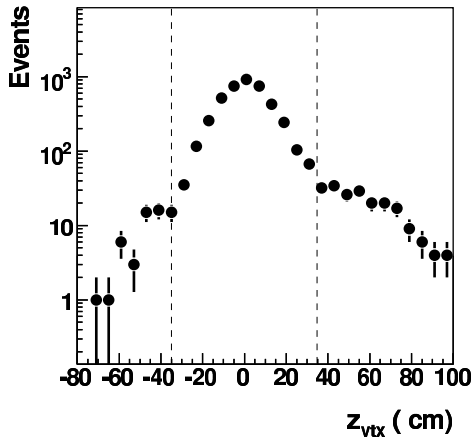

Figure 7.4: Vertex distribution for the CC data when all cuts except the vertex requirement are applied. The vertex requirement is indicated by the vertical dashed lines.

The remaining contribution of the background, which is 8.4% after the complete CC selection applied, is suppressed by the vertex requirement (see figure 7.4).

7.2.5 Kinematic Phase Space

The CC events occur when the incoming electron exchanges a W boson with one of the quarks in the proton and changes into a neutrino ($e^- p \to \nu X$). The final state neutrino escapes the detector unobserved causing an apparent missing transverse momentum $p_{T,miss}$. Therefore, one of the most important selection criteria in the CC analysis is the requirement on large missing transverse momentum $p_{T,miss}$[2]. Only events above the cut:

$$p_{T,miss} > 12 \text{ GeV} \tag{7.3}$$

are selected in order to have a "clean" CC sample since below this cut CC events cannot be triggered efficiently (see chapter 4) and the contribution from background is significantly larger.
The inelasticity y_h is required to be within the range

$$0.03 < y_h < 0.85 \tag{7.4}$$

on the basis of the following reasons:

- When the hadronic final state is scattered in the forward region of the LAr calorimeter part of the energy is lost in the beam pipe since the calorimeter starts at 4°. For events with $y_h < 0.03$, the hadronic final state is emitted at small θ angles, thus losing a substantial fraction of the particles, resulting in a decrease of the trigger efficiency (see figure 7.5). This is the reason for making the lower inelasticity cut on $y_h > 0.03$.

- If the hadronic final state is scattered in the central region of the calorimeter, due to the large pad capacities and the resulting high noise, the energy thresholds are kept at a high level. This leads to a decrease of the trigger efficiency (see figure 7.5). In addition, the Q_h^2 resolution of the hadronic method decreases with increasing y_h (see chapter 5). Thus, an inelasticity cut is made on $y_h < 0.85$.

The cut on the four momentum transfer squared (Q_h^2 cut):

$$Q_h^2 > 223 \text{ GeV}^2 \tag{7.5}$$

ensures that the analysis covers only the high Q_h^2 phase space, minimising the background contribution from photoproduction which has a very large cross section (see section 4.1). The phase space in the kinematic (x_h, Q_h^2) plane in which CC events are selected is illustrated in figure 7.6.

In figure 7.7 the $p_{T,miss}$ (a) and y_h (b) distributions of the CC data and simulated CC events together with all sources of *ep* background are shown, where all CC selection criteria except the phase space requirement are applied. As it can be seen the phase space requirement reduces the *ep* background contribution which is dominating at low

[2] $p_{T,miss}$ is reconstructed from all observed hadronic final state particles, therefore $p_{T,miss} = p_{T,h}$ is also often used.

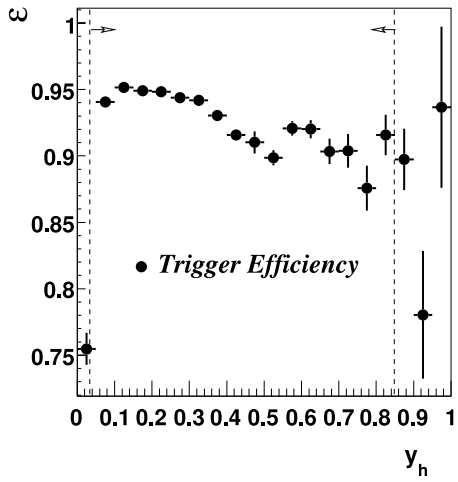

Figure 7.5: Trigger efficiency determined from PsCC events applying all selection criteria except the $0.03 < y_h < 0.85$ represented by the vertical dashed lines.

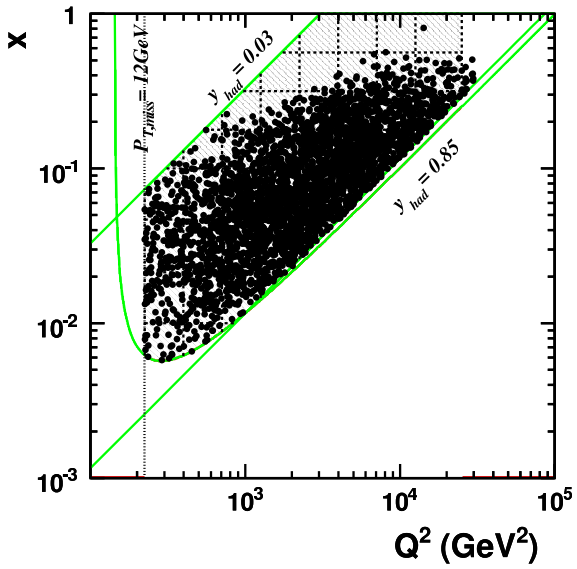

Figure 7.6: The phase space in x_h and Q_h^2 in which the CC interactions are measured. The vertical dashed line is the Q_h^2 cut at 223 GeV^2 whereas the $p_{T,miss}$ cut at 12 GeV is shown as the curve. The upper (0.85) and lower limit (0.03) in y_h are also shown.

$p_{T,miss}$ and low and high y_h, especially background originating from the NC events. After the complete CC selection criteria applied 14% of remaining background is reduced by the phase space requirement.

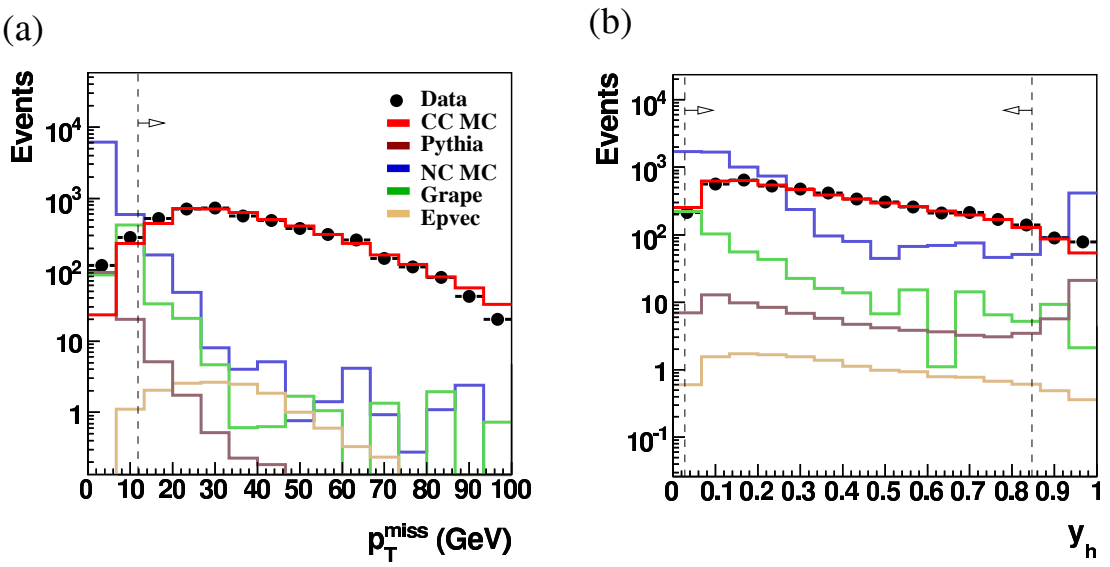

Figure 7.7: (a) $p_{T,miss}$ and (b) y_h distribution for the CC data together with CC simulated and background events when all cuts are applied except the phase space cuts. The cuts on $p_{T,miss} > 12$ GeV and $0.03 < y_h < 0.85$ are indicated by the dashed lines.

7.2.6 Rejection of *ep* Background

The main contamination of physics background in the sample of CC events originates from photoproduction and, to a much lesser extent, from NC events (see section 4.2.1). The *ep* background can fake a CC events due to the loss of energy by weak decays of the final state hadrons, mismeasurement of energies or limited geometrical acceptance of the detector.

Rejection of photoproduction events

In photoproduction events as well as in the NC events the energy flow is expected to be balanced in the transverse direction in contrast to the CC events. Discrimination between photoproduction and CC events can therefore be studied best in the plane transverse to the beam, as shown in figure 7.8. This feature is quantified by the so-called V_{ratio} quantity. V_{ratio} is defined as the ratio of the transverse energy flow antiparallel (V_{ap}) and parallel (V_p) to the direction of the transverse momentum for a given event as:

$$V_{ratio} \equiv \frac{V_{ap}}{V_p} \tag{7.6}$$

with

$$V_{ap} \equiv -\sum_i \frac{\vec{p}_{T,i} \cdot \vec{p}_{T,h}}{p_{T,h}} \quad for \quad \vec{p}_{T,i} \cdot \vec{p}_{T,h} < 0 \tag{7.7}$$

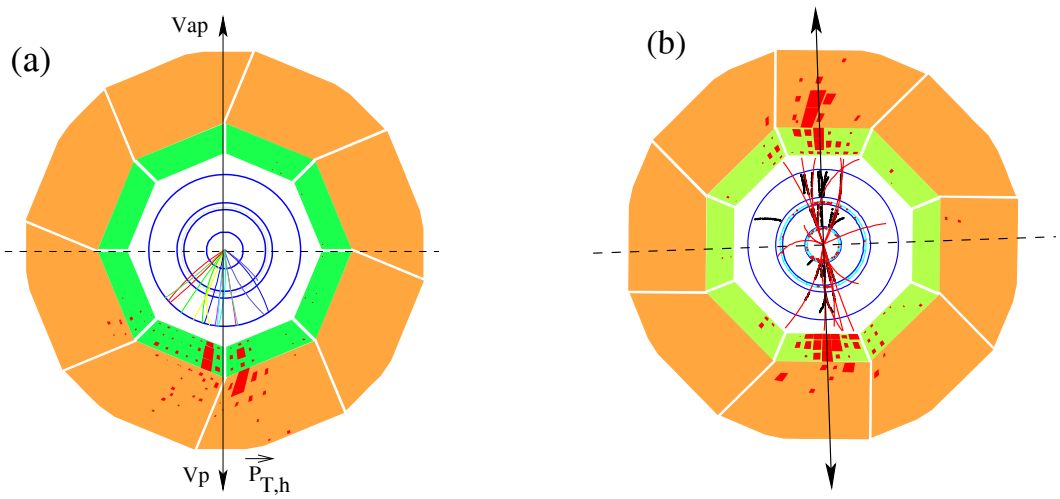

Figure 7.8: The radial view of a CC event (a) and a photoproduction event in the H1 detector (b). The V_p and V_{ap} are the energy flows parallel and antiparallel to the direction of the hadronic final state transverse momentum $p_{T,h}$ and are typically balanced for the photoproduction and the NC events.

and

$$V_p \equiv \sum_i \frac{\vec{p}_{T,i} \cdot \vec{p}_{T,h}}{p_{T,h}} \quad for \quad \vec{p}_{T,i} \cdot \vec{p}_{T,h} > 0 \tag{7.8}$$

where $\vec{p}_{T,i}$ represents the transverse vector of individual particles belonging to the hadronic final state whereas $\vec{p}_{T,h}$ represents the transverse vector sum of all particles in the hadronic final state. For CC events the transverse momentum component opposite to the hadronic final state V_{ap} is expected to be much smaller than that of the outgoing jet V_p (see figure 7.8 (a)), leading to $V_{ratio} \approx 0$. However, in γp as well as in NC events the energy flow is expected to be balanced, resulting in $V_{ratio} \approx 1$ (see figure 7.8 (b)). Figure 7.9 shows the V_{ratio} distribution for signal CC and γp background events in the phase space $p_{T,miss} > 12$ GeV and $0.03 < y_h < 0.85$. For CC events one expects very small values of V_{ratio} while at higher values of V_{ratio} the background dominates. A cut of:

$$\frac{V_{ap}}{V_p} < 0.25 \tag{7.9}$$

is suggested as a good separation of CC events and background (see figure 7.9). A large part of the remaining background contribution is significantly suppressed by using the correlation between the missing transverse momentum $p_{T,miss}$ and V_{ratio}. In contrast to the CC events, γp events are distributed at high values of V_{ratio} and low transverse momentum $p_{T,miss} (= p_{T,h})$. Therefore a parabola cut, as indicated in figure 7.10, is made in the $(p_{T,miss} - V_{ratio})$ plane.

Both V_{ratio} cuts together exclusively reject 32% of the remaining background.

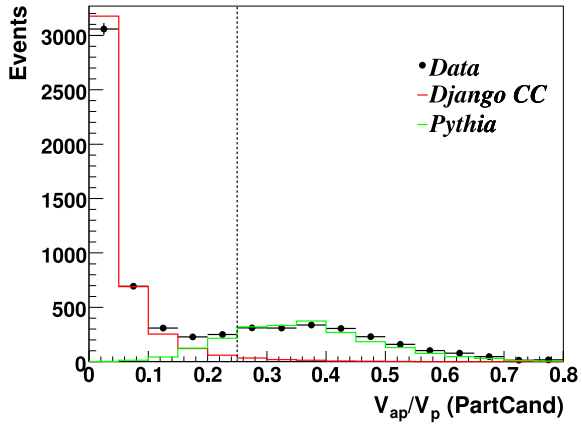

Figure 7.9: Distribution of V_{ratio} for the data, the CC MC and the γp background events applying all cuts except those against the photoproduction i.e. V_{ratio} and V_{ratio} versus $p_{T,Miss}$.

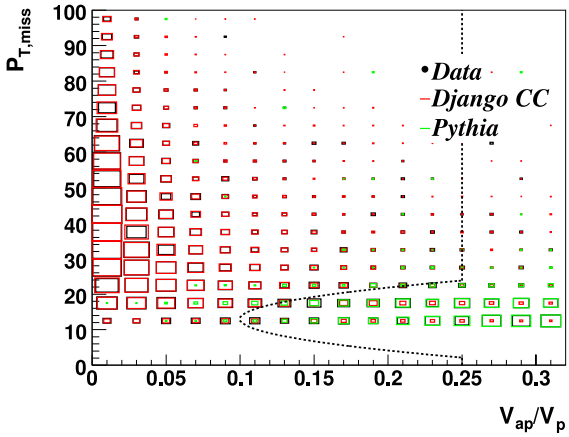

Figure 7.10: Distribution of V_{ratio} versus $p_{T,miss}$ for the data, the CC MC and the photoproduction MC, after applying all analysis cuts except the 2-dimensional cut. The dashed line represents the 2-dimensional cut used in the analysis for rejection of the photoproduction background.

Rejection of NC events

Most of the NC events are rejected by the V_{ratio} cut, and the remaining contribution is suppressed by the following requirements on the scattered electron

- The event contains an isolated track opposite to the hadronic final state (HFS). Here the track is defined as isolated [120] if there is no other track in a cone with the opening angle $\phi = 29°$. If the difference in the azimuthal angle $\Delta\phi$ between the track ϕ_{track} and the HFS ϕ_{HFS} satisfies the criteria:

$$\Delta\phi = |\phi_{track} - \phi_{HFS})| \geq 160° \tag{7.10}$$

the track is considered as the opposite to the HFS.

- The event contains an electron isolated from the HFS (or the nearest jet). The isolated electron satisfies the condition:

$$\Delta\phi = |\phi_e - \phi_{HFS})| \geq 160^\circ \tag{7.11}$$

where ϕ_e and ϕ_{HFS} are the electron and the HFS azimuthal angle, respectively. Additionally, it is required that the distance between the electron and the HFS (or the closest jet) D_{jet} in the $\eta - \phi$ space satisfies the following relation:

$$D_{jet} = \sqrt{\Delta\eta^2_{e-jet} + \Delta\phi^2_{e-jet}} > 1 \;\; (57.3^\circ). \tag{7.12}$$

- The event contains a scattered electron and a balanced transverse momentum $p_{T,h}/p_{T,e}$ as characteristic of a typical NC event:

$$0.75 < p_{T,h}/p_{T,e} < 1.05 \; . \tag{7.13}$$

These requirements exclusively suppresses the remaining NC background contribution of 1% which is not rejected by any other CC selection requirement.

7.2.7 Rejection of Non-*ep* Background

The remaining non-*ep* background (see section 4.2) has to be rejected by additional criteria based on the specific event topology and event timing. An efficient way to suppress the non-*ep* background contribution to the physics processes is to make use of the timing information from the CJC system and the LAr calorimeter. In addition, a set of the *topological non-ep background finders* based on the characteristic topological signature of cosmic events and beam-halo and beam-gas events has been defined (see section 4.2.2).

7.2.7.1 Event Timing

The pile-up events originating from different background interactions such as cosmic rays or halo muons, as well as beam gas and beam wall interactions will affect the reconstruction of the interesting physics events in the following ways:

- Cosmic rays or halo muon induced showers can add visible energy to low p_T interactions and may fake with high missing transverse energy.

- Beam-wall and beam-gas interactions can add energy to real physics interactions, affecting the reconstruction of the kinematic variables.

A very efficient way to detect the energy deposits out of time (mostly cosmics) is using the event timing from the drift chamber CJC ($T0_{CJC}$) and the LAr calorimeter ($T0_{LAr}$), which have to be in coincidence with the bunch crossing time. The drift chamber CJC timing $T0_{CJC}$ is the time when charged particles cross the CJC. The LAr calorimeter timing $T0_{LAr}$ is determined from the time structure of the energy deposition in the Big Towers. The resolution of $T0_{CJC}$ is approximately $\sigma \approx 2\ ns$ and the resolution of the $T0_{LAr}$ is approximately 10 ns for large energy depositions. In order to maintain a high selection efficiency the timing requirements are chosen as:

$$-0.54 \leq T0_{LAr} \leq +0.54\ BC \quad \text{and} \quad 410 \leq T0_{CJC} \leq 510 \text{ ticks} \tag{7.14}$$

where 500 $CJC\ ticks$ = 96 ns. The timing distributions $T0_{LAr}$ and $T0_{CJC}$, when applying all selection criteria except the timing requirement, are shown in figure 7.11 (a) and (b), respectively. Figure 7.12 illustrates the correlation of $T0_{LAr}$ versus $T0_{CJC}$ before applying timing requirements given in equation 7.14[3].

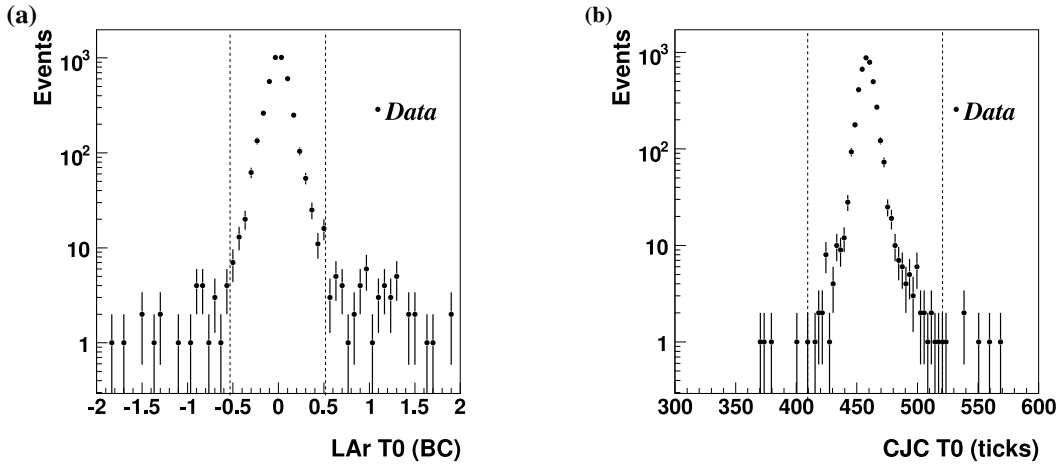

Figure 7.11: Timing distributions LArT0 (a) and CJCT0 (b) applying all selection criteria, except the timing requirement.

7.2.7.2 Non-*ep* Background Finders

The majority of non-*ep* background is rejected by a set of the topological algorithms which are based on the association of tracks and clusters in different subdetectors, with a pattern characteristic for cosmics, beam-gas and beam-halo events.

Three groups of non-*ep* background finders are currently defined and used by the different H1 physics analyses [122–124]. The background finders are bit-coded in the flags *Ibg*, *Ibgfm* and *Ibgam*. The *Ibg* flag is used to identify halo-muons and background

[3]The tuning of the timing requirements as well as efficiency determination of the timing selection is done using the PsCC events.

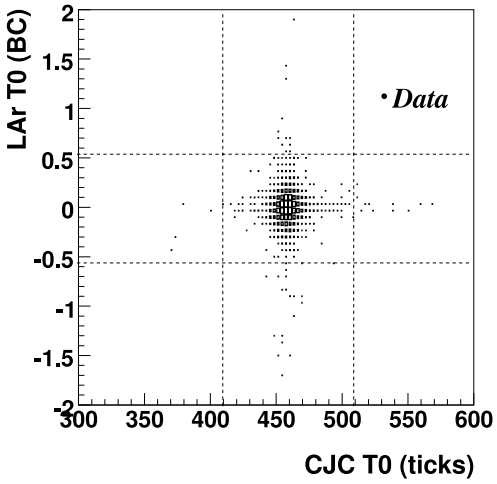

Figure 7.12: The event timing requirement for the selected $e^- p$ 2005 CC events, applying all selection criteria except the timing criterium (see equation 7.14) based on the CJCT0 and the LArT0. Dashed lines show the timing cut used in the analysis.

bit	finder	description
0	HALAR	longitudinal energy pattern in the LAr calorimeter
1	HAMULAR	longitudinal energy pattern in the LAr calorimeter with the energy deposition in the backward iron end cap
2	HAMUMU	horizontal muon track in the forward detector with the energy deposition in the backward iron end cap
3	HASPLAR	cluster in the inner forward part of the LAr calorimeter matching energy deposition in the SpaCal
4	HAMUIF	cluster in the inner forward part of the LAr calorimeter matching the energy deposition in the backward iron endcap
5	COSMUMU	two opposite muon tracks matching in direction
6	COSMULAR	at least one muon with 90% of the energy deposited in the corresponding LAr cluster
7	COSTALAR	two opposite clusters in the Tail Catcher with 85% of the energy deposited in the matching LAr cluster
8	COSTRACK	two CJC tracks with the opposite direction in space
9	COSLAR	isolated the highest energy LAr cluster with the small electromagnetic energy inside the cylinder

Table 7.3: Overview of the topological background finders encoded in the flag *Ibg*.

originating from cosmic ray muons. It is based on the topological requirements of detector components characteristic for each of the background sources. A short description of the background finder encoded in the flag *Ibg* can be found in table 7.3. The remaining background contribution is suppressed by the flags *Ibgam* and *Ibgfm* [124]. They are designed to identify the beam-gas background in addition to the beam-halo

and cosmic ray background events (see subsection 4.2.2). The non-*ep* background finders are applied to data and simulated events. In addition to all other CC cuts, the background finders reduce the remaining non-*ep* background contribution for 4.5%.

7.3 Visual Scanning

The final stage in the CC event selection is visual scanning. After applying all cuts 4144 events are scanned visually. In total 35 events have been identified as non-*ep* background and have been rejected. These events are mostly originating from the cosmic rays (about 35%), while the remaining events are the halo muons, beam-gas events, events with the noise in the LAr calorimeter. Only remaining non-*ep* background events are excluded from the final sample by visual scanning, since the remaining *ep* background is modelled by MC simulations and subtracted (see equation 4.7). An example of a halo shower event excluded by the scanning is shown in figure 7.13.

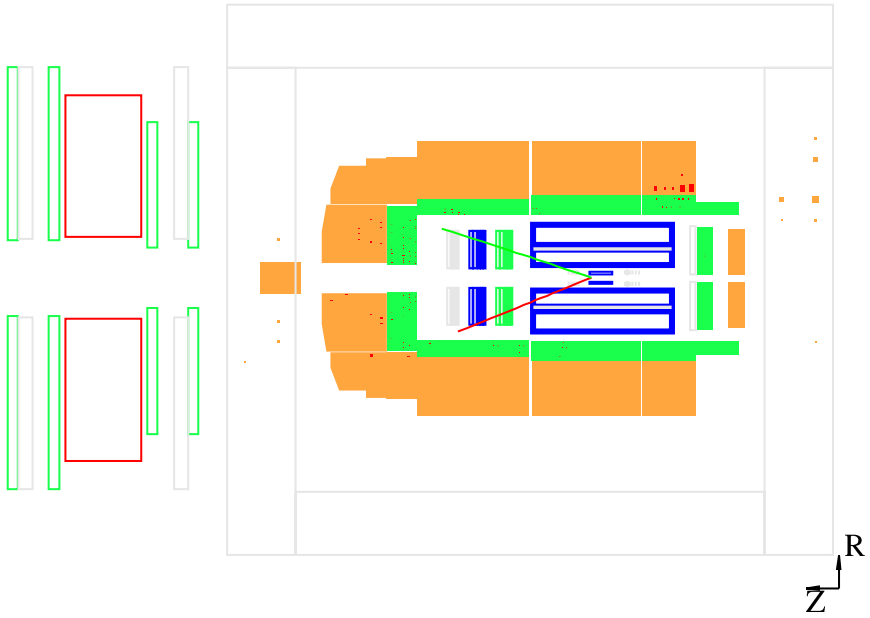

Figure 7.13: Halo shower in the central barrel region of the LAr calorimeter excluded by scanning.

7.4 Final CC Sample

After applying the complete set of the CC selection requirements the final sample of the LH and RH CC DIS for e^-p 2005 data has been obtained. The number of selected CC events per integrated luminosity in 1 pb^{-1} intervals versus the run number is illustrated in figure 7.14 for the LH (a) and the RH data (b). Similarly to the NC

	left-handed	right-handed
Luminosity	(68.6 ± 1.4) pb^{-1}	(29.6 ± 0.6) pb^{-1}
Polarisation	$(-27.0 \pm 1.3)\%$	$(37 \pm 1.8)\%$
CC data events	3379	730
NC MC events	16.1	6.7
γp MC events	37.5	16.0
lepton pair MC event	4.0	1.7
W production MC events	9.1	3.9

Table 7.4: Final selected LH and RH CC DIS events collected by the H1 detector in the $e^- p$ collisions during 2005. These data are used to measured the polarised CC DIS cross sections.

events, the CC event yields show stability during both periods of data taking.

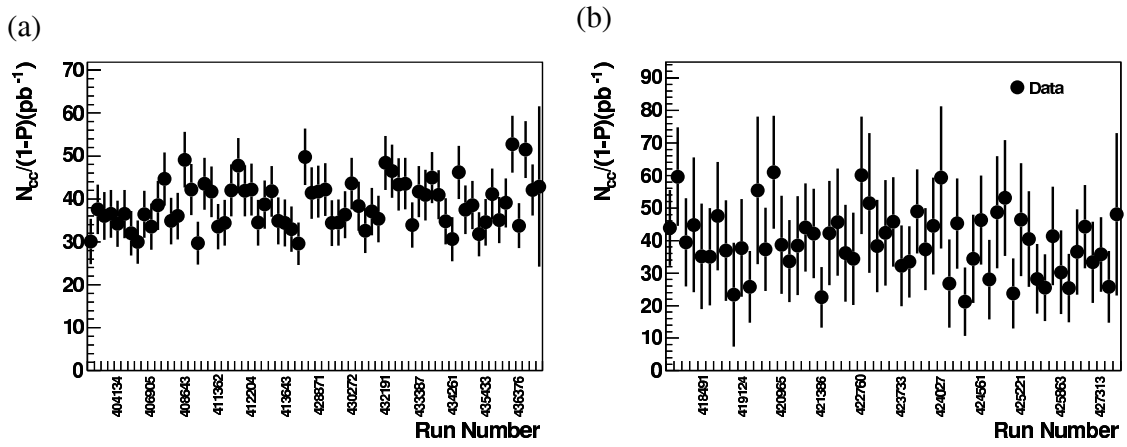

Figure 7.14: Event yield as a function of run number in the bins of equal luminosity for the selected $e^- p$ 2005 LH (a) and RH CC DIS events (b).

The non-ep background events have been successfully removed while the MC simulation takes into account small remaining ep background contribution. The dominating background source is the photoproduction which is located at low Q_h^2, low $E - p_z$ and middle values of Bjorken x_h (see figures 7.24, 7.25 and table 7.4). The NC events are distributed at middle Q_h^2, high $E - p_z$ and low x_h. As one can realise the relative background contribution is the same in the two data sets, as expected, since these events do not depend on the electron beam polarisation.

The Highest Q^2 CC DIS Event at the H1

The highest Q^2 CC event having $Q^2 = 78045$ GeV^2 taken by the H1 is shown in figure 7.15. The efficiencies derived from PsCC cannot be determined at such high Q^2 due to lack of statistics of NC events in this region of phase space. Therefore, this

event together with 4 other events from the LH data and 1 event from the RH data have not been included in the final CC event samples.

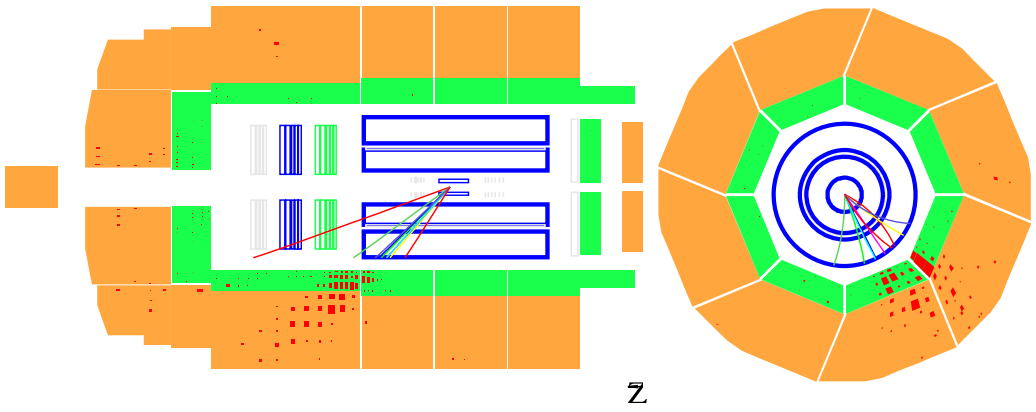

Figure 7.15: The side view (left) and the radial view (right) of CC event with the highest Q^2 taken in $e^- p$ collision by the H1 detector in year 2005.

7.5 Efficiency Determination Using PsCC Events

In principle, all efficiency corrections should be taken into account in the MC simulation and if it is properly done, no additional correction is needed. However, there are cases where the MC needs an additional correction (efficiency) to describe the data correctly. For example, the CC triggers and the event timing are not correctly simulated in the MC and it is therefore necessary to correct the MC. Additionally, the efficiency of CC selection using background finders which is usually determined from the MC is cross-checked using the PsCC events (see section 4.4). Since the accurate determination of efficiencies and their effect to the MC is very important for the cross section measurement (see section 4.1) this section is devoted to the efficiency determination.

The efficiency $\mathcal{E}$ is usually determined differentially in bins of x and Q^2 at which the cross section is measured and then applied as a correction factor to the CC MC (see equation 4.3). Any of above mentioned efficiencies $\mathcal{E}$ determined from the PsCC sample is calculated as:

$$\mathcal{E}(x,Q^2) = \frac{N^{sel}_{PsCC}(x,Q^2)}{N^{all}_{PsCC}(x,Q^2)} \tag{7.15}$$

where $N^{sel}_{PsCC}(x,Q^2)$ is the number of the PsCC events satisfying the CC selection requirement, while $N^{all}_{PsCC}(x,Q^2)$ is the number of all PsCC events in a given bin of x and Q^2.

7.5.1 Charged Current Trigger Efficiencies

The trigger efficiency of the CC subtriggers is determined from the PsCC events using equation 7.15, where $N^{sel}_{PsCC}(x,Q^2)$ represents the number of PsCC events which are triggered by any of the CC subtriggers i.e. $ST66 \| ST67 \| ST77$. The trigger efficiencies were determined for the LH and the RH data separately in order to monitor possible time dependencies although significant differences were not observed.

The trigger efficiencies as function of the missing transverse momentum $p_{T,miss}$ and the hadronic angle γ_h for the LH CC data are shown in figure 7.16 (a) and (b), respectively. The efficiency increases steeply with increasing $p_{T,miss}$ from $\approx 40\%$ at $p_{T,miss} = 12$ GeV (the analysis cut) to $> 95\%$ at $p_{T,miss} > 30$ GeV. The inefficiency at low γ_h is a consequence of the hadronic final state which, being scattered in the forward direction disappears partly in the beam pipe. The inefficiency at high γ_{had} corresponding to high y_h is a consequence of the hadronic final state scattered in the central barrel of the LAr calorimeter where the trigger efficiency is low (see subsection 7.2.5). The trigger efficiency in the x and Q^2 used to correct the MC is shown in figure 7.17 for the LH data sample.

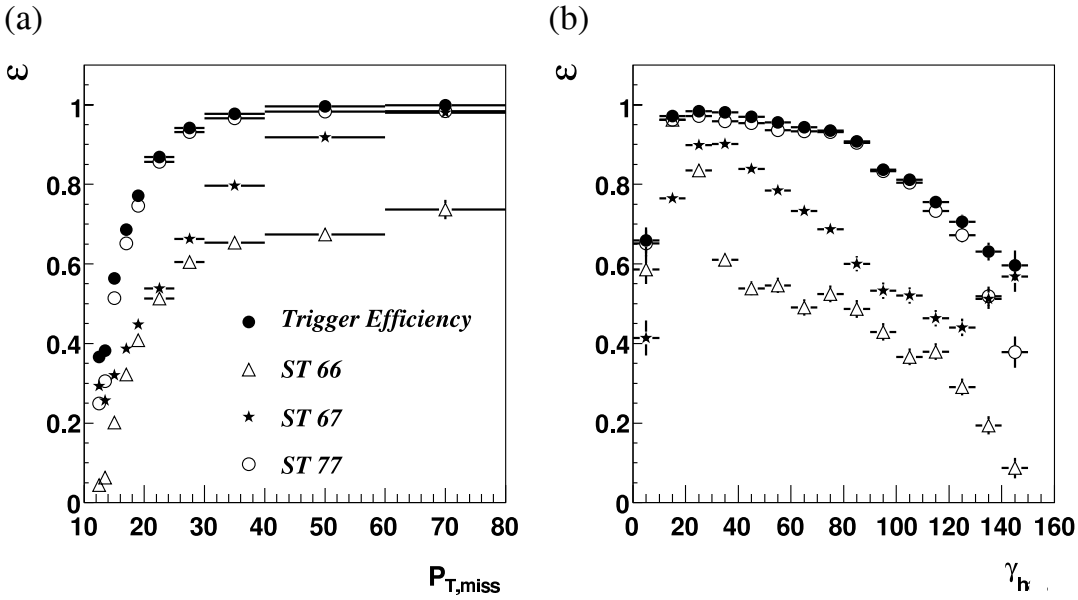

Figure 7.16: The trigger efficiency for the CC events versus $p_{miss,T}$ (a) and γ_h (b) determined from the PsCC events for the individual CC subtriggers ST66, ST67 and ST77 and for the global trigger efficiency i.e. $ST66 \| ST67 \| ST77$.

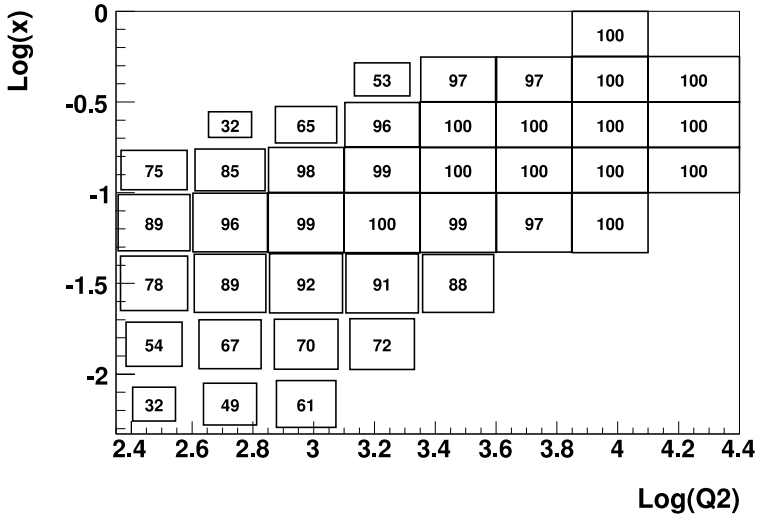

Figure 7.17: The CC trigger efficiency for condition $ST66 \| ST67 \| ST77$ in x and Q^2 bins in which the differential cross section is measured.

7.5.2 Background Finder and Event Timing Efficiency

The efficiency of the non-ep background finders is determined from the PsCC data and the CC MC using equation 7.15, where $N^{sel}_{PsCC}(x, Q^2)$ is

the number of PsCC events which pass the background condition $BGF = \{Ibg, Ibgam, Ibgfm, Ibg \| Ibgam \| Ibgfm\}$. This equation is used for the MC events as well. The background efficiency is determined for the complete data set i.e. the LH and the RH data together, since there is no reason to have different background finder efficiencies depending on the electron helicity.

The efficiencies of individual background finders in PsCC data and the CC MC are shown in figures 7.18, 7.19 and 7.20 as a function of hadronic angle γ_h (a). In general, the efficiency is very high (above 95%) almost over the entire detector. Somewhat lower efficiencies can be observed at low and high γ_h due to limited detector acceptance. Nevertheless, the ratio plots of the background finder efficiency in the PsCC data to that in the MC show small difference between the data and simulation which is only 1% for the *Ibgam* flag and less than 5% for the *Ibg* flag. The inefficiency at low and high γ_h bins for the *Ibg* background finder is mainly caused by the COSTA-LAR finder since the noise in the tail catcher is not taken into account in the MC simulation. The *Ibgam* finder is found to be efficient over the full γ_h range.

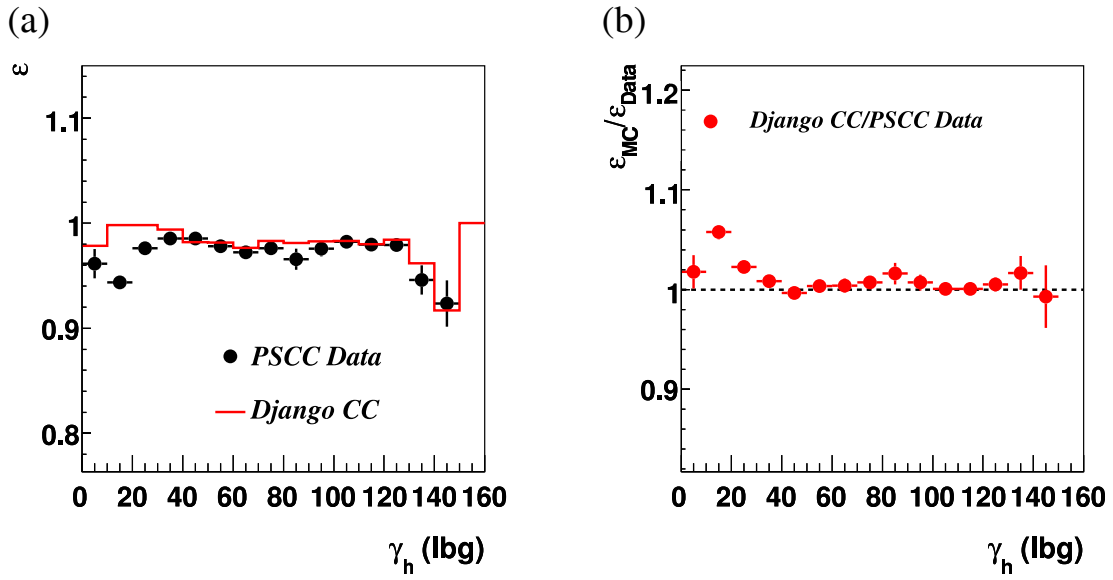

Figure 7.18: Background finder efficiency determined from the PsCC data and the CC MC (a) and their ratio (b) for the *Ibg* background finder.

Finally, a combined efficiency for all three background finder algorithms together is determined. However, a difference between the efficiency derived from the CC MC and the efficiency derived from the PsCC data was observed. Therefore, a re-weighting factor is determined for each (x, Q^2) bin where the cross section is measured as:

$$w_{corr}^{BGF}(x, Q^2) = \frac{\mathcal{E}_{MC}^{BGF}(x, Q^2)}{\mathcal{E}_{PsCC}^{BGF}(x, Q^2)} \tag{7.16}$$

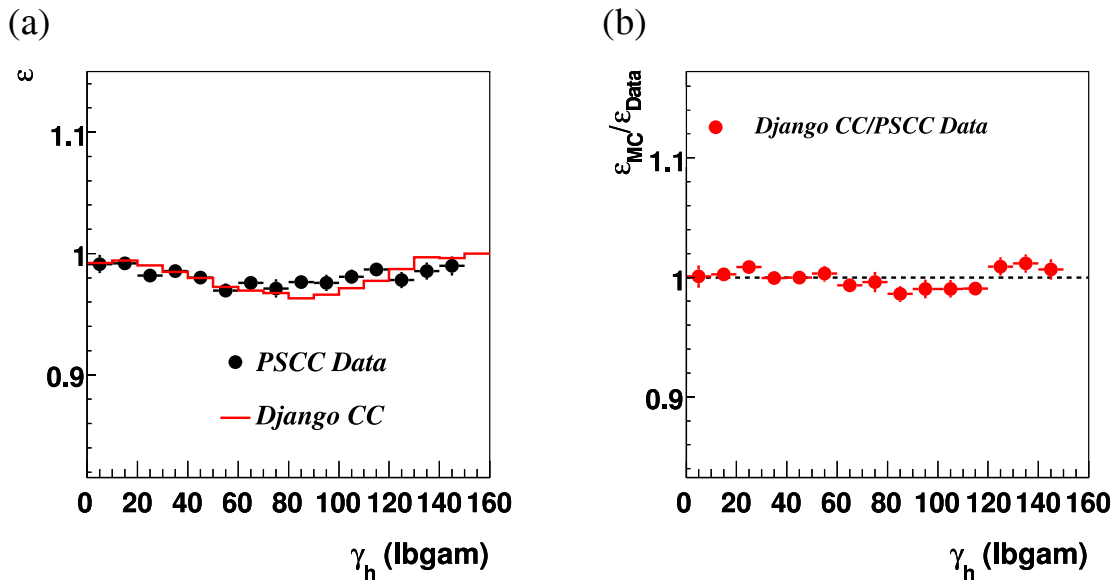

Figure 7.19: Background finder efficiency determined from the PsCC data and the CC MC (a) and their ratio (b) for the *Ibgam* background finder.

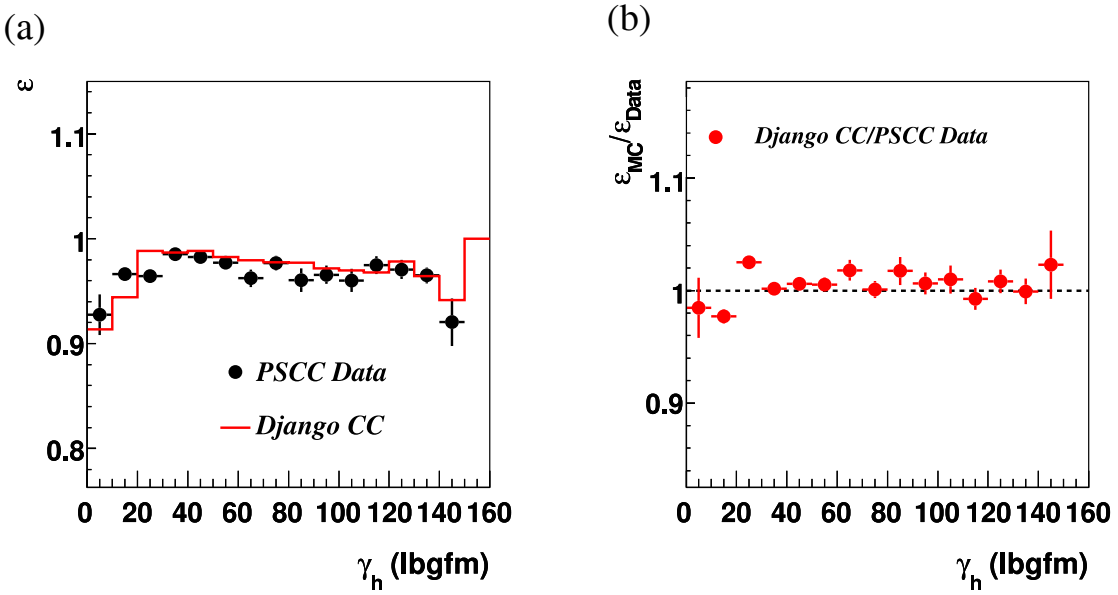

Figure 7.20: Background finder efficiency determined from the PsCC data and the CC MC (a) and their ratio (b) for the *Ibgfm* background finder.

in order to take into account all possible effects reflecting the data behaviour, which are not accounted for in the simulation. Since the timing requirement is also used for

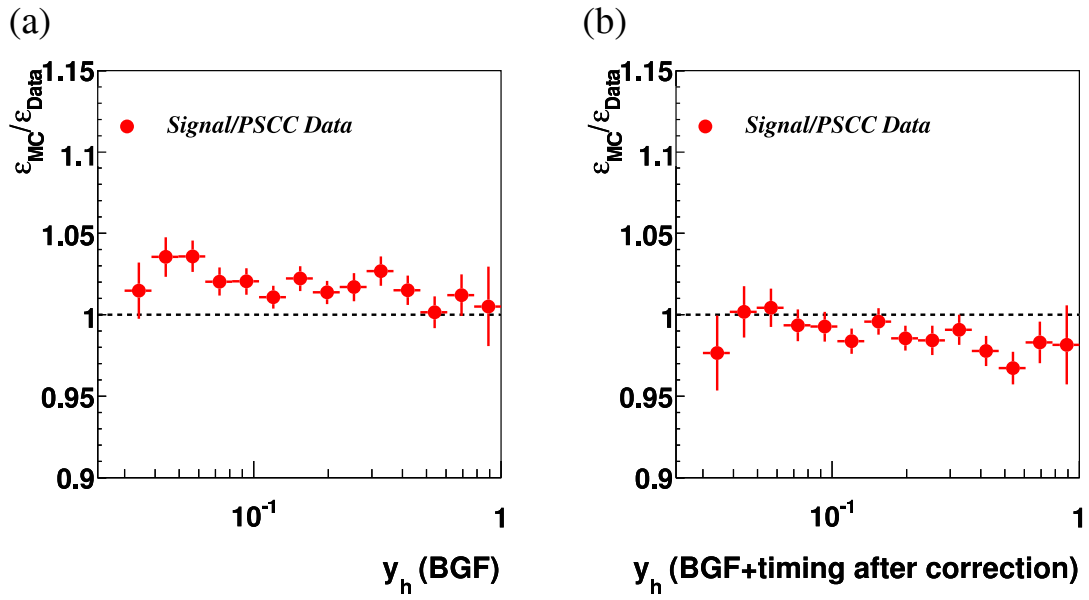

Figure 7.21: Ratio of the background finder efficiency determined from the Django and the PsCC data before (a) and after correcting the MC for the timing efficiency and the background finder efficiency determined from the PsCC (b).

the non-*ep* background rejection it has been combined with the corrected background efficiency resulting in the combined background and timing efficiency. The efficiency of the background finders and the event timing versus y_h before and after MC correction to take into account differences in efficiency with respect to the PsCC data is shown in figure 7.21 (a) and (b), respectively.

As a correction factor corrected background and timing efficiency is applied to the MC simulation in (x, Q^2) bins.

7.5.3 The Vertex Reconstruction Efficiency

The efficiency of the vertex reconstruction is determined from the PsCC events, the CC MC events and the PsCC MC [4] from equation 7.15, with $N^{sel}_{PsCC}(x, Q^2)$ being the number of the events satisfying the vertex requirement (see subsection 7.2.4).

The efficiency of the vertex requirement as a function of y_h for the PsCC data, the PsCC MC and the CC MC simulation is shown in figure 7.22 (a). Regardless of the sample used for the efficiency determination, the efficiency increases as a function of y_h from 30% at $y_h = 0.04$ to 100% at high y_h values. At lower y_h, which corresponds to the forward detector region, the efficiency is expected to be in general lower than at high y_h, i.e. the central detector region, since the vertex requirement is based only on the central tracking detector.

[4] PsCC MC events are made out of NC MC events which are passed through the PsCC program, so that all original electron information is discarded.

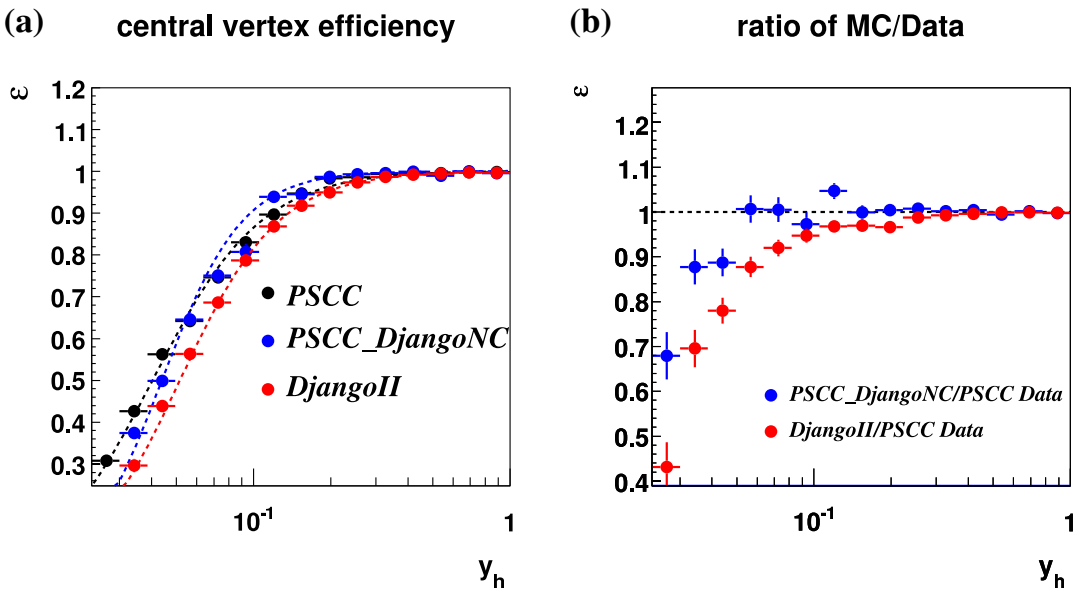

Figure 7.22: The efficiency of the vertex requirement in PsCC Data (from NC data), PsCC MC (derived from NC MC PsCC_DjangoNC) and from CC MC (a) and the ratio of different efficiencies (b).

However, a difference between the efficiencies observed from the ratios shown in figure 7.22 (b) has been observed. This has been understood as the consequence of different vertex reconstruction in the PsCC data and the CC MC: After removal of original electron hits from the NC event a new vertex fit is performed for the corresponding PsCC event from the central tracks and not from the original hits for technical reasons. In the CC data as well as in the CC simulation the vertex is reconstructed from the original event information which means the hits in the central drift chamber [125]. Thus, the vertex distribution in the CC data is well described by the simulation (see figure 7.23 (a)), while the PsCC data are well described by the PsCC MC (see figure 7.23 (b).

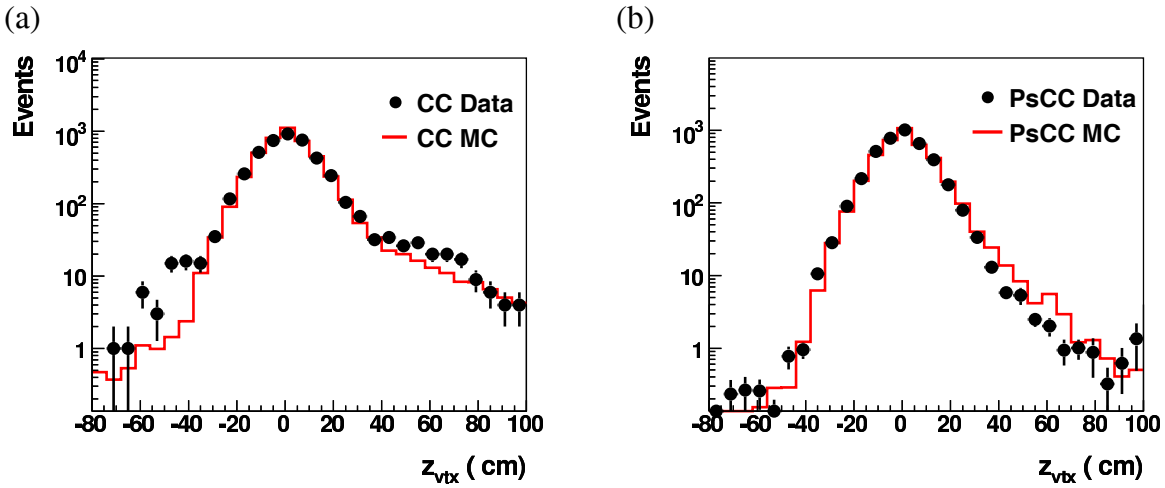

Figure 7.23: Vertex distribution for the final CC data and CC MC (a) and the PsCC data and the PsCC MC for 2005 data when z-vertex requirement is not applied (b).

7.6 Kinematic Distributions

Since the CC MC was corrected for effects that are present only in the data it is now expected that simulation fully describes data. The expected numbers of CC events obtained from the MC simulation are 3351 and 731 for the LH and the RH data, respectively. Comparing the expected numbers of the CC events with the final number of selected CC data shown in table 7.4 once can observe a very good agreement. This is also confirmed from the kinematic distributions of Q^2_h, $p_{T,h}$, $E-p_z$ and x_h illustrated in figures 7.24 and 7.25 for the LH and RH data, respectively. Thus, using the fact that the MC describes the data in every respect one can go a step further and extract the cross sections from the obtained numbers of the selected CC DIS events for both helicity states as will be discussed in the next chapters.

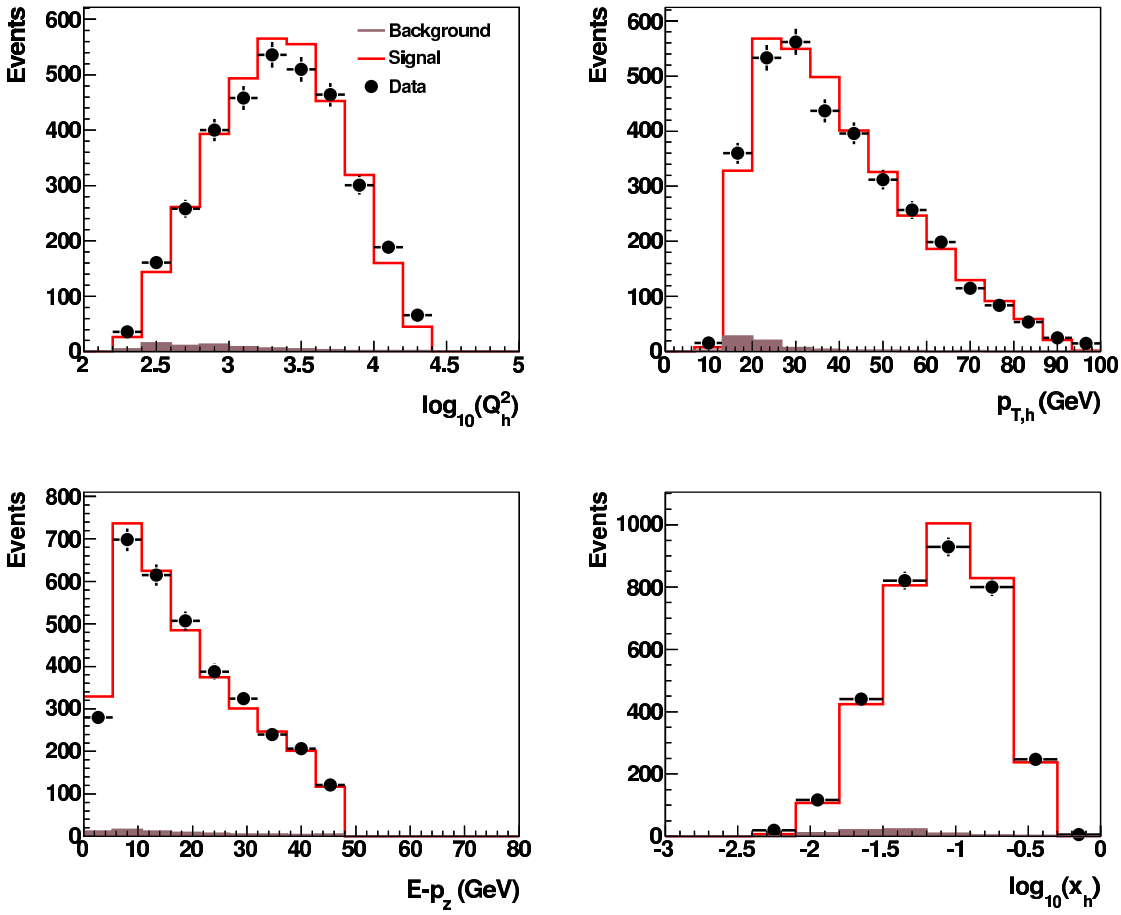

Figure 7.24: Distributions of the kinematic variables Q_h^2, $p_{T,h}$, $E - p_z$ and x_h for the selected CC LH data sample. The complete simulation containing the CC (signal) and background events (background) normalised to the experimental luminosity is compared to the data. The simulated background contamination is also shown.

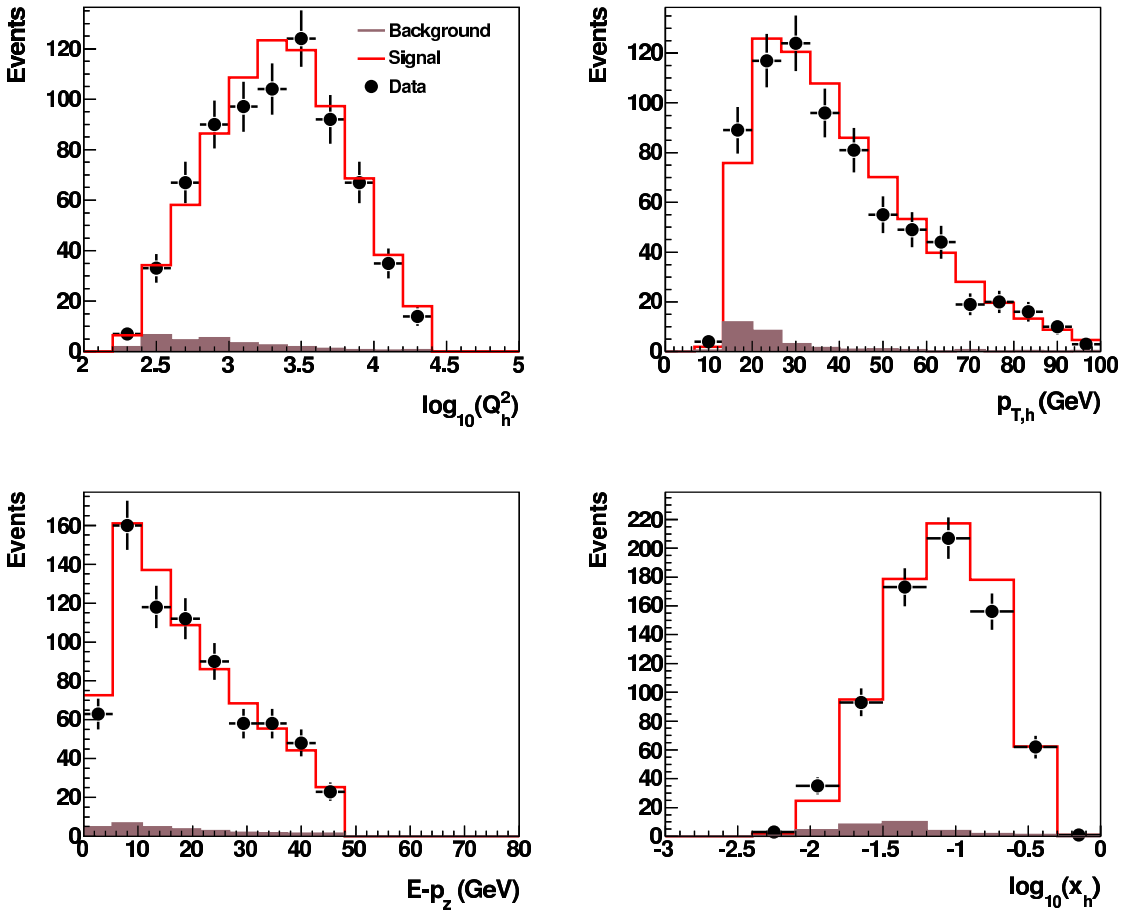

Figure 7.25: Distributions of the kinematic variables Q_h^2, $p_{T,h}$, $E - p_z$ and x_h for the selected CC RH data sample. The complete simulation containing the CC (signal) and background events (background) normalised to the experimental luminosity is compared to the data. The simulated background contamination is also shown.

Chapter 8

Cross Section Measurement Procedure

The principles of the cross section measurement introduced in chapter 4 will be applied here for the measurement of total and differential CC cross sections. The cross section extraction is discussed first. It is followed by the description of the binning used for the differential cross section measurements. The last section is concerned with the systematic uncertainties and their effects on the cross section measurement.

8.1 Calculation of the Total CC Cross Section

The general principles of the cross section measurement have been introduced in chapter 4 with the emphasis on the total cross section resulting in the following expression:

$$\sigma_{Born}^{meas} = \frac{N_{sel} - N_{bg}}{N_{sel}^{MC}} \cdot \frac{L^{MC}}{L^{data}} \cdot \sigma_{Born}^{MC} \tag{8.1}$$

where, of course, all inefficiencies for determination of N_{sel}^{MC}, as discussed in section 7.5, are taken into account.

8.2 Differential Cross Section Extraction

In addition to the total cross section, the measurements of the differential cross section has been performed in this thesis. The differential cross section is measured in selected regions of the phase space in the x-Q^2 plane called *bins*. The binning used in the current analysis is illustrated in figure 8.1. Similarly to the total cross section (see equation 8.1) the differential cross section is measured using bins of finite size in x and Q^2 as:

$$\frac{d^2\sigma^{meas}(x_{i,c}, Q^2_{i,c})}{dxdQ^2} = \frac{N_{sel} - N_{bg}}{N_{sel}^{MC}} \cdot \frac{L^{MC}}{L^{data}} \cdot \frac{d^2\sigma_{Born}^{MC}(x_{i,c}, Q^2_{i,c})}{dxdQ^2} \cdot \delta_i^{bc}. \tag{8.2}$$

Here δ_i^{bc} is called the *bin centre correction* and represents the correction from the cross section in a bin of finite size $\Delta x = (x_{i,max} - x_{i,min})$ and $\Delta Q^2 = (Q^2_{i,max} - Q^2_{i,min})$ to the bin centre $(x_{i,c}, Q^2_{i,c})$ position and is defined as:

$$\delta_i^{bc} = \frac{\frac{d^2\sigma}{dxdQ^2} \mid_{x=x_{i,c}, Q^2=Q^2_{i,c}}}{\int_{x_{i,min}}^{x_{i,max}} \int_{Q^2_{i,min}}^{Q^2_{i,max}} \frac{d^2\sigma}{dxdQ^2} dxdQ^2}. \tag{8.3}$$

The equation 8.2 is applied for the single differential cross sections, $d\sigma_{cc}/dQ^2$ and $d\sigma_{cc}/dx$, measured as a function of the kinematic variables Q^2 and x, respectively, and the double differential cross section, $d^2\sigma_{cc}/dxdQ^2$, measured in both variables x and Q^2.

The double differential cross section is usually presented in a form of the *reduced cross section*:

$$\bar{\sigma}_{cc}^{e^\pm p} = \frac{2\pi x}{G_F^2} \left[\frac{Q^2 + M_W^2}{M_W^2} \right] \frac{d^2\sigma_{cc}^{e^\pm p}}{dxdQ^2} = \phi_{cc}^{e^\pm p} \tag{8.4}$$

8.3 Bin Definition

A careful choice of the bin boundaries plays an important role since the measured differential cross sections are obtained from the number of events in the particular bin. There are two effects to be taken into account: too narrow binning will increase the statistical error and cause large migration effects between neighbouring bins, whereas too wide binning would result in measurement which gives much less information than it could have done otherwise. Therefore, the binning has to be optimised and in this analysis it was chosen to ensure that the resolution is always better than the bin size [126], resulting in three bins per order of magnitude in x and in Q^2. The binning used for measurement of differential cross sections is illustrated in figure 8.1, and the bin centres and boundaries are shown in tables 8.1 and 8.2, respectively.

bin centre values								
$Q^2[GeV^2]$	300	500	1000	2000	3000	5000	8000	15000
$log_{10}(Q^2)$	2.48	2.70	3.00	3.30	3.47	3.70	3.90	4.18
x	0.008	0.013	0.032	0.08	0.13	0.25	0.40	0.65
$log_{10}(x)$	-2.10	-1.89	-1.50	-1.10	-0.89	-0.60	-0.40	-0.19

Table 8.1: Definition of the $Q^2$and x bin centre values used for the measurement of the differential cross sections.

Furthermore, the cross section measurements are restricted to bins chosen accordingly to the high quality criteria based on the quantities *acceptance* ($\mathcal{A}$), *purity* ($\mathcal{P}$) and

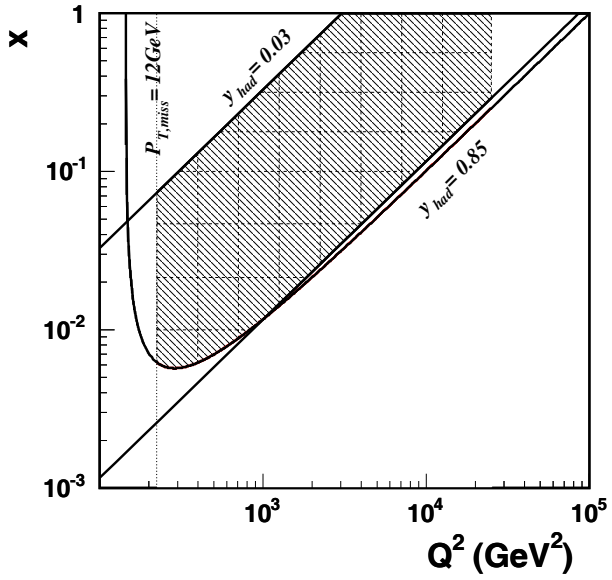

Figure 8.1: The phase space in which the CC interactions are measured. The $p_{T,miss}$ cut is shown as the curve (at 12 GeV), while the vertical dashed line represents the Q^2 cut. The upper (0.85) and lower limit (0.03) in y_h are also shown.

bin boundaries									
$Q^2[GeV^2]$	224	398	708	1259	2239	3981	7080	12589	25119
$log_{10}(Q^2)$	2.35	2.6	2.85	3.1	3.35	3.6	3.85	4.1	4.4
x	0.005	0.010	0.021	0.047	0.100	0.178	0.316	0.562	1.000
$log_{10}(x)$	-2.33	-2.0	-1.67	-1.33	-1.0	-0.75	-0.5	-0.25	-0.0457

Table 8.2: Definition of the Q^2 and x bin boundaries used for the measurement of the differential cross sections.

stability ($\mathcal{S}$). They are determined from the MC simulation and defined as

$$\mathcal{P}(i) = N^{MC}_{gen+rec}(i)/N^{MC}_{rec}(i) \quad (8.5)$$

$$\mathcal{S}(i) = N^{MC}_{gen+rec}(i)/N^{MC}_{gen+sel}(i) \quad (8.6)$$

$$\mathcal{A}(i) = N^{MC}_{rec}(i)/N^{MC}_{gen}(i) \quad (8.7)$$

where

- $N^{MC}_{rec+gen}(i)$ is the number of events generated and reconstructed in bin i;
- $N^{MC}_{rec}(i)$ is the number of events reconstructed in bin i;
- $N^{MC}_{gen+sel}(i)$ is the number of events generated in bin i which can be reconstructed in any bin;

- $N_{gen}^{MC}(i)$ is the number of events generated in bin i.

The purity, stability and acceptance used for the choice of bins for the single differential cross sections in Q^2 bins are shown in figures 8.2 and for x bins in figure 8.3 for both electron helicities. For the double differential cross section the purity, stability and acceptance are shown in figures 8.5 and 8.4 for the LH and RH data samples, respectively. The kinematic variables x and Q^2 are determined using the hadron reconstruction method (see chapter 5.3.1). At low x and correspondingly high y, the resolution of the hadron method is poor causing the purity to decrease, which means that events tend to migrate into neighbouring bins and are therefore assigned to the wrong bins. At high x and low y the hadronic final state goes forward causing a significant fraction of the missing transverse momentum $p_{T,miss}$ not being measured in the detector and resulting in a decrease of the stability.

The cross section measurement is performed in bins in which the purity and stability are larger than 30% for both helicites as indicated by lines in figures 8.2, 8.3 for the single differential cross sections and 8.4 for the double differential cross sections.

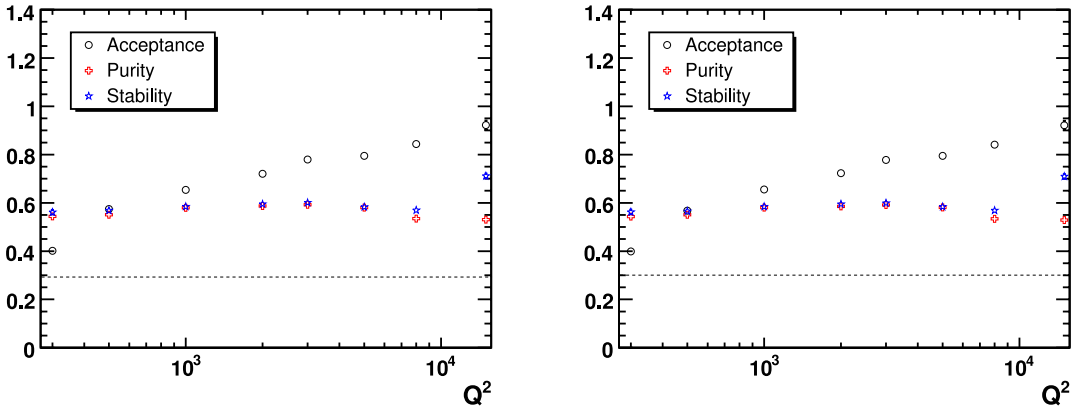

Figure 8.2: The acceptance, purity and stability for the LH and the RH data sets in bins of Q^2. The horizontal dashed line at 30% indicates the purity and stability requirement.

8.4 Systematic Uncertainties

The uncertainties related to the detector performance or selection inefficiency lead to *systematic* uncertainties (sometimes also called "systematic errors") on the cross section measurements.

The systematic uncertainties can be separated into errors *correlated* between all cross section measurements and errors which are *uncorrelated*. For instance, a correlated error on the hadronic energy measurement means that the hadronic energy could differ from the "true" hadronic energy scale which caused deviation from "true"

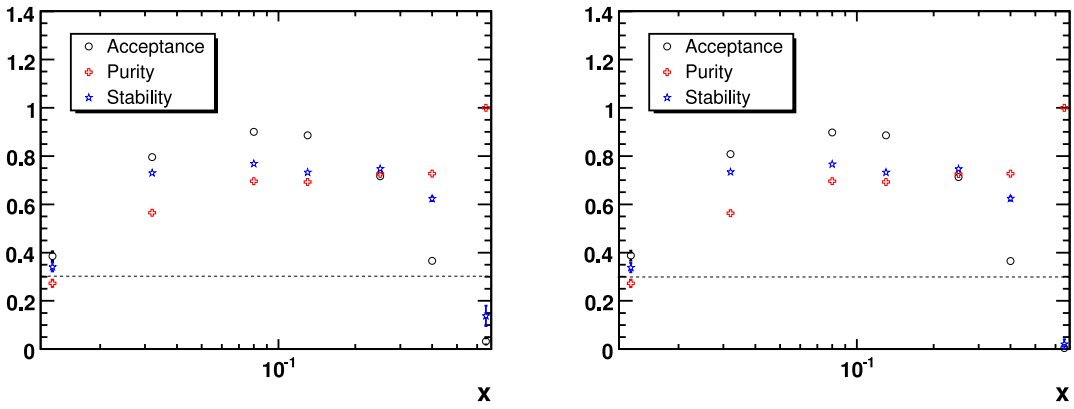

Figure 8.3: The acceptance, purity and stability for the LH and the RH data sets in bins of x. The cross section is measured for the purity and stability above the 30% requirement (dashed line).

cross section in all bins of x and Q^2 simultaneously. In contrast to the correlated, uncorrelated uncertainties can occur due to local fluctuations i.e. in specific bins of x and Q^2. As an illustration: the trigger efficiency at low x in one region of the LAr calorimeter has no impact on the efficiency at high x, which corresponds to different region of the calorimeter. There are also sources of errors which are considered as partially correlated and partially uncorrelated as for example the error on the luminosity measurement. Regardless of the correlation, all errors are assumed to be Gaussian to a good approximation.

The various contributions to the systematic uncertainties considered are the following:

- **Hadronic energy measurement**
  An uncorrelated uncertainty of 1.7% is assigned to the hadronic energy measured in the LAr calorimeter. In addition, 1% correlated component originating from the calibration method and the uncertainty on the reference electromagnetic scale is added in quadrature. This yields the total uncertainty on the hadronic energy measurement of 2% (see section 5.4).

- **Noise subtraction in the LAr calorimeter**
  The clusters from coherent noise in the LAr calorimeter are rejected by specific algorithms designed to recognise this noise in the LAr calorimeter (see section 5.4, figure 5.3). Therefore, a 10% correlated uncertainty is assigned to the energy measured in the LAr calorimeter which is attributed to noise.

- **Variation of cuts against photoproduction background**
  A correlated systematic uncertainty is assigned to the variation of variable V_{ratio} by ± 0.02, used for the rejection of photoproduction background, around the nominal value.

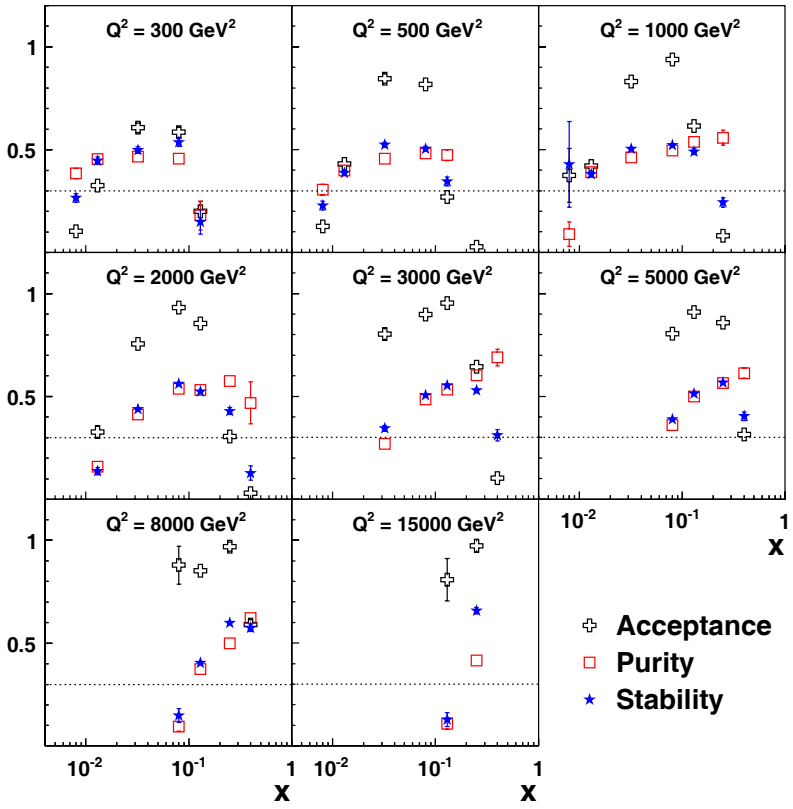

Figure 8.4: The acceptance, purity and stability for the LH data sample for fixed values of the Q^2 as a function of x. The horizontal dashed line at 30% indicates the purity and stability requirement.

- **Subtraction of the photoproduction background**
  A 30% correlated uncertainty on the subtracted photoproduction background is applied. It has been determined from the comparison of the data and the simulation in the phase space dominated by the photoproduction background [127].

- **Substraction of remaining sources of ep background**
  A 10% correlated uncertainty on the subtracted NC background and 20% uncertainty on the remaining sources of ep background [128] (W production, isolated leptons) has been assumed [126].

- **Efficiency of background finders and timing requirement**
  A y_h dependent uncorrelated uncertainty assigned to the event losses introduced by the non-ep background finders and the timing requirement. The uncertainty has been estimated as the difference between the combined background finder and timing efficiency determined from the PsCC data and the efficiency deter-

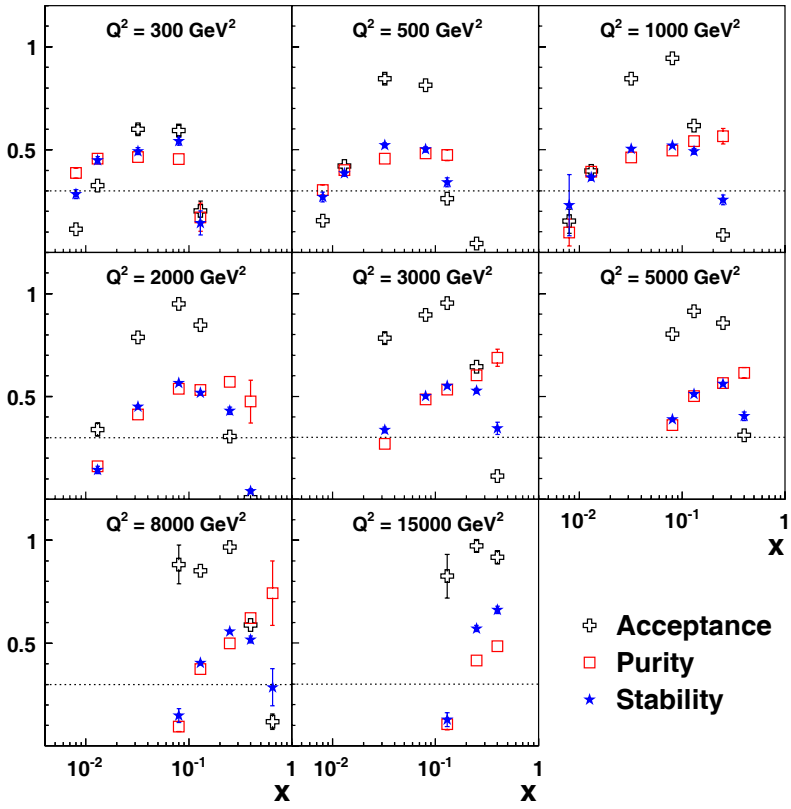

Figure 8.5: The acceptance,purity and stability for the RH data sample for fixed values of the Q^2 as a function of x. The horizontal dashed line at 30% indicates the purity and stability requirement.

mined from the CC MC to be (see subsection 7.5.2, figure 7.21):
3% for $y_h < 0.1$,
2% for $y_h > 0.1$.

- **Trigger efficiency**
  An uncorelated sysematic uncertainty on the trigger efficiency is determined as $15\%(1-\mathcal{E}) \oplus Err^{sta}_{PsCC}$ [126]. Here $15\%(1-\mathcal{E})$ is the trigger inefficiency and Err^{sta}_{PsCC} is the statistical uncertainty of the PsCC sample and results in 1%.

- **QED radiative corrections**
  QED radiative corrections are estimated from the CC MC. An uncorrelated error of 1% for the total cross section has been assumed [129]. For the double differential cross section this error varies with the phase space region and is at most 2%.

- **Vertex reconstruction efficiency**
  A y_h dependent uncorrelated uncertainty on the vertex reconstruction efficiency has been estimated from the difference between the PsCC data and the PsCC MC (see subsection 7.5.3) to be:
  15% for $0.015 < y < 0.06$,
  7% for $0.06 < y < 0.1$,
  4% for $0.1 < y < 0.2$
  1% for $y > 0.2$.

- **Variation of the PDF**
  The MC events used to unfold the cross section are generated using MRSH PDF and re-weighted to the H1 PDF 2000 in order to describe the H1 data as good as possible. The influence on the cross section from the variation of PDFs were investigated using MRSH, CTEQ4 and H1 PDF 2000 via the difference in the acceptance. An uncorrelated error of 0.5% has been estimated.

- **Luminosity**
  A global uncertainty of 2% on the luminosity measurement for both LH and RH data samples has been estimated.

- **Polarisation**
  A global uncertainty of 5% on the polarisation measurement yields an absolute uncertainty on the polarisation measurement of 1.3% for the LH sample and 1.8% for the RH sample.

Effect of the Systematic Uncertainties on the Cross Section Measurements

The total systematic uncertainty is derived by adding the systematic uncertainties described in this section in quadrature and results in about 3.7%. The largest contribution to the systematic uncertainty originates from the vertex reconstruction efficiency in PsCC data which has been understood as a consequence of the different vertex reconstruction in the PsCC data and the CC MC (see section 7.5.3). All systematic errors for the cross section measurement for e^-p CC DIS are listed in table 8.3. In addition, there are uncertainties on the luminosity and polarisation measurement as has been previously discussed. The uncertainties presented in table 8.3 are used for any cross section. For the total CC cross section, in addition, the luminosity error of 2% has been added in quadrature to the total systematic uncertainty. On the other hand the polarisation uncertainty has been used also for the total CC cross section as the uncertainty on the polarisation axis as will be discussed in section 9.1.

source	**uncertainty**	**effect on σ_{cc}**
hadronic scale	$\pm 2\%$	0.3%
noise subtraction	$\pm 10\%$	0.3%
trigger efficiency	$\pm 15\%(1-\mathcal{E}) \oplus Err^{sta}_{PsCC}$	1.39%
vertex efficiency	y dependent	2.3%
V_{ap}/V_p cut	± 0.02	0.3%
γp background subtraction	$\pm 30\%$	0.5%
NC background subtraction	$\pm 10\%$	$< 0.1\%$
other ep background subtraction	$\pm 10\%$	$< 0.3\%$
non-ep background finders	y dependent	2.1%
radiative corrections		0.8%
PDF acceptance		0.5%
total systematic uncertainty		$\approx 3.7\%$

Table 8.3: Effect of the systematic uncertainties on the CC cross section measurement for e^-p 2005 data.

Chapter 9

Results and Interpretation

In this chapter the CC cross sections measured in the collisions of longitudinally polarised electrons with the unpolarised protons in the H1 experiment are presented. The measurements are performed for both positive (RH) and negative (LH) electron polarisation. The *polarised CC cross sections* are obtained in the form of the total cross section σ_{cc}^{tot}, the differential cross sections $d\sigma_{cc}/dQ^2$ and $d\sigma_{cc}/dx$, and the double differential cross section $d^2\sigma_{cc}/dxdQ^2$.

In addition, two data sets having positive and negative polarisations are merged and corrected for the residual polarisation in order to obtain an unpolarised data set and to measure the *unpolarised CC cross sections*. The unpolarised data, with increased statistics, give a better insight into the proton structure and provide the possibility of the comparison to the HERA I results [25]. The measured cross sections are compared to the Standard Model predictions. In addition, the unpolarised CC data are used to extract the CC structure function F_2^{cc}. The measurement of the F_2^{cc} has been compared to the Standard Model prediction as well as to the previous CCFR and ZEUS results.

Part of the cross section results presented in this thesis are H1 preliminary results [130] the basis of a future official publication as it will be pointed out later.

9.1 Polarised Charged Current Cross Section

The polarisation dependence of the CC cross section is well defined within the Standard Model framework and is characterised by the CC cross section being directly proportional to the fraction of the LH electrons in the beam, i.e. by the absence of the RH weak currents. Therefore, the longitudinal electron polarisation P_e (see equation 2.60) at HERA provides the possibility for a new test of the Standard Model, more precisely its weak part, by measuring the polarisation dependence of the CC cross section.

9.1.1 The Polarisation Dependence of the Total CC Cross Section

In the year 2005 two CC data sets corresponding to LH and RH electron polarisations were collected by the H1 experiment (see chapter 7). These data sets are used to measure the total polarised CC cross sections for the two corresponding polarisation states. The measurements performed in the kinematic range $Q^2 > 400$ GeV^2 and $y < 0.9$ in this analysis lead to the following results:

$$\sigma_{cc}^{tot}(P_e = 37\%) = 34.5 \pm 1.4_{sta} \pm 1.5_{sys} \text{ pb} \tag{9.1}$$

$$\sigma_{cc}^{tot}(P_e = -27\%) = 70.9 \pm 1.3_{sta} \pm 3.0_{sys} \text{ pb} \tag{9.2}$$

where values labelled as *sta* and *sys* correspond to the statistical and the systematic uncertainty, respectively. The systematic uncertainty includes all uncertainties listed in table 8.3 as well as the absolute uncertainty of 2% on the luminosity measurement.

The measured CC cross sections for both electron helicity states together with the errors are shown in figure 9.1. The uncertainties on the polarisation measurement, which are 1.3% for the LH and 1.8% for the RH data, are shown on the x axis (P_e), but are not visible since they are smaller than the bullet size.

In order to get a more complete picture about the polarisation dependence of the total CC cross section the unpolarised HERA I cross section has been added to figure 9.1. Thus, the measurements of the total unpolarised CC cross sections, based on 16.4 pb^{-1} of e^-p data collected in years 1998-99, were recalculated in the same phase space:

$$\sigma_{cc}^{tot}(P_e = 0) = 57.0 \pm 2.2_{sta} \pm 1.4_{sys} \text{ pb.} \tag{9.3}$$

The measurements can be compared to the Standard Model expectations obtained using the parton density function based on the H1 PDF 2000 fit [40]:

$$\sigma_{cc}^{tot}(P_e = 37\%) = 35.7 \pm 0.4 \text{ pb} \tag{9.4}$$

$$\sigma_{cc}^{tot}(P_e = 0) = 56.7 \pm 0.6 \text{ pb} \tag{9.5}$$

$$\sigma_{cc}^{tot}(P_e = -27\%) = 72.0 \pm 0.8 \text{ pb.} \tag{9.6}$$

The uncertainty on the Standard Model expectations combines the uncertainties from the experimental data used in the H1 PDF 2000 fit as well as model uncertainties [40]. The results in figure 9.1 confirm a linear dependence of the total CC cross section on the longitudinal electron beam polarisation. For a fully RH electron beam with $P_e = +1$, the cross section is in agreement with zero as expected in the Standard Model.

A linear fit to the polarisation dependence of the total CC cross section is performed taking into account the correlated systematic uncertainties between the measurements. It is indicated in figure 9.1 by the line while its uncertainty is illustrated as the light band. The fit provides a good description of the data with $\chi^2 = 0.6$ for

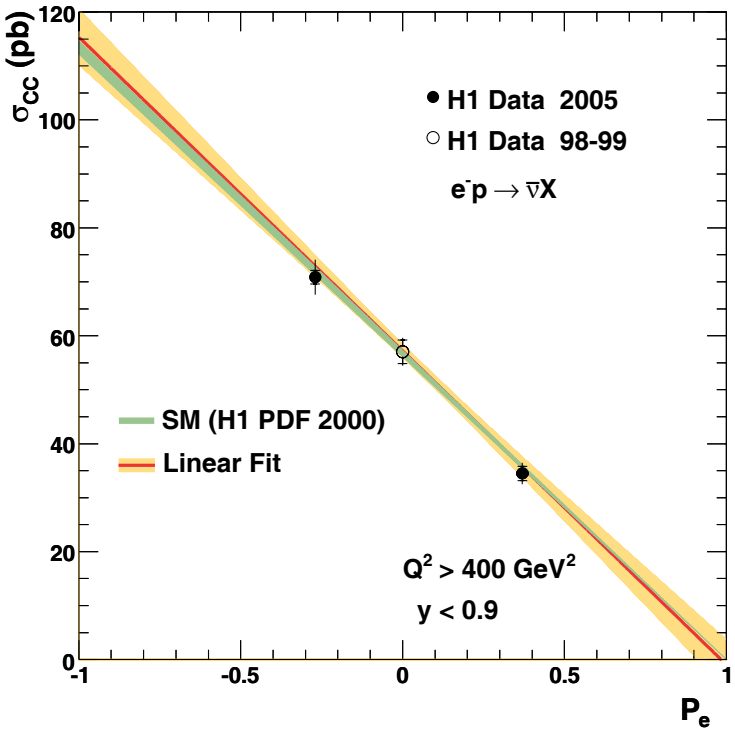

Figure 9.1: The total e^-p CC cross section σ_{cc}^{tot} (points) as function of the lepton beam polarisation P_e. The data are compared to the Standard Model prediction based on the H1 PDF 2000 fit (dark band). A linear fit to the data is shown as dark line with a shaded light band which corresponds to the error band. The statistical errors are indicated by the inner error bars, while the outer error bars show the total errors. The polarisation errors shown as uncertainty on the polarisation axis P_e can not be seen since they are smaller than the symbol sizes.

one degree of freedom. The cross section extrapolation to $P_e = +1$ for the measured e^-p CC cross section gives:

$$\sigma_{cc}^{tot}(P_e = +1) \quad = \quad -1.4 \pm 2.9_{sta} \pm 1.9_{sys} \pm 2.9_{pol} \text{ pb} \tag{9.7}$$

where the quoted errors correspond to the statistical (*sta*), systematic (*sys*) and polarisation related (*pol*) systematic uncertainties. The extrapolated cross section is consistent with the Standard Model prediction of a vanishing cross section for a fully RH electron beam. The corresponding upper limit on $\sigma_{cc}^{tot}(P_e = +1)$ is 7.6 pb. This result excludes the existence of RH CC mediated by a boson of mass $M(W_{RH}^-) < 189.5$ GeV at 95% confidence level [131], assuming Standard Model couplings and a massless right-handed ν_e.

It is also possible to fit the measured cross sections by fixing the cross section at $P_e = +1$ to zero. This yields a cross section at $P_e = 0$ of $\sigma_{cc}^{e^-p}(P_e = 0) = (57.16 \pm 1.1)$pb with $\chi^2/dof = 0.7$. As can be seen the fitted value agrees well with the Standard

Model expectation of (56.7 ± 0.6) pb.

All results on the measurement of the total polarised CC cross section performed by the H1 and the ZEUS collaboration together with the Standard Model prediction based on the H1 PDF 2000 fit are illustrated in figure 9.2. It can be seen that the polarisation dependence of the total CC cross section measured for the e^-p and e^+p data with the H1 and ZEUS detectors are in a good agreement.

The measured polarisation dependence of the CC cross sections from the HERA experiments is also in good agreement with the Standard Model which predicts the absence of the RH weak CCs, leading to vanishing CC cross sections for e^+p *at* $P_e = -1$ *and* e^-p *at* $P_e = +1$.

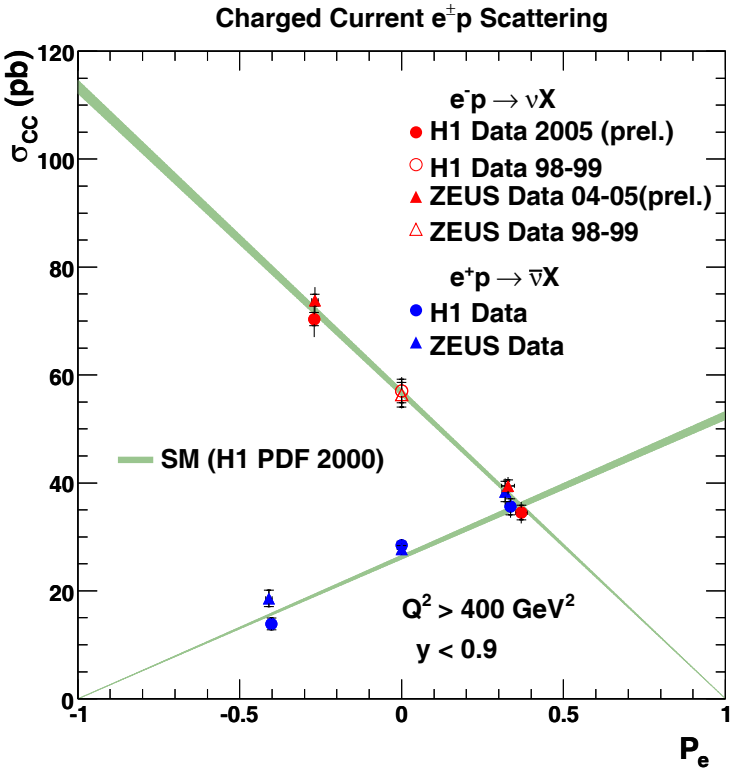

Figure 9.2: The total CC cross section σ_{cc}^{tot} as function of the lepton beam polarisation P_e, measured by the H1 and ZEUS collaborations for the e^-p and the e^+p data. The data are compared to the Standard Model prediction based on the H1 PDF 2000 fit (dark band). The statistical errors are indicated by inner error bars, while the outer error bars show the total errors. The polarisation errors shown as uncertainty on the polarisation axis P_e can not be seen since they are smaller than the symbol sizes.

9.1.2 The Q^2 Dependence of the Polarised CC Cross Section

The polarised single differential CC cross section $d\sigma_{cc}/dQ^2$ for the LH and the RH e^-p data is measured in the kinematic region $y < 0.9$. The cross section measurement is performed as a function of Q^2 only in bins which have the purity and the stability at least 30% (see figure 8.2). The results are compared with the Standard Model expectations based on the H1 PDF 2000 fit for the parton densities inside the proton and shown in figure 9.3. As can be seen, the LH and the RH cross sections are

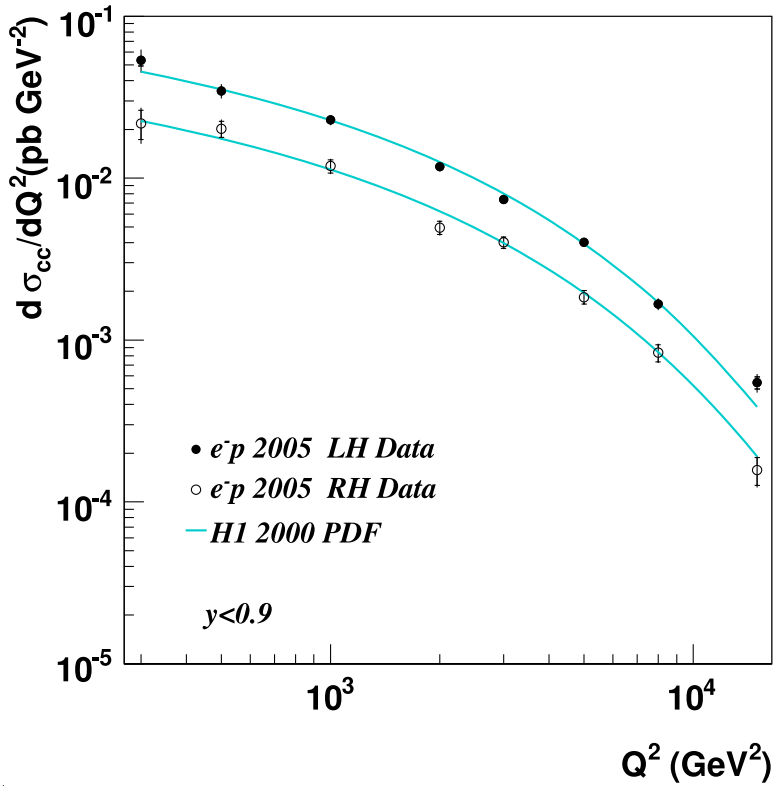

Figure 9.3: The polarised differential CC cross section, $d\sigma_{cc}/dQ^2$ as function of Q^2 measured for $y < 0.9$ is compared with the Standard Model expectation determined from the H1 PDF 2000. The statistical errors are indicated by the inner error bars, while the outer error bars show the total error. The 2% normalisation uncertainty is not included in the error bars.

different, as expected already from the total cross sections, due to dependence of the CC cross section on the electron polarisation P_e, (see section 2.8). Using equation 2.73 one can write the ratio of two cross sections at any level of differentiability as:

$$\frac{\sigma_{cc}^{LH}}{\sigma_{cc}^{RH}} = \frac{(1 - P_e^{LH}) \cdot \sigma_{cc}^{unpol}}{(1 - P_e^{RH}) \cdot \sigma_{cc}^{unpol}} \tag{9.8}$$

where P_e^{LH} and P_e^{RH} are polarisation of the LH and the RH CC data set, respectively, while σ_{cc}^{unpol} is the unpolarised CC cross section. Then, replacing the corresponding

polarisations by $P_e^{LH} = -0.27$ and $P_e^{RH} = 0.37$ in equation 9.8 gives the ratio of two cross sections:

$$\frac{\sigma_{cc}^{LH}}{\sigma_{cc}^{RH}} = \frac{1 + 0.27}{1 - 0.37} \approx 2 \tag{9.9}$$

nicely seen in figures 9.1 and also in 9.3. The CC cross sections $d\sigma_{cc}/dQ^2$ drop by a few orders of magnitude as a function of Q^2 due to the W boson propagator as well as due to the decreasing quark density at high x. Note that the high values of x correspond to the high values of Q^2.

The measured CC cross sections are well described by the theoretical expectation, based on the Standard Model (see figure 9.3). Only the measurement at the $Q^2 = 2000$ GeV^2 is observed to be low with respect to the Standard Model prediction in the RH data sample. This particular measurement has been carefully studied and no reason related to the detector performance has been found. The deviation is probably due to a statistical fluctuation.

The measured cross sections are listed in appendix tables B.1 and B.2 for both helicity states.

9.1.3 The x Dependence of the Polarised CC Cross Section

The polarised single differential CC cross section $d\sigma_{cc}/dx$ is measured for both helicities in the kinematic domain $Q^2 > 1000$ GeV^2 and $y < 0.9$. Only bins which have the purity and the stability above 30% (see figure 8.3) are used to measure the x dependence of the polarised cross section. The theoretical prediction evaluated using the H1 PDF 2000 fit describes the measured cross sections for the LH and the RH data sets well within the errors as illustrated in figure 9.4. The cross sections rise towards lower x is a consequence of the sea quark contribution to the proton structure as will be discussed in subsection 9.2.3. At the very low x a decrease of the Standard Model expectation curve takes place due to a chosen phase space.

The experimental results together with the statistical and systematic errors for the LH and the RH data samples are given in appendix tables B.3 and B.4, respectively.

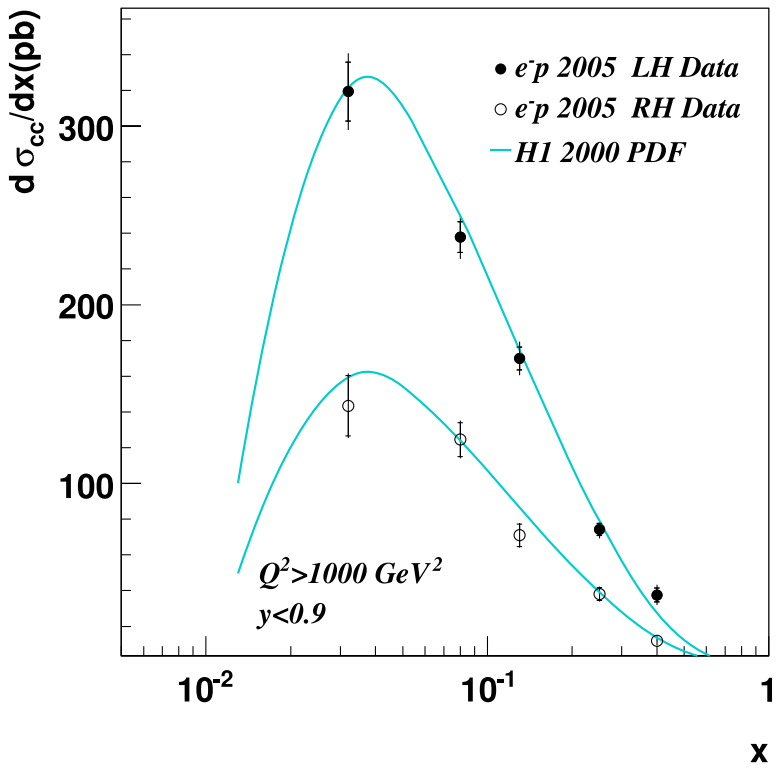

Figure 9.4: The polarised CC cross section, $d\sigma_{cc}/dx$ as function of x compared to the Standard Model expectation, determined from the H1 PDF 2000 fit. The statistical errors are indicated by inner error bars, while the outer error bars show the total error. The 2% normalisation uncertainty is not included in the error bars.

9.1.4 Polarised Double Differential CC Cross Section

The polarised double differential CC cross section $d^2\sigma_{cc}/dxdQ^2$ is measured in the kinematic domain of $300 < Q^2 < 25000$ GeV^2 and $0.008 < x < 0.65$. The differential cross section is presented in form of the reduced cross section $\bar{\sigma}_{cc}$ (see section 8.2 for details). The measurements of the reduced cross sections are performed only at values of x and Q^2 given in table 8.1 which have the acceptance and the purity at least 30% as indicated in figures 8.4 and 8.5 for the two data sets.

The reduced cross section at different Q^2 values as functions of x together with the theoretical expectations are displayed in figures 9.6 and 9.5 for the LH and the RH data sample, respectively.

As can be seen from figures 9.5 and 9.6, the measured reduced CC cross sections for the LH and the RH data are well described by the Standard Model. Corresponding values of the measured cross section for both electron helicity states are given in appendix tables B.5 and B.6.

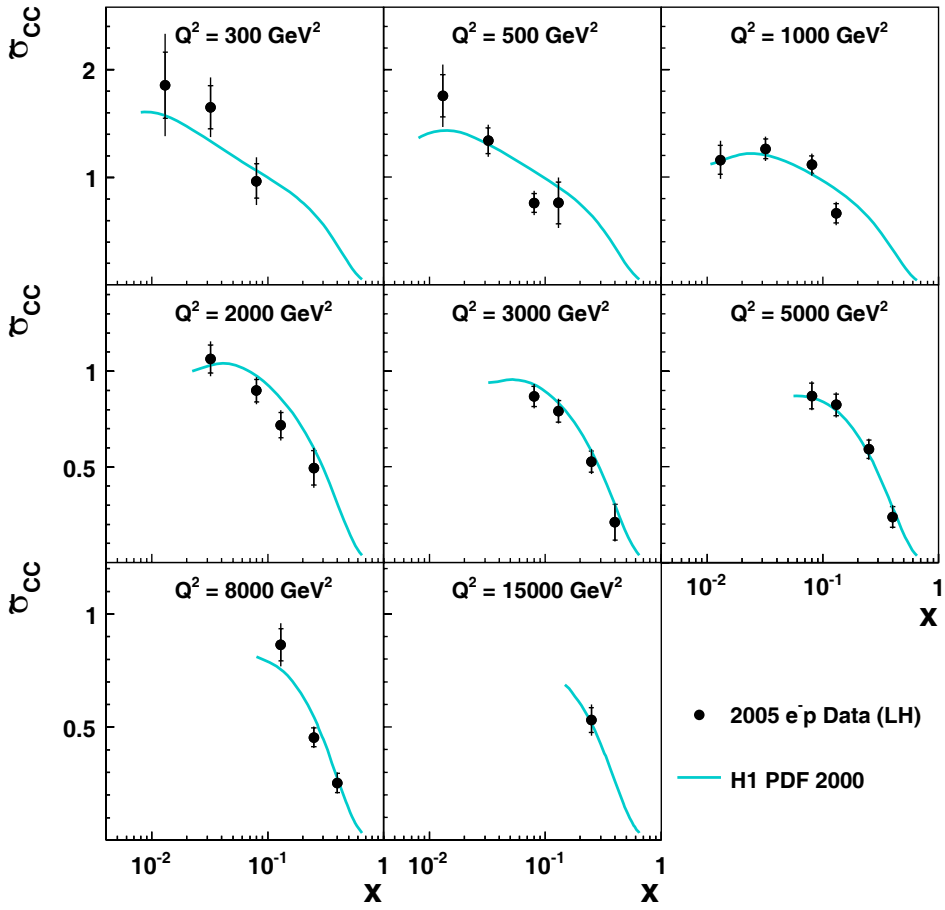

Figure 9.5: The reduced polarised CC cross section $\tilde{\sigma}_{cc}$ for the LH data sample as a function of x at fixed values of Q^2 and the Standard Model prediction based on the H1 PDF 2000 fit are shown. The statistical errors are indicated by the inner error bars, while the outer error bars show the total error. The normalisation uncertainty of 2% is not shown in the error bars.

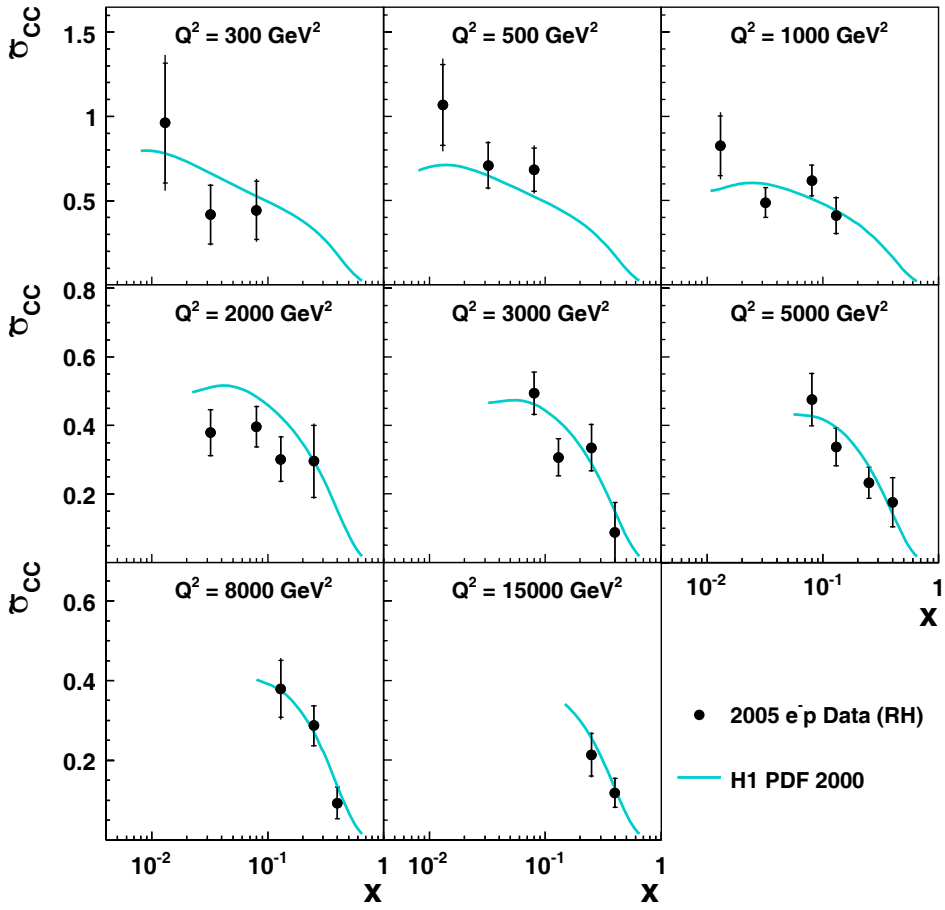

Figure 9.6: The reduced polarised CC cross section $\bar{\sigma}_{cc}$ measured for the RH data sample as a function of x at fixed values of Q^2 and the Standard Model prediction based on the H1 PDF 2000 fit are shown. The statistical errors are indicated by the inner error bars, while the outer error bars show the total error. The normalisation uncertainty of 2% is not shown in the error bars.

9.2 Unpolarised Charged Current Cross Sections

As has been discussed already in section 9.1, the measurement of the total CC cross section as a function of polarisation gives a new experimental insights into the weak interactions, confirming the electroweak Standard Model expectation. In particular, the polarised differential CC cross sections at any level of differentiability are reasonably well described by the theory prediction. This fact gives the possibility to merge the LH and the RH data in order to obtain the unpolarised HERA II CC data sample and make an additional step in the cross section measurement.

The increased statistics of the unpolarised HERA II CC data has several advantages:

- The unpolarised data gives the possibility to compare these results to the previous HERA I measurement.
- At HERA I [25] the collected integrated luminosity was only 16.4 pb^{-1}, while at HERA II (2005) the collected integrated luminosity is 98.2 pb^{-1}. It means that the electron data can be looked in with the highest possible precision since the HERA start in 1992.
- Increased statistics will give a better insights into the quark content of the proton.
- The unpolarised e^-p CC data together with the previously taken unpolarised e^+p CC data can be used to extract the CC structure function F_2^{cc}.

The unpolarised HERA II CC data sample is derived by merging the LH and the RH data sets. In this way the *residual polarisation* of $P_{res} = -7.7\%$ has been obtained as:

$$P_{res} = \frac{P_{LH} \cdot L_{\text{L}} + P_{RH} \cdot L_{\text{R}}}{L_{\text{L}} + L_{\text{R}}}. \tag{9.10}$$

Here $P_{LH}(P_{RH})$ is the mean polarisation of the LH (RH) data weighted by the corresponding luminosities and $L_{\text{L}}(L_{\text{R}})$ is the integrated luminosity of LH (RH) sample (see table 7.4). Finally, the measured cross section is corrected for the residual polarisation in order to obtain the unpolarised measurement.

The unpolarised differential cross sections are measured in bins which satisfy the quality criteria similarly to the polarised data sets i.e. the purity and the stability are required to be at least 30% (see section 8.3).

9.2.1 The Q^2 Dependence of the Unpolarised CC Cross Section

As for the polarised cases, the Q^2 dependence of the unpolarised CC cross section $d\sigma_{cc}/dQ^2$ is measured in the kinematic region of $y < 0.9$. The results together with

the Standard Model CC cross section prediction determined using the H1 PDF 2000 are shown in figure 9.7 (a). The ratio of the measured to the Standard Model cross sections in figure 9.7 (b) shows that data are well described by the theory expectation.

The measured unpolarised CC cross section at different values of Q^2 together with the uncertainties is given in appendix table B.7.

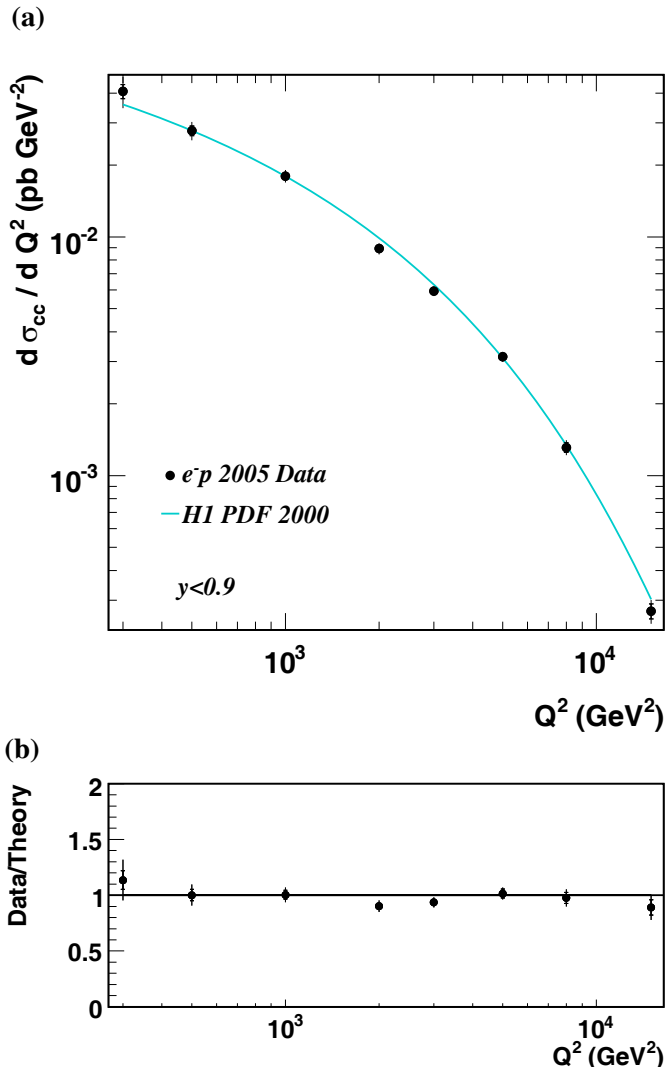

Figure 9.7: The Q^2 dependence of the unpolarised CC cross section, $d\sigma_{cc}/dQ^2$ and the Standard Model expectation determined from the H1 PDF 2000 fit (a). The ratio of measured cross section to the theoretical prediction based on the H1 PDF 2000 fit (b). The statistical errors are indicated by inner error bars, while the outer error bars show the total error. The normalisation uncertainty of 2% is not included in the errors.

A comparison of the e^-p CC cross sections based on the data collected in year 2005 and the e^+p CC cross sections based on the data taken in period 2003-2004 from the H1 preliminary results [130] are shown in figure 9.8. As has been discussed in sub-

section 2.8.1 due to coupling to the different quark flavours and helicity dependence, the e^-p CC cross section is higher 6 times compared to the e^+p CC cross section. However, this difference is not fixed and depends on Q^2 as can be nicely seen in figure 9.8. At low Q^2 the difference between two cross sections is a factor of about 2-3 while at high Q^2 it is about a factor of 10. This gives an additional Q^2 dependent factor to the counting factor 6 previously discussed. The reason lies in the see quark contribution which dominates at low Q^2 (low x), and it is about the same in e^-p and e^+p. Approaching the larger values of the Q^2 the valence quark contribution becomes more and more important and in the end the dominant one (see figure 9.8), resulting in the higher e^-p CC cross section with respect to the e^+p CC cross section.

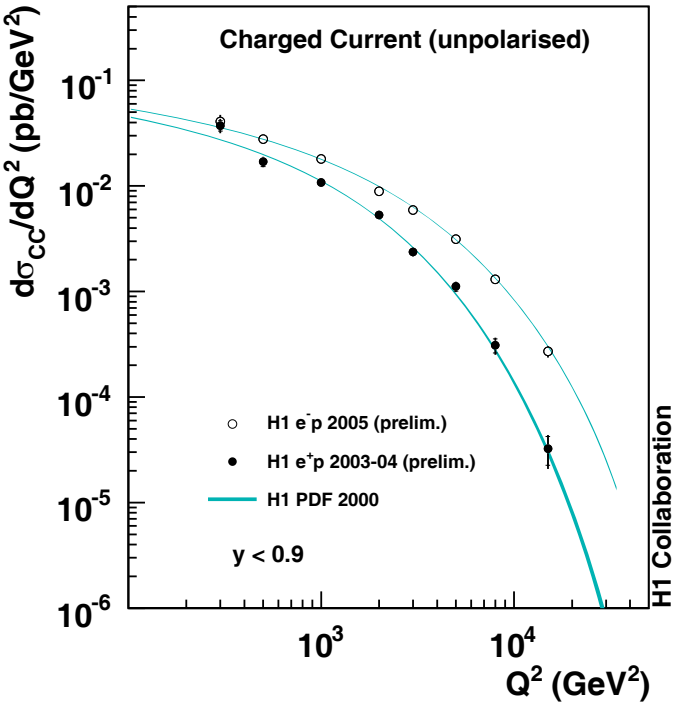

Figure 9.8: Comparison of the Q^2 dependence of the e^-p and e^+p unpolarised CC cross sections, $d\sigma_{cc}/dQ^2$. The experimental results are compared to the Standard Model expectation determined from the H1 PDF 2000 fit. The statistical errors are indicated by the inner error bars, while the outer error bars show the total error. The normalisation uncertainty of 2% for the e^-p data and 1.3% for the e^+p data is not included in the errors.

9.2.2 The x Dependence of the Unpolarised CC Cross Section

The x dependence of the unpolarised CC cross section $d\sigma_{cc}/dx$ is measured in the same kinematic region as the polarised cross sections corresponding to $Q^2 > 1000$ GeV^2 and $y < 0.9$. The experimental results compared to the Standard Model can be seen in figure 9.9 (a). From the ratio of two cross section shown in figure 9.9 (b) can be seen that data are described well by the Standard Model expectation based on the H1 PDF 2000 fit.

The measurements together with the uncertainties are listed in appendix table B.8.

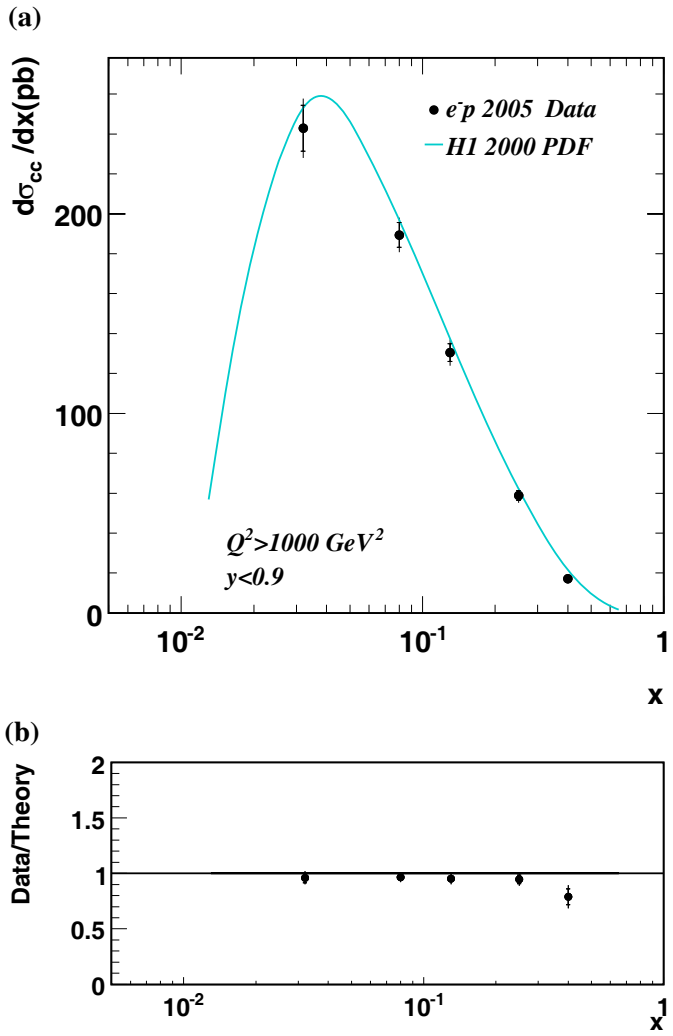

Figure 9.9: The x dependence of the unpolarised CC cross section $d\sigma_{cc}/dx$ together with the Standard Model expectation determined from the H1 PDF 2000 fit (a). The ratio of measured cross section to the theoretical prediction based on the H1 PDF 2000 fit (b). The statistical errors are indicated by inner error bars, while the outer error bars show the total error. The normalisation uncertainty of 2% is not included in the errors.

9.2.3 The Unpolarised Double Differential CC Cross Section

The unpolarised reduced CC cross sections $\bar{\sigma}_{cc}$ is measured in the same phase space as the polarised one, i.e. $300 < \mathrm{Q}^2 < 25000$ GeV^2 and $0.08 < x < 0.65$. The results compared to the theoretical expectations are shown in figure 9.10. As it can be seen from the ratio of the measured to the Standard Model cross sections shown in figure 9.11 the expectation from the H1 PDF 2000 fit is found to give a very good description of the measured CC cross section.

The results obtained together with the uncertainties are given in appendix table B.9.

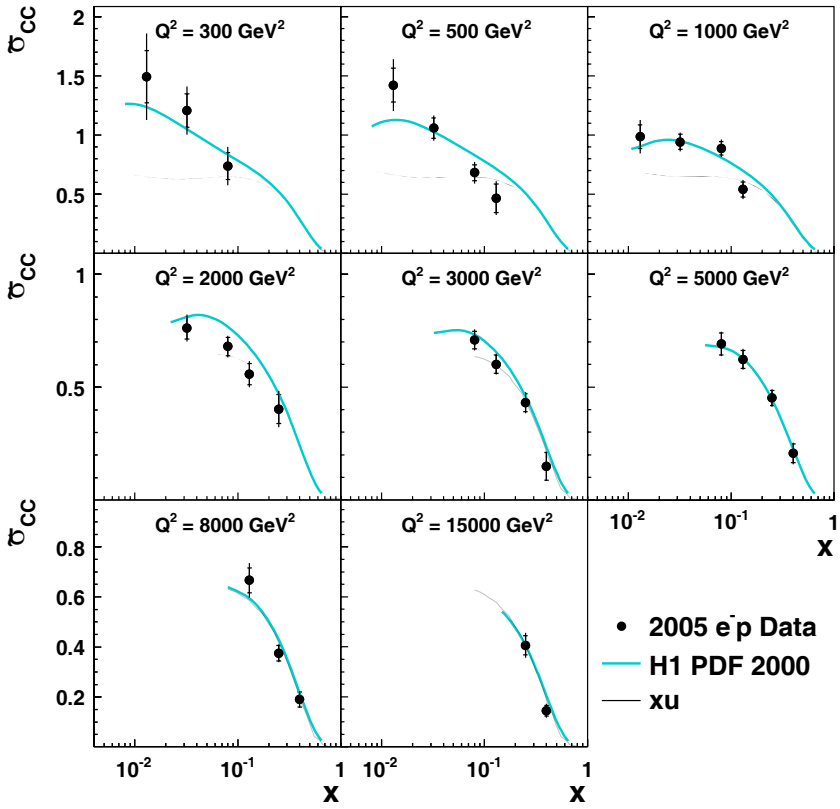

Figure 9.10: The reduced unpolarised CC cross section measured as a function of x for eight different values of Q^2 for 2005 data (points) for e^-p scattering. The data are compared to the Standard Model prediction based on the H1 PDF 2000 fit (light line). The dark curve represents the u quark density. The statistical errors are indicated by the inner error bars, while the outer error bars show the total error. The normalisation uncertainty of 2% is not included in the errors.

The unpolarised CC cross sections can be used to obtain the u quark density. It is well known that precise knowledge of u quark distribution can be obtained from the

NC events since the u quark dominates over the contribution from the d quark in NC interactions due to its charge and its larger contribution to the structure function. However, it is still very interesting to have a look into the u quark distribution from e^-p interactions as an independent check, with the best possible statistics of the HERA CC data up to now. This can be done using the reduced cross section $\bar{\sigma}_{cc}$ which at a first order in QCD for $e^-p \to \nu_e X$ depends directly on the quark density distribution as:

$$\bar{\sigma}_{CC}(e^-p) = x[u + c + (1-y)^2(\bar{d} + \bar{s})]. \tag{9.11}$$

The fact that at high x the contribution from the sea is small leads to the following expression of the cross section:

$$\bar{\sigma}_{CC} \approx xu. \tag{9.12}$$

Thus, it is used to constrain the valence u quark distribution at high x and high Q^2.

Figure 9.10 also shows the expected contribution from the u quark which is dominating in the e^-p CC cross section for high x and Q^2. The observed rise of the cross section towards low x is understood as the contribution of the sea quarks. The result from HERA II together with the unpolarised CC cross section from the HERA I, obtained in 1998-1999, is displayed as a function of x for different Q^2 values in figure 9.12. The HERA I and HERA II results are, within the errors, in a reasonable agreement with each other. One should note that the HERA II unpolarised CC data are based on a 6 times larger statistics than HERA I.

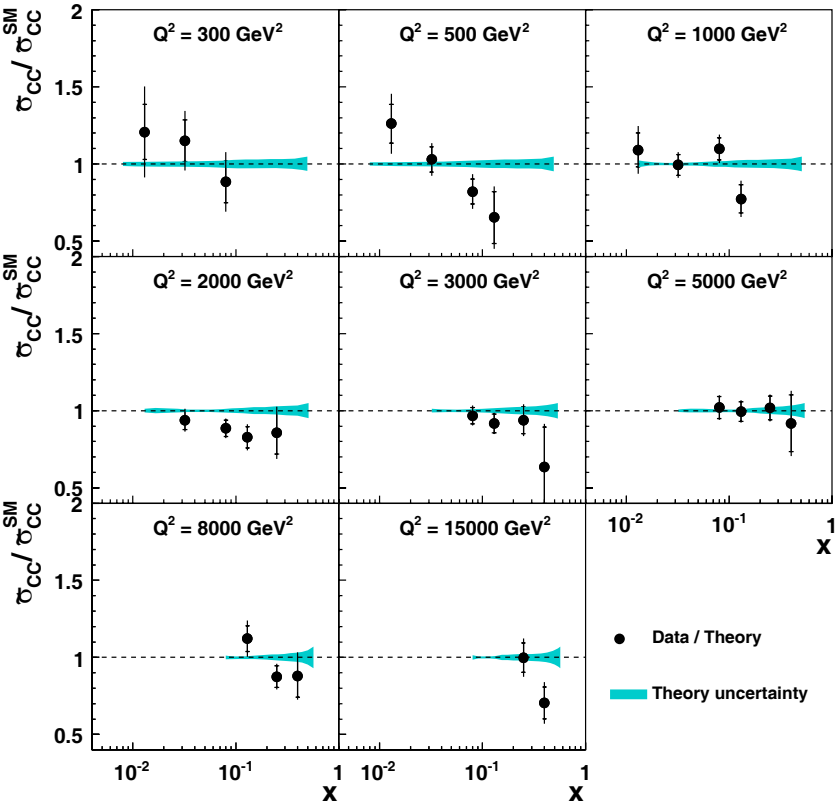

Figure 9.11: The ratio of the measured reduced polarised CC cross sections for 2005 e^-p data to the Standard Model expectation using the H1 PDF 2000 fit as a function of x for eight different values of Q^2. The shadowed band around 1 shows the Standard Model uncertainty. The statistical errors are indicated by the inner error bars, while the outer error bars show the total error. The normalisation uncertainty of 2% is not included in the errors.

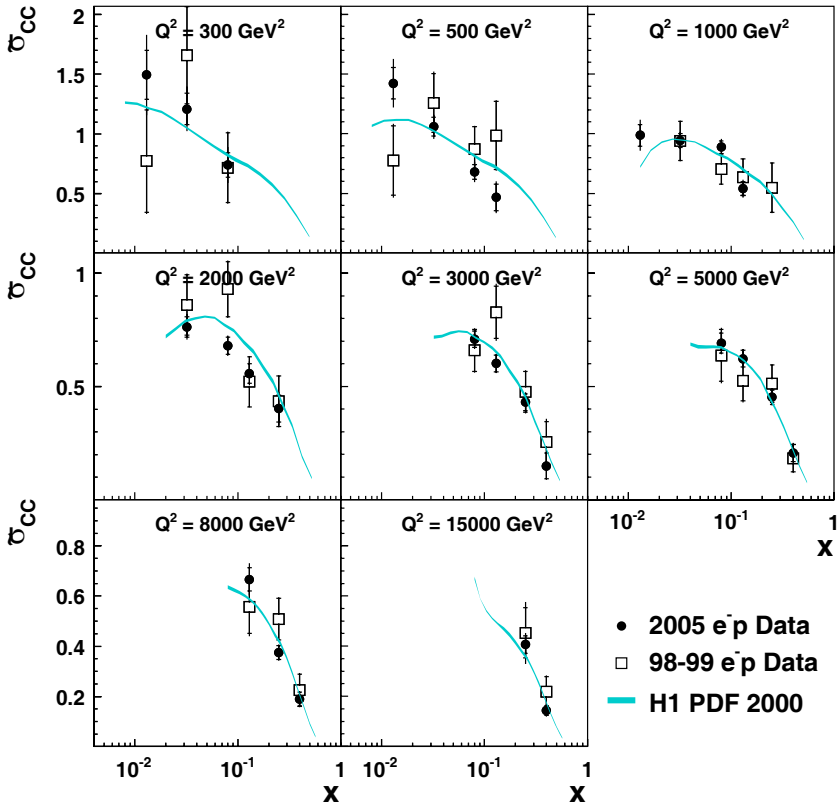

Figure 9.12: The measured unpolarised reduced CC cross sections for 2005 data (points) taken during HERA II phase and 1998-99 data (squares) taken during HERA I phase, compared to the Standard Model expectation using the H1 PDF 2000 fit. The cross sections are shown as a function of x for eight different values of Q^2.The statistical errors are indicated by the inner error bars, while the outer error bars show the total error. The normalisation uncertainty of 2% is not included in the errors.

9.3 Extraction of the Charged Current Structure Function F_2^{cc}

As it has been mentioned in chapter 2 the structure functions data have been playing an important role in the understanding of the structure of matter and QCD. The CC structure function F_2^{cc} has been measured in the neutrino-nucleon scattering experiments as the sum of ν_μ and $\bar{\nu}_\mu$ cross sections. It is therefore interesting to compare the measured structure function F_2^{cc} from H1 with the results obtained in the neutrino-nucleon scattering experiment (CCFR).

The CC DIS double differential cross section is defined by three structure functions $F_2^{cc\pm}$, $xF_3^{cc\pm}$ and $F_L^{cc\pm}$ (see equation 2.64). However, in the major part of the kinematic domain the contribution of the proton structure function $F_2^{cc\pm}$ is dominant, while $xF_3^{cc\pm}$ and $F_L^{cc\pm}$ have much smaller contributions. Therefore, the CC structure function F_2^{cc} can be extracted from the e^+p and e^-p data. In this analysis the unpolarised e^-p 2005 data are combined with the previous unpolarised e^+p data collected in 2003-04. The unpolarised data are used in order to compare to results obtained from the CCFR and ZEUS experiments and also to gain higher statistics. The CC structure function F_2^{cc} is related to the sum of the e^+p and the e^-p differential cross sections in the following way [132]:

$$F_2^{cc} = F_2^{cc+} + F_2^{cc-} \tag{9.13}$$

$$= \frac{4\pi x}{G_F^2}\left[\frac{Q^2+M_F^2}{M_F^2}\right]^2 \frac{1}{Y_+}\left(\frac{d^2\sigma_{cc}^{e^+p}}{dxdQ^2} + \frac{d^2\sigma_{cc}^{e^-p}}{dxdQ^2}\right) + \Delta(xF_3^{cc}, F_L^{cc}). \tag{9.14}$$

Using the reduced cross sections, the CC structure function F_2^{cc} is extracted as:

$$F_2^{cc} = \frac{2}{Y_+}(\bar{\sigma}_{cc}^- + \bar{\sigma}_{cc}^+) + \Delta(xF_3^{cc}, F_L^{cc}). \tag{9.15}$$

Here $\Delta(xF_3^{cc}, F_L^{cc})$ represents a correction term that takes into account the xF_3^{cc} and the F_L^{cc} structure functions which contribution is small with respect to F_2^{cc}. The correction term is defined as:

$$\Delta(xF_3^{cc}, F_L^{cc}) = \frac{Y_-}{Y_+}(xF_3^{cc+} - xF_3^{cc-}) + \frac{y^2}{Y_+}(F_L^{cc+} - F_L^{cc-}). \tag{9.16}$$

The value of the correction term $\Delta(xF_3^{cc}, F_L^{cc})$ is obtained using the H1 PDF 2000 fit [25]. The dominant uncertainty on the structure function measurement is statistical. The systematic uncertainty is determined in the following way:

- the correlated errors in e^-p and e^+p measurements are treated as correlated between two measurements;
- the uncorrelated errors in e^-p and e^+p measurements are treated as uncorrelated;

- the luminosity errors, which are 2% for e^-p and 1.3% for e^+p data, are assumed to contain correlated and uncorrelated components. The correlated component is taken to be 0.5%.

The H1 measurement of the structure function F_2^{cc} is performed for the following values of $x = 0.013, 0.032, 0.08, 0.13, 0.025, 0.40$ as a function of Q^2. The measurement in the highest $x = 0.65$ bin is not performed due to absence of the e^+p CC measurement in this kinematic region. The obtained results are shown in figure 9.13 in comparison with the Standard Model expectation based on the H1 PDF 2000 fit. The data are well described by the expectation. The measured F_2^{cc} structure function, together with the correction term, statistical, systematic and the total error are given in table B.10. From table it can be seen that the correction term is smaller than the uncertainties on the measurement for low values of Q^2, but becomes important at higher values of Q^2.

The measurement of the CC structure function F_2^{cc} obtained in this analysis has been compared to results obtained by the ZEUS and CCFR experiments. However, these experiments perform the measurement of F_2^{cc} at different values of x and Q^2. Therefore, in order to make the comparison it was necessary to correct the measurements from other experiments and to "move" values in x, while keeping the Q^2 dependence. The measured cross section for CCFR (ZEUS) ($F_2^{cc,meas}(x_{old}, Q^2)$, moved to the closest value of x where H1 measurement is performed ($F_2^{cc,meas}(x_{H1}, Q^2)$), is obtained using the H1 PDF 2000 fit in the following way:

$$F_2^{cc,meas}(x_{H1}, Q^2) = F_2^{cc,meas}(x_{old}, Q^2) f^{cc,corr} \tag{9.17}$$

$$\tag{9.18}$$

where x_{H1} and x_{old} stands for the value of x used in H1 and CCFR (ZEUS), respectively. The correction factor $f^{cc,corr}$ has been calculated as:

$$f^{cc,corr} = \frac{F_2^{cc,th}(x_{H1}, Q^2)}{F_2^{cc,th}(x_{old}, Q^2)} \tag{9.19}$$

where $F_2^{cc,th}(x_{H1}, Q^2)$ and $F_2^{cc,th}(x_{old}, Q^2)$ represent the theoretical cross sections obtained at value of x used in H1 and that used in CCFR (ZEUS). The statistical and systematic uncertainties are corrected in the same way as the structure function (see equation 9.19) to the values of x at which the H1 measurements have been performed.

The corresponding results for F_2^{cc} measured by the ZEUS collaboration [132, 133] are also shown in figure 9.13. The H1 and ZEUS results are consistent and are well described by the Standard Model prediction evaluated using the H1 PDF 2000 fit. The measurements of the CC structure function F_2^{cc} determined by the H1 and ZEUS experiments provide complementary measurement of the structure function obtained at a fixed target neutrino scattering experiment, CCFR [134, 135], thus extending the measurement to a significantly higher Q^2 region. The fixed target results from the $\nu_\mu Fe$ interactions measured by the CCFR collaboration, after correcting for 5.6% due

to the non-isoscalar target effects (see [134]), are also shown in figure 9.13. Note that these CCFR results have shown very good agreement with the results obtained by the NuTev collaboration [136]. As can be seen the prediction gives reasonable description of the experimental results. However none of the measurements, i.e. the new H1, ZEUS or CCFR have been used in the H1 PDF 2000 fit which is based on the H1 data taken at HERA I.

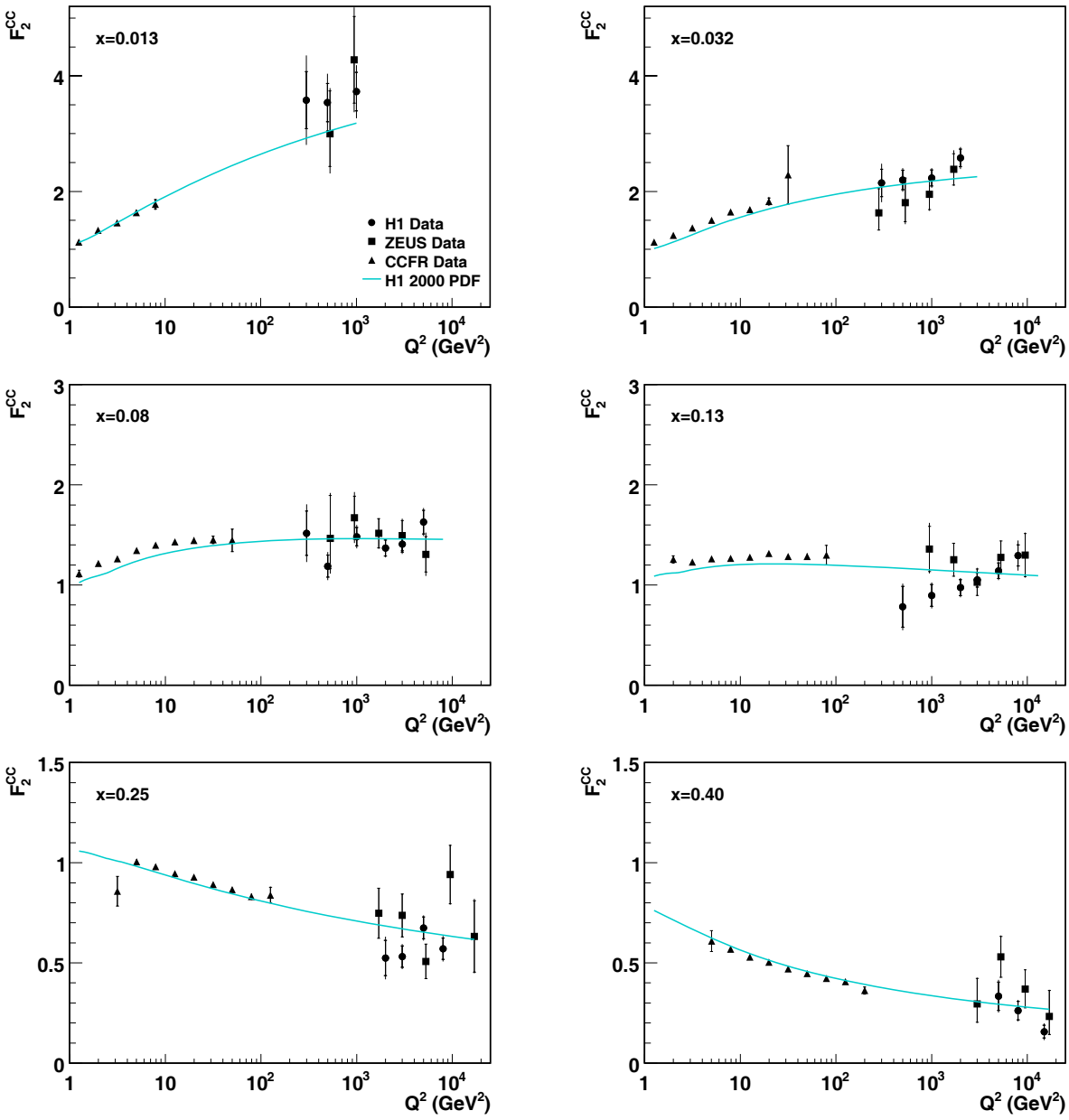

Figure 9.13: The structure function F_2^{CC} as a function of Q^2 for different values of x extracted from H1 data (solid points) compared to CCFR measurements corrected for non-isoscalar target (triangles) and the ZEUS data (boxes). The expectation of the Standard Model is based on the H1 PDF 2000 fit and shown as a solid line. The luminosity uncertainties of 2% for the e^-p data and 1.3% for the e^+p data are included in the systematic errors. The statistical errors are indicated by the inner error bars, while the outer error bars show the total errors.

Chapter 10

Summary and Outlook

In this thesis the first measurements of the e^-p Charged Current Deep Inelastic Scattering (CC DIS) cross sections with longitudinally polarised electrons have been presented. The measurements were performed using the data taken by the H1 detector at HERA in the year 2005. In total 68.6 pb^{-1} luminosity of left-handed polarised e^-p data, corresponding to an average polarisation of $P_e = (-27 \pm 1.3)\%$ and 29.6 pb^{-1} luminosity of right-handed polarised e^-p data, corresponding to an average polarisation $P_e = (+37 \pm 1.8)\%$ have been collected and used in the present analysis.

Special emphasis has been put out on the studying of the LAr trigger performance at the HERA II as the main trigger system for the high Q^2 events taken with the H1 detector. Based on online monitoring and offline data analysis during the period 2002-2005 the trigger has shown very good performance. In addition, the possible improvements in the trigger rate reduction for the coming data taking period in 2006-07 have been described.

All aspects necessary for the cross section measurement have been discussed in detail. Since the precision of the cross section extraction relies on the correct MC simulation it was ensured that the simulation describes the data in every respect leading to the following results:

- **The polarisation dependence of the total e^-p CC DIS cross section**
  The first measurement of the e^-p CC DIS cross section as a function of the polarisation has been performed in the kinematic domain of $Q^2 > 400$ GeV^2 and $y < 0.9$. The measured cross sections for both helicity states are in a good agreement with the expectations from the Standard Model based on the H1 PDF 2000 fit and confirm a linear dependence of the total CC cross section on the electron beam polarisation.

- **Limit on the mass of a hypothetical right-handed boson W_R**
  A linear fit to the polarisation dependence of the total e^-p CC DIS cross section has been performed taking into account the correlated systematic uncertainties between the measurements. The CC DIS cross section extrapolated to $P_e = +1$ is found to vanish, consistent with the Standard Model expectation. This

excludes the existence of weak CC mediated by a hypothetical right-handed W_R boson with a mass below 189.5 GeV at the 95% confidence level.

- **Polarised differential cross sections $d\sigma_{cc}/dQ^2$, $d\sigma_{cc}/dx$, $d^2\sigma_{cc}/dxdQ^2$**
  In addition to the total CC cross section, the single differential cross sections $d\sigma_{cc}/dQ^2$ and $d\sigma_{cc}/dx$ have been measured for the left-handed and the right-handed electron polarisation as well. While $d\sigma_{cc}/dQ^2$ has been measured for $y < 0.9$, $d\sigma_{cc}/dx$ has been measured for $Q^2 > 1000$ GeV^2 and $y < 0.9$. The measurements of the double differential cross section $d^2\sigma_{cc}/dxdQ^2$ in the kinematic range $300 < Q^2 < 25000$ GeV^2 and $0.08 < x < 0.65$ for both helicity states have been performed as well. The Standard Model prediction is found to give good description of the all obtained differential cross sections.

- **Unpolarised single and double differential cross sections**
  The left-handed and the right-handed data sets have been combined and corrected for the remaining residual polarisation in order to obtain an unpolarised data set. The unpolarised data makes it possible to have a look into the e^-p data collected by the H1 detector with the highest possible statistics since the HERA start in 1992. The Standard Model expectation which is based on the parton density functions from the H1 PDF 2000 fit has shown good agreement with the measured cross sections over the entire phase space.

- **Extraction of the valence u quark distribution**
  Using the higher statistics of the unpolarised e^-p CC DIS, the *valence u quark* distribution at high x and high Q^2 has been extracted.

- **Charged Current Structure Function F_2^{cc}**
  The unpolarised e^-p and e^+p double differential cross sections from HERA II have been used in order to extract the CC structure function F_2^{cc}. The theoretical expectation based on the H1 PDF 2000 fit gives good description of the measured structure function. Additionally, these results are compared to the corresponding results of the CC $\nu_\mu Fe$ and $\bar{\nu}_\mu Fe$ interactions from CCFR and to $e^\pm p$ the ZEUS measurements obtained at HERA I.

These results together with the measurement of the e^+p CC DIS cross section performed in 2003-2004 confirm the absence of right-handed weak currents as expected in the Standard Model. Additionally, together with the previous and currently taken data, the results presented in this thesis will be used for a general QCD fit which will give a better constraint on the parton distribution functions in the proton and even more, an improved understanding of perturbative QCD.

Appendix A

LAr Trigger Data Quality Checks

Details of the data quality checks concerning the LAr trigger performance in 2002-05 are presented in this chapter. First, the readout and simulation of the LAr trigger as the basis for the data quality checks are introduced. They are followed by an offline the data quality analysis, where the internal consistency of the LAr trigger is checked as well as the comparison to the other trigger systems.

A.1 Trigger Readout

During the actual data taking the information produced by the LAr trigger is stored in local pipelines. When an event is triggered the pipelines are stopped and the information is transferred after passing all trigger levels, to permanent storage media. For detailed checks of the timing in the LAr trigger system the information is read out not only for the bunchcross where the interaction happened but also for 4 BC's before and after the interaction BC. So all nine BCs are read out for each quantity in the LAr chain. The readout of the LAr calorimeter is composed of three different and independent parts (see figure 3.1): FADC ("ADC"), Adder tree (trigger elements "RAM") and CTL read out. While "ADC" and "RAM" are read out by the LAr system itself, the CTL reads independently the trigger elements ("RAM") produced in the LAr trigger system. The independent and different readouts open up possibilities for checking the internal consistency of the LAr trigger operation and provide the information for a detailed comparison with simulations of the hardware operation.

A.2 Trigger Simulation

A powerful tool to check the proper operation of the hardware is the detailed simulation of the essential functions of the electronics. The simulation is divided into two major parts: a simulation of the analog electronics and a simulation of the digital electronics. The simulation of the analog part is done using real data from calorimeter cells as input. The goal is rebuilding the analog signal path. The simulation starts

with the summing of the geometrical pad energies to trigger cell energies which are used as input to the simulation chain. Then the calorimeter TC energies are summed up into TTs. This value is then shaped in the proper way to simulate a sinus-shaped signal with a width of about 9 BC's for the positive part. After that the noise simulation is done. A noise pulse height is selected from a spectrum proportional to the detector capacity corresponding to the TT. The time of the maximum BC is at random , since thermal electronic noise is a random process. The TT signal including the noise is then passed to the simulation of the AGM where the pulse is compared to a threshold specific for a given TT. Next, the discriminated TT signals are summed up into BTs. The final step of the analog simulation of the energy signal is the digitisation process where the $1\mu s$ pulse is converted to 8 bit numbers at 9 points, 96 ns apart (BCs). This conversion takes account of the correct calibration. Besides the energy signals also the $t0$ bits are simulated, where first the sums of EM and HAD parts are computed for all TTs for all nine BCs. In case that the amplitude in the nominal interaction BC is higher than a corresponding threshold, the $t0$ bit is set for the BT.

With all digital information ($t0$ bits and FADC counts) generated, the simulation of the digital part starts. It is based on the recalculation of the global quantities, starting from the FADC input values. The recalculation is done for all nine BCs and takes into account all lookup tables and thresholds for the digital summing loaded into the hardware. One should note, however, that the calculation of the lookup tables loaded into the hardware is done by a dedicated online computer connected to the hardware. In the simulation other types of processors are used (typically PC's) which usually have different ways of doing the floating point arithmetic and the float to integer conversion. One therefore has to be prepared to see sometimes (small) differences in the comparison of simulated and actual lookup tables.

The basic simulation package of the LAr trigger is TTOOL [137] which contains the complete simulation of the analog and digital parts. More details are given in section A.4.

A.3 An Charged Current Event in the LAr trigger

An example of the detailed trigger information for one event, on which the diagnostics study has been based, is given in table A.1. It contains FADC energies, BT bits, adder tree quantities (see subsection 3.6.2.1 and A.4), trigger elements and subtriggers fired for the given event.

The event dump is composed of three parts: the FADC section, the adder tree section and the CTL section. The FADC energies are printed for nine bunch-crosses (BC), i.e. the central BC when interaction actually occurs, four BCs before and four BCs after (labelled from -4 to +4) the time of interaction. The FADCs are grouped into different topological regions of the detector IF, FB and CB (see section 3.4.2). Furthermore, the BTs are marked which are associated with a $t0$ bit or are identified as

"electrons": The different BT bits are combined for each bunch cross in the following way: $1000 * t0$ bit + 10∗electron1 bit + electron2 bit. As discussed in the hardware section 3.6.2.1, a certain energy threshold has to be passed for the BT in order to set an electron or $t0$ bit. While the electron bits stay on as long the energy is above threshold, the $t0$ bit should be on (by construction) for only one bunch cross to uniquely flag the time of interaction.

In addition to the FADCs, the adder tree values calculated by the hardware are printed out: the topological sums, the global sums, the number counters for the bit quantities, and the trigger elements (TEs). The topological sums are formed from the FADC energies which are deposited in the various calorimeter regions (IF, FB, CB). Each region is divided into 4 quadrants, labelled for example as CBQ0, CBQ1, CBQ2, CBQ3. Note that a simple summing of the FADC energies in the corresponding areas will not give the exact sum in adder tree quantities. This is because the FADC energies from the EM and HAD parts are weighted in the hardware by look-up tables and then added to the total energy sums. Furthermore, the weighted BTs are discriminated against individual thresholds before the summing to cut out noise. So a BT may not contribute at all to the sums after the weighting and thresholding. The sums are finally compared to three thresholds, building up the trigger elements. The discriminating quantities of each TE are encoded in two bits providing different thresholds which are sent to the CTL and to the L2NN and L2TT trigger systems at the second trigger level. These are: topological sums, global sums and BT counters. At the same time they are simulated using the FADC energies. They have to be in agreement with each other as demonstrated in event A.1.

In the program developed here the results of the trigger simulations were used in the form of the data field READDER provided by TTNT [137], where the adder tree quantities were recalculated on the basis of all FADCs readout and the known calibration and lookup tables. If the hardware readout and the simulation are not in agreement in table the letter "R" is printed.

In the last section (quantities are named starting with "TE") the bit information read out from the CTL are displayed. These bits are read out from an independent system and can therefore serve for comparisons with the information generated in the LAr trigger hardware and read out from the FADCs and the adder tree.

Readout in the Central Bunch Cross

The central bunch cross readout error is shown in table A.2. In the FB region a large energy deposition is seen from FADC 286 (BT 143), even firing BT $t0$ in the central BC. Other FADCs in the FB region have a small energies and therefore do not contribute in the adder tree summing. The simulation and readout agree in the adder tree except for the central BC where an obvious problem is seen. The pulse both in data and simulation looks like a healthy physics pulse, but in readout it looks strange since it has exactly zero in the central BC. In the adder tree simulation the central value is "physical". So there is a suspicion that the central bunch cross readout for

run 382420	**event 5515**								
IF region									
Fadc 22	0	0	0	0	6	7	7	5	5
Fadc 70	0	0	0	6	6	6	5	0	0
Fadc 131	0	0	6	10	13	14	12	10	6
Fadc 138	0	0	0	5	8	10	10	7	0
Fadc 139	0	0	0	0	5	6	6	5	0
Fadc 144	0	0	0	6	6	5	0	0	0
Fadc 186	0	0	0	0	7	8	8	7	5
Fadc 222	0	0	0	7	9	9	7	5	0
FB region									
Fadc 326	0	0	6	8	8	7	6	0	0
Fadc 336	0	6	31	52	66	72	65	46	22
BT 168				11	11	11	11	1	
Fadc 337	0	0	0	5	6	5	5	0	0
Fadc 338	0	0	0	0	0	9	10	10	7
Fadc 344	0	8	21	26	21	21	19	14	6
Fadc 345	0	19	29	35	36	39	41	38	23
CB region									
Fadc 408	0	0	0	0	8	7	0	0	0
Fadc 410	0	0	0	0	8	8	10	10	6
Fadc 468	0	0	0	5	9	0	0	0	0
Fadc 470	0	0	0	10	11	7	0	0	0
Fadc 502	0	0	0	6	7	0	0	0	0
Adder tree									
1 IFQ0	0	0	0	0	8	9	9	0	0
3 IFQ2	0	0	8	14	43	49	46	36	8
4 IFQ3	0	0	0	0	10	10	0	0	0
5 IFTot	0	0	8	14	61	68	55	36	8
7 IFquad	0	0	0	0	16	16	16	16	0
8 IFtotD	0	0	0	0	1	1	1	1	0
18 CBQ1	0	0	0	7	0	0	0	0	0
19 CBQ2	0	0	0	17	0	0	0	0	0
21 CBTot	0	0	0	17	0	0	0	0	0
28 FBQ2	0	29	82	119	129	138	131	120	72
29 FBQ3	0	0	0	0	0	0	0	0	18
30 FBTot	0	29	82	119	129	138	131	120	90
31 Bartot	0	29	82	136	129	138	131	120	90
32 FBquad	0	16	48	48	48	48	48	48	0
33 FBtotD	0	1	3	3	3	3	3	3	0
34 BartotD	0	0	1	2	2	2	2	2	0
42 Eweight	0	0	0	0	11	13	11	8	0
44 Etrans	0	24	64	91	102	109	112	92	0
45 EtransD	0	0	2	3	3	3	3	0	0
46 Ex	0	244	225	211	209	205	203	213	0
47 ExD	0	244	225	211	209	205	203	213	0
48 Ey	0	254	251	248	246	246	244	245	0
49 EyD	0	254	251	248	246	246	244	245	0
50 EmissD	0	0	3	3	3	3	3	0	0
51 Ele1	0	0	0	1	1	1	1	0	0
52 Ele1D	0	0	0	1	1	1	1	0	0
53 Ele2	0	0	0	1	1	1	1	1	0
54 Ele2D	0	0	0	1	1	1	1	1	0
CTL									
1 TE Ele1	0	0	0	1	1	1	1	0	0
2 TE Ele2	0	0	0	1	1	1	1	1	0
80 TE IFTot	0	0	0	0	1	1	1	1	0
84 TE FBTot	0	1	1	1	1	1	1	1	1
85 TE FBTot	0	0	1	1	1	1	1	1	1
100 TE Etrans	0	0	0	1	1	1	1	1	0
101 TE Etrans	0	0	1	1	1	1	1	1	0
102 TE Emiss	0	0	1	1	1	1	1	1	0
103 TE Emiss	0	0	1	1	1	1	1	1	0
ST fired	67	71	75	76	77	78			

Table A.1: Charged Current event in raw data where can be seen large *Etmiss* energy as signature of CC event.Two $t0$ fired at the same BC are another characteristic of CC events which $t0$ is sinchronized with HERA clock.

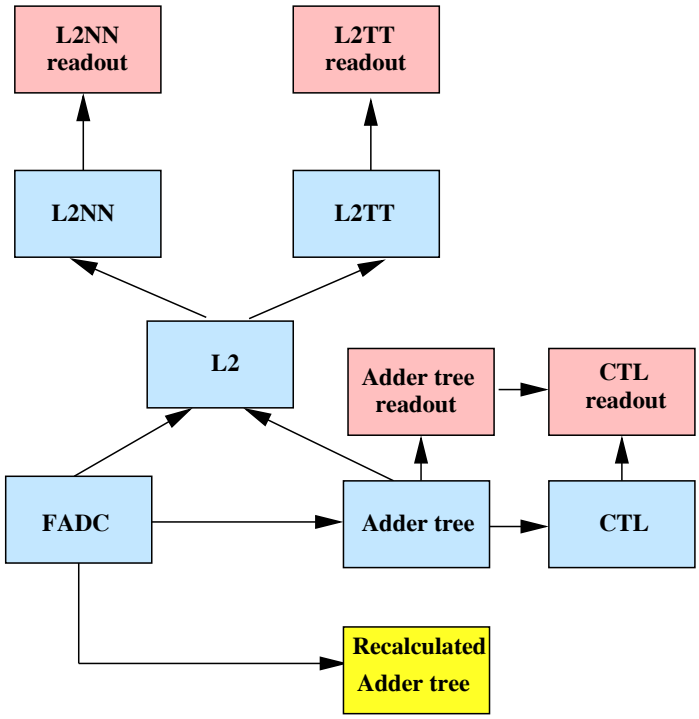

Figure A.1: A schematic view of the data stream from the LAr trigger.

the adder tree failed. There is even more confirmation of this problem in the TEs which are delivered and read out from the CTL and the L2TT systems[1].

A.4 Ntuple for the LAr Trigger

TTNT is a software package which provides easy access to H1 LAr calorimeter and its trigger information. Its basis is the TTOOL package which contains the complete simulation of the trigger. This package also provides access to different kinds of information on the other detector elements (such as the CTL). Investigation of general event properties is available via array of variables which are defined within the TTOOL structure, such as EVENT = event number, EVVTX = event vertex, EVVT0 = event $T0$, etc. All output informations from LAr trigger electronics are available for analysis via TTNT and organised in the "Adder tree". For a detailed analysis of the adder tree, the arrays DAADDER (i, j) and READDER (i, j) are used. Here i denotes number of BC and j is an index of the element in the adder tree. DAADDER (9, 59) contains the actual adder tree information for all nine bunch crosses, as they are read off from the ATES bank of H1. This information is available from trigger

[1]Note that at L2 only central bunch cross is readout.

run 341401	**event 17244**								
FB region									
Fadc 286	11	42	95	143	180	188	166	105	27
BT 143		1	11	11	1011	11	11	11	
Fadc 335	0	0	0	0	6	6	6	6	0
Fadc 344	0	0	0	0	0	7	10	9	0
Fadc 351	0	0	0	0	0	5	8	8	0
Fadc 374	0	0	0	0	5	5	0	0	0
Adder tree									
26 FBQ0	0	43	98	148	0	195	172	109	28
R	0	43	98	148	187	195	172	109	28
30 FBTot	0	43	98	148	0	195	172	109	28
R	0	43	98	148	187	195	172	109	28
31 Bartot	0	65	98	148	0	195	172	109	28
R	0	65	98	148	187	195	172	109	28
32 FBquad	0	1	3	3	0	3	3	3	0
R	0	1	3	3	3	3	3	3	1
33 FBtotD	0	1	3	3	0	3	3	3	0
R	0	1	3	3	3	3	3	3	1
34 BartotD	0	0	1	2	0	3	3	1	0
R	0	0	1	2	3	3	3	1	0
42 Eweight	0	0	1	0	0	0	0	0	0
43 EweightD	0	0	0	0	0	0	0	0	0
44 Etrans	0	36	84	126	0	166	146	92	0
R	0	36	84	126	159	166	146	92	23
45 EtransD	0	0	3	3	0	3	3	0	0
R	0	0	3	3	3	3	3	3	0
46 Ex	0	3	8	12	0	15	14	8	0
R	0	3	8	12	15	15	14		8 2
47 ExD	0	3	8	12	0	15	14	8	0
48 Ey	0	17	40	61	0	81	71	45	0
R	0	17	40	61	78	81	71	45	11
49 EyD	0	17	40	61	0	81	71	45	0
50 EmissD	0	0	3	3	0	3	3	0	0
R	0	0	3	3	3	3	3	3	0
51 Ele1	0	0	1	1	0	1	1	1	0
R	0	0	1	1	1	1	1	1	0
52 Ele1D	0	0	1	1	0	1	1	1	0
R	0	0	1	1	1	1	1	1	0
53 Ele2	0	1	1	1	0	1	1	1	0
R	0	1	1	1	1	1	1	1	0
54 Ele2D	0	1	1	1	0	1	1	1	0
R	0	1	1	1	1	1	1	1	0
59 AnT0D	0	0	0	0	0	1	0	0	0
CTL									
0 TE BtT0	0	0	0	0	1	0	0	0	0
1 TE Ele1	0	0	1	1	1	1	1	1	0
2 TE Ele2	0	1	1	1	1	1	1	1	0
84 FBTot	0	1	1	1	1	1	1	1	1
85 FBTot	0	0	1	1	1	1	1	1	0
100 Etrans	0	0	1	1	1	1	1	1	0
101 Etrans	0	0	1	1	1	1	1	1	0
102 Emiss	0	0	1	1	1	1	1	1	0
103 Emiss	0	0	1	1	1	1	1	1	0
L2TT									
L2ADDER 44					159				
L2ADDER 46					15				
L2ADDER 48					78				
L2ADDER 51					1				
L2ADDER 53					1				
L2ADDER 57					1				

Table A.2: Event with wrong readout in the central bunch cross.

readout. On the other hand, all trigger quantities can be reconstructed using existing FADC information via READDER (9, 59). If there is no error, READDER (i, j) and DAADDER (i, j) are equal, If this is not the case, an inconsistency, i.e. a problem in the system, is diagnosed. For the investigation of the LAr triggers an independent readout is used, coming from the CTL, encoded in the array TREL (9,192), which contains all the trigger elements for all nine bunchcrosses. The bit information from the LAr BTs is also stored in the CTL readout for the nine bunchcrosses around the interaction point (electron 1,electron 2, BT $T0$). Using this set of variables is possible to check the timing of the LAr trigger and the $T0$. The various quantities determined by the LAr trigger are shown in table A.3.

Nr.	name	short description	value	user
topological sums:				
1	IFQ0		[0.255]	L2
2	IFQ1	energy sum of the	[0,255]	L2
3	IFQ2	IF quadrants	[0,255]	L2
4	IFQ3		[0,255]	L2
5	IFTOT	IF total energy	[0.255]	L2
6	FTOT	sum IF and PLUG	[0,255]	L2
7	IFQUAD	discrim.IF quadrants	[0,255]	intern
8	IFTOTD	discrim.IF total energy	[0,3]	CTL
9	IFTOTD	discrim.IF+PLUG energy	[0,3]	CTL
10	PLUGQ0		[0,255]	L2
11	PLUG1	energy sum of the	[0,255]	L2
12	PLUGQ2	PLUG quadrants	[0,255]	L2
13	PLUGQ3		[0,255]	L2
14	PLUGTOT	PLUG total energy	[0,255]	L2
15	PLUGQUAD	discrim. PLUG quadrants	[0,255]	intern
16	PLUGTOTD	discrim. PLUG energy	[0,3]	CTL
17	CBQ0		[0,255]	L2
18	CBQ1	energy sum of the	[0,255]	L2
19	CBQ2	CB quadrants	[0,255]	L2
20	CBQ3		[0,255]	L2
21	CBTOT	CB total energy	[0,255]	L2
22	BCKTOT	sum of CB and SpaCal	[0,255]	intern
23	CBQUAD	discrim.CB quadrants	[0,255]	intern
24	CBTOTD	discrim.CB total energy	[0,3]	CTL
25	BCKTOTD	discrim.CB+SpaCal energy	[0,3]	CTL
26	FBQ0		[0,255]	L2
27	FBQ1	energy sum of the	[0,255]	L2
28	FBQ2	FB quadrants	[0,255]	L2
29	FBQ3		[0,255]	L2
30	FBTOT	FB total energy	[0,255]	L2
31	BARTOT	sum of FB and	[0,255]	L2
32	FBQUAD	discrim.FB quadrants	[0,255]	intern
33	FBTOTD	discrim.FB total energy	[0,3]	CTL
34	BARTOTD	discrim.FB+CB energy	[0,3]	CTL
35	SPACQ0		[0,255]	L2
36	SPACQ1	energy sum of the	[0,255]	L2
37	SPACQ2	SpaCal quadrants	[0,255]	L2
38	SPACQ3		[0,255]	L2
39	SPACTOT	SpaCal total energy	[0,255]	L2
40	SPACQUAD	discrim.SpaCal quadrants	[0,255]	intern
41	SPACTOTD	discrim.SpaCal energy	[0,3]	CTL
global sums:				
42	EWEIGHT	free programmable: $\sum BTf(I_{BT}, E_{BT})$	[0,255]	L2
43	EWEIGHTD	discrim. E_{weight}	[0,3]	CTL
44	ETRANS	trans.energy:	[0,255]	L2
45	ETRANSD	discrim.trans.energy	[0,3]	CTL
46	EX	x-projection:$\sum BTE_{BT}sin(\theta_{BT})cos(\phi_{BT})$	[0,255]**	L2
47	EXD	discrim .E_x	[0,3]	CTL
48	EY	y-projection:$\sum BTE_{BT}sin(\theta_{BT})sin(\phi_{BT})$	[0,255]**	L2
49	EYD	discrim.E_y	[0,3]	CTL
50	EMISSD	discrim.$E_T^{miss} = \sqrt{E_x^2 + E_y^2}$	[0,3]	CTL

Nr.	name	short description	value	user
Big Tower Bits:				
51	ELE1	number of electrons_1-BT-bits	[0,255]	L2
52	ELE1D	$N_{BT}(electron_1) > NELE1_{min}$	[0,1]	CTL
53	ELE2	number of electron_2-BT-bits	[0,255]	L2
54	ELE2D	$N_{BT}(electron_2) > NELE2_{min}$	[0,1]	CTL
55	BRT0	number of LAR_BigRay BT bits	[0,255]	L2
57	BTT0	number of $T0$ bits fed through	[0,255]	L2
58	BTT0D	$N_{BT}(T0) > NT)_{min}$	[0,1]	CTL
59	ANT0D	number of all BT $T0$ bits,analog $T0$	[0,255]	intern

Table A.3: Overview over the adder tree of the LAr trigger:global sums and BT numbers *user: Trigger level using the signal: LAr-trigger internal, CTL-L1 or L2 ** The values [-1,-128] are mapped to the interval [255,128]: $-1 \rightarrow 255$, $-2 \rightarrow 254$,... $-128 \rightarrow 128$

Trigger System	**Trigger Elements Sent to the L2**
L2NN	$0, 1, 2, 3, 4, 16, 17, 18, 19, 20, 25, 26, 27, 28, 29, 41, 43, 45, 47, 50, 52, 54, 56$
L2TT	$0, 1, 2, 3, 4, 41, 43, 45, 47, 50, 52, 54, 56$

Table A.4: LAr trigger elements sent to the L2 trigger systems.

Appendix B

Tables of Results

Abrevations for the uncertainties used in tables of results:

- δ_{sta} the relative statistical uncertainty;
- δ_{sys} the relative systematic uncertainty;
- δ_{tot} the relative total uncertainty;
- δ_{unc} the total uncorrelated systematic uncertainty;
- δ^{h}_{unc} the contribution of the hadronic energy uncertainty to the uncorrelated uncertainty;
- δ_{cor} the total correlated systematic uncertainty;
- δ^{V+}_{cor} the contribution from a positive variation of one standard deviation of the Pythia subtraction error;
- δ^{h+}_{cor} the contribution from a positive variation of one standard deviation of the hadronic energy error;
- δ^{N+}_{cor} the contribution from a positive variation of one standard deviation of the uncertainty due to noise subtraction error.

Note that the contribution due to a positive variation of subtraction *ep* background (δ^{B+}_{cor}) originating from the NC, lepton-pair and W production is not included in tables. It can be recalculated from the sum of correlated errors (δ_{cor}) and correlated uncertainties given in tables (δ^{V+}_{cor},δ^{h+}_{cor},δ^{N+}_{cor}). This error will have a certain sign, for instance $\delta^{B+}_{cor} > 0$ would correspond to decrease of the cross section.

B.1 Differential CC Cross Sections

Q^2 (GeV^2)	$d\sigma_{cc}/dQ^2$ (pb/GeV^2)	δ_{sta} (%)	δ_{sys} (%)	δ_{tot} (%)	δ_{unc} (%)	δ^h_{unc} (%)	δ_{cor} (%)	δ^{V+}_{cor} (%)	δ^{h+}_{cor} (%)	δ^{N+}_{cor} (%)
300	5.37e-02	8.0	14.1	16.2	11.4	4.0	8.3	7.3	-2.3	-0.7
500	3.46e-02	5.7	8.0	9.8	7.2	3.2	3.6	4.6	-2.0	-0.3
1000	2.29e-02	4.4	5.3	6.8	5.0	2.0	1.7	3.2	-1.0	0.3
2000	1.18e-02	4.0	4.4	6.0	4.1	1.8	1.6	2.4	-1.2	0.3
3000	7.36e-03	4.0	3.3	5.2	3.1	0.6	1.2	1.8	0.6	0.4
5000	4.02e-03	4.3	3.4	5.4	3.1	1.3	1.4	1.4	0.7	0.4
8000	1.67e-03	5.6	6.1	8.3	5.4	4.6	2.8	1.1	2.3	0.8
15000	5.45e-04	8.5	10.1	13.2	8.8	6.6	5.0	1.0	4.3	0.6

Table B.1: The e^-p LH CC cross section $d\sigma_{cc}/dQ^2$ measured in the kinematic region $y < 0.9$. The normalisation uncertainty of 2% is not included in the uncertainties.

Q^2 (GeV^2)	$d\sigma_{cc}/dQ^2$ (pb/GeV^2)	δ_{sta} (%)	δ_{sys} (%)	δ_{tot} (%)	δ_{unc} (%)	δ^h_{unc} (%)	δ_{cor} (%)	δ^{V+}_{cor} (%)	δ^{h+}_{cor} (%)	δ^{N+}_{cor} (%)
300	2.19e-02	20.4	14.8	25.1	11.4	4.0	9.4	7.4	-2.2	0.8
500	2.02e-02	11.5	8.1	14.1	7.2	3.2	3.8	2.6	-2.0	-0.3
1000	1.19e-02	9.4	5.4	10.8	5.0	2.0	2.0	0.6	-1.0	0.6
2000	4.95e-03	9.5	4.4	10.4	4.0	1.8	1.7	0.4	-1.2	0.5
3000	4.00e-03	8.3	3.4	8.9	3.1	0.6	1.4	0.5	0.7	0.6
5000	1.85e-03	9.6	3.5	10.2	3.1	1.2	1.5	0.5	0.7	0.6
8000	8.31e-04	12.1	6.1	13.6	5.4	4.6	2.8	0.5	2.3	0.7
15000	1.57e-04	19.5	9.9	21.9	8.3	7.7	5.5	0.5	5.0	0.8

Table B.2: The e^-p RH CC cross section $d\sigma_{cc}/dQ^2$ measured in the kinematic region $y < 0.9$. The normalisation uncertainty of 2% is not included in the uncertainties.

x	$d\sigma_{cc}/dx$ (pb)	δ_{sta} (%)	δ_{sys} (%)	δ_{tot} (%)	δ_{unc} (%)	δ^h_{unc} (%)	δ_{cor} (%)	δ^{V+}_{cor} (%)	δ^{h+}_{cor} (%)	δ^{N+}_{cor} (%)
0.0320	3.19e+02	5.2	4.0	6.5	3.6	1.6	1.6	1.0	-0.8	0.2
0.0800	2.38e+02	3.6	3.2	4.8	3.0	0.6	1.2	1.5	-0.5	0.5
0.1300	1.70e+02	3.7	3.7	5.3	3.4	1.1	1.3	2.2	0.7	0.4
0.2500	7.42e+01	4.5	4.8	6.6	4.4	2.8	1.9	2.4	1.5	-0.3
0.4000	3.77e+01	10.2	10.8	14.8	9.4	5.5	5.3	3.0	3.1	-3.2

Table B.3: The e^-p LH CC cross section $d\sigma_{cc}/dx$ measured in the kinematic region of $Q^2 > 1000\ GeV^2$ and $y < 0.9$. The normalisation uncertainty of 2% is not included in the uncertainties.

x	$d\sigma_{cc}/dx$ (pb)	δ_{sta} (%)	δ_{sys} (%)	δ_{tot} (%)	δ_{unc} (%)	δ^{h}_{unc} (%)	δ_{cor} (%)	δ^{V+}_{cor} (%)	δ^{h+}_{cor} (%)	δ^{N+}_{cor} (%)
0.0320	1.43e+02	11.8	4.0	12.4	3.5	1.7	1.8	0.3	-0.9	0.3
0.0800	1.24e+02	7.6	3.2	8.3	3.0	0.6	1.3	0.5	0.5	0.5
0.1300	7.09e+01	8.9	3.7	9.6	3.5	1.1	1.4	0.5	0.7	0.6
0.2500	3.81e+01	9.6	4.8	10.8	4.4	2.8	2.0	0.5	1.5	0.4
0.4000	1.20e+01	20.7	9.4	22.8	7.9	7.3	5.1	0.5	4.4	-1.2

Table B.4: The e^-p RH CC cross section $d\sigma_{cc}/dx$ measured in the kinematic region of $Q^2 > 1000\ GeV^2$ and $y < 0.9$. The normalisation uncertainty of 2% is not included in the uncertainties.

Q^2 GeV^2	x	$\bar{\sigma}_{cc}$ (pb)	δ_{sta} (%)	δ_{sys} (%)	δ_{tot} (%)	δ_{unc} (%)	δ^{h}_{unc} (%)	δ_{cor} (%)	δ^{V+}_{cor} (%)	δ^{h+}_{cor} (%)	δ^{N+}_{cor} (%)
300	0.0130	1.86	16.6	19.4	25.5	13.7	3.3	13.7	12.6	-2.3	1.9
300	0.0320	1.65	12.2	11.5	16.7	8.8	3.8	7.3	5.8	-2.1	0.2
300	0.0800	0.97	16.4	15.8	22.8	14.7	4.7	5.7	2.2	-2.7	-2.1
500	0.0130	1.77	11.2	11.9	16.3	9.1	4.0	7.7	6.9	-1.9	-0.4
500	0.0320	1.33	8.9	6.4	11.0	5.5	3.1	3.3	1.4	-1.9	-0.1
500	0.0800	0.76	11.5	9.2	14.8	8.5	3.2	3.4	0.2	-2.2	0.9
500	0.1300	0.77	25.5	17.1	30.7	14.9	1.1	8.4	0.3	-0.6	-6.5
1000	0.0130	1.17	11.4	9.8	15.0	7.1	2.5	6.7	6.0	-1.4	0.3
1000	0.0320	1.26	7.2	5.0	8.8	4.3	3.0	2.6	-0.5	-1.4	0.6
1000	0.0800	1.11	7.2	5.3	8.9	4.8	1.0	2.2	0.2	-0.6	1.0
1000	0.1300	0.67	13.4	9.3	16.3	8.4	1.8	3.8	0.3	-1.0	-2.3
2000	0.0320	1.06	6.9	4.8	8.4	4.2	2.3	2.3	0.2	-1.5	0.2
2000	0.0800	0.90	6.5	4.0	7.6	3.4	1.6	2.1	-0.2	-1.2	0.3
2000	0.1300	0.71	9.1	5.8	10.8	5.3	1.7	2.4	0.3	-1.1	0.7
2000	0.2500	0.49	18.0	10.8	21.0	8.5	3.3	6.7	0.3	1.6	-5.1
3000	0.0800	0.86	6.1	3.5	7.0	2.9	1.3	1.9	0.3	0.9	0.7
3000	0.1300	0.79	7.2	3.7	8.1	3.0	0.6	2.1	0.3	0.8	0.8
3000	0.2500	0.53	10.6	5.7	12.0	5.0	1.4	2.7	0.3	0.7	-0.7
3000	0.4000	0.22	44.8	15.5	47.4	7.8	2.6	13.4	0.3	1.7	-9.8
5000	0.0800	0.87	7.8	3.5	8.5	2.8	0.7	2.1	-0.3	0.4	0.4
5000	0.1300	0.82	6.9	3.6	7.8	2.8	1.3	2.3	0.3	1.3	0.7
5000	0.2500	0.59	8.1	4.1	9.0	3.4	1.8	2.2	0.3	0.9	0.1
5000	0.4000	0.24	23.0	11.2	25.6	8.2	6.8	7.6	0.3	4.1	-3.8
8000	0.1300	0.86	8.2	7.3	11.0	6.1	5.6	4.1	0.2	3.1	1.4
8000	0.2500	0.45	9.1	4.9	10.4	4.0	3.2	2.8	0.3	1.7	0.6
8000	0.4000	0.25	16.7	8.2	18.6	6.4	5.8	5.2	0.3	3.4	-1.1
15000	0.2500	0.53	10.3	8.0	13.1	6.7	6.2	4.3	0.3	3.4	0.4

Table B.5: The e^-p LH CC cross section $d^2\sigma_{cc}/dxdQ^2$ measured in the kinematic region of $300 < Q^2 < 25000$ GeV^2 and $0.013 < x < 0.65$. The normalisation uncertainty of 2% is not included in the uncertainties.

Q^2 GeV^2	x	$\bar{\sigma}_{cc}$ (pb)	δ_{sta} (%)	δ_{sys} (%)	δ_{tot} (%)	δ_{unc} (%)	δ^h_{unc} (%)	δ_{cor} (%)	δ^{V+}_{cor} (%)	δ^{h+}_{cor} (%)	δ^{N+}_{cor} (%)
300	0.0130	0.97	36.9	20.0	42.0	13.8	3.3	14.5	12.7	-2.3	2.1
300	0.0320	0.42	41.8	12.4	43.6	9.0	3.8	8.6	5.8	-2.1	0.3
300	0.0800	0.44	38.8	16.1	42.0	14.7	4.7	6.6	2.2	-2.7	-2.1
500	0.0130	1.08	22.5	12.3	25.6	9.4	4.0	7.9	6.9	-1.9	0.4
500	0.0320	0.70	18.9	6.6	20.1	5.5	3.1	3.7	1.4	-1.9	0.3
500	0.0800	0.68	18.6	9.3	20.8	8.6	3.2	3.6	0.4	-2.2	1.1
1000	0.0130	0.83	21.4	10.7	23.9	8.3	2.4	6.8	6.0	-1.4	0.5
1000	0.0320	0.49	18.0	5.2	18.8	4.2	3.0	3.0	-0.5	-1.5	0.8
1000	0.0800	0.62	14.7	5.4	15.7	4.9	1.0	2.3	0.5	0.7	1.0
1000	0.1300	0.41	25.9	9.2	27.5	8.4	1.7	3.8	0.5	-1.0	-2.3
2000	0.0320	0.38	17.7	4.6	18.2	3.8	2.4	2.5	0.4	-1.5	0.4
2000	0.0800	0.40	14.9	4.0	15.4	3.4	1.6	2.1	0.4	-1.2	0.4
2000	0.1300	0.30	21.5	5.9	22.3	5.3	1.8	2.6	0.5	-1.1	0.9
2000	0.2500	0.29	35.5	11.0	37.1	8.6	3.5	6.8	0.5	1.9	-5.1
3000	0.0800	0.49	12.4	3.7	13.0	3.1	1.6	2.1	0.5	1.1	0.7
3000	0.1300	0.31	17.6	3.8	18.0	3.1	0.7	2.2	0.5	0.8	0.8
3000	0.2500	0.34	20.3	5.7	21.0	5.0	1.4	2.8	0.5	0.7	-0.7
3000	0.4000	0.09	100.2	15.3	101.3	7.5	2.8	13.4	0.5	1.8	-9.7
5000	0.0800	0.48	16.1	3.6	16.4	2.8	0.7	2.2	0.5	0.4	0.5
5000	0.1300	0.34	16.4	3.8	16.9	2.9	1.4	2.5	0.5	1.4	0.9
5000	0.2500	0.23	19.7	4.2	20.1	3.5	1.8	2.3	0.5	0.9	0.3
5000	0.4000	0.18	40.9	11.2	42.4	8.2	6.8	7.7	0.5	4.1	-3.8
8000	0.1300	0.38	18.8	7.4	20.2	6.2	5.6	4.1	0.4	3.1	1.4
8000	0.2500	0.29	17.5	4.9	18.2	4.0	3.1	2.8	0.5	1.7	0.6
8000	0.4000	0.09	42.5	8.1	43.2	6.2	5.6	5.2	0.5	3.3	-1.2
15000	0.2500	0.21	25.1	8.1	26.4	6.7	6.3	4.4	0.5	3.4	0.7
15000	0.4000	0.12	30.6	12.0	32.8	9.7	9.4	7.0	0.5	6.1	1.2

Table B.6: The e^-p RH CC cross section $d^2\sigma_{cc}/dxdQ^2$ measured in the kinematic region measured in the kinematic region of $300 < Q^2 < 25000$ GeV^2 and $0.013 < x < 0.65$. The normalisation uncertainty of 2% is not included in the uncertainties.

Q^2 (GeV^2)	$d\sigma_{cc}/dQ^2$ (pb/GeV^2)	δ_{sta} (%)	δ_{sys} (%)	δ_{tot} (%)	δ_{unc} (%)	δ^h_{unc} (%)	δ_{cor} (%)	δ^{V+}_{cor} (%)	δ^{h+}_{cor} (%)	δ^{N+}_{cor} (%)
300	4.07e-02	7.4	14.3	16.1	11.5	4.2	8.6	7.4	-2.5	-0.8
500	2.78e-02	5.1	8.0	9.5	7.1	3.2	3.7	2.7	-1.9	-0.3
1000	1.80e-02	4.0	5.2	6.5	4.9	1.9	1.8	0.7	-0.9	0.4
2000	8.91e-03	3.7	4.4	5.7	4.0	1.8	1.7	0.2	-1.2	0.3
3000	5.92e-03	3.6	3.4	4.9	3.1	0.6	1.3	0.3	0.6	0.5
5000	3.14e-03	3.9	3.5	5.2	3.2	1.3	1.5	0.3	0.8	0.4
8000	1.31e-03	5.1	6.0	7.9	5.4	4.5	2.7	0.3	2.1	0.8
15000	2.70e-04	7.8	9.7	12.4	8.1	7.4	5.4	0.3	4.9	0.8

Table B.7: The e^-p unpolarised CC cross section $d\sigma_{cc}/dQ^2$ measured in the kinematic region of $y < 0.9$. The normalisation uncertainty of 2% is not included in the uncertainties.

x	$d\sigma_{cc}/dQ^2$ (pb)	δ_{sta} (%)	δ_{sys} (%)	δ_{tot} (%)	δ_{unc} (%)	δ^h_{unc} (%)	δ_{cor} (%)	δ^{V+}_{cor} (%)	δ^{h+}_{cor} (%)	δ^{N+}_{cor} (%)
0.0320	2.43e+02	4.7	3.9	6.1	3.5	1.6	1.6	-0.2	-0.7	0.3
0.0800	1.89e+02	3.3	3.2	4.6	3.0	0.6	1.2	0.3	-0.5	0.5
0.1300	1.30e+02	3.5	3.7	5.1	3.5	1.1	1.3	0.3	0.7	0.5
0.2500	5.89e+01	4.1	4.7	6.3	4.3	2.7	1.9	0.3	1.5	-0.3
0.4000	1.71e+01	9.1	9.5	13.2	78.0	7.4	5.1	0.3	4.4	-1.1

Table B.8: The e^-p unpolarised CC cross section $d\sigma_{cc}/dx$ measured in the kinematic region of $Q^2 > 1000\ GeV^2$ and $y < 0.9$. The normalisation uncertainty of 2% is not included in the uncertainties.

Q^2 GeV^2	x	$\bar{\sigma}_{cc}$ (pb)	δ_{sta} (%)	δ_{sys} (%)	δ_{tot} (%)	δ_{unc} (%)	δ^h_{unc} (%)	δ_{cor} (%)	δ^{V+}_{cor} (%)	δ^{h+}_{cor} (%)	δ^{N+}_{cor} (%)
300	0.0130	1.45	15.1	19.2	24.5	13.5	-3.8	13.7	12.5	-2.9	2.0
300	0.0320	1.20	11.7	12.0	16.8	9.1	-4.3	7.8	5.9	-2.5	0.2
300	0.0800	0.75	15.2	15.8	21.9	14.6	-4.4	76.0	2.0	-2.7	-2.3
500	0.0130	1.40	10.0	11.7	15.4	8.7	-3.8	7.8	7.0	-1.8	0.5
500	0.0320	1.06	8.1	6.3	10.2	5.4	-2.9	3.2	1.3	-1.5	0.1
500	0.0800	0.69	9.8	9.4	13.6	8.7	-3.5	3.6	0.3	-2.4	0.8
500	0.1300	0.50	25.7	17.3	31.0	15.0	-1.4	8.7	0.3	-0.7	-6.7
1000	0.0130	0.96	10.1	9.8	14.1	6.9	-2.2	7.0	6.3	-1.1	0.4
1000	0.0320	0.94	6.7	5.0	8.4	4.2	-3.0	2.7	-0.5	-1.4	0.5
1000	0.0800	0.89	6.5	5.3	8.4	4.8	-1.0	2.3	0.3	0.6	0.9
1000	0.1300	0.54	11.9	9.3	15.1	8.4	-1.4	3.9	0.3	-1.2	-2.3
2000	0.0320	0.767	6.5	4.5	7.9	3.8	-2.2	2.4	0.3	-1.5	0.4
2000	0.0800	0.69	6.0	3.9	7.1	3.4	-1.5	2.0	0.3	-1.1	0.4
2000	0.1300	0.55	8.4	5.9	10.3	5.4	-2.0	2.6	0.3	-1.0	0.8
2000	0.2500	0.41	16.1	11.3	19.7	8.7	3.8	7.2	0.3	1.7	-5.6
3000	0.0800	0.70	5.5	3.6	6.6	2.9	1.5	2.0	0.3	0.9	0.8
3000	0.1300	0.60	6.6	3.7	7.6	3.0	0.5	2.1	0.3	0.6	0.9
3000	0.2500	0.43	9.4	5.7	11.0	5.0	1.2	2.8	0.3	0.9	-0.7
3000	0.4000	0.16	40.9	16.0	43.9	8.9	4.8	13.3	0.3	1.9	-9.4
5000	0.0800	0.71	7.0	3.6	7.9	2.9	0.7	2.2	-0.3	0.6	0.4
5000	0.1300	0.63	6.4	3.7	7.3	2.8	1.1	2.3	0.4	1.2	0.8
5000	0.2500	0.45	7.5	4.2	8.6	3.5	1.9	2.3	0.4	0.9	0.2
5000	0.4000	0.20	20.0	11.5	23.1	8.3	7.0	8.0	0.3	4.3	-3.9
8000	0.1300	0.66	7.5	7.2	10.4	6.0	5.5	4.0	0.3	2.9	1.6
8000	0.2500	0.37	8.1	5.0	9.5	4.1	3.2	2.8	0.3	1.7	0.5
8000	0.4000	0.19	15.5	7.8	17.4	5.9	5.2	5.1	0.3	3.0	-1.0
15000	0.2500	0.40	9.6	7.8	12.3	6.4	5.9	4.4	0.3	3.4	0.6
15000	0.4000	0.14	14.6	12.2	19.0	9.9	9.6	7.1	0.3	6.2	1.2

Table B.9: The e^-p unpolarised CC cross section $d^2\sigma_{cc}/dxdQ^2$ measured in the kinematic region measured in the kinematic region of $300 < Q^2 < 25000$ GeV^2 and $0.013 < x < 0.65$. The normalisation uncertainty of 2% is not included in the uncertainties.

B.2 Charged Current Structure Function F_2^{cc}

Q^2	x	F_2^{cc}	$\Delta(xF_3^{cc}, F_L^{cc})$	δ_{sta}	δ_{sys}	δ_{tot}
300	0.013	3.58	0.03	0.49	0.60	0.78
500	0.013	3.54	0.06	0.33	0.37	0.50
1000	0.013	3.73	0.22	0.33	0.32	0.46
300	0.032	2.15	-0.00	0.24	0.23	0.33
500	0.032	2.20	-0.00	0.17	0.12	0.20
1000	0.032	2.23	-0.00	0.14	0.10	0.17
2000	0.032	2.58	0.03	0.15	0.11	0.19
300	0.080	1.52	-0.00	0.22	0.18	0.29
500	0.080	1.19	-0.01	0.11	0.09	0.14
1000	0.080	1.48	-0.02	0.09	0.07	0.12
2000	0.080	1.37	-0.04	0.08	0.05	0.09
3000	0.080	1.41	-0.05	0.08	0.06	0.10
5000	0.080	1.63	-0.09	0.12	0.08	0.14
500	0.130	0.78	-0.01	0.20	0.11	0.23
1000	0.130	0.90	-0.01	0.11	0.07	0.13
2000	0.130	0.97	-0.03	0.08	0.05	0.10
3000	0.130	1.05	-0.05	0.07	0.04	0.08
5000	0.130	1.14	-0.08	0.08	0.05	0.09
8000	0.130	1.30	-0.13	0.10	0.11	0.15
2000	0.250	0.52	-0.02	0.09	0.06	0.11
3000	0.250	0.53	-0.03	0.05	0.03	0.06
5000	0.250	0.67	-0.05	0.05	0.03	0.06
8000	0.250	0.57	-0.08	0.05	0.04	0.06
5000	0.400	0.33	-0.02	0.07	0.04	0.08
8000	0.400	0.26	-0.03	0.05	0.02	0.05
15000	0.400	0.16	-0.06	0.03	0.03	0.04

Table B.10: The CC structure function F_2^{cc} measured using the unpolarised e^+p CC data and the unpolarised e^-p CC data collected in years 2003-04 and 2005, respectively, together with the correction term $\Delta(xF_3^{cc}, F_L^{cc})$ is given. In addition, the statistical (δ_{sta}), the systematic (δ_{sys}) and the total (δ_{tot}) uncertainties are given. The uncertainty of 1.3% for the e^+p data and uncertainty of 2% for the e^-p data due to luminosity measurement are included in the uncertainties.

Bibliography

[1] R. W. McAlister and R. Hofstadter. *Phys.Rev*, **102**, page 851, 1956.

[2] E.D. Bloom et al. High-Energy inelastic *ep* Scattering at 6° and 10°. *Phys. Rev. Lett.*, **23**, pages 930–934, 1969.

[3] M. Gell-Mann. A schematic model of baryons and mesons. *Phys. Lett.*, **8**, pages 214–215, 1964.

[4] T.D. Lee and C.N. Yang. Questions of Parity Conservation in Weak Interactions. *Phys.Rev*, **104**, page 254, 1956.

[5] R.P. Feynman and M. Gell-Mann. *Phys.Rev*, **109**, page 193, 1958.

[6] E.C.G. Sudarshan and R.E. Marshak. *Phys.Rev*, **109**, page 1860, 1958.

[7] S. L. Glashow. *Nucl. Phys.*, **22**, page 579, 1961.

[8] S. Weinberg. *Phys. Rev. Lett.*, **19**, page 1264, 1967.

[9] A. Salam. Originally printed in Swartholm: Elementary Particle Theory, Proceedings Of The Nobel Symposium Held 1968 At Lerum Sweden, Stockholm. *Phys. Rev.*, , pages 367–377, 1968.

[10] F. Halzen and A.D. Martin. QUARKS AND LEPTONS: An Introductory Course in Modern Particle Physics. John Wiley & sons, 1984.

[11] I.J.R. Aitchison and A.J.G. Hey. Gauge Theories in Particle Physics. Adam Hilger, 1989.

[12] D. Perkins. Introduction to High Energy Physics. Addison-Wesley Publishing Company, 1984.

[13] J.D. Bjorken and E.A. Paschos. Inelastic Electron-Proton and γ-Proton Scattering and the Structure of the Nucleon. *Phys. Rev.*, **185**, pages 1975–1982, 1969.

[14] R.P. Feynman. Photon-Hadron-Interaction. W.A.Benjamin, Inc., Advance Book Program, Reading Massachusetts, 1972.

[15] C.G. Callan and D.J. Gross. High-Energy Electroproduction and the Constitution of the Electric Current. *Phys. Rev. Lett.*, **22**, pages 156–159, 1969.

[16] H. Abramowizc CDHS Collaboration. *Z. Phys.*, **C 17**, page 283, 1983.

[17] D. J. Fox et al. *Phys. Rev. Lett.*, **33**, page 1504, 1974.

[18] Y. Watanabe et al. *Phys. Rev. Lett.*, **35**, page 898, 1975.

[19] D.J. Gross and F.Wilczek. *Phys. Rev. Lett.*, **30(26)**, page 1343, 1973.

[20] D.J. Gross and F.Wilczek. *Phys. Rev.*, **D8(10)**, page 3633, 1973.

[21] Y.L. Dokshitzer. Calculation of structure functions of deep inelastic scattering and e^+e^- annihilation by perturbation theory in quantum chromo dynamics. *Sov. Phys. JTEP*, **46**, pages 641–653, 1977.

[22] V.N. Gribov and L.N. Lipatov. Deep Inelastic *ep* Scattering in Perturbation Theory. *Sov. Journ. Nucl. Phys.*, **15**, pages 438–450, 1972.

[23] V.N. Gribov and L.N. Lipatov. e^+e^--Pair Annihilation and Deep Inelastic *ep* Scattering in Perturbation Theory. *Sov. Journ. Nucl. Phys.*, **15**, pages 675–684, 1972.

[24] G. Altarelli and G. Parisi. Asymptotic Freedom in Parton Language. *Nucl. Phys.*, **B126**, pages 298–318, 1977.

[25] H1 Collaboration, C. Adloff et al. Measurement of Neutral and Charged Current Cross Sections in Electron-Proton Collisions at High Q^2. *Eur. Phys. J.*, **C19**, page 269, 2001.

[26] BCDMS Collaboration, A. C. Benvenuti et al. A High Statistics Measurement of the Proton Structure Functions $F_2(x, Q^2)$ and R from Deep Inelastic Muon Scattering at High Q^2. *Phys. Lett.*, **B223**, page 485, 1989.

[27] NMC Collaboration, M. Arneodo et al. Measurement of the proton and the deuteron structure functions F_2^p and F_2^d. *Phys. Lett.*, **B364**, pages 107–115, 1995.

[28] http://pdg.lbl.gov/.

[29] C.S. Wu et al. *Phys.Rev*, **105**, page 1413, 1957.

[30] C. Kiesling. Tests of the Standard Theory of Electroweak Interactions. Springer-Verlag Berlin Heidelberg, 1988.

[31] N. Cabibbo. *Phys.Rev.Lett.*, **10**, page 531, 1963.

[32] H. Yukawa. *Proc.Phys.-Math.Soc.Japan*, **17**, page 48, 1935.

[33] S.A. Bludman. *Nuovo Cimento*, **9**, page 443, 1958.

[34] P.W. Higgs. *Phys.Rev.Lett.12*, **12**, page 132, 1965.

[35] P.W. Higgs. *Phys.Rev.Lett.12*, **145**, page 1156, 1966.

[36] J.W Rohlf. Modern Physics from α to Z^0. John Wiley & Sons.Inc.

[37] UA1 Collaboration, G. Arnison et al. *Phys.Rev.Lett.B*, **122**, 1983.

[38] UA1 Collaboration, M. Banner et al. *Phys.Rev.Lett.B*, **122**, 1983.

[39] D. Griffiths. Introduction to Elementary Particles. HARPER & ROW, PUBLISHERS, New York, 1987.

[40] C. Adloff et al. Measurement and QCD Analysis of Neutral and Charged Current Cross Sections at HERA. *Eur.Phys.J.*, **C30**, page 1, 2003.

[41] Particle Data Group, L. Alvarez-Gaume et al. Review of Particle Physics. *Phys. Lett. B*, , page 592, 2004.

[42] A. Aktas et al. First Measurement of Charged Current Cross Sections at HERA with Longitudinally Polarised Positrons. *Phys. Lett. B.*, **634**, pages 176–179, 2006.

[43] P. Schmüser. The Electron Proton Colliding Beam Facility HERA. *Nucl. Instrum. Meth.*, **A235**, pages 201–208, 1984.

[44] H1 Collaboration, I. Abt et al. The H1 Detector at HERA. DESY Report DESY-93-103, DESY, 1993.

[45] ZEUS Coll. The ZEUS Detector. Status Report, 1993.

[46] HERMES Collaboration. HERMES Technical Design Report, 1993. DESY PRC-93-06.

[47] M.Dohlus et al. Report from the HERA Taskforce on Luminosity Optimization: Theory and First Luminosity Scans. Technical report, DESY, 2003.

[48] A.A. Sokolov and I.M. Ternov. On polarisation and spin effects in the theory of synchrotron radiation. *Sov.Phys.Dokl.*, **8**, pages 1203–1205, 1964.

[49] J. Böhme. Precision Measurement with the Transverse Polarimeter at HERA II. *Eur. Phys. J.*, **C30**, pages 1067–1069, 2004.

[50] M. Beckman et al. The Longitudinal Polarimter at HERA. *Nucl.Instrum.Meth.*, **A 479**, page 334, 2002.

[51] F. Zomer. A high power Fabry-Pereot resonator for Compton Polarimetry with the longitudinally polarised lepton beams at HERA. Habilitation, Orsay, 2003. also available at http://www-h1.desy.de/publications/theses_list.html.

[52] W. Lorenzon [HERMES Collaboration]. 7th International Workshop on Polarized Gas Targets and Polarised Beams, 1997. DESY-HERMES-97-68.

[53] H1 Collaboration, I. Abt et al. The H1 detector at HERA. *Nucl. Instrum. Meth.*, **A386**, pages 310–347, 1997.

[54] H1 Collaboration, I. Abt et al. The tracking calorimeter and muon detectors of the H1 experiment at HERA. *Nucl. Instrum. Meth.*, **A386**, pages 348–396, 1997.

[55] W. Brückner et al. Upgrade of the H1 Forward Neutron Calorimeter. H1–Note H1-11/99-578, DESY, 2000.

[56] H1 Collaboration. Proposal to Upgrade the LAr Calorimeter Trigger: The Jet Trigger. Technical Report DESY-PRC-99-02, DESY, 1999.

[57] H1 Collaboration. Proposal for Installation of a Very Forward Proton Spectrometer in H1 after 2000. H1–Note H1-5/00-582, DESY, 2000.

[58] J. Bürger et al. The Central Jet Chamber of the H1 Experiment. *Nucl. Instrum. Meth.*, **A279**, pages 217–222, 1989.

[59] P. Marage et al. Construction of a cylindrical MWPC for the central tracking detector of H1. *Nucl. Phys. Proc. Suppl.*, **16**, page 518, 1990.

[60] K. Müller et al. Construction and performance of a thin cylindrical multi wire proportional chamber with cathode pad readout for the H1-Experiment. *Nucl. Instrum. Meth.*, **A312**, pages 457–466, 1992.

[61] S. Burke et al. Track finding and fitting in the H1 Forward Track Detector. *Nucl. Instrum. Meth.*, **A373**, pages 227–260, 1996.

[62] G.A. Beck et al. Radial Wire Drift Chambers for the H1 Forward Track Detector at HERA: Design, Construction and Performance. *Nucl. Instrum. Meth.*, **A283**, pages 471–476, 1989.

[63] H1 Collaboration. A Forward Silicon Tracker for H1. H1–Note DESY-PRC-99-02, DESY, 1999.

[64] I. Tsurin. The Backward Silicon Track Trigger of the HERA Experiment H1. Dissertation, Univeristat Berlin, 2003.

[65] M. Cuje et al. H1 High Luminosity Upgrade 2000, CIP and Level 1 Vertex Trigger, 2000.

[66] M.C. Urban. The new CIP2k z-Vertex Trigger for the H1 Experiment at HERA. Dissertation, Universität Zürich, 2004.
also available at http://www-h1.desy.de/publications/theses_list.html.

[67] H1 Calorimeter Group, B. Andrieu et al. The H1 Liquid Argon Calorimeter System. *Nucl. Instrum. Meth.*, **A336**, pages 460–498, 1993.

[68] H. Oberlack H. Wellisch, J. Kubenka and P. Schacht. H1–Note H1-02/94-346, DESY, 1994.

[69] W.J. Willis et al. Liquid-Argon Ionization Chambers as Total-Absorption Detectors. *Nucl. Instrum. Meth.*, **120**, pages 221–236, 1974.

[70] H1 Calorimeter Group, B. Andrieu et al. Results from Pion Calibration Runs for the H1 Liquid Argon Calorimeter and Comparisons with Simulations. *Nucl. Instrum. Meth.*, **A336**, pages 499–509, 1993.

[71] H1 Calorimeter Group, B. Andrieu et al. Beam tests and calibration of the H1 liquid argon calorimeter with electrons. *Nucl. Instrum. Meth.*, **A350**, pages 57–72, 1994.

[72] H1 Spacal Group, R.-D. Appuhn et al. The H1 lead/scintillating-fibre calorimeter. *Nucl. Instrum. Meth.*, **A386**, pages 397–408, 1997.

[73] T. Nicholls et al. H1 SPACAL Group. Performance of an Electromagnetic Lead / Scintillating Fiber Calorimeter for the H1 Detector. *Nucl. Instrum. Meth.*, **A374**, pages 149–156, 1996.

[74] W. Bethe and W. Heitler. On the Stopping of Fast Particles and on the Creation of Positive Electrons. *Proceedings of the Royal Society*, **A146**, pages 83–112, 1934.

[75] N. Gogitidze and S. Levonian. An Offline Luminosity Determination for the H1 e^+p Data. H1–Note H1-01/96-471, DESY, 1996.

[76] E. Elsen. Aspects of the H1 trigger and data acquisition system. Prepared for 2nd Annual Conference on Electronics for Future Colliders, Chestnut Ridge, N.Y., 19-21 May 1992.

[77] H. Krehbiel. The H1 Trigger Decider: From Trigger Elements to L1-Keep. H1–Note H1-09/92-239, DESY, 1992.

[78] M. zur Nedden et all. H1 Liquid Argon Trigger: Overview, Simulation and Performance. H1–Note H1-04/01-592, DESY, 2001.

[79] T. Carli et al. Performance of the H1 LAr Trigger in 1994. H1–Note H1-07/95-445, DESY, 1995.

[80] C. Beigbeder. Level 2 Topological Trigger (L2TT) Hardware. H1–Note H1-07/98-547, DESY, 1998.

[81] J.K. Köhne et al. Realization of a second level neural network trigger for the H1 experiment at HERA. *Nucl. Instrum. Meth.*, **A389**, pages 128–133, 1997.

[82] A. Baird et al. *IEEE Trans. Nucl. Sci.*, **48**, page 1276, 2001.

[83] H. Kuester. On the treatment of calorimeter cells and clusters in H1REC and PHAN Physics analysis. Internal Software Note 45-03, DESY, 1994.

[84] H. Spiesberger at al. Radiative Corrections at HERA. In W. Buchmüller and G. Ingelmann, *Proceedings of the Workshop: Physics at HERA*, volume 2, pages 798–839. DESY, October 1992.

[85] K.Rüter. Untersuchung des schwachen geladenen Stroms in tiefinelastischen Positron-Proton Kollisionen mit dem H1-Detektor am HERA Speicherring. Dissertation, Ludwig-Maximilians-Univ. Muenchen, 1996.
also available at http://www-h1.desy.de/publications/theses_list.html.

[86] A.D. Martin, R.G. Roberts and W.J. Stirling. Parton distributions updated. *Phys. Lett.*, **B306**, pages 145–150, 1993. Erratum, Phys. Lett. **B309**, 1993, page 492.

[87] A.D. Martin, R.G. Roberts and W.J. Stirling. Erratum. *Phys. Lett.*, **B309**, page 492, 1993.

[88] G. Ingelman. LEPTO Version 6.1 - The Lund Monte Carlo for Deep Inelastic Lepton-Nucleon Scattering. In W. Buchmüller and G. Ingelmann, *Proceedings of the Workshop: Physics at HERA*, volume 3, pages 1366–1394. DESY, October 1992.

[89] J. Meyer. Guide for the H1 simulation program H1SIM. Internal Software–Note 03-11/89, DESY, 1989.

[90] R. Brun et al. GEANT3 User's Guide. *CERN-DD/EE-84-1*, 1987.

[91] M. Peters. Die parametrisierte Simulation elektromagnetischer Schauer. Dissertation, MPI München, 1992.

[92] M. Rudowicz. Hadronische Schauersimulation für den H1-Detektor. Dissertation, MPI München, 1992.

[93] G.A. Schuller and H. Spiesberger. DJANGO: The Interface for the Event Generators HERACLES and LEPTO. In W. Buchmüller and G. Ingelmann, *Proceedings of the Workshop: Physics at HERA*, volume 3, pages 1419–1432. DESY, October 1992.

[94] H. Spiesberger. private communication.

[95] H. Spiesberger A. Kwiatkowski and H.J. Mohring. HERACLES: An Event Generator for *ep* Interactions at HERA Energies including Radiative Processes: Version 1.0. *Comp. Phys. Comm.*, **69**, pages 155–172, 1992.

[96] L. Lonnblad. ARIADNE Version 4 – A program for simulation of QCD cascades implementing the color dipole model. *Comp. Phys. Comm.*, **71**, pages 15–31, 1992.

[97] T. Sjöstrand. PYTHIA 5.6 and JETSET 7.3: Physics and manual.

[98] T. Sjöstrand and M. Bengtsson. The Lund Monte Carlo for Jet Fragmentation and e^+e^- Physics – Jetset Version 6.3 – An Update. *Comp. Phys. Comm.*, **43**, pages 367–379, 1987.

[99] T. Sjöstrand. High-energy-physics event generation with PYTHIA 5.7 and JETSET 7.4. *Comp. Phys. Comm.*, **82**, pages 74–89, 1994.

[100] M. Glück, E. Reya and A. Vogt. Dynamical parton distributions of the proton and small x physics. *Z. Phys.*, **C67**, page 433, 1995.

[101] M. Glück, E. Reya and A. Vogt. Photonic parton distributions. *Phys. Rev.*, **D46**, pages 1973–1979, 1992.

[102] C. Diaconu et al. H1EPVEC-$W^{\pm}$ and Z production Monte Carlo Generator Based on EPVEC, 1999.

[103] T. Abe et al. GRAPE-Dilepton (Version 1.0). In G. Ingelmann H. Jung A. T. Doyle, G. Grindhamer, *Proceedings of the Workshop Monte Carlo Generators for HERA Physics*, page 566. DESY, 1998/99.

[104] H. Spiesberger B. Heinemann, S. Ries. Radiative Corrections for Charged Current Scattering: A Comparison of Computer Codes.

[105] H. Spiesberger et al. Radiative Corrections at HERA. In W. Buchmüller and G. Ingelmann, *Proceedings of the Workshop: Physics at HERA*, volume 2, pages 798–839. DESY, October 1992.

[106] A. Schoening. Untersuchung von Prozessen mit virtuellen und reellen $W^{\pm}$-Bosonen am H1-Detektor bei HERA. Dissertation, Univ.Hamburg, 1996.
also available at http://www-h1.desy.de/publications/theses_list.html.

[107] F. Keil. Dijet Production in Charged and Neutral Current e^+p Interactions at High Q^2 at HERA. Dissertation, Univ. Heidelberg, 2001.
also available at http://www-h1.desy.de/publications/theses_list.html.

[108] A. Blondel and F. Jacquet. In U. Amaldi, *Proceedings of the Study of an ep Facility for Europe*, page 391. DESY 79/48, 1979.

[109] S. Bentvelsen et al. Reconstruction of (x, Q^2) and extraction of structure functions in neutral current scattering at HERA. In W. Buchmüller and G. Ingelmann, *Proceedings of the Workshop: Physics at HERA*, volume 1, pages 23–40. DESY, 1992.

[110] U. Bassler and G. Bernardi. On the kinematic reconstruction of deep inelastic scattering at HERA. *Nucl. Instrum. Meth.*, **A361**, pages 197–208, 1995.

[111] U. Bassler and G. Bernardi. Structure function measurements and kinematic reconstruction at HERA. *Nucl. Instrum. Meth.*, **A426**, pages 583–598, 1999.

[112] B. Portheault M. Peez and E. Sauvan. An Energy Flow Algorithm for Hadronic Reconstruction in OO: Hadroo2. H1–Note H1-01/05-616, DESY, 2005.

[113] QHQTRK manual. (Heavy Flavor Working Group track selection code by Lee West).

[114] J. Cao and Z. Zhang. Towards an Unbiased Measurement of Kinematic Variables at Low y Region. H1–Note H1-12/99-590, DESY, 1999.

[115] Z. Zhang at al. M. Jacquet. Absolute Hadronic Jet Calibration of the H1 Liquid Argon Calorimeter. H1–Note H1-04/99-571, DESY, 1999.

[116] B. Vujičić. Study of the Liquid Argon Trigger in the H1 Detector at HERA II. Diploma Thesis, University of Montenegro, Faculty of Science, 2003.

[117] T. Nicholls H. Rick J. Coughlan, E. Elsen and H. C. Schultz-Coulon. A General Scheme for Optimization of Trigger Rates in an Experiment with Limited Bandwidth.

[118] B. Antunović et al. nElan Proposal for High Q^2 Triggers in 2006, 2006.

[119] J. Zimmermann. Statistical Learning in High Energy and Astro Physics. Dissertation, LMU Munchen, 2005.
also available at http://www-h1.desy.de/publications/theses_list.html.

[120] The H1OO Group. The H1OO Physics Analysis Project, 2005.

[121] A. Nikoforov. PhD Thesis (in preparation). Dissertation, Ludwig-Maximilians-Universität München, 2006.
will be available at http://www-h1.desy.de/publications/theses_list.html.

[122] L. Negri et al. A minimal Comprehensive set of Muon Background Topological Finders for High p_t Physics Analysis. H1–Note H1-10/96-498, DESY, 1996.

[123] E. Chabert et al. Qbgfmar: An Updated Phan Package for Cosmic and Halo Muon Topological Rejection in High p_t Physics Analysis. H1–Note H1-11/98-556, DESY, 1998.

[124] Ch. Veelken. H1 non-*ep* Background Finder-Rejection of Cosmic Muon and Beam-Halo Events in the H1OO Framework. H1–Note H1-09/02-603, DESY, 2003.

[125] R. Placakyte. First Measurement of Charged Current Cross Section with Longitudinally Polarised Positrons at HERA. Dissertation, Ludwig-Maximilians-Universität München, 2006.
also available at http://www-h1.desy.de/publications/theses_list.html.

[126] B. Heinemann. Measurement of Charged Current and Neutral Current Cross Sections in Positron-Proton Collisions at $\sqrt{s} \backsimeq 300$ GeV. Dissertation, Universität Hamburg, 1999.
also available at http://www-h1.desy.de/publications/theses_list.html.

[127] A. Aktas. Messung von Polarisierten Wirkungsueschnitten des Geladened Stromes bei HERA. Dissertation, Universität Hamburg, 2005.
also available at http://www-h1.desy.de/publications/theses_list.html.

[128] H1 Collaboration, A. Aktas et al. A General Search for New Phenomena in *ep* Scattering at HERA. *Phys. Lett. B*, **602**, page 602, 2004.

[129] Z. Zhang B. Portheault. Radiative corrections for Charged Current Process at HERA Revisited. H1–Note H1-11/04-614, DESY, 2004.

[130] H1 Collaboration, B. Antunović. Charged Current Interactions in Electron-Proton Collisions at HERA II. In *talk presented on XIIIth International Workshop on Deep Inelastic Scattering, Tsukuba*, 2006.

[131] Z. Zhiqing. private communication.

[132] ZEUS Collaboration. Measurement of high-Q^2 charged current cross section in e^+p deep inelastic scattering at HERA. *Nucl. Instrum. Meth.*

[133] http://www-zeus.desy.de/physics/sfew/PUBLIC/sfew_results/published/cc-9900/f2.dat.

[134] U. Yang. A Measurement of Differential Cross Sections incharged Current Neutrino Interactions on Iron and a Global Structure Function Analysis. Dissertation, University of Rochester, 2001.

[135] http://hep.uchicago.edu/ ukyang/neutrino/sf/f2-table.final.

[136] M. Tzanov. Precise Measurement of the Differential Cross Section for $\nu - Fe$ and $\bar{\nu}$-Fe Scattering. In *talk presented on XIIIth International Workshop on Deep Inelastic Scattering, Tsukuba*, 2005.

[137] B. Reisert and Th. Schörner. An Ntuple Interface for the LAr Trigger Software Package. Technical Report H1-05/00-583, 2000.

Acknowlegements

This thesis would not have been possible without the contributions and help of many people.

First of all I would like to thank my supervisor Prof. Christian Kiesling for giving me the opportunity to work within the H1 group at MPIM. I am grateful for his enormous enthusiasm and incredible patience in teaching and discussions since I have started to work within the H1 group. I very much appreciate that he has found time for detailed proof-reading of this thesis.

I wish to express my gratitude to Prof.dr. Othmar Biebel for kindly accepting to be my second advisor.

In particular, I owe a debt of thanks to Vladimir Chekelian, whose continuous interest and useful advises were of great help. I am especially grateful for his guidance in the structure function measurement and his critical reading of the thesis.

Furthermore, I am very greateful to Eram Rizvi, Zhiqing Zhang and Emanuel Sauvan for clear explanations and advises related to the analysis, especially for their cheering my spirit during the hard time of the DIS preliminaries.

The H1 group in Munich: Ana Dubak, Bob Olivier, Ludger Janaushek, Ringaile Placakyte and Jens Zimmermann made the work much easier with long "tea break" discussions, enjoyable table tennis games and friendly atmosphere during past years. In particular, I would like to thank Ringaile Placakyte with whom I shared the office during past years, for discussions, jokes and great coffee. Many thanks go to Ana Dubak and Burkard Reisert who found time to read the draft of this thesis.

I would also like to thank to my uncle Borko who should be blamed for my deep interesting in physics.

A special thank you goes to my family: mother, father, my sweet sisters for their enormous love, understanding and support I have been getting through all my life.

Finally, a deep thank you deserves my husband Dragan who with love shared all my ups and downs in the last year. His jokes, optimism and support helped me to survive whenever I was wondering does this work make sense.